ANALYSIS OF COMPOSITE BEAMS WITH AIRFOIL CROSS-SECTIONS WITH I-SECTION STIFFENER UNDER TENSION AND BI-DIRECTIONAL MOMENTS

by

PETER LEBOULLUEC

DISSERTATION

Submitted in partial fulfillment of the requirements
for the degree of Doctor of Philosophy at
The University of Texas at Arlington
September 2016

Arlington, Texas

Supervising Committee:

Wen S. Chan, Supervising Professor
Ashfaq Adnan, Co-Advisor
Kent Lawrence
Robert Taylor

DEDICATION

I dedicate this dissertation to my mother and father who instilled in me a hard work ethic and persistence. Also to my wife who gave me courage and support to pursue my PhD.

ACKNOWLEDGEMENTS

I thank Dr. Wen S. Chan, my Supervising Professor, for his continued support and guidance throughout my graduate studies. I thank Dr. Ashfaq Adnan, my Co-Advisor, for his encouragement and support and also thank my Supervising Committee including Dr. Kent Lawrence and Dr. Robert Taylor for their input, teachings, and advice.

Many individuals have also provided a helping hand notably in the experimental section of my work. They include Glaucio Carley, Sawyer Stuart, Anirudh Markkassery, and Scott Berggren who helped me fabricate my composite wings, Amit Murlidhar, Sakit Thapliyal and Yobani Martinez who helped make 3D printed fixtures, Kermit Beird who gave advice in manufacturing and testing of my wings, and Sakit Thapliyal, Rajni Chahal, and Eric Wu who helped to test experimental specimens. I also thank the UTA formula team for allowing me to use one of their airfoil molds and to their composite crew who gave me many tips helping me to fabricate good airfoils.

September 9, 2016

ABSTRACT

ANALYSIS OF COMPOSITE BEAMS WITH AIRFOIL CROSS-SECTIONS WITH I-SECTION STIFFENER UNDER TENSION AND BI-DIRECTIONAL MOMENTS

Peter LeBoulluec, PhD
The University of Texas at Arlington, 2016

Supervising Professor: Wen S. Chan

Co-Advisor: Ashfaq Adnan

Annual wind power generation capacity in the US has increased from 3 gigawatts in 2000 to 61 gigawatts in 2013 and is on track to fulfill 20% of projected U.S. electricity needs (305 gigawatts) by 2030. To enable the increase in electricity generation of wind turbines, longer blades are being designed which require improved engineered blades to handle higher loads. Thus, the wind turbine industry is turning to the use of carbon-epoxy composite materials to take advantage of their low weight yet high strength ratio and improved fatigue resistance. Current analyses to design turbine blades utilize either Finite Element Analysis programs, which are time consuming and costly for conducting parametric studies in the preliminary design stage, or use analytical solutions which are inaccurate or too complex.

In this research, an analytical model based on Narrow Beam Theory, a modification of Classical Lamination Theory, will be made and coded into MATLAB to quickly conduct structural analyses on portions of composite turbine blades with airfoil

cross-sections. Various laminate layups can be studied with the current model as well as various airfoil cross-sections. This analysis will predict the structural stiffnesses and stresses and strains in individual composite plies of airfoil blades with and without I-beam stiffeners under axial and bending loads. Results will be validated using ANSYS FEM and with experimental specimens. The experimental work consists of fabricating laminates to obtain basic material properties and fabricating uniform airfoil wings to conduct a transversely loaded bending test to find flapwise bending stiffness.

I-beams will also be analyzed separately from airfoil cross-sections to understand their stiffness and stress characteristics and to investigate Narrow Beam Theory. Thus, by enabling a quick and simple, yet accurate static analysis on composite turbine blades, improved initial designs can be determined in an early design phase to allow more efficient, reliable, and economical turbine blades to be made.

TABLE OF CONTENTS

LIST OF ILLUSTRATIONS

LIST OF TABLES

CHAPTER 1

INTRODUCTION

Wind turbines are one of the most promising producers of electricity to reduce the world's dependence on fossil fuels. In 2013, the United States produced 4.5% (61 GW) of its electricity consumption by wind energy, and in comparison, only 1% of electricity from solar energy in 2015. The US Department of Energy [1] has planned to enable production of 20% of U.S. electricity from wind energy by the year 2030. Globally, wind energy is expected to produce 12% of the world's electricity needs by 2020 and 23% by 2040 [2].

To facilitate the increased energy generation of wind turbines, turbine blades are made longer to capture more of the wind energy. Since the 1970's, most turbine blades have been composed of fiberglass composite material using a thermoset epoxy [3]. Composite materials such as fiberglass and carbon epoxy have high specific strength and stiffness, corrosion resistance, low thermal expansion, design flexibility, and reduced part count which make them good candidates for turbine blades. The maximum length of turbine blades used today are approximately 65 meters and there are prototype designs using 100 meter blades by, for example, Sandia National Laboratories. These long blades are sometimes made with carbon epoxy caps which are flanges of the stiffener [4].

A turbine blade consists of a root end that bolts to a rotor hub, a transition section that transitions from the circular root end to the maximum chord airfoil shape, and an airfoil section that transforms the wind to mechanical energy. Down the length of the

airfoil section, from the largest chord length to the blade tip, multiple airfoil shapes are often used. This is shown in Figure 1.1 which is a prototype design of a 100 meter blade by Sandia National Laboratories. Each airfoil cross section shown has a unique shape [5]. Inside the blade, spars are used which are attached to the upper to lower skin surfaces by the use of flanges. Spars can be in the form of I-beams, box channels, D-spars, or other. The skins are normally a composite sandwich construction. Typically, the upper and lower surfaces are made separately then adhesively joined together with the spar. Components of typical wind turbine beam cross sections are shown in Figures 1.2 and 1.3.

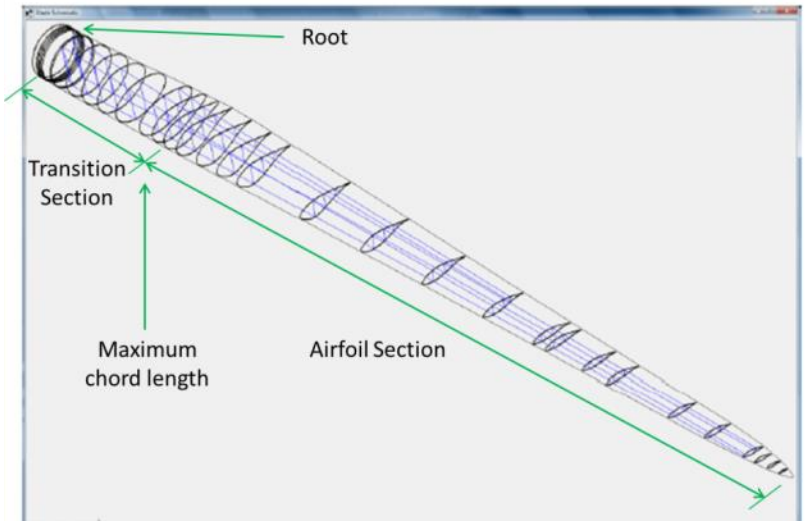

Figure 1.1 Complete blade with visible cross sections

(from Griffith, Sandia Labs, 2011 [5])

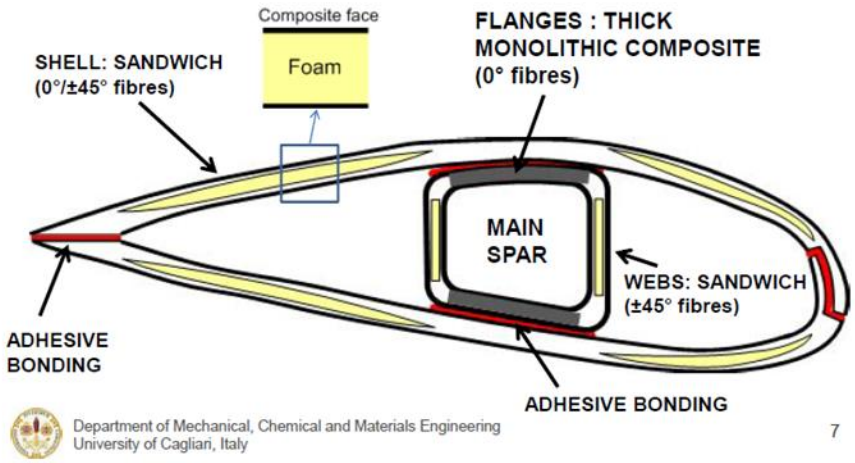

Figure 1.2 Components of wind turbine blade, cross sectional view

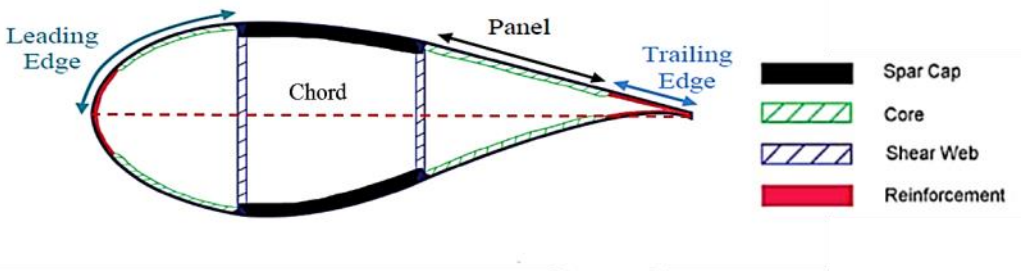

Figure 1.3 Components of wind turbine blade, cross sectional view, alternate design (from Griffith, Sandia Labs, 2011 [5])

DESIGNING THIN-WALLED BEAMS

A wind turbine blade can be modeled as a closed section cantilever beam with a thin wall assumption. The thin wall assumption is valid when the maximum cross section dimension to skin thickness (or depth) ratio is greater than 10. The actual minimum chord to thickness ratio of Sandia's 100 meter blade (shown in Figure 1.1) is 61 in the skin panels and 72 in the spar flange area [5].

THIN WALL BEAM THEORY

Most thin walled beam theory is based on work done by Vlasov around World War II for aircraft wings. Vlasov created the first thin walled beam theory for isotropic material, also called “warping torsion” or “non-uniform torsion”, for open and closed beam sections using isotropic material. For comparison, the classical theory is St. Venant’s “circulatory torsion” or “uniform torsion” theory. Given a torsional load, St. Venant’s theory assumes the cross-section remains rigid during twisting, out of plane warping is not constrained, cross sections remain planar, and the rate of twist is constant in the longitudinal direction. This allows for only tangential shear stresses linearly varying across the thickness in response to a torsional load where the torsional stiffness is (polar moment of inertia times shear modulus). St. Venant’s theory is useful for uniform beams which are long enough such that any restraint effects which inhibit warping due to torsion will decay and can be neglected.

However, warping is often constrained due to boundary conditions, a localized torsional moment, distributed moments, or when the beam’s cross-section changes and should be taken into account in certain cases. Under each of these warp constraint conditions, the cross sections do not remain planar (non-uniform warping), thus axial loads inducing bi-moments are present, as seen in Figure1.4 under primary torsion. Note that St. Venant’s shear stress effects, which are equal to the torsional loading, are still present. Thus, warping constraints produce a warping stiffness which causes an increase in the structural torsional stiffness especially for open thin walled cross-sections but can sometimes be ignored for closed thin walled cross-sections [6]. However, composite materials are very flexible in shear such that the cross-section

should not be considered infinitely rigid. Also, the constrained warping effects decay at a slower rate for composites than for isotropic material so restrained warping should be considered for composites [7,8] for accurate analyses.

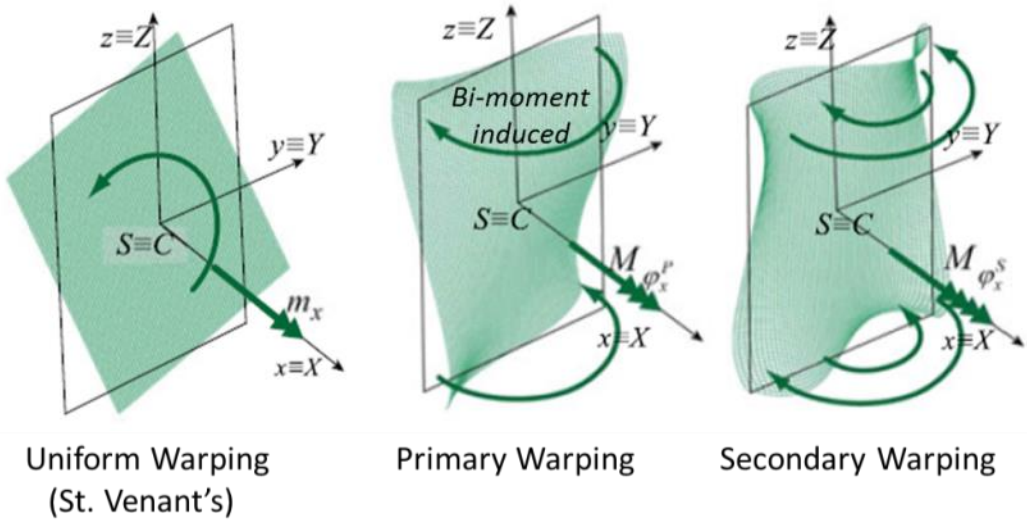

Figure 1.4 Constrained cross-section end of beam illustrating forms of warping (from Sapountzakis, 2015 [9])

Vlasov formulated analytical solutions for primary warping in the late 1930's [10]. Secondary warping becomes significant when either the wall thickness of beams increases, shear deformation is of importance, using anisotropic material [11], or for special cases such as circular cross-sections. Otherwise, primary warping is dominant over secondary warping for thin walled beams. Solutions for secondary warping or higher-order shear deformation were later added by Gjelsvik [12] concerning metallic thin walled beams.

In the 1970's, researchers started studying composite thin walled beams. In 1979, Mansfield and Sobey [13] developed a cylindrical tube model, one or two cells, for helicopter rotor blades and introduced the concepts of elastic tailoring. Using composite

laminate theory (Love-Kirchoff assumption), Bauld and Tzeng [14] extended Vlasov's theory to open section beams with midplane symmetry in 1984.

Many researchers analyzed rectangular shaped cross-sectional beams as an approximation of an airplane wing or rotor blade. In 1987, Bauchau, Coffenberry, and Rehfield [15] made a comprehensive analysis of composite thin walled box beams with closed sections while including the non-classical effects of transverse shear and restrained warping. Bank and Melehn [16] expanded on Timoshenko's beam theory to account for shear deformations by use of a shear correction factor on multi-cell composite box beams.

In 1992, Chandra and Chopra [17] gave analytical solutions verified by bending, torsional, extensional, and vibrational experiments on antisymmetric two-celled composite box and elliptical blades. This solution included non-uniform warping and transverse shear effects under a plane strain assumption. Along with this study, Smith and Chopra [18] gave experimental evidence that the effects of shear and warping during bending of composite thin walled box beams are significant, as shown in Figure 1.5. Note that the shear plot is obtained from an unbalanced and unsymmetric laminate. It should be noted that Smith and Chopra used a laminate of $[15]_{6T}$ to enhance the bending and twisting effect as seen in the left figure. However, common layups, for example symmetric laminates such as $[\pm 45/0]_S$, used for blades exhibit an insignificant twisting effect due to bending.

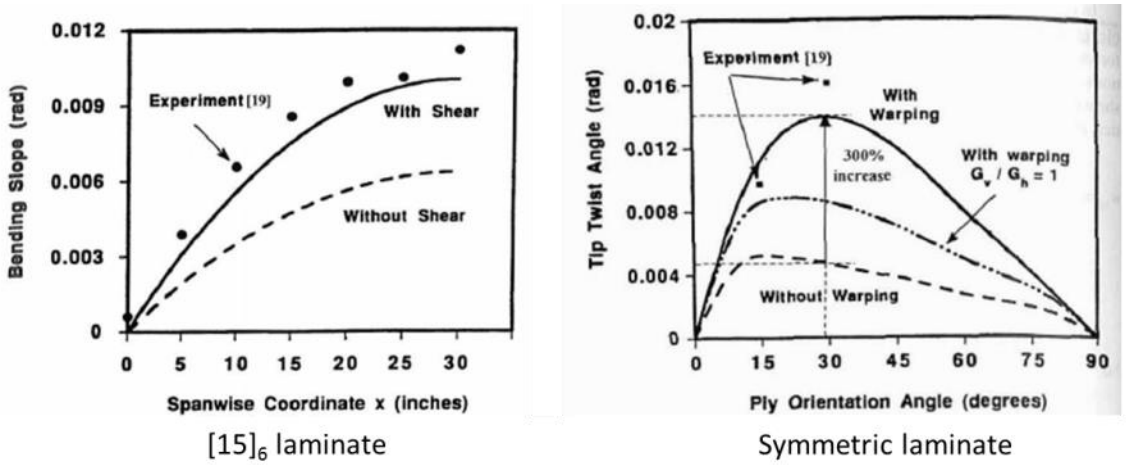

Figure 1.5 Experimental evidence of shear and warping effects on composite box beams (Smith and Chopra [18])

Non-uniform first order warping and transverse shear effects were also included in a simplified theory by Wu and Sun in 1992 [19]. They used more general assumptions than those of Vlasov. Kim and White in 1997 [20] produced one of the first theories on thin and thick walled composite closed section beams and accounted for three dimensional elastic effects. They included transverse shear and primary and secondary torsional warping effects. They found that secondary warping can be neglected with thin walled beams but is significant with thick walled beams.

In 2006, Librescu and Song [21,22] at Virginia Tech developed a comprehensive geometrically nonlinear theory based on Galerkin's variation method for anisotropic thin or thick walled beams. They took into consideration many non-classical effects including transverse shear, and primary and secondary warping. Pre-twisted, tapered beams, end and lateral loads, and body forces were also dealt with. Structural and dynamic properties were derived. Only box and elliptical beams were studied and the method is complex.

Much more research has been made over the years on variations (shown below) of thin walled composite beams that won't be covered here. Jung and Chopra [23] give a good review of thin walled beam research before the year 2000.

- approach (displacement, stress, mixed; Classical Lamination Theory, smear),
- beam DOF (degree of freedom), (Euler-Bernoulli, St. Venant, Vlasov, higher-order shear deformation (HSDT)),
- constitutive relations (plane stress, plane strain),
- shell wall DOF (membrane, thin plate, HSDT),
- tailoring (passive, active), and
- dynamic analysis (bucking, vibration, time dependent excitation).

ANALYTICAL METHODS FOR WIND TURBINE BLADES

Analytical and finite element analysis of wind turbine blades based on thin walled beam theory have occurred relatively recently with the trend towards larger turbine blades. Prior to this, blades were improved mainly through trial and error. Most analytical methods used today for wind turbine blades can be divided up into ones using Classical Lamination Theory (CLT), smear properties, variational methods, or combinations of these as a basis. To analyze airfoils or other complex cross-sections, most break up the section into discrete finite elements and integrate them to find the overall structural properties.

Smear property methods have been used by numerous researchers including Park in 2009 [24], Wang in 2014 [25], and by the Dutch Knowledge Centre Wind Turbine Materials and Construction. These methods find axial, bending, and torsional

cross-sectional stiffnesses about a cross-section but do not calculate composite ply strains and stresses. Park's method, KSec2D, finds the stiffness of arbitrary cross-sections using composite laminate plate theory with a modulus weighted approach on isotropic equations. Wang's model, called Composite Blade Cross-Section Analysis or CBCSA, uses a weighting method based on CLT and uses a shear flow theory to find torsional stiffness. For a composite airfoil with shear webs, Wang's stiffness results are similar to Precomp's results (will be reviewed later) except Wang's calculation for torsional stiffness is 30 to 45% higher than Precomp's. However, Wang only compares an isotropic symmetric airfoil with finite element analysis. The Dutch Knowledge Center developed the FAROB tool which considers constant shear flow and can analyze hygrothermal loads. FAROB does not find the shear center and is not suited for arbitrary shaped cross-sections. FAROB is the structural analysis tool under FOCUS6, an FEA tool, which conducts dynamic analyses including a fatigue, buckling, and modal analysis [26].

Most analyses are a modification of CLT and perform a cross-sectional analysis yielding moments of inertias, axial, bending and torsional stiffness, mass, and shear center. Two such analysis tools capable of handling arbitrary sections with webs are Pre-Processor for Computing Composite Blade Properties (Precomp) created by Bir in 2001 [27] at the National Renewable Energy Laboratory (Bir, 2001), and Cross-sectional Stability of Anisotropic Blades (CROSTAB) developed at the Energy Research Centre of the Netherlands. Precomp adapts CLT with a constant shear flow approach, keeps web sections normal to the chord, neglects hoop stresses in flanges, and allows free warping. Also, transverse shearing is negligible (consequence of CLT) and the

section is free to warp (St. Venant's theory). CROSTAB also adapts CLT with shear flow. Bending and torsional stiffness are neglected in sectional property calculations and CROSTAB does not determine the shear center location. Neither Precomp or CROSTAB find stresses and strains in the composite laminate plies [26].

An approach for 3D arbitrary composite structures was developed by Hodges, Cesnik, Yu, and Volovoi [28] at Georgia Tech which is used by the helicopter industry today. Their theory breaks the 3D problem into a linear 2D analysis conducted by a variational asymptotic approach (VAM), and a geometrically exact 1D beam analysis. The 1D beam analysis allows for pre-twist, curved beams, and nonlinear effects without the use of tensor analysis, and finds the displacements (thus strains and stresses) over the whole continuum, thus is geometrically exact. Approximations are made in a 2D VAM analysis, developed by Berdichevsky in 1976 [29], which gives the best accuracy due to the VAM. The asymptotic correct functions are then used in classical engineering models such as Euler-Bernoulli, Timoshenko, or the Vlasov model. The actual tool is called VABS (Variational Asymptotic Approach Beam Sectional Analysis). Data is inputted into the VABS via PreVABS which takes information directly from a CAD package. The time and effort to run VABS is about the same as for Precomp.

Chen, Yu, and Capellaro [26] evaluated the results of each of these tools except for Wang's tool. Overall, VABS outperforms the other tools in predicting 2D structural properties for isotropic circular cross sections, anisotropic elliptical pipe, and an isotropic symmetric airfoil. When compared to analytical solutions or ANSYS solid element analysis for these cross-sectional configurations, VABS results are very similar. An actual airfoil with 5 varying skin compositions and 2 webs normal to the chord with

full elastic coupling was also checked. Precomp and CROSTAB had differences in most coupling terms by over 100% from VABS and subsequently, their stiffnesses were an average of 40% different than VABS. Also, Precomp's shear center was far off. VABS is a very accurate tool but the theory behind it is complex.

Furthermore, various finite element analyses have been conducted to obtain accurate results for structural properties and to conduct dynamic analyses. However, these take more time and are more expensive than analytical methods so, primarily, only analytical methods will be discussed here.

MOTIVATION FOR RESEARCH

Due to complex geometries of and the use of composite materials in blades in addition to stiffeners and tapering and pre-twist of the blade, existing finite element analyses take much time and are costly. Some analyses may use both finite element analyses and analytical solutions and can be quite accurate such as VABS, but are complex to understand. In an initial design phase to analyze airfoil beams as used on wind turbines, an engineer needs an understandable method to give quick and accurate results.

This research aims to develop a simplified approach based on modified Classical Lamination Theory for beam structures which is robust enough to analyze many parameters including airfoil shapes, stacking sequence, layers and stiffeners, and accurately find the stiffness and ply stresses of the beam. Loads considered will be axial and bi-directional bending moments about the centroid. Although the torsion is one of the loading conditions considered in design, this research will investigate will investigate

only bi-directional bending and tension. The centroid, stiffnesses including axial and bidirectional bending, and stresses in composite plies will be predicted and results will be verified with finite element analysis (FEA). Analytical stiffness and strain results subject to flapwise bending will be compared to experimental test specimen results. This research is a continuation of works by Chan and his former students: Syed, Rios, Parambil, Sanghavi, and Kora [30,31,32,33,34].

For this research, simplified blades are modeled using the 4-series NACA airfoil types as seen in Figure 1.6. The root and transition section will not be analyzed. The airfoil will be made from a monolithic laminate skin (no core used) using only one type of composite material. I-beamed stiffened airfoils as seen in Figure 1.7 will also be studied. Symmetric and non-symmetric airfoil cross-sectional geometries will be analyzed as well as the use of symmetric, unsymmetric and unbalanced airfoil skin laminates.

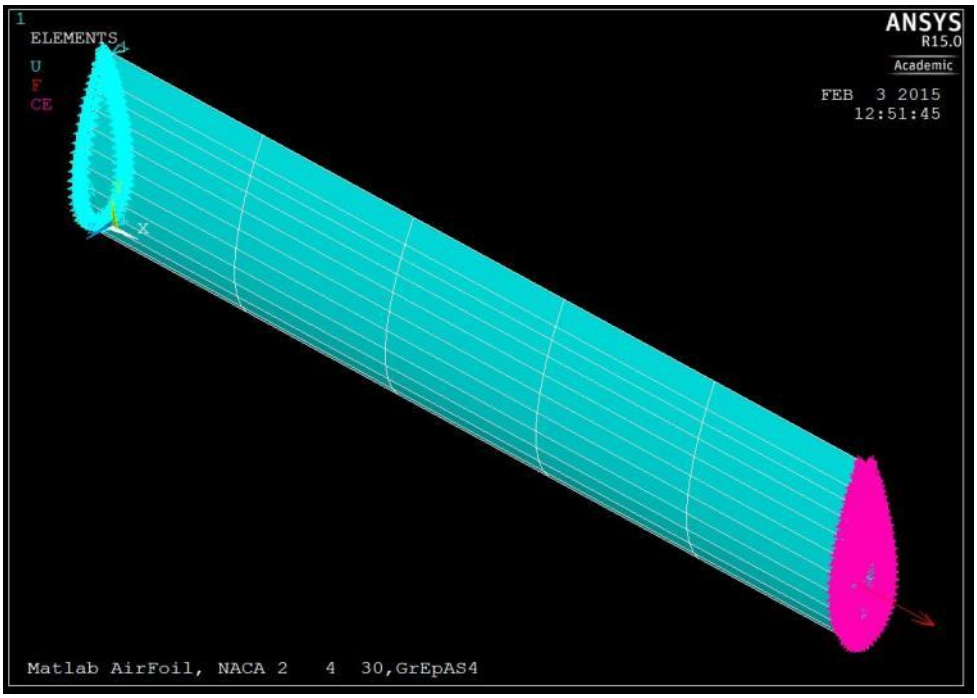

Figure 1.6 Typical FEA model with axial load applied at centroid, airfoil is NACA 2430 series

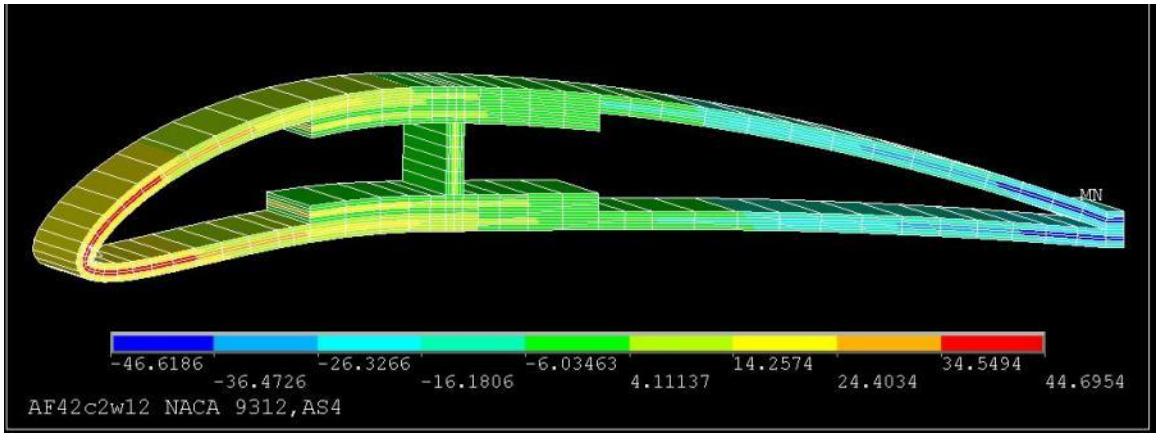

Figure 1.7 Cross-section of I-beam stiffened NACA 9312 series airfoil blade with stress contours

CHAPTER 2

NARROW BEAM PREDICTION OF THE BEHAVIOR OF AN I-BEAM UNDER AXIAL AND BI-DIRECTIONAL LOADS

Study of an I-beam is conducted to gain an understanding of its behavior, become familiar with and check predictions by Narrow Beam Theory on airfoils, gain experience to develop MATLAB code to run the analytical method, create APDL code to create models in ANSYS, and conduct post processing of FEM (Finite Element Method) results. The analytical methods used in this research are based on Classical Lamination Theory thus a brief overview of Classical Lamination Theory is given. This is followed by a discussion on developing equivalent mechanical and thermal properties for composite lamina, laminates, and structures such as the I-beam. Finally, the predictions of Narrow Beam Theory are compared to FEM on various I-beams and conclusions are given.

CLASSICAL LAMINATION THEORY

On a micro-scale level, a composite lamina is made up of fiber and resin which each have unique properties. To efficiently analyze a composite structure however, averaged properties of a lamina are utilized assuming perfect bonding between the fibers and resin. A lamina is defined by material properties in the principal material coordinate system as shown in Figure 2.1. Laminates can be classified as thin orthotropic materials. An orthogonal material has 3 mutually perpendicular planes which have unique properties from each other. For example, planes 1-2, 2-3 and 1-3 all have

unique properties and are symmetric relative to each plane. Orthotropic materials exhibit no extension-shear coupling and have 9 independent material constants whereas an anisotropic material has 21 independent material constants. The composite plate however has a plane of symmetry which is the 2-3 plane, making it transversely isotropic. Thus, material properties in the 2-3 plane are interchangeable (ie. $E_2 = E_3$), leaving 5 independent constants.

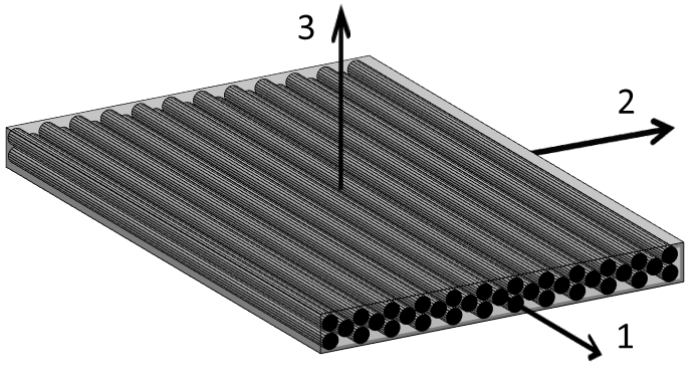

Figure 2.1 Lamina plate with principal material coordinate system

The compliance stress-strain relationship for a transversely isotropic material is,

$$\begin{pmatrix} \varepsilon_1 \\ \varepsilon_2 \\ \varepsilon_3 \\ \gamma_{23} \\ \gamma_{13} \\ \gamma_{12} \end{pmatrix} = \begin{pmatrix} S_{11} & S_{12} & S_{12} & 0 & 0 & 0 \\ & S_{22} & S_{23} & 0 & 0 & 0 \\ & & S_{22} & 0 & 0 & 0 \\ & & & 2(S_{22}-S_{23}) & 0 & 0 \\ & sym & & & S_{55} & 0 \\ & & & & & S_{55} \end{pmatrix} \cdot \begin{pmatrix} \sigma_1 \\ \sigma_2 \\ \sigma_3 \\ \tau_{23} \\ \tau_{13} \\ \tau_{12} \end{pmatrix}. \qquad (2\text{-}1)$$

Since a composite laminate is normally thin, it is easy to deform the laminate in the 3-direction so stresses in the 3-direction, which is out-of-plane of the plate, are negligible compared to stresses that are in-plane to the plate. Thus, a plane stress condition can be applied. This condition means that stresses in-plane to the plate are at

least an order of magnitude larger than stresses out-of-plane to the plate. Thus, according to Figure 2.2 on the right which shows the positive stresses on a small element of composite, stresses in the out-of-plane direction, σ_3, τ_{13} and τ_{23}, for a composite laminate are negligible and can be set to zero. Stresses in the in-plane direction, σ_1, σ_2 and τ_{12}, should be considered.

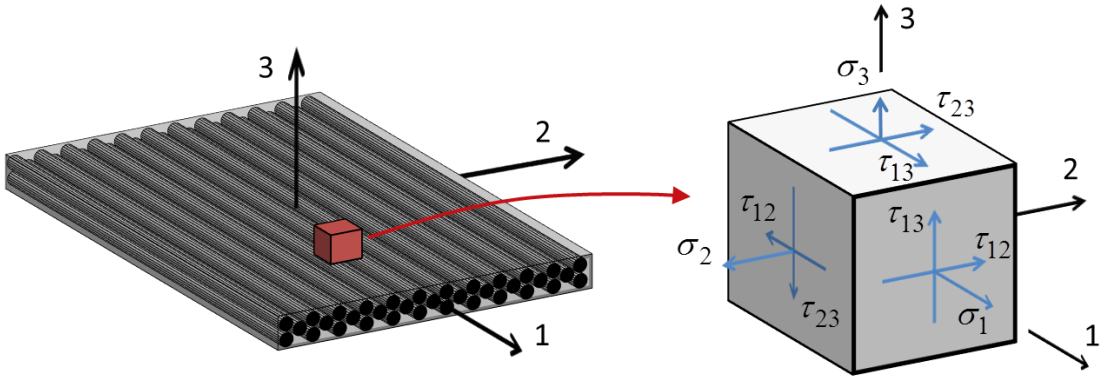

Figure.2.2 Composite lamina principal material directions and stresses on small representative element of lamina

Making the plane stress assumption, the compliance matrix simplifies to,

$$\begin{pmatrix} \varepsilon_1 \\ \varepsilon_2 \\ \gamma_{12} \end{pmatrix} = \begin{pmatrix} S_{11} & S_{12} & 0 \\ & S_{22} & 0 \\ sym & & S_{66} \end{pmatrix} \begin{pmatrix} \sigma_1 \\ \sigma_2 \\ \tau_{12} \end{pmatrix} = \begin{pmatrix} 1/E_1 & -\nu_{12}/E_1 & 0 \\ -\nu_{21}/E_2 & 1/E_2 & 0 \\ 0 & 0 & 1/G_{12} \end{pmatrix} \begin{pmatrix} \sigma_1 \\ \sigma_2 \\ \tau_{12} \end{pmatrix} \qquad (2\text{-}2)$$

Note that strain in the 3-direction, ε_3, is left out of this simplified matrix where,

$$\varepsilon_3 = S_{12}\sigma_1 + S_{23}\sigma_2 \qquad (2\text{-}3)$$

ε_3 can be used to find the changes in thickness of laminates due to in-plane loads and to find out-of-plane Poisson's ratios, however, this research will not use ε_3.

Given the plane stress condition, lamina material properties, including hygrothermal properties, that are considered for composite analysis include the:

- elastic modulus in the longitudinal or 1-direction: E_1,
- elastic modulus in the transverse or 2-direction: E_2,
- shear modulus in the 1-2 plane, G_{12},
- Poisson's ratio in the 1-2 plane, ν_{12}, (note, $\nu_{21} = \nu_{12}(E_2/E_1)$)
- coefficients of thermal expansion in the 1-2 plane, α_1, α_2, and
- coefficients of hygroscopic expansion due to moisture in the 1-2 plane, β_1, β_2.

By making the plane stress assumption, this precludes an analysis of delamination due to edge effects, imperfections such as waviness or voids, and stress concentration areas which all involve 3D stresses. However, for general static, dynamic, buckling, etc. structural analyses, the plane stress assumption does give accurate results of in-plane stresses.

The 3x3 simplified compliance matrix, equation 2.2, can be inverted yielding a 3x3 stiffness matrix shown below which is referred to as the reduced stiffness matrix since it incorporates the plane stress assumptions and essentially reduces the analysis to a 2D state.

$$\begin{pmatrix} \sigma_1 \\ \sigma_2 \\ \tau_{12} \end{pmatrix} = \begin{pmatrix} Q_{11} & Q_{12} & 0 \\ & Q_{22} & 0 \\ sym & & Q_{66} \end{pmatrix} \begin{pmatrix} \varepsilon_1 \\ \varepsilon_2 \\ \gamma_{12} \end{pmatrix} \qquad (2\text{-}4)$$

This reduced stiffness matrix characterizes a lamina. A laminate however is made up of lamina stacked in varying orientations as shown in Figure 2.3.

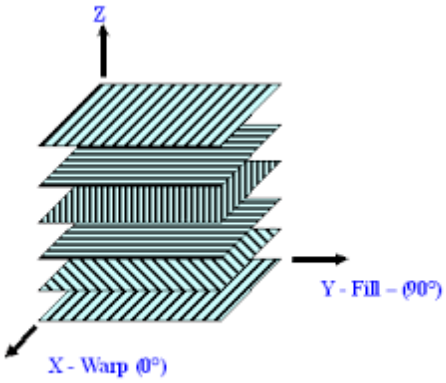

Figure 2.3 Laminate with exposed lamina

To characterize the whole laminate, a Cartesian global coordinate system, x-y-z system, is designated where the x-axis is in the direction of the primary load and the x-y plane is in the geometric middle of the laminate. The properties of each lamina must be added up to obtain the properties of the laminate. The first step to do this is to rotate each lamina's 2D properties in the 1-2 plane to the x-y global plane as seen in Figure 2.4. Note that $'\phi'$ is negative when the 1-2 coordinates rotate in the counter-clockwise direction.

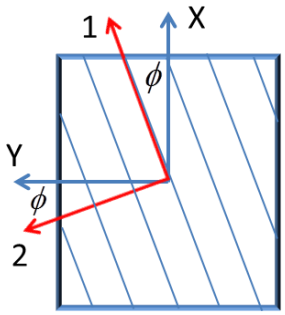

Figure 2.4 Rotation of lamina 1-2 plane to the x-y global plane

Mathematically, the rotation is accomplished by transformation of the reduced stiffness matrix as follows,

$$\left[\overline{Q}\right]_{x-y} = \left[T_\sigma(-\theta)\right]\cdot[Q]_{1-2}\left[T_\varepsilon(\theta)\right] = \left[T_\varepsilon(\theta)\right]^T\cdot[Q]_{1-2}\left[T_\varepsilon(\theta)\right], \qquad (2\text{-}4)$$

where the transformation matrices are,

$$\left[T_\sigma(\theta)\right] = \begin{pmatrix} m^2 & n^2 & 2mn \\ n^2 & m^2 & -2mn \\ -mn & mn & m^2-n^2 \end{pmatrix} \text{ and}$$

$$\left[T_\varepsilon(\theta)\right] = \begin{pmatrix} m^2 & n^2 & mn \\ n^2 & m^2 & -mn \\ -2mn & 2mn & m^2-n^2 \end{pmatrix}, \qquad (2\text{-}5)$$

where $m = \cos\theta$ and $n = \sin\theta$. $\left[\overline{Q}\right]_{x-y}$ is used to denote the reduced stiffness matrix of a lamina transformed to the global coordinate system. The stress-strain relation for each lamina can then be defined in the global coordinate system by:

$$\begin{pmatrix} \sigma_x \\ \sigma_y \\ \tau_{xy} \end{pmatrix} = \begin{pmatrix} \overline{Q}_{11} & \overline{Q}_{12} & \overline{Q}_{16} \\ & \overline{Q}_{22} & \overline{Q}_{26} \\ sym & & \overline{Q}_{66} \end{pmatrix}\cdot\begin{pmatrix} \varepsilon_x \\ \varepsilon_y \\ \gamma_{xy} \end{pmatrix} \text{ or } [\sigma]_{x-y} = \left[\overline{Q}\right]_{x-y}[\varepsilon]_{x-y}. \qquad (2\text{-}6)$$

To characterize the laminate, a few assumptions must be made concerning the deformation of the laminate. These assumptions that Classical Lamination Theory is based on are known as the Kirchoff Hypothesis which was developed in the mid 1800's. The theory states that, assuming a laminate plate is subject to a variety of loadings including point or distributed normal loads and moments, the normal denoted by AA' in Figure 2.5 will remain a straight line under deformation, keep its original length, and be normal to each lamina's interface.

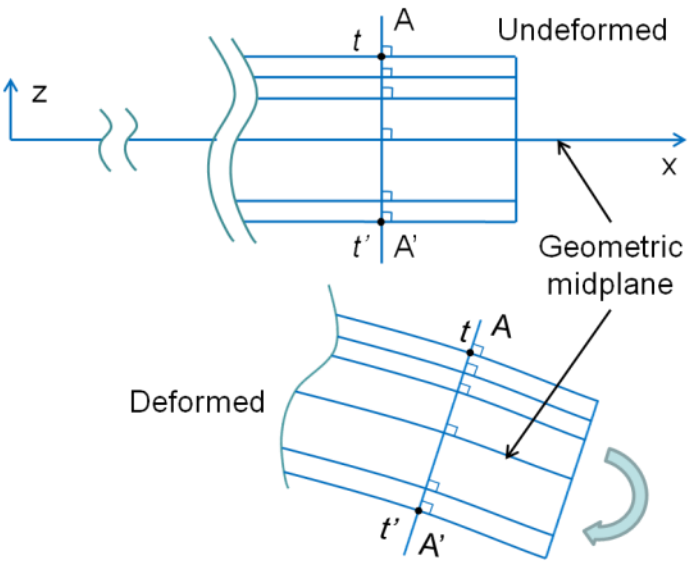

Figure 2.5 Cross sections showing normal before and after deformation

In effect, the plate curvature is approximated as a constant given small rotation angles allowing the normal AA' to translate and rotate under deformation and stay straight.

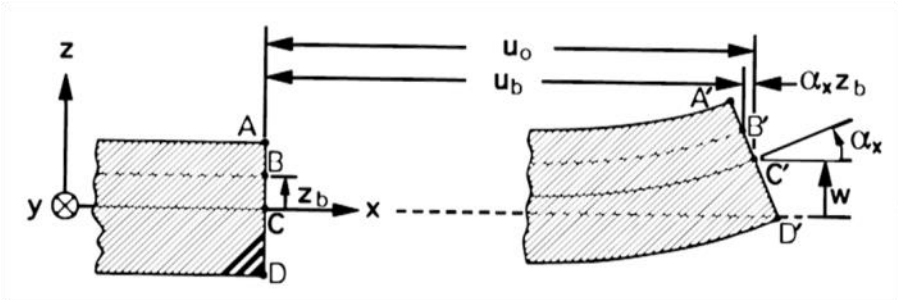

Figure 2.6 Constant curvature

Looking at the side view of a beam or plate as in Figure 2.6, the displacement at any point in the laminate is based on the midplane displacements, denoted by the 'o' subscript, and the curvature as follows,

$$u = u_o - \alpha_x z, \quad v = v_o - \alpha_y z, \quad w = w_o = w_o(x, y) \,. \tag{2-7}$$

z is the distance from a point to the midplane along the z-axis. The strain at any point in the laminate can then be defined by the behavior of the midplane of the laminate as follows,

$$\begin{aligned} \varepsilon_x &= \frac{\partial u}{\partial x} = \frac{\partial u_o}{\partial x} - z\frac{\partial^2 w}{\partial x^2} = \varepsilon_x^o + z\kappa_x \\ \varepsilon_y &= \frac{\partial v}{\partial y} = \frac{\partial v_o}{\partial y} - z\frac{\partial^2 w}{\partial y^2} = \varepsilon_y^o + z\kappa_y \\ \gamma_{xy} &= \frac{\partial u}{\partial y} + \frac{\partial v}{\partial x} = \frac{\partial u_o}{\partial y} + \frac{\partial v_o}{\partial x} - 2z\frac{\partial^2 w}{\partial x \partial y} = \gamma_{xy}^o + z\kappa_{xy} \end{aligned} \,. \tag{2-8}$$

This can be put in matrix form as follows,

$$\begin{bmatrix} \varepsilon_x \\ \varepsilon_y \\ \gamma_{xy} \end{bmatrix}_k = \begin{bmatrix} \varepsilon_x^o \\ \varepsilon_y^o \\ \gamma_{xy}^o \end{bmatrix} + z\begin{bmatrix} \kappa_x \\ \kappa_y \\ \kappa_{xy} \end{bmatrix}. \tag{2-9}$$

At any point in the laminate, displacement and strain are linearly dependent on z and can be expressed by the response of the midplane. Note that in Kirchoff's Hypothesis, the through-thickness shear strain, ε_z, is assumed to be equal to zero to avoid inconsistencies in the equations, however, under the plane stress condition, ε_z is not zero as evidenced by equation 2.3.

Using Kirchoff's hypothesis, stress for each lamina in equation 2.6 can be written in terms of the midplane strains, curvature and z as follows,

$$\left\{\sigma_{x-y}\right\}_k = \left[\overline{Q}_{x-y}\right] \left(\left\{\varepsilon_{x-y}^o\right\}_k + z\left\{\kappa_{x-y}\right\}\right) \tag{2-10}$$

where k denotes the layer. To relate plate normal forces and moments to stress and strain, consider the following plate under loading.

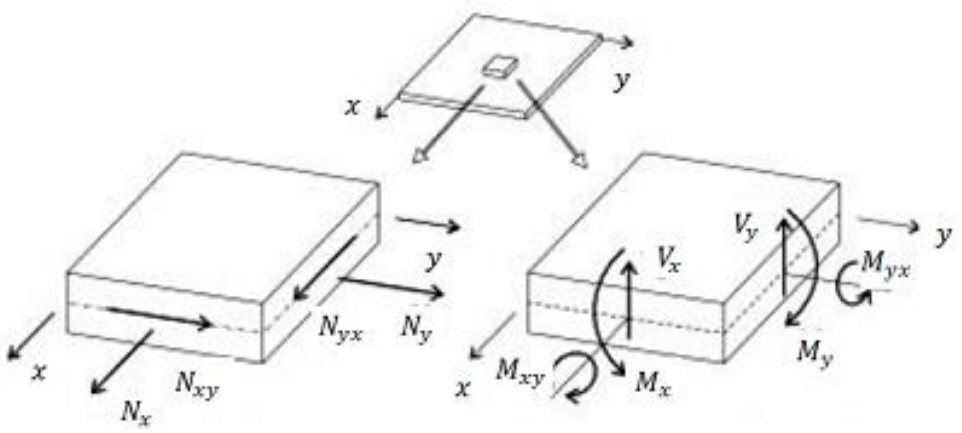

Figure 2.7 In-plane plate forces and moments

To identify each lamina in the laminate, k is used to denote the stacking sequence from the minus z-axis ($k=1$) to the positive z-axis ($k=n$). The distance z is also denoted by the distance from each lamina interface from the midplane. This designation is seen in Figure 2.8 below.

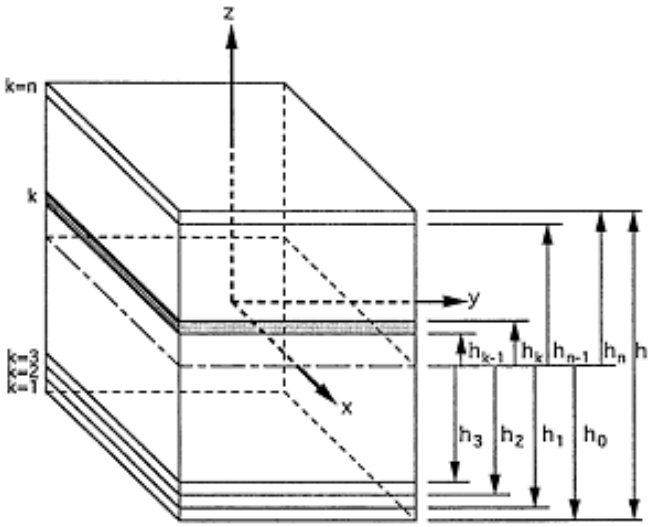

Figure 2.8 each lamina within the laminate

The normal forces and moments are related to the lamina stress as follows,

$$\begin{bmatrix} N_x \\ N_y \\ N_{xy} \end{bmatrix} = \sum_{k=1}^{n} \int_{h_{k-1}}^{h_k} \begin{bmatrix} \sigma_x \\ \sigma_y \\ \tau_{xy} \end{bmatrix}_k dz, \qquad \begin{bmatrix} M_x \\ M_y \\ M_{xy} \end{bmatrix} = \sum_{k=1}^{n} \int_{h_{k-1}}^{h_k} \begin{bmatrix} \sigma_x \\ \sigma_y \\ \tau_{xy} \end{bmatrix}_k z dz \,. \tag{2-11}$$

The normal force and moment are with respect to the width of the laminate thus their units are lb/in and lb respectively. Subbing in equation 2-10 for the stresses,

$$\begin{aligned} \{N\} &= \sum_{k=1}^{n} \int_{h_{k-1}}^{h_k} \left[\overline{Q}_{x-y}\right]_k \left(\left\{\varepsilon^o\right\} + z\{\kappa\}\right) dz \\ \{M\} &= \sum_{k=1}^{n} \int_{h_{k-1}}^{h_k} \left[\overline{Q}_{x-y}\right]_k \left(\left\{\varepsilon^o\right\} + z\{\kappa\}\right) z dz \end{aligned} \,. \tag{2-12}$$

For simplification, 3x3 matrices A, B, C are used in place of the material properties as follows,

$$\left[A_i, B_i, D_i\right] = \sum_{k=1}^{n} \int_{h_{k-1}}^{h_k} \left[1, z, z^2\right] \left[\overline{Q}_{x-y}\right]_k dz \,. \tag{2-13}$$

The normal in-plane forces and moments can then be related to the midplane strains, ε^o_{x-y}, and curvatures, κ_{x-y}, in the following matrix,

$$\begin{Bmatrix} N_{x-y} \\ M_{x-y} \end{Bmatrix} = \begin{bmatrix} A & B \\ B & D \end{bmatrix} \begin{Bmatrix} \varepsilon^o_{x-y} \\ \kappa_{x-y} \end{Bmatrix} \tag{2-14}$$

$$\begin{bmatrix} A & B \\ B & D \end{bmatrix} = \begin{bmatrix} A_{11} & A_{12} & A_{16} & B_{11} & B_{12} & B_{16} \\ A_{12} & A_{22} & A_{26} & B_{12} & B_{22} & B_{26} \\ A_{16} & A_{26} & A_{66} & B_{16} & B_{26} & B_{66} \\ B_{11} & B_{12} & B_{16} & D_{11} & D_{12} & D_{16} \\ B_{12} & B_{22} & B_{26} & D_{12} & D_{22} & D_{26} \\ B_{16} & B_{26} & B_{66} & D_{16} & D_{26} & D_{66} \end{bmatrix},$$

where the ABD matrix is a 6x6 element stiffness matrix and represents the material properties of each lamina and the geometry of the laminate. The $[A]$ matrix is the extensional stiffness matrix with units of lb/in., the $[B]$ matrix is the extensional bending coupling stiffness matrix with units of lb., and the $[D]$ matrix is the bending stiffness matrix with units of $lb \cdot in$.

Thus, when in-plane forces are applied to a laminate plate, the midplane strains and curvatures can be found based on the ABD matrix. The midplane strains and curvatures can then be used to find the strains at each ply surface using equation 2-9. Once the ply surface strains are found which are in the global direction, the strains can be found in the principal material coordinates with the $T_\varepsilon(\theta)$ transformation matrix. Stresses then in the 1-2 or x-y direction can be found for each lamina surface using equation 2-6.

EQUIVALENT MECHANICAL AND THERMAL PROPERTIES OF COMPOSITE MATERIALS

Composite materials consist of multiple constituents with various properties. Analysis of composite structures using the property of each individual constituent can

be insurmountable. Structural behavior of this material, in general, is heterogeneous. To overcome this difficulty, the continuum hypothesis is utilized which models the structure of the material as a continuum by use of statistical averaging process. This continuum hypothesis involves certain measures associated with properties that govern the deformability of the media [35]. Common to this approach is selection of a unit cell representative of the level of the interest in composites, such as lamina, laminate or structure level. Homogenized material properties, or equivalent properties, are determined for this unit cell by using statistically averaged material properties according to the structural response and/or deformation of the unit cell under loading.

A number of methods have been reported in the literature for predicting the equivalent moduli of a laminate. A common technique is to find a set of equivalent properties to represent an orthotropic angle ply or laminate as a homogeneous lamina, as seen in Figure 2.9.

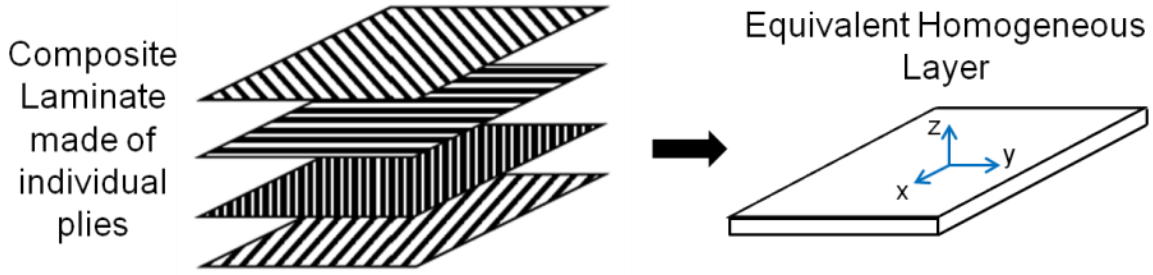

Figure 2.9 Orthotropic laminate represented

by an equivalent homogeneous lamina

This technique is commonly used in Finite Element Analysis (FEA) to represent a composite laminate as one layer to reduce the degrees of freedom in the model. However, in this homogenization approach, an equivalent layer representing

unsymmetric and/or unbalanced laminates or off-axis laminas will exhibit anisotropic behavior. Thus, extension-shear coupling terms, $\eta_{x,xy}$, $\eta_{y,xy}$, $\eta_{xy,x}$, and $\eta_{xy,y}$, will exist but FEA inputs for anisotropic properties only include E_x, E_y, ν_{xy}, and G_{xy}. By ignoring shear deformation caused by normal stress, FEA results will thus be inaccurate for unsymmetric and/or unbalanced laminates.

Research using the homogenized approach includes the following. Pagano [36] evaluated moduli of anisotropic plates using micromechanics. Sun and Li [37] developed a model for determining the 3rd dimensional modulus. An equivalent property method was developed and applied by Sun and Liao [38] to the thick composite laminates with unbalanced nodal forces on a free edge to obtain more accurate stresses in the vicinity of the high stress gradient region.

In deriving the equivalent properties of a laminate, Chan and Chou [39] took the laminate structural response into consideration to include a coupling effect of combined axial and bending loads for unbalanced & unsymmetric laminates. Chan and Chen [5] used this modified method to develop closed form solutions of effective moduli that account for bending and shear induced deformation. Equivalent thermal properties of laminates resulting from lumping layers were investigated by Chan et.al. [40].

This study will focus on developing equivalent coefficients of thermal expansion of homogenized laminates by taking into account induced curvature and shear deformation. Laminas will be first analyzed to compare the modified method to the conventional method. The modified method will be used to predict equivalent properties of symmetric, un-symmetric, and un-balanced laminates. The equivalent properties will

be compared to the convention method and equivalent ply stresses are compared to FEA results.

For the structural case, the narrow beam assumption, developed by Chan and Rios [42], is utilized which uses an effective stiffness matrix of the structure. Analysis of a composite I-beam by the modified method has been conducted by Parambil [8]. Parambil's derivation and results did not include D_z and D_{xz}, and only considered average ply stresses across the width of symmetric laminates. Derivation of D_z and D_{xz} was performed by Rios [32]. Rios applied this to a z-section beam. However, only a symmetric case was studied and ply stresses were found at only 4 points on the cross-section.

In this research, the modified method will be used on an I-beam structure subject to axial and bending loads, M_x and M_y, to predict the centroid, effective axial and bending stiffness, and ply stresses. Width to depth ratios of 1 to 2 and 1 to 4 will be studied to check on the validity of the narrow beam assumption on somewhat wide beams. CERIG and RBE3 constraints will be compared to check differences when applying loading on a rigid body and free end constraint. Also, I-beams consisting of symmetric, unsymmetric, and/or unbalanced laminates will be studied.

ANALTYICAL MODELS OF EQUIVALENT PROPERTIES

Lamina Equivalent Properties: Conventional Method

Consider an angle ply lamina under tension. The equivalent properties of an arbitrary angle degree lamina can be obtained from the ratio of the corresponding

average stress and strain. Since a lamina is thin, the plane stress condition is assumed. The strain/stress relationship of a lamina in x-y coordinates is given in eqn. 1.

$$\begin{pmatrix} \varepsilon_x \\ \varepsilon_y \\ \gamma_{xy} \end{pmatrix} = \begin{pmatrix} \bar{S}_{11} & \bar{S}_{12} & \bar{S}_{16} \\ \bar{S}_{12} & \bar{S}_{22} & \bar{S}_{26} \\ \bar{S}_{16} & \bar{S}_{26} & \bar{S}_{66} \end{pmatrix} \begin{pmatrix} \sigma_x \\ \sigma_y \\ \tau_{xy} \end{pmatrix} = \begin{pmatrix} 1/E_x & -\nu_{xy}/E_x & \eta_{xs}/E_x \\ -\nu_{yx}/E_y & 1/E_y & \eta_{ys}/E_x \\ \eta_{xs}/E_x & \eta_{ys}/E_x & 1/G_{xy} \end{pmatrix} \begin{pmatrix} \sigma_x \\ \sigma_y \\ \tau_{xy} \end{pmatrix} \qquad (2\text{-}15)$$

.

In the conventional method, equivalent properties can be easily obtained by isolating a single load to find the corresponding property. In this exercise, we can obtain the smeared properties: longitudinal and transverse moduli, E_x, E_y, Poisson's ratio, ν_{xy}, shear modulus, G_{xy}, and coefficient of thermal expansion, α_{x-y}, as shown below:

$$E_x = \frac{1}{\bar{S}_{11}}, \quad E_y = \frac{1}{\bar{S}_{22}}, \quad \nu_{xy} = -\frac{\bar{S}_{12}}{\bar{S}_{11}}, \quad G_{xy} = \frac{1}{\bar{S}_{66}} \qquad (2\text{-}16)$$

$$\left\{\alpha_{x-y}\right\} = \left[T_\varepsilon\left(-\theta\right)\right]\left\{\alpha_{1-2}\right\}. \qquad (2\text{-}17)$$

The subscripts 1-2 and x-y refer the material and global coordinate systems, respectively. It should be noted that this approach yields a 0^o lamina with shear deformation.

Lamina Equivalent Properties: Modified Method

In the modified method, the angle lamina is represented by a set of properties of a 0^o lamina of the same material. To make an off-axis lamina equivalent to a 0^o lamina ply, the induced shear strain due to tension is suppressed in the modified method as

illustrated in Figure 2.10. This causes the equivalent E_x calculated by the modified method to be greater than the conventional E_x property since it is a resistance to extension as well as shear deformation.

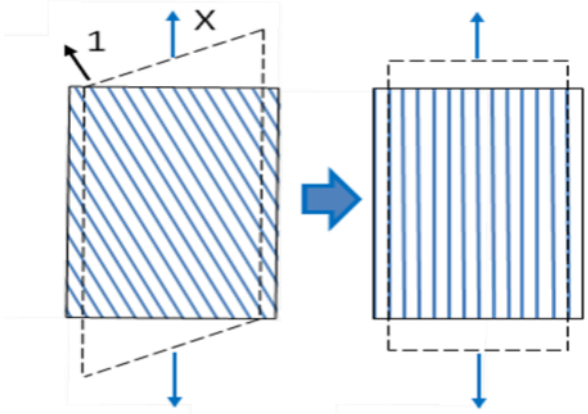

Figure 2.10 Modified Method creating 0^o lamina ply

while suppressing shear strain

From equation 2.15, the process of suppressing shear strain uses matrix substitution which is detailed in equations 2-18 to 2-22. To suppress the shear strain, the shear strain is zeroed out which allows the shear force to be written in terms of stress in the x and y direction.

$$\gamma_{xy} = 0 \rightarrow \bar{S}_{16}\sigma_x + \bar{S}_{26}\sigma_y + \bar{S}_{66}\tau_{xy} = 0$$

$$\tau_{xy} = -\left(\frac{\bar{S}_{16}}{\bar{S}_{66}}\sigma_x + \frac{\bar{S}_{26}}{\bar{S}_{66}}\sigma_y\right) \qquad (2\text{-}18)$$

Equation 2-18 can now be substituted into equation 2-15 and longitudinal and transverse strain can be expressed as follows.

$$\varepsilon_X = \bar{S}_{11}\sigma_X + \bar{S}_{12}\sigma_y + \bar{S}_{16}\left(-\frac{\bar{S}_{16}}{\bar{S}_{66}}\sigma_X - \frac{\bar{S}_{26}}{\bar{S}_{66}}\sigma_y\right)$$

$$\varepsilon_X = \left(\bar{S}_{11} - \frac{\bar{S}_{16}^2}{\bar{S}_{66}}\right)\sigma_X + \left(\bar{S}_{12} - \frac{\bar{S}_{16}\bar{S}_{26}}{\bar{S}_{66}}\right)\sigma_y \qquad (2\text{-}19)$$

$$\varepsilon_y = \bar{S}_{12}\sigma_x + \bar{S}_{22}\sigma_y + \bar{S}_{26}\tau_{xy}$$

$$\varepsilon_y = \left(\bar{S}_{12} - \frac{\bar{S}_{16}\bar{S}_{26}}{\bar{S}_{66}}\right)\sigma_x + \left(\bar{S}_{22} - \frac{\bar{S}_{26}^2}{\bar{S}_{66}}\right)\sigma_y \qquad (2\text{-}20)$$

These equations for strain can be written in matrix form as

$$\begin{Bmatrix}\varepsilon_x \\ \varepsilon_y\end{Bmatrix} = \begin{bmatrix}R_1 & R_2 \\ R_2 & R_3\end{bmatrix}\begin{Bmatrix}\sigma_x \\ \sigma_y\end{Bmatrix} \qquad (2\text{-}21)$$

where

$$R_1 = \bar{S}_{11} - \frac{\bar{S}_{16}^2}{\bar{S}_{66}},\quad R_2 = \bar{S}_{12} - \frac{\bar{S}_{16}\bar{S}_{26}}{\bar{S}_{66}},\quad R_3 = \bar{S}_{22} - \frac{\bar{S}_{26}^2}{\bar{S}_{66}}. \qquad (2\text{-}22)$$

If only tension is applied, longitudinal strain and the longitudinal elastic modulus of the equivalent lamina can be expressed as:

$$\varepsilon_X = R_1\sigma_X \;\rightarrow\; E_X = \frac{1}{R_1}\ . \qquad (2\text{-}23)$$

Poisson's ratio can also be found with an applied tensile load as,

$$\nu_{xy} = -\frac{\varepsilon_y}{\varepsilon_x} = -\frac{R_2\sigma_x}{R_1\sigma_x} = -\frac{R_2}{R_1}. \qquad (2\text{-}24)$$

If a transverse force is only applied, then the transverse modulus can be obtained as:

$$\varepsilon_y = R_3\sigma_y \;\rightarrow\; E_y = \frac{1}{R_3}. \qquad (2\text{-}25)$$

The shear modulus, G_{xy}, can be obtained by suppressing axial deformation in both the x- and y-directions while applying a shear stress. From equation 2-15, the longitudinal and transverse stress can be written in terms of the shear stress as follows. First, isolating the axial strains,

$$\begin{Bmatrix}\varepsilon_x\\ \varepsilon_y\end{Bmatrix} = \begin{bmatrix}\bar{S}_{11} & \bar{S}_{12}\\ \bar{S}_{12} & \bar{S}_{22}\end{bmatrix}\begin{Bmatrix}\sigma_x\\ \sigma_y\end{Bmatrix} + \begin{Bmatrix}\bar{S}_{16}\\ \bar{S}_{26}\end{Bmatrix}\tau_{xy} = \begin{Bmatrix}0\\ 0\end{Bmatrix}$$

$$\begin{Bmatrix}\sigma_x\\ \sigma_y\end{Bmatrix} = -\begin{bmatrix}\bar{S}_{11} & \bar{S}_{12}\\ \bar{S}_{12} & \bar{S}_{22}\end{bmatrix}^{-1}\begin{Bmatrix}\bar{S}_{16}\\ \bar{S}_{26}\end{Bmatrix}\tau_{xy} \qquad (2\text{-}26)$$

$$\begin{Bmatrix}\sigma_x\\ \sigma_y\end{Bmatrix} = \left(\frac{-1}{\bar{S}_{11}\bar{S}_{22} - \bar{S}_{12}^2}\right)\begin{bmatrix}\bar{S}_{22} & -\bar{S}_{12}\\ -\bar{S}_{12} & \bar{S}_{11}\end{bmatrix}\begin{Bmatrix}\bar{S}_{16}\\ \bar{S}_{26}\end{Bmatrix}\tau_{xy}$$

$$\begin{Bmatrix}\sigma_x\\ \sigma_y\end{Bmatrix} = \begin{Bmatrix}\dfrac{\bar{S}_{12}\bar{S}_{26} - \bar{S}_{22}\bar{S}_{16}}{\bar{S}_{11}\bar{S}_{22} - \bar{S}_{12}^2} & \dfrac{\bar{S}_{12}\bar{S}_{16} - \bar{S}_{11}\bar{S}_{26}}{\bar{S}_{11}\bar{S}_{22} - \bar{S}_{12}^2}\end{Bmatrix}^T \tau_{xy} \qquad (2\text{-}27)$$

Substituting equation 2-26 back into equation 2-15 and solving for shear stress,

$$\gamma_{xy} = \begin{Bmatrix}\bar{S}_{16} & \bar{S}_{26}\end{Bmatrix}\begin{Bmatrix}\sigma_x\\ \sigma_y\end{Bmatrix} + \bar{S}_{66}\tau_{xy} \qquad (2\text{-}28)$$

Plugging equation 2-27 into equation 2-28 to put this in terms of shear stain,

$$\gamma_{xy} = \frac{\tau_{xy}}{G_{xy}} = \left\{\bar{S}_{16}\left(\frac{\bar{S}_{12}\bar{S}_{26} - \bar{S}_{22}\bar{S}_{16}}{\bar{S}_{11}\bar{S}_{22} - \bar{S}_{12}^2}\right) + \bar{S}_{26}\left(\frac{\bar{S}_{12}\bar{S}_{16} - \bar{S}_{11}\bar{S}_{26}}{\bar{S}_{11}\bar{S}_{22} - \bar{S}_{12}^2}\right) + \bar{S}_{66}\right\}\tau_{xy} \qquad (2\text{-}29)$$

The shear modulus is thus found.

In summary, the resulting expressions are given below:

$$E_x = \frac{1}{\bar{S}_{11} - \frac{\bar{S}_{16}^2}{\bar{S}_{66}}}, \quad E_y = \frac{1}{\bar{S}_{22} - \frac{\bar{S}_{26}^2}{\bar{S}_{66}}}, \quad \nu_{xy} = -\left(\frac{\bar{S}_{12} - \frac{\bar{S}_{16}\bar{S}_{26}}{\bar{S}_{66}}}{\bar{S}_{11} - \frac{\bar{S}_{16}^2}{\bar{S}_{66}}} \right) \qquad (2\text{-}30)$$

$$G_{xy} = 1 \Bigg/ \left[\bar{S}_{16} \left(\frac{\bar{S}_{12}\bar{S}_{26} - \bar{S}_{22}\bar{S}_{16}}{\bar{S}_{11}\bar{S}_{22} - \bar{S}_{12}^2} \right) + \bar{S}_{26} \left(\frac{\bar{S}_{12}\bar{S}_{16} - \bar{S}_{11}\bar{S}_{26}}{\bar{S}_{11}\bar{S}_{22} - \bar{S}_{12}^2} \right) + \bar{S}_{66} \right].$$

It should be noted that the equivalent properties for a laminate does not represent the structural response of the equivalent 0^o laminate.

Laminate Equivalent Properties: Conventional Method

Within a laminate, external loads are distributed to each ply relative to a ply's stiffness and orientation. The structural response of the whole laminate can be found by integrating the stiffness of each ply relative to the global coordinates and distance about the mid-plane. Hence, the equivalent modulus of a 0^o laminate can be considered a property relative to the mid-plane of a laminate. Considering the plane stress condition, the constitutive equation of a laminate is given as:

$$\begin{Bmatrix} \varepsilon^o \\ \kappa \end{Bmatrix} = \begin{bmatrix} a & b \\ b^T & d \end{bmatrix} \begin{Bmatrix} N \\ M \end{Bmatrix} \qquad (2\text{-}31)$$

where $\{\varepsilon^o\}$ and $\{\kappa\}$ are the mid-plane strains and curvatures, respectively, in the x-, y-, and xy-directions. $\{N\}$ and $\{M\}$ are the 3x1 load matrices of the in-plane and the out-of-plane loads. $[a]$, $[b]$, and $[d]$ are 3x3 matrices of compliance, coupling, and flexibility of the laminate. $[b]^T$ is the transpose of $[b]$. Note that matrix $[b]$ is not

symmetric in general. Hence, $[b]^T \neq [b]$. The average stress of the laminate can be obtained by the following equation as:

$$\{\bar{\sigma}\} = \frac{\{N\}}{t} \qquad (2\text{-}32)$$

where t is the thickness of the laminate. Equating the stress and the corresponding strain component, the material properties are obtained:

$$E_x = \frac{1}{a_{11}t},\ E_y = \frac{1}{a_{22}t},\ \nu_{xy} = -\frac{a_{21}}{a_{11}},\ G_{xy} = \frac{1}{a_{66}t}. \qquad (2\text{-}33)$$

Laminate Equivalent Properties: Modified Method

Using conventional method properties, the equivalent 0^o laminate under tension will exhibit a shear deformation or curvature if the original laminate is either unsymmetrical and/or unbalanced. For unsymmetric laminates, there will be an extension-bending coupling stiffness due to a non-zero $[B]$ matrix as shown in Figure 2.11.

Figure 2.11 Laminate experiencing bending induced by normal load

For unbalanced laminates, in-plane extension-shear coupling stiffness exist due to non-zero A_{16} and A_{26} terms and bending-twisting coupling stiffness exist due to non-zero D_{16} and D_{26} terms exist. The equivalent 0^o laminate should take into account this stiffness.

The modified method accomplishes this by suppressing the shear deformation and curvature.

To suppress curvature first given a tensile load, a moment is required which can be substituted out of the constitutive equation, equation 2-15, as follows,

$$\kappa = 0 \;\rightarrow\; b^T N + dM = 0 \;\rightarrow\; M = -d^{-1} b^T N$$
$$\varepsilon^o = aN + bM = \left(a - bd^{-1}b^T\right)N = PN \qquad (2\text{-}34)$$

$$\text{where } [P] = [a] - [b][d]^{-1}[b]^T . \qquad (2\text{-}35)$$

The constitutive equation now becomes:

$$\begin{pmatrix} \varepsilon_x^o \\ \varepsilon_y^o \\ \gamma_{xy}^o \end{pmatrix} = \begin{pmatrix} \overline{P}_{11} & \overline{P}_{12} & \overline{P}_{16} \\ \overline{P}_{12} & \overline{P}_{22} & \overline{P}_{26} \\ \overline{P}_{16} & \overline{P}_{26} & \overline{P}_{66} \end{pmatrix} \begin{pmatrix} N_x \\ N_y \\ N_{xy} \end{pmatrix} \qquad (2\text{-}36)$$

Shear deformation is then suppressed. This matrix substitution is similar to the substitution for the lamina where equation 2-36 is now written in the following terms:

$$\gamma_{xy}^o = 0 \;\rightarrow\; \overline{P}_{16}N_x + \overline{P}_{26}N_y + \overline{P}_{66}N_{xy} = 0$$
$$N_{xy} = -\left(\frac{\overline{P}_{16}}{\overline{P}_{66}}N_x + \frac{\overline{P}_{26}}{\overline{P}_{66}}N_y\right) \qquad (2\text{-}37)$$

Substituting this back into equation 2-36, the strain terms can be solved for as follows:

$$\varepsilon_x^o = \left(\overline{P}_{11} - \frac{\overline{P}_{16}^2}{\overline{P}_{66}}\right)N_x + \left(\overline{P}_{12} - \frac{\overline{P}_{16}\overline{P}_{26}}{\overline{P}_{66}}\right)N_y \qquad (2\text{-}38)$$

$$\varepsilon_y^o = \left(\overline{P}_{12} - \frac{\overline{P}_{16}\overline{P}_{26}}{\overline{P}_{66}} \right) N_x + \left(\overline{P}_{22} - \frac{\overline{P}_{26}^2}{\overline{P}_{66}} \right) N_y \,. \qquad (2\text{-}39)$$

If only tension is applied, longitudinal strain and the longitudinal elastic modulus of the equivalent lamina can be expressed as:

$$E_X = \frac{\varepsilon_x^o}{t \cdot N_X} = \frac{1}{\left(P_{11} - \frac{P_{16}^2}{P_{66}} \right) t} \,. \qquad (2\text{-}40)$$

Poisson's ratio can also be found with an applied tensile load as,

$$\nu_{xy} = -\frac{\varepsilon_y^o}{\varepsilon_x^o} = -\left(\frac{P_{12} - \frac{P_{16}P_{26}}{P_{66}}}{P_{11} - \frac{P_{16}^2}{P_{66}}} \right). \qquad (2\text{-}41)$$

If a transverse force is only applied, then the transverse modulus can be obtained as:

$$E_y = \frac{\varepsilon_y^o}{t \cdot N_y} = \frac{1}{\left(P_{22} - \frac{P_{26}^2}{P_{66}} \right) t} \,. \qquad (2\text{-}42)$$

To obtain the shear modulus G_{xy}, laminate strains $\varepsilon_x^o = \varepsilon_y^o = 0$ to ensure pure shear deformation when N_{xy} is applied. The laminate constitutive equation is modified as shown which includes the presence of N_x and N_y for the suppression of ε_x^o and ε_y^o.

$$\begin{pmatrix} 0 \\ 0 \\ \gamma_{xy}^{o} \end{pmatrix} = \begin{pmatrix} P_{11} & P_{12} & P_{16} \\ & P_{22} & P_{26} \\ sym & & P_{66} \end{pmatrix} \begin{pmatrix} N_x \\ N_y \\ N_{xy} \end{pmatrix} \qquad (2\text{-}43)$$

N_x and N_y are then substituted back into the constitutive equation similar to the derivation for the lamina. The shear modulus is expressed as:

$$G_{xy} = \left(1/t\right) \Bigg/ \left[P_{66} - P_{16}\left(\frac{P_{22}P_{16} - P_{12}P_{26}}{P_{11}P_{22} - P_{12}^2} \right) - P_{26}\left(\frac{P_{11}P_{26} - P_{12}P_{26}}{P_{11}P_{22} - P_{12}^2} \right) \right]. \qquad (2\text{-}44)$$

Equivalent Coefficient of Thermal Expansion, CTE, for Laminate

To find the equivalent coefficient of thermal expansion of the laminate, the same approach can be used in determining the equivalent modulus by replacing the mechanical loads with the thermally induced loads due to a temperature change.

Under the conventional approach, the constitutive equation (eqn 6) is used as follows:

$$\begin{Bmatrix} \varepsilon^{o} \\ \kappa \end{Bmatrix} = \begin{bmatrix} a & b \\ b^{T} & d \end{bmatrix} \begin{Bmatrix} N^{Th} \\ M^{Th} \end{Bmatrix}. \qquad (2\text{-}45)$$

Replacing the strain terms with:

$$\varepsilon_x^{o} = \bar{\alpha}_x \Delta T, \quad \varepsilon_y^{o} = \bar{\alpha}_y \Delta T, \qquad (2\text{-}46)$$

the coefficients of thermal expansion using the conventional methods are expressed as:

$$\left\{ \alpha_{x,y} \right\} = \left\{ [a] N^{Th} + [b] M^{Th} \right\} \frac{1}{\Delta T}. \qquad (2\text{-}47)$$

Under the Modified Method, $\varepsilon^{o} = [P]\{N\}$ can be rewritten as:

$$\begin{Bmatrix} \varepsilon_x^o \\ \varepsilon_y^o \end{Bmatrix} = \begin{bmatrix} P_{11} - \dfrac{P_{16}^2}{P_{66}} & P_{12} - \dfrac{P_{16}P_{26}}{P_{66}} \\ sym & P_{22} - \dfrac{P_{26}^2}{P_{66}} \end{bmatrix} \begin{Bmatrix} N_x^{Th} \\ N_y^{Th} \end{Bmatrix}, \qquad (2\text{-}48)$$

where N_x^{Th} and N_y^{Th} are the thermally induced loads which are obtained from Classical Lamination Theory.

$$\alpha_x = \left[\left(P_{11} - \frac{P_{16}^2}{P_{66}} \right) N_x^{Th} + \left(P_{12} - \frac{P_{16}P_{26}}{P_{66}} \right) N_y^{Th} \right] \frac{1}{\Delta T}$$
$$\alpha_y = \left[\left(P_{12} - \frac{P_{16}P_{26}}{P_{66}} \right) N_x^{Th} + \left(P_{22} - \frac{P_{26}^2}{P_{66}} \right) N_y^{Th} \right] \frac{1}{\Delta T} \qquad (2\text{-}49)$$

It is noted that N_x^{Th} and N_y^{Th} are a function of ΔT. Hence, α_x and α_y are not a function of ΔT.

Structural Equivalent Properties: Conventional Method vs. Modified Method

Composite I-beam structures with uniform cross-sections through the length are used as examples to evaluate the equivalent structural properties by the conventional and modified methods. The I-beam structural properties considered in this research include centroid, axial, and bi-directional bending stiffness. In the conventional method, the equivalent moduli described in the previous section are used for each laminate. The structural properties are then derived often using isotropic material techniques.

For example, the axial stiffness of the structure, $\overline{EA}^{conv}$, is found by summing the axial stiffness's of each laminate. The centroid is found by taking a summation of

moments about the y-axis and dividing by the sum of the axial loads. The structural bending stiffness's, $\overline{D}_x^{conv}$, $\overline{D}_z^{conv}$ and $\overline{D}_{xz}^{conv}$, can be found as follows.

$$\overline{EA}^{conv} = E_x A \quad \overline{D}_x^{conv} = E_x I_y \quad \overline{D}_z^{conv} = E_x I_z \quad \overline{D}_{xz}^{conv} = E_x I_{yz} \qquad (2\text{-}50)$$

where A is the area, E_x is the elastic modulus in the x-direction, and I_y, I_z and I_{yz} are the moments of inertia of the I-beam cross-section.

Stresses can be recovered using the conventional method by finding the strain and curvatures at the centroid of the structure using the stiffness's provided above as shown below.

$$\begin{Bmatrix} \varepsilon_x^c \\ k_x^c \\ k_z^c \end{Bmatrix} = \begin{bmatrix} \overline{EA} & 0 & 0 \\ 0 & \bar{D}_x & \bar{D}_{xz} \\ 0 & \bar{D}_{xz} & \bar{D}_z \end{bmatrix}_{conv}^{-1} \begin{Bmatrix} \bar{N}_x \\ \bar{M}_x \\ \bar{M}_z \end{Bmatrix} \qquad (2\text{-}51)$$

The strains and curvatures of each laminate are obtained from the $[abd]$ matrix of the laminate and ply stresses are found using the material property and orientation of each ply.

In the modified method, the constitutive equations of the top and bottom flanges and the web are first obtained based on a composite narrow beam behavior. The sectional properties, centroid, axial stiffness, and bending stiffness of composite I-beam can be derived. For clarification of parameters used in the following equations, a typical I-beam cross section is illustrated in Figure 2.12 below. 'C' is the assumed centroid of the I-beam and the x-direction is in the plane of the paper.

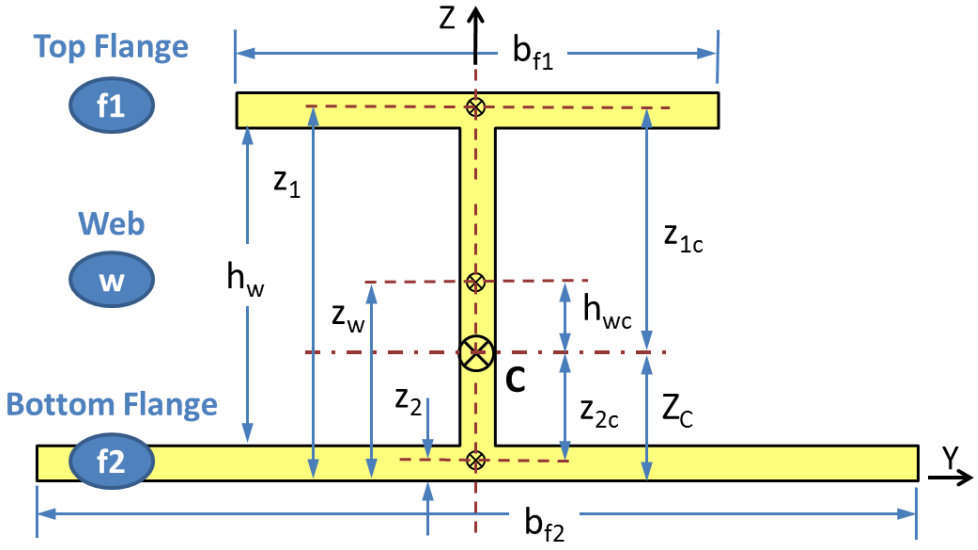

Figure 2.12 Composite I-beam dimensions

An illustration of the structural response for a narrow beam under a bending load, M_x, is shown in Figure 2.13. Both undeformed and deformed shapes are shown. The moment is denoted as M_x since composite notation is used where the moment induces stresses in the x-direction. The top of the beam is under longitudinal compression which, due to the Poisson's effect, causes expansion in the lateral or y-direction. Conversely, the bottom of the beam experiences longitudinal tension leading to lateral compression. For a narrow beam as shown, there is considerable flexibility in the y-direction thus allowing for the assumption that $u_y \neq 0 \Rightarrow N_y = 0$ and $k_y \neq 0 \Rightarrow M_y = 0$. Similarly, a narrow beam is easy to twist and shear, thus allowing for $N_{xy} = M_{xy} = 0$. However, for a narrow I-beam laminate, the flanges are constrained by the web. Hence, k_{xy} is assumed to be zero and M_{xy} is non-zero.

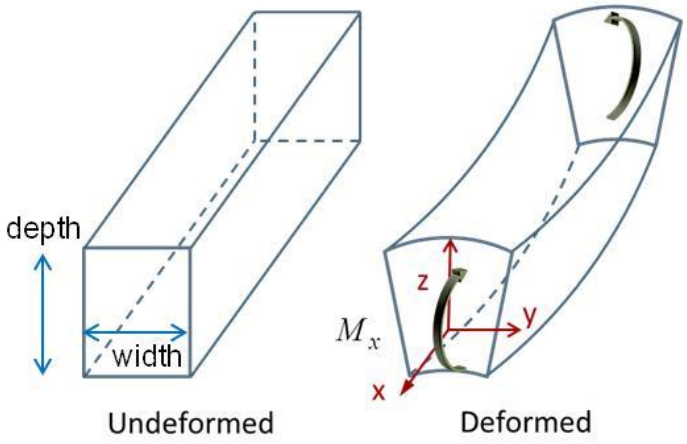

Figure 2.13 Narrow beam under bending

For the I-beam, the flanges and web can be treated as independent laminates. Applying the Narrow Beam Theory assumptions discussed for the I-beam, a simplified one dimensional relationship between stress and strain can be obtained for each of these members. This was done in reference [40] and is briefly reviewed below.

Applying Narrow Beam Theory, the 6x6 stiffness matrix for each member noted by 'i', equation 2-14, can be simplified into the following constitutive equation as:

$$\begin{Bmatrix} \varepsilon_x^o \\ k_x^o \\ k_{xy}^o \end{Bmatrix}_i = \begin{bmatrix} a_{11} & b_{11} & b_{16} \\ b_{11} & d_{11} & d_{16} \\ b_{16} & d_{16} & d_{66} \end{bmatrix}_i^{-1} \begin{Bmatrix} N_x \\ M_x \\ M_{xy} \end{Bmatrix}_i . \qquad (2\text{-}52)$$

Assuming twisting is negligible, then for each member,

$$k_{xy}^o = 0 = b_{16} N_x + d_{16} M_x + d_{66} M_{xy} \qquad (2\text{-}53)$$

and solving for the twisting moment,

$$M_{xy} = -\left(\frac{b_{16}}{d_{66}} N_x + \frac{d_{16}}{d_{66}} M_x \right) . \qquad (2\text{-}54)$$

Equation 2-52 can then be simplified by substituting in the twisting moment, equation 2-54,

$$\begin{Bmatrix} \varepsilon_x^o \\ k_x^o \end{Bmatrix} = \begin{bmatrix} a_{11} & b_{11} \\ b_{11} & d_{11} \end{bmatrix} \begin{Bmatrix} N_x \\ M_x \end{Bmatrix} + \begin{Bmatrix} b_{16} \\ d_{16} \end{Bmatrix} \begin{bmatrix} -b_{16}/d_{66} & -d_{16}/d_{66} \end{bmatrix} \begin{Bmatrix} N_x \\ M_x \end{Bmatrix} \qquad (2\text{-}55)$$

which simplifies to:

$$\begin{Bmatrix} \varepsilon_x^o \\ k_x^o \end{Bmatrix}_i = \begin{bmatrix} a_{11} - \frac{b_{16}^2}{d_{66}} & b_{11} - \frac{b_{16} d_{16}}{d_{66}} \\ b_{11} - \frac{b_{16} d_{16}}{d_{66}} & d_{11} - \frac{d_{16}^2}{d_{66}} \end{bmatrix}_i \begin{Bmatrix} N_x \\ M_x \end{Bmatrix}_i = \begin{bmatrix} a^* & b^* \\ b^* & d^* \end{bmatrix}_i \begin{Bmatrix} N_x \\ M_x \end{Bmatrix}_i . \qquad (2\text{-}56)$$

Thus, we are left with a one dimensional equation for each member of the I-beam. The stiffness matrix can be found by taking the inverse of the 1D abd* constitutive equation:

$$\begin{bmatrix} A^* & B^* \\ B^* & D^* \end{bmatrix}_i = \begin{bmatrix} a^* & b^* \\ b^* & d^* \end{bmatrix}_i^{-1} . \qquad (2\text{-}57)$$

Based on this ABD* matrix, expressions for the centroid, equivalent axial stiffness, and equivalent bending stiffness were derived in reference [33] and are listed below. Appendix A gives a further review of Narrow Beam Theory.

$$Z_c = \frac{A^*_{x,f1} b_{f1} z_1 + A^*_{x,f2} b_{f2} z_2 + A^*_{x,w} h_w z_w}{A^*_{x,f1} b_{f1} + A^*_{x,f2} b_{f2} + A^*_{x,w} h_w} \qquad (2\text{-}58)$$

$$\overline{EA} = A^*_{x,f1} b_{f1} + A^*_{x,f2} b_{f2} + A^*_{x,w} h_w \qquad (2\text{-}59)$$

$$\overline{D}_x = \sum_{i=1}^{2} b_{fi}\left(A_{i,fi} z_{ic}^2 + 2B_{i,fi} z_{ic} + D_{i,fi}\right) + A_{i,w}\left(\frac{1}{12} h_w^3 + h_w h_{wc}^2\right) \qquad (2\text{-}60)$$

$$\bar{D}_{xz} = b_{f1}\left(A_{f1}^* z_{f1} + B_{f1}^*\right) y_{f1} + b_{f2}\left(A_{f2}^* z_{f2} + B_{f2}^*\right) y_{f2} + \left(A_w^* y_w + B_w^*\right) h_w z_w . \qquad (2\text{-}61)$$

Stress Analysis of Composite I-beam

The stress analysis using the modified method has been presented in works by Parambil [33] and Rios [32] and is also reviewed in Appendix A.

RESULTS COMPARING MODIFIED METHOD TO CONVENTIONAL METHOD WITH LAMINA AND LAMINATES

The material used for the analytical and FEA analyses is IM6G/3501-6 graphite/epoxy which has mechanical and thermal properties listed below in Table 2.1. Ply thickness considered is 0.005 inches.

Table 2.1 Properties of IM6G/3501-6 graphite/epoxy

Property	Symbol	Units	Value
Longitudinal Modulus	E_1	(Msi)	24.5
Transverse Modulus	E_2	(Msi)	1.3
Shear Modulus	G_{12}	(Msi)	0.94
Poisson's Ratio	v_{12}		0.31
Longitudinal Thermal Expansion Coefficient	α_1	(10^{-6}/F^o)	-0.5
Transverse Thermal Expansion Coefficient	α_2	(10^{-6}/F^o)	13.9

Lamina Study

Fiber orientations considered are: 0, 15, 30, 45, 60, 75 and 90 degrees. Only one ply of a specific orientation is considered at one time. Figure 2.14 shows a comparison of equivalent global properties derived from the conventional and modified method.

The conventional method yields the same results as the modified method for 0 and 90 degree laminas since there is no coupling between extension and shear. However, for off-angled laminas, the equivalent E_x, E_y, and G_{xy} properties calculated by the modified method are higher than those obtained by the conventional method. This was predicted since the modified method suppresses the shear deformation which increases the stiffness of the lamina.

It should be noted that the modified method of lamina equivalent properties is to represent equivalent 0^o properties of the given laminate.

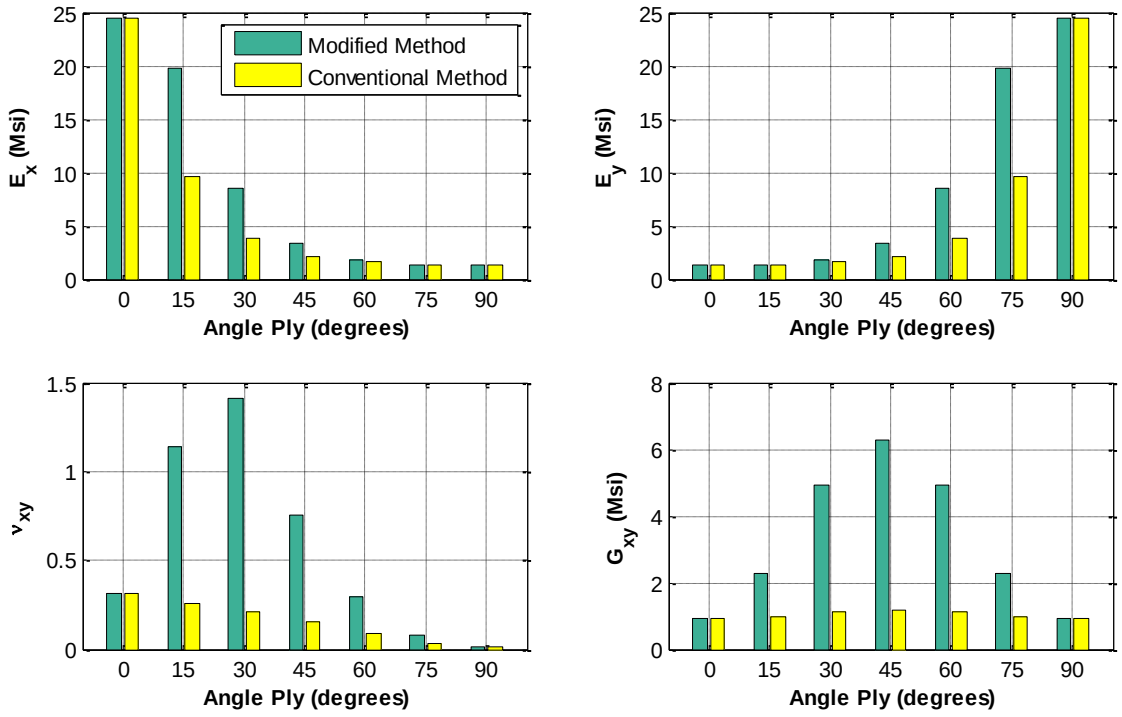

Figure 2.14 Comparing equivalent material properties of individual lamina plies between Modified Method and Conventional Method

Laminate Study

Various stacking sequences of an 8-ply laminate have been chosen to represent symmetric, unsymmetric, balanced, and unbalanced layups or combinations thereof. These stacking sequences are:

Table 2.2 Stacking sequences utilized

Stacking Sequence	Symmetric	Balanced	Exception
$[\pm\theta/0/90]_S$	Yes	Yes	
$[\pm\theta/0/90]_{2T}$	No	Yes	
$[\theta_2/0/90]_S$	Yes	No	Balanced when $\theta = 0^o$ or 90^o
$[\theta_2/0/90]_{2T}$	No	No	Balanced when $\theta = 0^o$ or 90^o

θ is the ply orientation which varies as 0, 15, 30, 45, 60, 75, and 90 degrees. For the case of a symmetrical laminate, coupling stiffness matrix [B] = 0. For the case of a balanced laminate stiffness, shear coupling terms A_{16} = A_{26} =0. Figures 2.15 through 2.18 show the calculated equivalent in-plane properties of the various laminates.

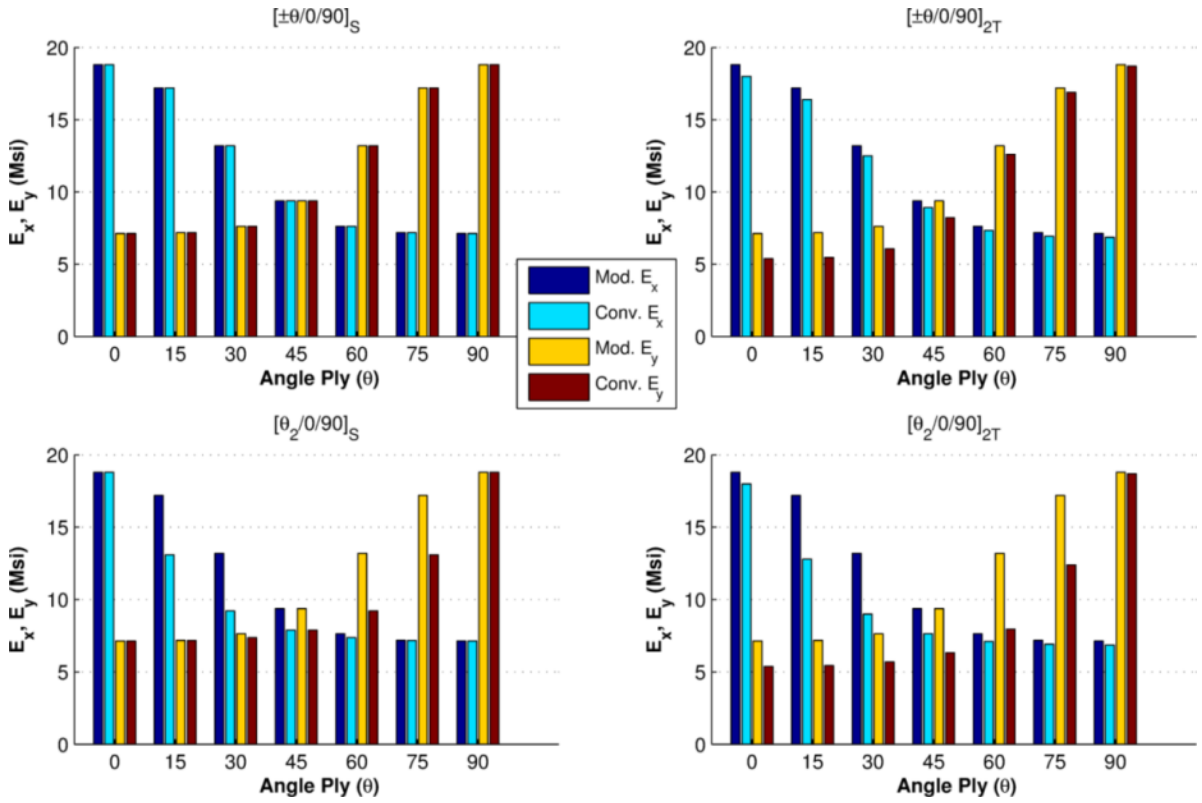

Figure 2.15 Comparing equivalent longitudinal and transverse moduli, E_x and E_y, of various laminates between Modified Method and Conventional Method

The main difference between the modified and conventional method is that the modified method mathematically suppresses the extension-shear coupling and bending-twisting coupling whereas the conventional method ignores these effects. Thus, for symmetric and balanced laminates, all effective properties derived from the modified and conventional method should be identical. This is verified for all material properties

in Figures 2.15 to 2.18 with the $[\pm\theta/0/90]_S$ stacking sequence, and with the $[\theta_2/0/90]_S$ when $\theta =$ 0° or 90°.

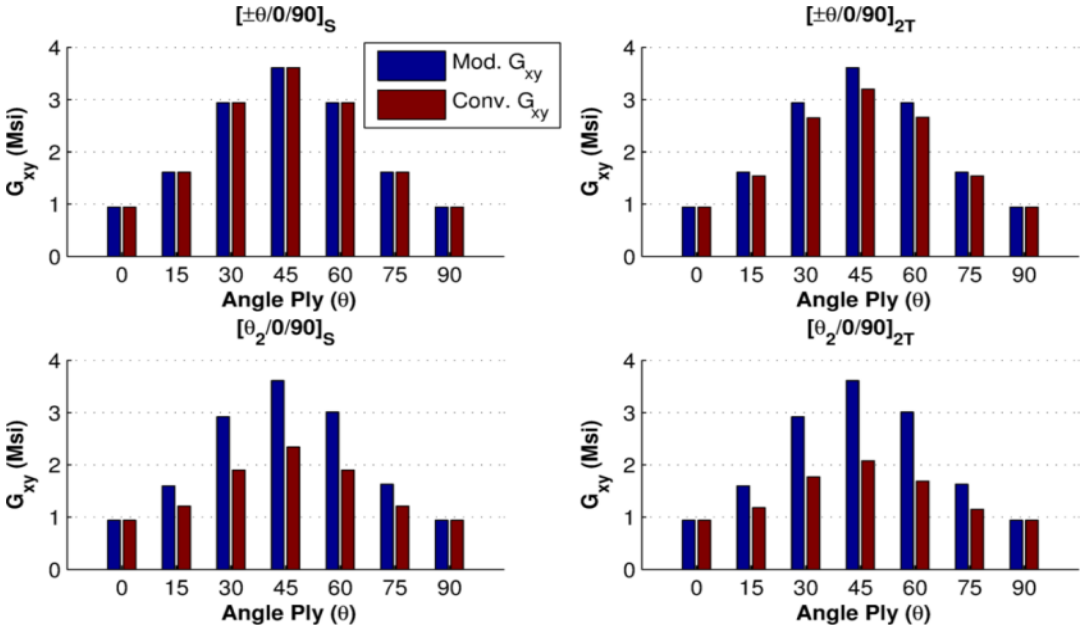

Figure 2.16 Comparing equivalent shear modulus, G_{xy}, of various laminates

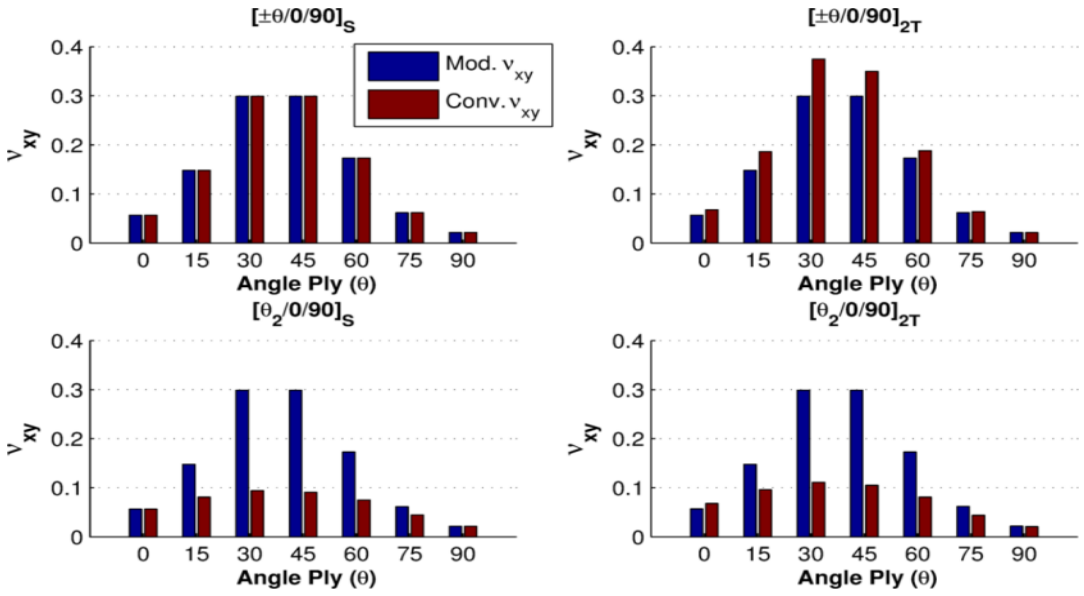

Figure 2.17 Comparing equivalent poisson's ratio, v_{xy}, of various

The largest equivalent moduli differences between the modified method and conventional method are normally with the unsymmetric and unbalanced $[\theta_2/0/90]_{2T}$ layup. This is as expected due to the suppression of the extension-shear and extension-bending coupling.

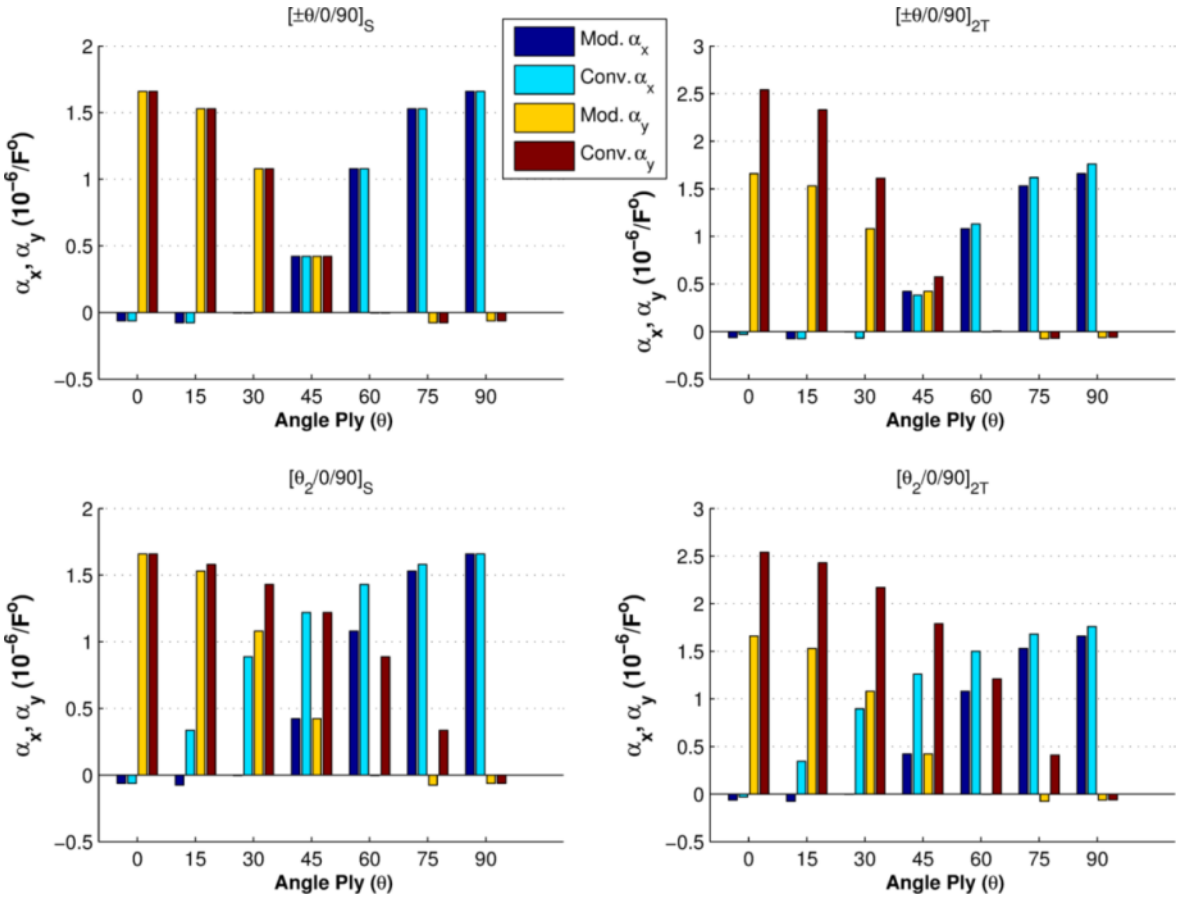

Figure 2.18 Comparing equivalent coefficients of thermal expansion, α_x and α_y , of various laminates between Modified Method and Conventional Method

The equivalent Poisson's ratio between that calculated by the modified and conventional method varied with unsymmetric/balanced and unbalanced/symmetric laminates. The same trend is observed with equivalent coefficients of thermal expansion values.

A summary of the percent differences between the modified method and conventional method is shown in Table 2.3.

Table 2.3 Comparison of material properties between modified and conventional method

Theta (degrees)	0	15	30	45	60	75	90
E_x (psi)							
$[+\Theta/-\Theta/0/90]_S$	0.0%	0.0%	0.0%	0.0%	0.0%	0.0%	0.0%
$[+\Theta/-\Theta/0/90]_{2T}$	4.3%	4.7%	5.3%	4.9%	3.8%	3.5%	3.8%
$[\theta 2/0/90]_S$	0.0%	23.8%	30.2%	16.0%	3.5%	0.1%	0.0%
$[\theta 2/0/90]_{2T}$	4.3%	25.6%	31.8%	18.6%	6.8%	3.8%	3.8%
E_y (psi)							
$[+\Theta/-\Theta/0/90]_S$	0.0%	0.0%	0.0%	0.0%	0.0%	0.0%	0.0%
$[+\Theta/-\Theta/0/90]_{2T}$	24.5%	23.8%	20.6%	12.5%	4.5%	1.7%	0.5%
$[\theta 2/0/90]_S$	0.0%	0.1%	3.5%	16.0%	30.2%	23.8%	0.0%
$[\theta 2/0/90]_{2T}$	24.5%	24.2%	25.4%	32.5%	39.8%	27.9%	0.5%
G_{xy} (psi)							
$[+\Theta/-\Theta/0/90]_S$	0.0%	0.0%	0.0%	0.0%	0.0%	0.0%	0.0%
$[+\Theta/-\Theta/0/90]_{2T}$	0.0%	4.3%	9.9%	11.4%	9.5%	4.3%	0.0%
$[\theta 2/0/90]_S$	0.0%	24.4%	34.9%	35.2%	36.9%	25.8%	0.0%
$[\theta 2/0/90]_{2T}$	0.0%	26.3%	39.4%	42.4%	43.9%	29.4%	0.0%
υ_{xy}							
$[+\Theta/-\Theta/0/90]_S$	0.0%	0.0%	0.0%	0.0%	0.0%	0.0%	0.0%
$[+\Theta/-\Theta/0/90]_{2T}$	19.2%	25.7%	25.4%	17.1%	8.7%	3.1%	0.9%
$[\theta 2/0/90]_S$	0.0%	45.3%	68.6%	69.6%	56.6%	28.0%	0.0%
$[\theta 2/0/90]_{2T}$	19.3%	35.1%	62.9%	64.9%	53.2%	29.0%	4.5%
$\alpha_x(10\text{-}6/^oF)$							
$[+\Theta/-\Theta/0/90]_S$	0.0%	0.0%	0.0%	0.0%	0.0%	0.0%	0.0%
$[+\Theta/-\Theta/0/90]_{2T}$	51.8%	2.7%	1733.8%	9.5%	4.6%	5.9%	6.0%
$[\theta 2/0/90]_S$	0.0%	536%	23530%	189%	32.4%	3.3%	0.0%
$[\theta 2/0/90]_{2T}$	51.8%	548%	23741%	199%	38.9%	9.8%	6.0%
$\alpha_y(10\text{-}6/^oF)$							
$[+\Theta/-\Theta/0/90]_S$	0.0%	0.0%	0.0%	0.0%	0.0%	0.0%	0.0%
$[+\Theta/-\Theta/0/90]_{2T}$	53.0%	52.3%	49.1%	36.0%	203.2%	6.0%	4.4%
$[\theta 2/0/90]_S$	0.0%	3.3%	32.4%	189%	23530%	536%	0.0%
$[\theta 2/0/90]_{2T}$	53.0%	58.8%	101%	324%	32026%	632%	4.4%

I-BEAM RESULTS COMPARING MODIFIED METHOD TO FEA

I-beam Finite Element Models

Narrow Beam Theory predictions are compared to FEA results for two types of I-beams as shown in Figure 2.19. The Tall I-beam model has a web width of 1 inch and the Short model has a web width of 0.5 inches. The top and bottom flange widths are 1 and 2 inches, respectively, for both models.

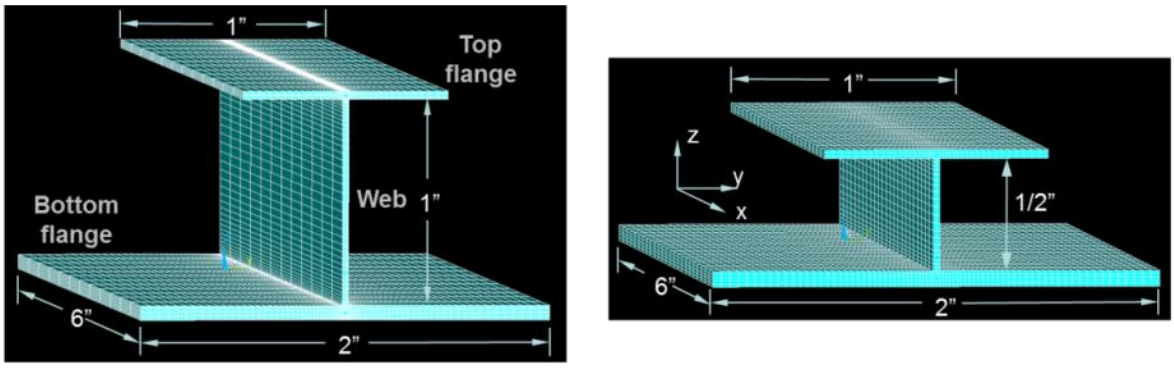

Figure 2.19 Finite Element Models of Tall and Short I-beams

Solid element, SOLID186, is used which has 20 nodes per element and each node has 3 degrees of freedom [44]. Solid elements were used to ensure out of plane strains and stresses are modeled accurately. Each model has a minimum of 165,000 degrees of freedom. Models were constructed by using MATLAB to make an APDL text file which defines keypoints, creates volumes from the keypoints, then meshes the volumes with the appropriate local coordinate system.

For the mesh, there is an element per composite layer, thus the thickness of each element is 5 thousands of an inch. A zoomed view of a typical mesh is seen in Figure 2.20. The mesh of the web and flanges is denser closer to the web-flange

interface and linearly increases in element width with the distance away from this interface. The flange mesh at the web interface matches the web mesh such that the thickness and width of the flange elements are both 0.005 inches.

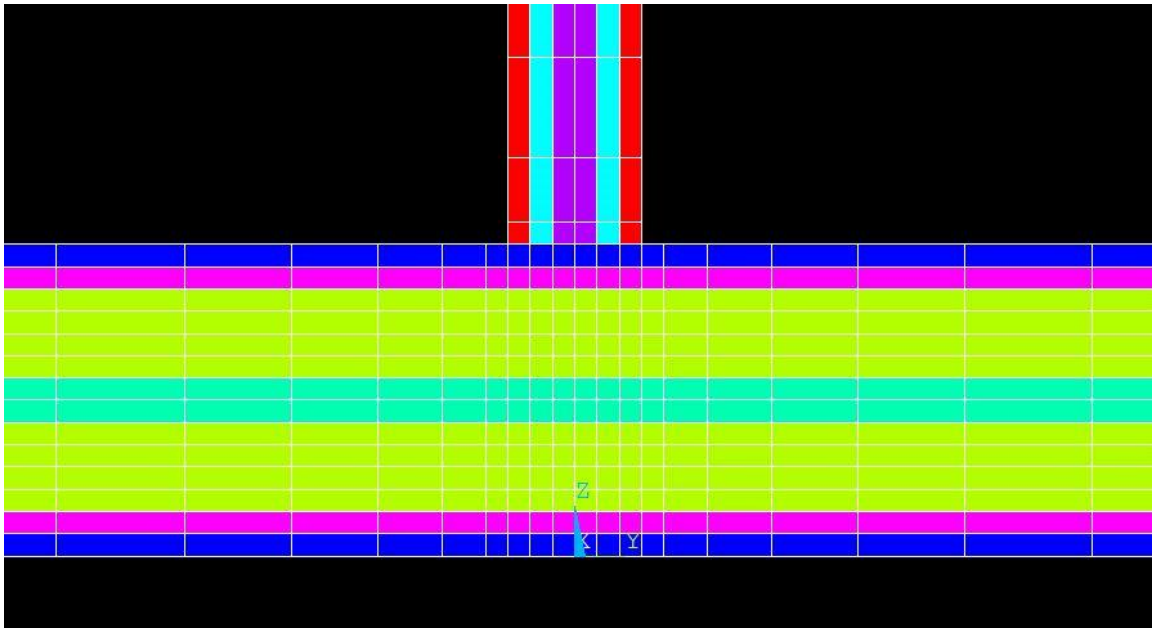

Figure 2.20 Mesh used for I-beam, element coordinate system shown

The element coordinate system is assigned by first rotating the global coordinate system relative to the x-axis, then rotating it about the z-axis in the plane of each ply. An example of the APDL code to show how to define the element coordinate system for the web is as follows.

```
CSYS,0                          ! Working in global crd system first
CLOCAL,20,CART,0,0,0,0,90,0     ! Rotating 90 degrees about x-axis
CSYS,20                         ! Work in CSYS,20
CLOCAL,30,CART,0,0,0,45,0,0     ! Rotate CSYS,20 in plane of laminate
        ! Using mapped mesh commands not shown here
ESYS,30                         ! Defines element coordinate system
VSEL,S,VOLU,,1                  ! Selects volume to mesh
VMESH,ALL                       ! Meshes selected volume(s)
```

The fixed end of the model is fully constrained at each node as seen at the far end in the upper left hand corner in Figure 2.21. Loads are applied to a master node at the centroid of the cross section on the other end of the beam in the lower right hand corner of Figure 2.21 with either CERIG or RBE3 linear constraint equations. The centroid, displacement, and stress are measured in the middle of the beam using an RBE3 constraint.

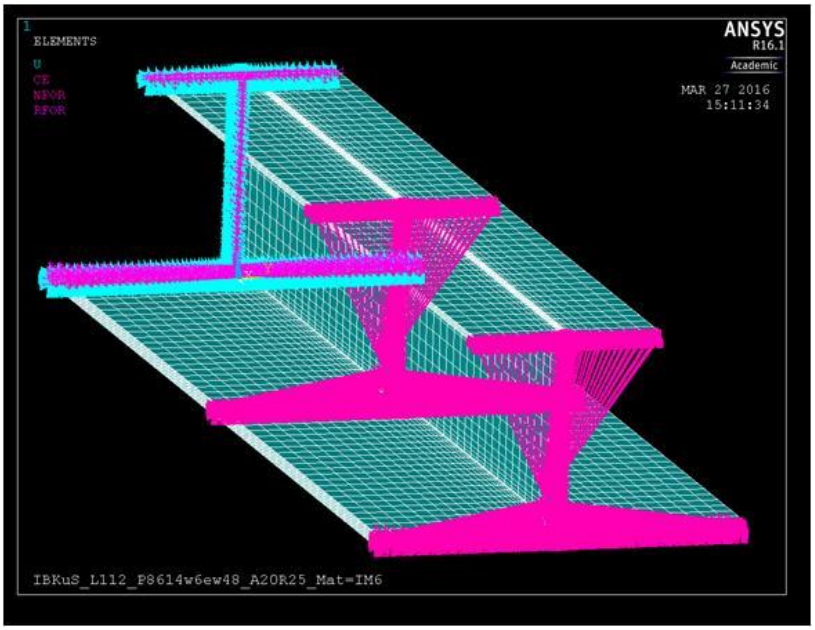

Figure 2.21 I-beam model showing far end at upper left fully constrained, near end using a CERIG constraint for loads, and middle with an RBE3 constraint

Both the CERIG and RBE3 constraints use a master node which is attached to a MASS21 point element located at the centroidal cross-section of the I-beam. The master node has 6 DOFs (3 for translation and 3 for rotation) which are defined by the MASS21 element. The master node is attached to slave nodes which in this case are all the nodes at the desired cross-section. The CERIG command sets up a ‘Constraint Equation based RIGid region’ which holds the slave nodes or cross section rigid but

allows 6 DOFs as defined by the master node. Essentially, the slave nodes have dependent DOFs and the master node has independent conditions. With the RBE3 command, the role of the slave and master node are switched where the slave nodes have independent DOFs and the master node is the dependent node reflecting the average of all the slave nodes.

As mentioned, both constraints are both used to distribute a load to the end of the beam. The CERIG constraint is appropriate for cases where the beam is actually a portion of a structure such as a part of a wing between bulkheads. The RBE3 constraint treats the beam as an isolated cantilever where the end is free to deform. Thus, the deformation behavior varies based on which constraint is used to apply loads as seen in Figure 2.22 which shows a tall I-beam model with unsymmetric laminates subject to an axial load. In reality, beams fall between these two conditions so both cases are considered in this analysis for the tall model.

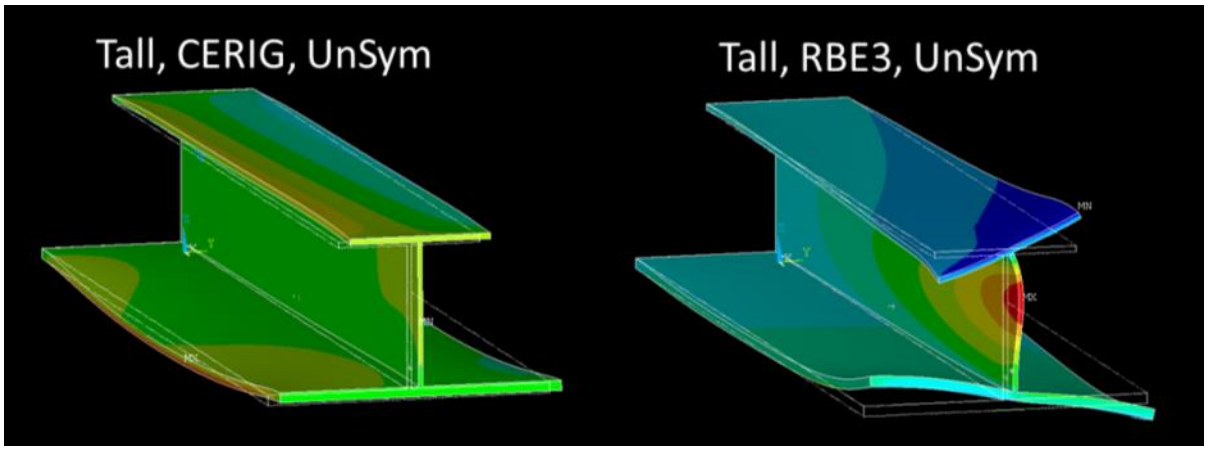

Figure 2.22 Comparing deformation of CERIG and RBE constraints with Tall, unsymmetric model under tensile loading

The meshed aspect ratios are kept a width-to-thickness ratio of 10 to 20 and a length-to-thickness ratio of 25. These aspect ratios are chosen based on a convergence study as shown in Figure 2.23 below. In this figure, 'P325' stands for 3 plies for upper flange, 2 plies for web, and 5 plies for lower flange. 'P8614' is similar having 8 plies for upper flange, 6 plies for web, and 14 plies for lower flange. 'P325 Length' checks length-to-thickness aspect ratio which range from 200 to 10 corresponding to the data points. 'P325 Width' checks the width-to-thickness AR (aspect ratio) for the P325 I-beam whose data points range from an AR of 30 to 2. 'P8614 Width' data points range from an AR of 30 to 10.

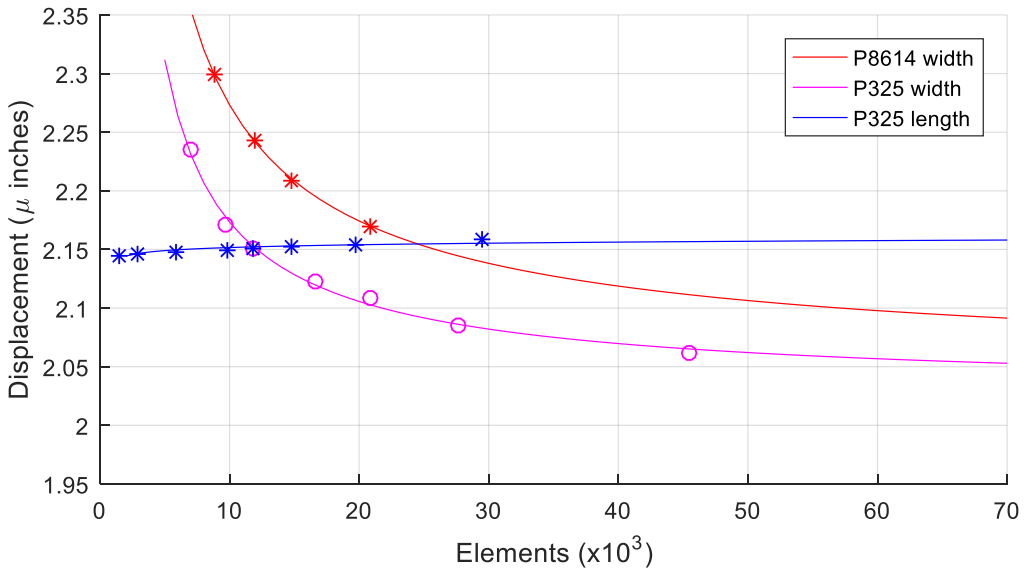

Figure 2.23 Convergence plot of I-beam

The structural width-to-depth ratio is 2 and 4 for the Tall and Short I-beams, respectively. The Short I-beam will test the Narrow Beam Theory with a slightly wide beam with a width-to-depth ratio of 4.

Stress readings were taken from elements located at middle section of the beam. Post processing of stress in the global direction of each element from ANSYS was done using MATLAB.

Axial stiffness is determined by,

$$EA = \frac{\text{x-displacement}}{\text{axial load}} \quad . \qquad (2\text{-}62)$$

Bending stiffness is determined by use of the Bernoulli-Euler equation for cantilever beams with an applied moment at the free end as follows,

$$EI = -\frac{ML^2}{2z} \qquad (2\text{-}63)$$

where M is the moment applied, L is the length of the beam, and z is the displacement in the z-direction.

Four layup configurations studied which are shown in Table 2.4. In addition, the length is varied for the Tall beam FEM from 6 to 12 inches. Also, two methods of applying loads will be studied, one with the CERIG constraint and the other with the RBE constraint.

Table 2.4 I-beam Layup Variations

	Sym, Bal	**unSym, Bal**	**Sym, unBal**	**unSym, unBal**
Top Flange	$[\pm 45/0/90]_S$	$[\pm 45/90/0]_{2T}$	$[45_2/90/0]_S$	$[45_2/90/0]_T$
Web	$[\pm 45/0]_S$	$[0/45_2/-45_2/0]_T$	$[45_2/0_2/\pm 45]_T$	$[0/45_3/-45/0]_T$
Bottom Flange	$[\pm 45/0_4/90]_S$	$[0_2/90/0_2/\pm 45]_{2T}$	$[-45_4/90/0_2]_S$	$[0_2/90/0_2/45_2]_{2T}$

The layups chosen in Table 2.4 consider how the I-beam is manufactured which is illustrated in Figure 2.24. One or more plies are used on the outer surface of the web

which also becomes external plies to the flanges. These are the C-shaped plies on either side of the web. Thus, for the symmetric & unbalanced layup, the lower outer ply of the top flange is +45 degrees which is +45 degrees on the web but is -45 degrees on the top of the bottom flange.

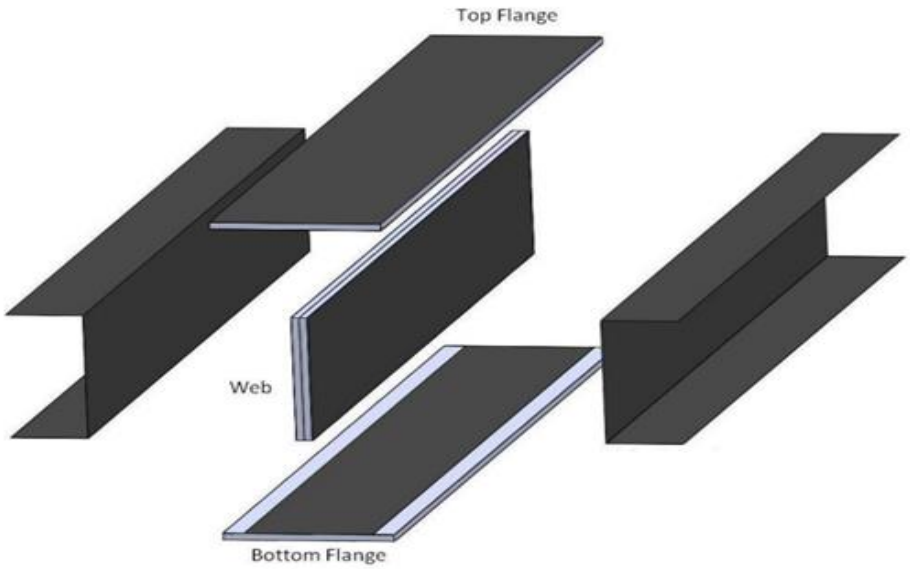

Figure 2.24 Typical layup of I-beam (adapted from [45])

Composite I-beam Analysis, Centroid and Stiffness

Table 2.5 shows a comparison of I-beam structural properties between the Narrow Beam Theory (NBT) and conventional analytical methods for the tall model with 6 and 12 inch lengths.

Table 2.5 Comparison of NBT and Conventional Method

using the tall model at 6 and 12 inch lengths

Model	Layup	Method	Length (in)	Centroid Height (in)	Axial Stiffness (lb-in)	Bending Stiffness D_x (lb-in^2)	Bending Stiffness D_z (lb-in^2)
Tall	Sym, Bal	NBT	6	-2.0%	-0.1%	-1.3%	11.4%
			12	-0.5%	0.0%	-0.2%	0.4%
		Conv	6	-1.9%	-0.1%	31.8%	0.0%
			12	-0.4%	0.0%	33.3%	-9.8%
	UnSym, Bal	NBT	6	3.2%	-0.7%	-5.1%	-0.3%
			12	-0.9%	-0.6%	-2.0%	0.0%
		Conv	6	0.0%	-4.4%	25.4%	-14.1%
			12	-4.0%	-4.3%	29.6%	-13.8%
	Sym, UnBal	NBT	6	-5.4%	-2.3%	-8.6%	3.7%
			12	1.4%	-0.4%	0.1%	-2.2%
		Conv	6	-5.5%	-2.4%	-4.2%	4.6%
			12	1.4%	-0.4%	4.9%	-1.3%
	UnSym, UnBal	NBT	6	-5.4%	2.9%	2.7%	13.7%
			12	-3.0%	0.1%	0.3%	-1.2%
		Conv	6	-37.2%	37.5%	43.8%	47.3%
			12	-9.2%	-5.5%	41.2%	-17.0%

The values in this table are percentages showing the difference between the predicted values and values obtained from ANSYS FEA. The layups refer to the layups presented in Table 2.4. Note that bending stiffness D_{xz} was not included since its value is very low.

Comparing the Narrow Beam Theory (NBT) Method to the Conventional, NBT has lower error percentages than the conventional method using a 6 inch length beam

for most centroid and stiffness values with the exception of the cells highlighted in purple. For beams with length of 12 inches, NBT values are all lower in error than those predicted by the conventional method. Also, NBT predictions using the 12 inch beam are consistently lower in error than NBT predictions using the 6 inch beam. The 6 inch length may experience more end constraints effects which cause some NBT predictions to be away from FEA estimations. Note that conventional method prediction errors with the 12 inch beam did not always decrease as compared to the errors with the 6 inch model.

Table 2.6 compares the centroid and stiffness predictions of the tall and short 6 inch length models. In this table, under 'Model', 'Width: F1=1", W=1", F2=2"' refers to the width of the upper flange, web, and lower flange in inches. A CERIG constraint at one end of the beam is used to apply loads at the cross-sectional centroid.

For the short model, NBT is more accurate in predicting the centroid and stiffnesses as compared to the conventional method with the exception of the bottom yellow highlighted cell for axial stiffness with the unsymmetric and unbalanced layups. At the same layup, the bending stiffness, D_X, is 5.3% different from the FEA estimation which can be considered acceptable. The short model NBT predictions are overall better than those using the tall model whereas conventional stiffness predictions are worse for the short beam compared to the tall beam. This is a surprising finding since the Narrow Beam Theory should work better in narrow beams such as the tall I-beam.

Table 2.6 Structural property comparison between the

Modified and Conventional Analytical Method

CERIG Constraint			% Difference from FEM Results			
Model	**Layup**	**Method**	**Centroid Height (in)**	**Axial Stiffness (lb-in)**	**Bending Stiffness D_x ($lb\text{-}in^2$)**	**Bending Stiffness D_z ($lb\text{-}in^2$)**
Tall, Width F1=1" W=1" F2=2"	Sym, Bal	NBT	-2.0%	-0.1%	-1.3%	11.4%
		Conventional	-1.9%	-0.1%	31.8%	0.0%
	UnSym, Bal	NBT	3.2%	-0.7%	-5.1%	-0.3%
		Conventional	0.0%	-4.4%	25.4%	-14.1%
	Sym, UnBal	NBT	-5.4%	-2.3%	-8.6%	3.7%
		Conventional	-5.5%	-2.4%	-4.2%	4.6%
	UnSym, UnBal	NBT	-5.4%	2.9%	2.7%	13.7%
		Conventional	-11.4%	-2.9%	44.6%	-4.6%
Short, Width F1=1" W=1/2" F2=2"	Sym, Bal	NBT	-0.4%	-0.1%	-1.4%	0.1%
		Conventional	-0.2%	-0.1%	36.5%	-8.4%
	UnSym, Bal	NBT	0.1%	-0.7%	-3.8%	-0.4%
		Conventional	-3.2%	-4.7%	33.1%	-12.7%
	Sym, UnBal	NBT	-1.5%	1.3%	-1.1%	-2.3%
		Conventional	-1.5%	1.3%	4.5%	-2.6%
	UnSym, UnBal	NBT	0.9%	3.5%	5.3%	-3.7%
		Conventional	-6.0%	-2.7%	57.6%	-18.1%

When looking at the deflections of the full I-beam models in ANSYS, the Tall, symmetric and unbalanced (UnBal) I-beam case exhibits twisting under a tensile load as compared to the unsymmetric case (UnSym) as seen in Figure 2.25. In this figure, loading is applied to the master node of a CERIG constraint. This seems to cause the

predictions of NBT for centroid and bending stiffness, D_X, to be larger in error for the unbalanced layup compared to the unsymmetric layup and the symmetric and balanced layup. However, these prediction errors are close to an acceptable value of 5% and are alleviated when using a 12 inch beam.

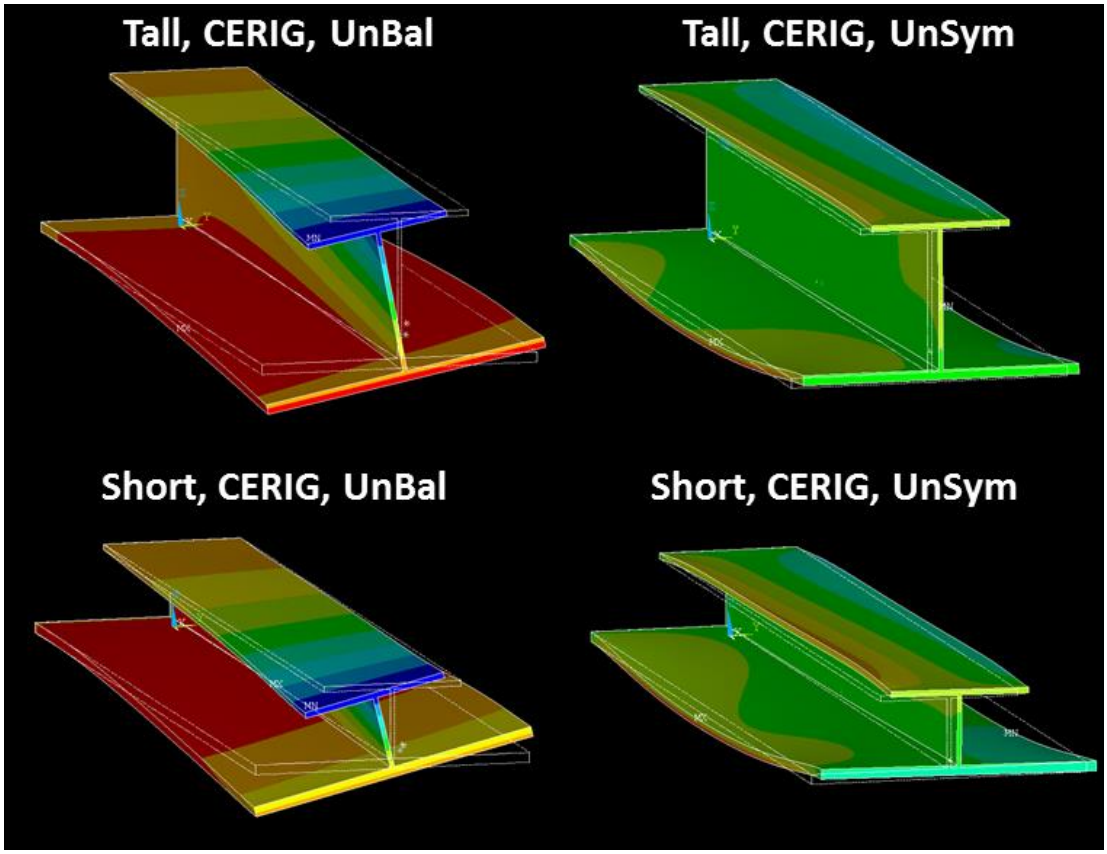

Figure 2.25 Deformation comparison of Tall I-beam models under tensile loading. FEM beam is 6 inches long. Color scheme shows deflection in the y-direction.

Composite I-beam Analysis, Ply Stress

Stress analyses are made for each layup variation shown in Table 2.4 for the tall model with lengths of 6 and 12 inches, and short model with length of 6 inches. Plots for all variations with a 6 inch length are found in Appendix B.

For most models and load cases, the ply stresses predicted by the NBT was within five percent or less of the FEM. A summary of notable discrepancies of significant ply stresses between the NBT and FEA is shown in Table 2.7. Note, F_x is an axial load, M_x is a moment about y-axis, and M_z is a moment about z-axis. 'L' is for beam length. The percentages shown in Table 2.7 are the difference between ply stress predictions by NBT compared to those estimated by FEA. The stresses used for this comparison are from 6 points across the width of the flanges and 8 points across the width of the web. These points do not include stress at the end points which are affected by end effects and stress close to the web-flange interface which are affected by the stress concentrations in this region as shown in Figure 2.28. NBT does not account for stress concentrations and end effects. The percentage shown is the stress difference at each point between the NBT and FEA along the width. Thus, for a plot as shown in Figure 2.26, the difference in the stress for the zero degree ply is 11 percent even though if the stress is averaged then compared, the difference would be close to zero. Stress obtained from FEA is noted by a solid curve and stress from NBT is noted by the dotted line of which there are 10 data points across the width of the member.

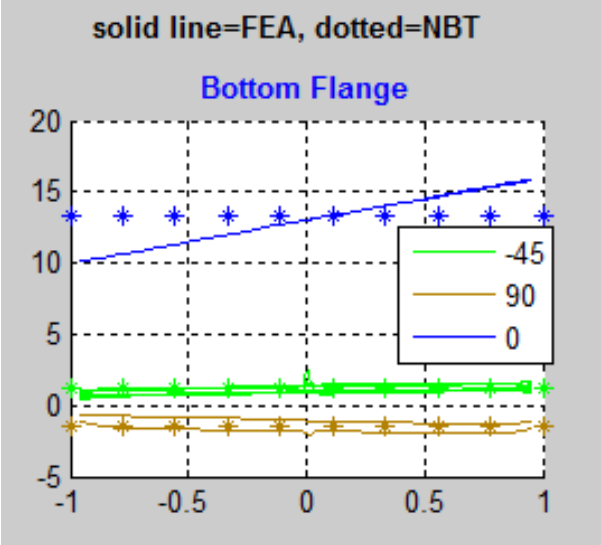

Figure 2.26 Comparing stresses between FEA and NBT

Table 2.7 Notable Discrepancies between the NBT and FEA of significant ply stresses.

Top and Bot correspond to top and bottom flange.

	Model	L	Lay-up of I-beam (member, load, % difference)			
		(in)	Sym, Bal	UnSym	UnBal	UnSym, UnBal
CERIG	Short	6	all stresses < 3%	Top, F_x 4% Bot, M_x 5%	Top, F_x 8% Bot, F_x 16%	Top, F_x 10% Bot, F_x 10% Bot, M_x 7%
	Tall	6	all stresses < 3%	Top, F_x 7% Bot, M_x 3%	Top, F_x 7% Bot, F_x 11%	Top, F_x 10% Bot, F_x 19% Bot, M_x 3%
	Tall	12	all stresses < 3%	Top, F_x 1%	Top, F_x 4.5% Bot, F_x 7%	Top, F_x 5% Bot, F_x 9%
RBE3	Tall	6	Top, F_x 3% Top M_z 42%	Top, F_x 7% Top M_z 44%	Top, F_x 7% Bot, F_x 12% Top, M_z 16%	Top, F_x 20% Bot, F_x 21% Top, M_z 50%
	Tall	12	Top, F_x 1% Top M_z 34%	Top, F_x 1% Top M_z 40%	Top, F_x 5% Bot, F_x 8% Top, M_z 12%	Top, F_x 10% Bot, F_x 10% Top, M_z 44%

In Table 2.7, only significant ply stresses are considered. In most cases, stress in the principal material direction, σ_{11}, is the significant stress. 'L' represents the length of the beam. For each model and beam length, 3 load cases were considered separately in this table, an axial force, F_x, a moment about the y-axis, M_x, and a moment about the z-axis, M_z. All 3 members of the I-beam are considered but the web has no notable discrepancies or has very low stresses thus does not appear in the table. For the flanges, 'Top' and 'Bot' indicate the top and bottom flange. Note that Appendix B does include a 4th load case which is a combined loading of F_x, M_x, and M_z but this is only a superposition of each of these loads applied separately.

For the CERIG constraint case, predictions in all significant ply stresses for the symmetric, balanced I-beam model are within 3% of stresses estimated by FEA. The accuracy of predicted σ_{11} stress values for models with a half inch web length are very similar to that of one inch with the exception of the bottom flange of the unsymmetric and unbalanced model as seen highlighted in yellow in Figure 2.27 with an applied moment M_x. The bottom flange in this layup has 8 zero plies which are all visible in blue in this figure since they experience different stresses due to bending about the y-axis.

As illustrated in Figure 2.28, differences in predicted σ_{11} stress compared to FEA on the bottom flange are larger with the half inch web model due to more pronounced constraint induced stresses. The first ply stresses of the half inch web experience much higher relative stress range fluctuations than that of the one inch web. This occurs because the half inch web model experiences a larger torsional rotation due to flanges

closer to the shear center. Figure 2.28 compares the σ_{11} stresses of the short and tall, unsymmetric and unbalanced models with an applied moment of M_x along the xy-plane of the bottom flange. The short or ½ inch web model experiences much more stress compared to the 1 inch web model since the flanges are closer to the neutral axis. Also, the predictions of σ_{11} in the 90° plies of the bottom flange are not very accurate but these are not considered as significant stress compared to the σ_{11} stress on the 0° plies. Overall, the Narrow Beam Theory can be applied to I-beams with 4:1 width to depth ratios with little error.

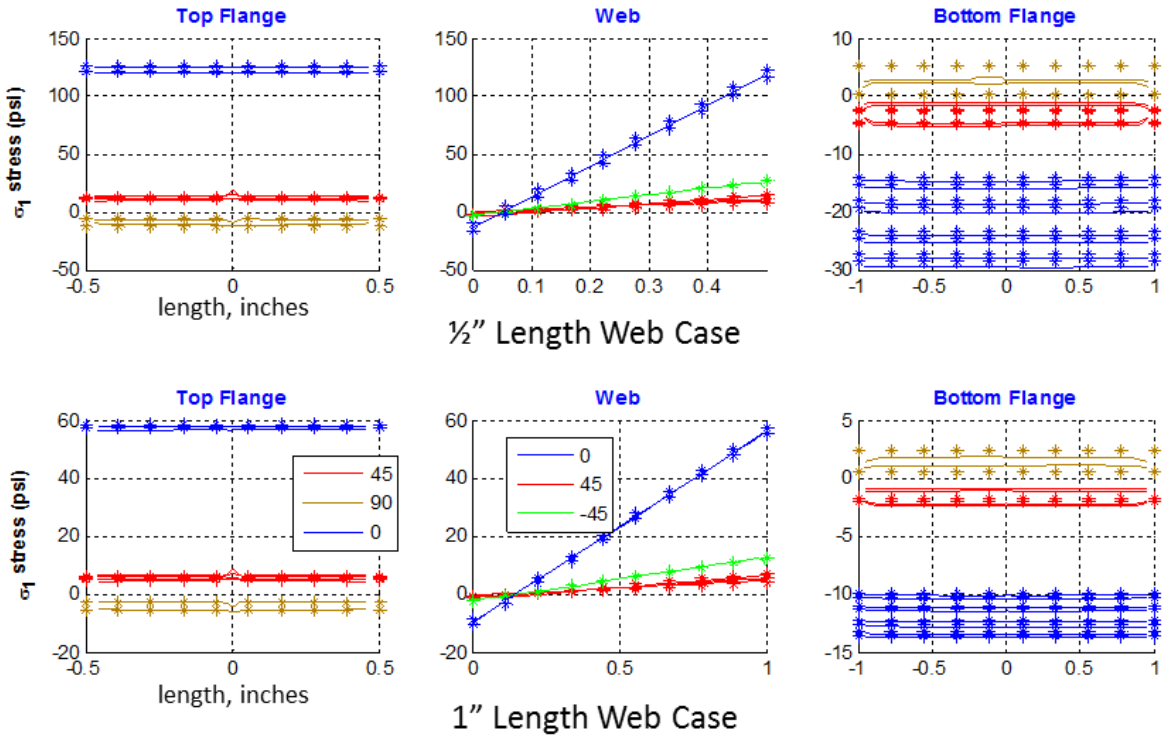

Figure 2.27 Comparison of the ½" length web to the 1" length web unsymmetric and unbalanced case, M_x load, considering σ_{11}. NBT stresses are dotted lines and FEA stresses are solid lines.

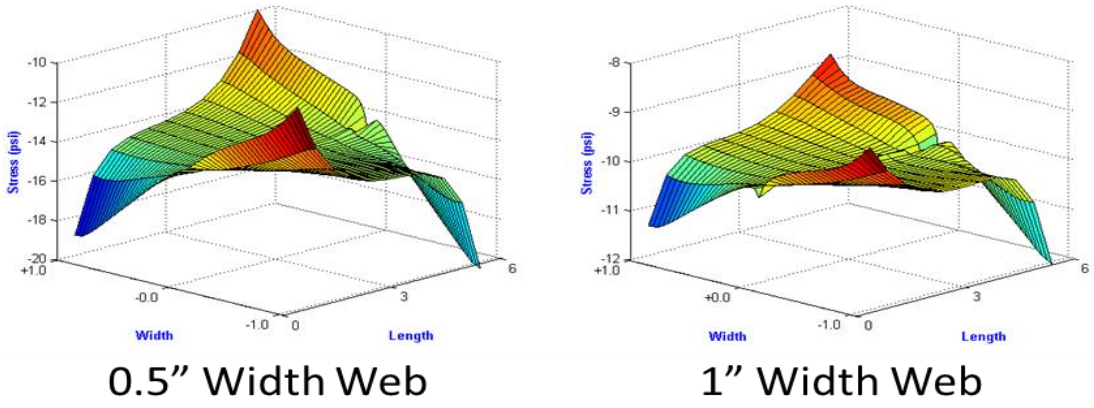

Figure 2.28 Comparison of the ½” width web to the 1” width web, unsymmetric and unbalanced case, M_x load, bottom flange, first ply, considering σ_{11}.

A poor prediction of σ_{11} using CERIG of 7% resulted from the unsymmetric model in the 0^o ply of the top flange with an applied axial force, highlighted in blue in Table 2.8. This is for the model of 6 inch length but when checking the same model and conditions with the 12 inch length, this error reduced to 1%. This is illustrated in Figure 2.29. Similar results are found with the unbalanced case in the top and bottom flanges also shown in Figure 2.29.

The 12 inch length model is less affected by the rigid body constraints applied at both ends of the beam, CERIG and fixed constraints. This is illustrated in Figure 2.30 where the σ_{11} stress across the width and length of the 0^o ply of the bottom flange due to an axial load is compared between the 6 and 12 inch length unsymmetric models. The overall stress is flatter and lower over the length and width of the beam for the 12 inch model. The end constraint-induced stresses affect the stresses more throughout the length of the shorter beam than those of the longer beam.

The NBT method obviously does not predict the end constraint-induced stresses, stress concentrations where the web meets the flanges, and edge stresses at the end of the flanges.

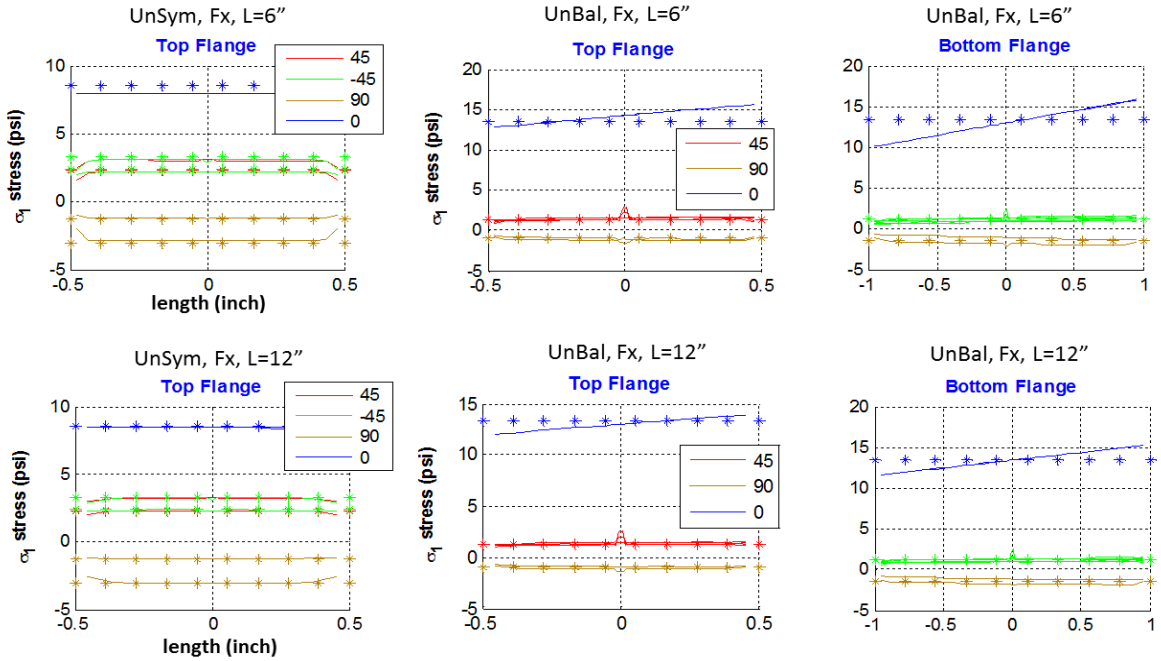

Figure 2.29 Comparison between 6 and 12 inch length CERIG constrained models with poor analytical predictions. NBT stresses are dotted lines and FEA stresses are solid lines.

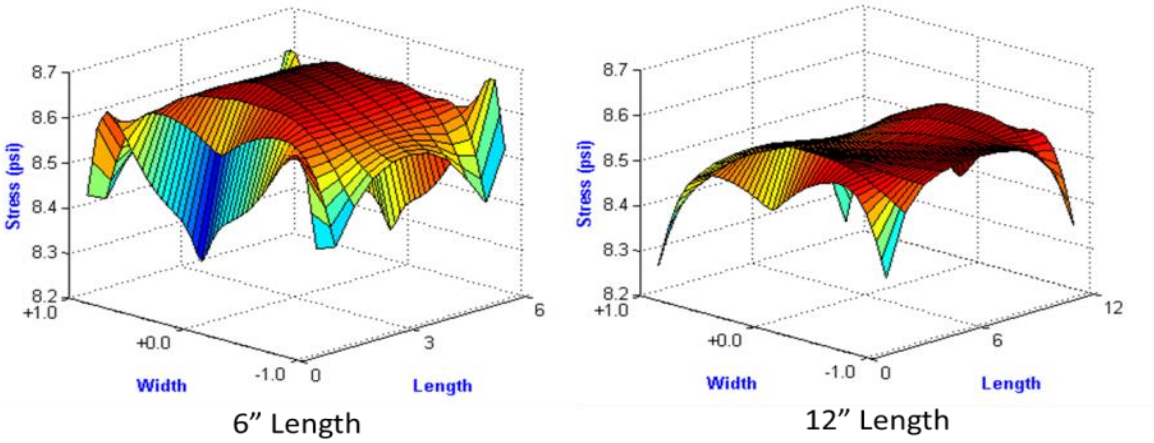

Figure 2.30 Comparison of σ_{11} stresses in the 0° ply of bottom flange, unsymmetric, tall model under axial load with CERIG constraint. Stresses from 0.5” to 5.5” and 1” to 11” length for the 6” and 12”length models, respectively, are shown.

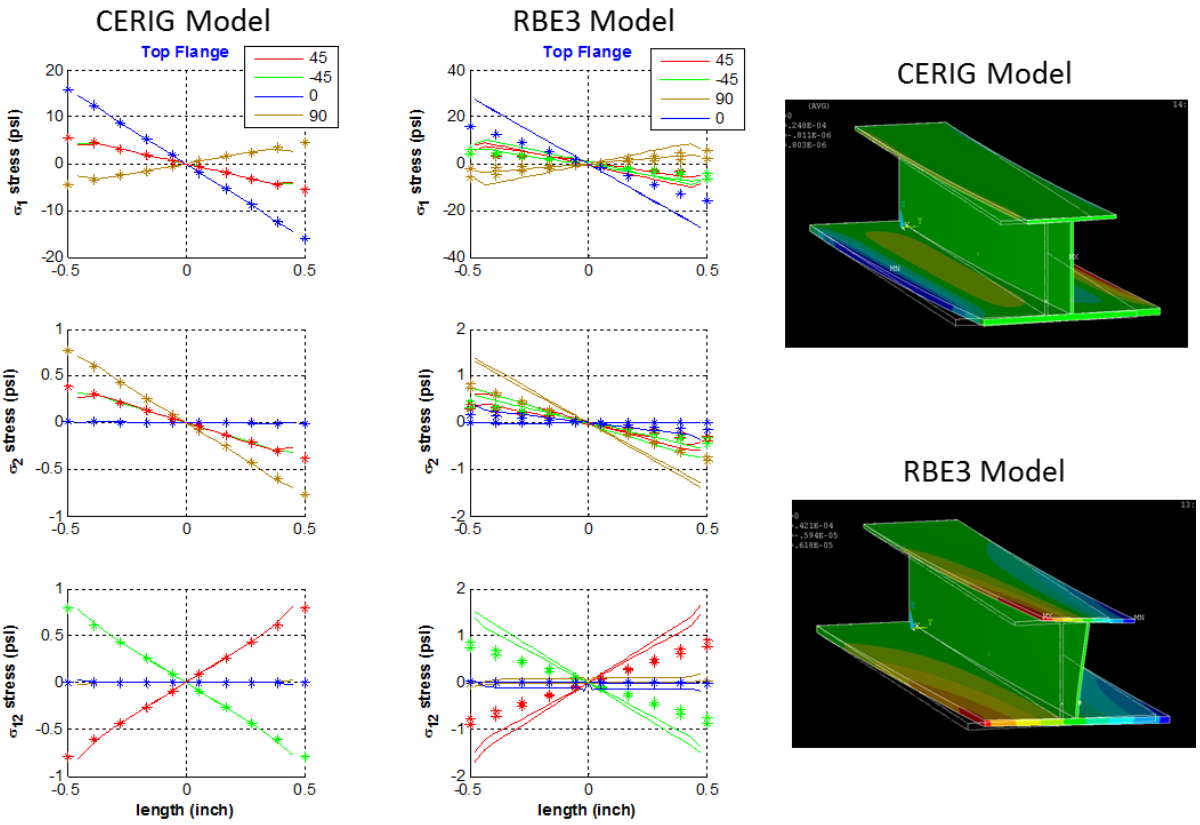

Figure 2.31 Comparison of σ_{11} ply stresses between CERIG and RBE3 constraint. Model is tall, unsymmetric, 6” length under M_z applied moment. NBT stresses are dotted lines and FEA stresses are solid lines. FEM plots to the right show deflection due to M_z with colors representing z-displacement.

A comparison of σ_{11} ply stresses between the CERIG and RBE3 constraints is shown in Figure 2.31 using the tall, unsymmetric model, 6 inch length, under an M_z applied moment. As shown with the full FEM on the right in Figure 2.31, the RBE3

constraint allows a slight rotation about the x-axis due to M_z which is constrained in the CERIG model. Note that only the boundary of the unloaded model is shown. This rotation with the RBE3 constraint causes additional stresses in the top flange as evidenced in the top flange stress vs. width plots. These additional stresses are not predicted by the NBT. The differences in stress between NBT and FEA are highlighted in green in Table 2.7.

From Table 2.7, the 12” length beam does not alleviate the stresses caused by M_z much for each lay-up since a rotation is still present with the RBE3 constraint model (highlighted in green in Table 2.7). Similar to the CERIG models, the σ_{11} stresses in 0° ply of the top and bottom flanges due to an axial load for each lay-up are alleviated using the 12” length model as compared to that of the 6” model for all layup variations.

SUMMARY

A concept of equivalent properties for lamina, laminate, and structure levels is presented. Methods that are considered include the modified method and the conventional method. Equivalent properties calculated by the modified method takes into consideration the structure behavior of an equivalent zero degree lamina. Hence, the induced curvature and the shear deformation are suppressed for unsymmetrical and unbalanced laminates under applied axial or thermal loading, and the induced axial and shear deformation are suppressed under an applied bending moment.

A comparison between the modified and conventional method on equivalent properties of individual laminas validated the modified model. The equivalent moduli of

the modified method for laminates that are not symmetric & balanced are greater than those of the conventional method since these moduli restrict couplings. Also, symmetric & unbalanced laminates yielded higher differences between the equivalent moduli of the modified and conventional methods than the unsymmetric & balanced laminates. For all equivalent properties with the exception of the Poisson's ratio, the unsymmetric and unbalanced laminates yielded the highest difference between the modified and conventional method.

For symmetric & balanced, and symmetric & unbalanced laminates under an axial load, the modified method gives reasonable predictions for the σ_x ply stresses. For unsymmetric laminates, the differences between the modified method and FEA for the σ_x stress in 0^o plies varies were as high as 26% and averaged around 8% for the unsymmetric laminates considered. Thus, for unsymmetric layups, the modified method could be used for rough estimates of σ_x stress given axial loading conditions. In the case of the thermal load, the modified method gives reasonable predictions for the σ_x^{TH}, and τ_{xy}^{TH} ply stresses for thermally loaded symmetric and balanced, and unsymmetric and unbalanced laminates.

In predicting the centroid and axial and bi-directional bending stiffness for the structural case of the I-beam, Narrow Beam Theory is consistently more accurate than the conventional method with almost all results under 5% as compared to FEA. However, in cases where twisting rotation is present such as the unbalanced model, the NBT accuracy can be over 5% for the tall model but under 5% for the short model and can be improved by considering a longer beam.

The accuracy of predicting ply stress using the NBT depends on the constraint used in the FEM and the length of the beam analyzed. For a length to height ratio of 3 to 1 using the CERIG constraint to apply loads, the axial loading case yielded significant ply stress errors over 5%. However, for length to width ratios of 6 to 1, the additional stress caused by the constrained ends are reduced by the longer length causing most significant stresses to be under 5% with the exception of the bottom flange under axial loading. Using the RBE3 constraint to apply loads, the stress prediction caused by axial loading was similar to the CERIG case. However, an applied M_z moment caused large errors in the significant stresses of the top flange which was only slightly alleviated by using a longer length beam. Overall, most predicted ply stresses are under 5% using NBT. Also, the NBT is valid for I-beams with width to depth ratios of 1 to 4.

In summary, the modified method is a significant improvement over the conventional method and can be used in analysis of laminates in most cases. The modified method also can be used to analyze the centroid, stiffness', and ply stresses for structures similar to the I-beam with prediction errors mostly under 5%.

CHAPTER 3

ANALYTICAL METHOD TO ANALYZE AIRFOIL BLADES UNDER AXIAL AND BI-DIRECTIONAL MOMENTS

A modification of Narrow Beam Theory is used to analyze composite airfoil cross-sections. The analytical method developed is a semi-closed solution which breaks up an airfoil profile into discrete elements and treats each element as a laminate. The laminate properties are rotated, then the Narrow Beam Theory is applied to find the stiffness properties. An alternative closed form method can be developed however this has not been developed in this research.

For this analysis, structural stiffness parameters obtained are the axial and bi-directional moment. A term is derived for the coupling between the bi-directional moments. Axial and bending stiffness terms are found about the centroid. Axial forces and moments about the centroid can induce torsion and will be considered but these coupling stiffness terms will not be determined in this analysis. Airfoils with and without an I-beam stiffener will be analyzed.

DISCRETIZING AIRFOIL PROFILE

The Narrow Beam Theory (NBT), similar to that was used to analyze the I-beam structure in Chapter 2, will be used. Before applying NBT, the cross-section of the airfoil must be chopped into discrete elements. This can be visualized in Figure 3.1.

Each element is a quadrilateral, oriented to match the contour of the airfoil. Each element is then treated as a laminate where Classical Lamination Theory can be

applied and the laminate ABD matrix can be found relative to the laminate x'- y'-z' axes. Note that the x-axis points out from the page. Each elemental 6x6 $[ABD]$ matrix, as shown in equation 2-14, is rotated about the x-axis to align with the global x-y-z coordinate system.

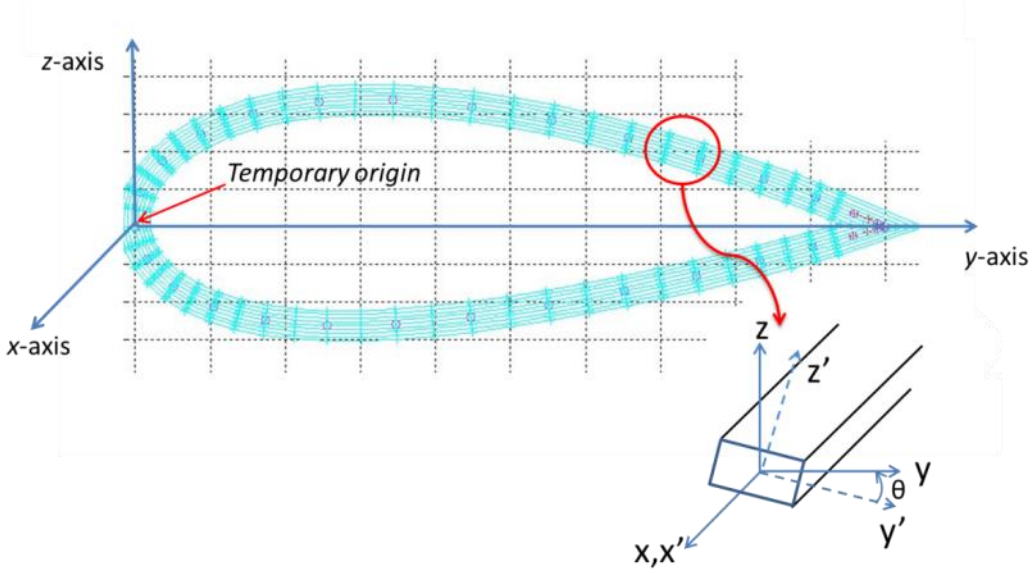

Figure 3.1 Dividing the Airfoil Contour into Discrete Elements

The global x-y-z coordinate system is chosen where the y-axis is the chord of the airfoil. The chord runs in a straight line from the leading edge point to trailing edge point of the airfoil. This helps to minimize the rotation of elements to the global x-y-z axes. Other global coordinate systems could be chosen but this was not performed in this research.

Addition of an I-beam stiffener or any other stiffener can be made and the same discretizing and ABD rotation can be performed. Figure 3.2 shows an I-beam stiffened airfoil studied in this research. In Chapter 2, the I-beam has straight flanges but in this

case, the flanges must follow the profile of the airfoil. Thus, to have good accuracy, the flanges are broken into elements as shown in the close-up image.

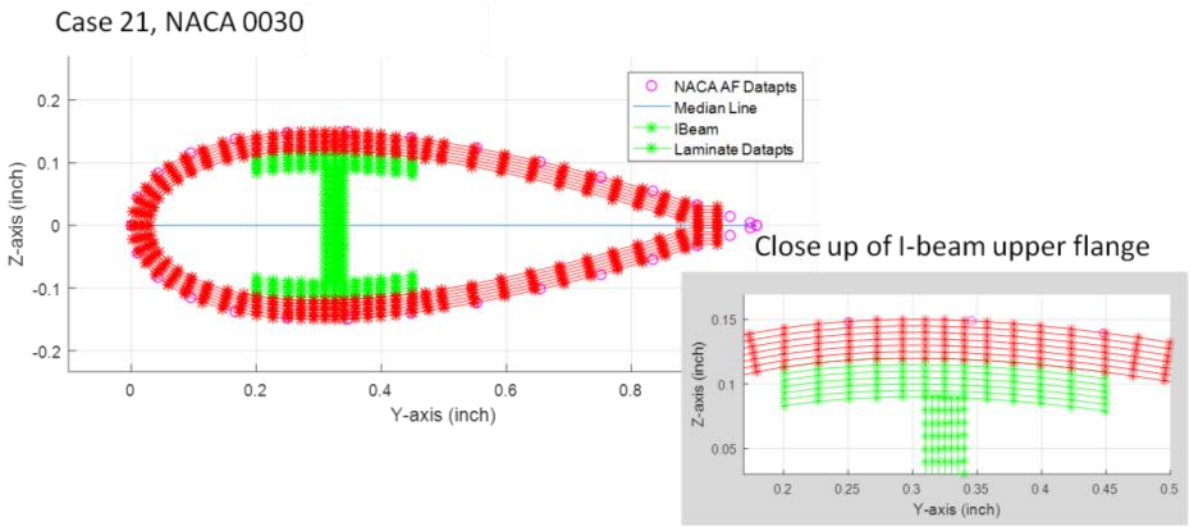

Figure 3.2 MATLAB generated model of NACA 0030 airfoil cross-section with I-beam stiffener

Note that the entire thickness of the profile is populated by elements. The MATLAB code generated for this research was used to conduct the analytical study as well as make an ANSYS model. Thus, the identical model was used for both analyses in which MATLAB is used to make an APDL code to generate the model in ANSYS. If no ANSYS model needs to be generated, then only a single curve is needed for the airfoil and I-beam profile. The curve then can be moved to the midplane of the laminate skin and the analytical method can be conducted. This works because the ABD matrix from Classical Lamination Theory relates strains and curvatures with structural load at the midplane.

ROTATION OF ELEMENT ABD

Rotation from the laminate x'-y' plane to the global x-y plane is shown in Figure 3.3. θ is the rotation angle to the y global axis . b_i is also shown which is the width of the element.

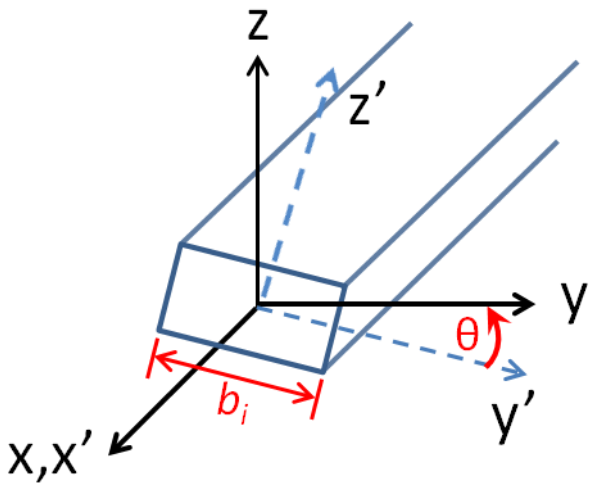

Figure 3.3 Rotation from laminate x'-y' direction to global x-y direction

Rotation of the 6x6 $[ABD]$ matrix is performed by transforming each 3x3 matrix which comprises the 6x6 $[ABD]$ matrix. This is done because the 3x3 matrices labeled as A, B, and D are 2 dimensional matrices in terms of x' and y'. The 6x6 $[ABD]$ matrix is thus a 2D matrix which requires 2D transformation matrices. Using the A matrix as an example, transformation about the x-axis towards the y-axis is,

$$[A^r_{x-y}]_i = [T_\sigma(-\theta_i)] \bullet [A_{x'-y'}]_i \bullet [T_\varepsilon(\theta_i)], \tag{3-1}$$

where the subscript 'i' represents each element of the airfoil and superscript 'r' indicates rotation by the transformation matrix about the x-axis to align with the global x-y-z coordinate system.

This same transformation formula is also used to rotate the B and D matrices about the x-axis. Note that rotation in Figure 3.3 is positive but the angle of the element is negative. The transformation matrices about the x-axis are:

$$[T_\sigma(\theta_i)] = \begin{bmatrix} 1 & 0 & 0 \\ 0 & m^2 & 0 \\ 0 & 0 & m \end{bmatrix} = [T_\varepsilon(\theta_i)], \tag{3-2}$$

where $m = \cos(\theta)$. By transforming the $[ABD]_i$ matrix, the rotated $[ABD]_i^r$ matrix is obtained:

$$[ABD]_i^r = \begin{bmatrix} A^r & B^r \\ B^r & D^r \end{bmatrix}_{i,y-axis}. \tag{3-3}$$

CONVERTING ELEMENT ABD INTO A 1D MATRIX: WIDE BEAM APPROACH

A popular technique to analyze structures is known as the wide beam approach which is often used by engineers in industry. Essentially, the beam is modeled as a wide plate as shown in Figure 3.4. Under a moment M_x, the plate experiences curvature in the z direction (k_x) but very little curvature in the y direction (k_y) except at the end of the plate. Also, there is strain in the x-direction but very little in the y direction. Thus, $\varepsilon_y, \gamma_{xy}, k_y,$ and k_{xy} are approximated to equal zero.

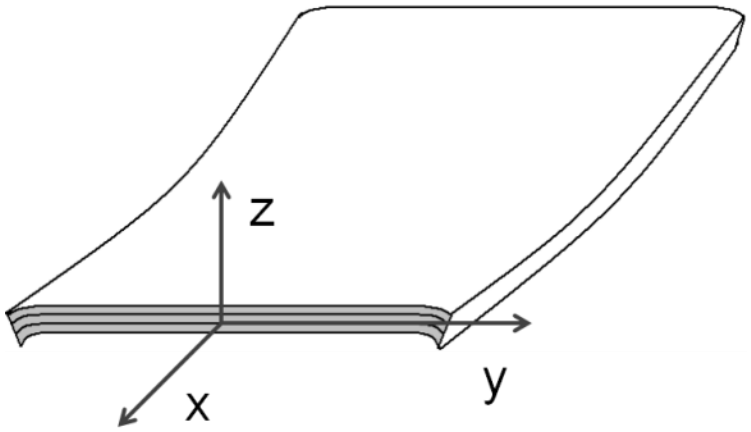

Figure 3.4 beam deformation due to moment (from Rios [32])

These assumptions are applied to the cross-sectional $\left[ABD\right]^r$ matrix and a simplified one dimensional, 2x2 matrix is derived.

$$\begin{Bmatrix} N_x \\ M_x \\ N_y \\ N_{xy} \\ M_y \\ M_{xy} \end{Bmatrix}_i = \begin{bmatrix} A_{11} & B_{11} & A_{12} & A_{16} & B_{12} & B_{16} \\ B_{11} & D_{11} & B_{12} & B_{16} & D_{12} & D_{16} \\ A_{12} & B_{12} & A_{22} & A_{26} & B_{22} & B_{26} \\ A_{16} & B_{16} & A_{26} & A_{66} & B_{26} & B_{66} \\ B_{12} & D_{12} & B_{22} & B_{26} & D_{22} & D_{26} \\ B_{16} & D_{16} & B_{26} & B_{66} & D_{26} & D_{66} \end{bmatrix}^r_{i,y-axis} \bullet \begin{Bmatrix} \varepsilon_x^o \\ k_x^o \\ \varepsilon_y^o \\ \gamma_{xy}^o \\ k_y^o \\ k_{xy}^o \end{Bmatrix}_i , \tag{3-4}$$

$$\begin{Bmatrix} N_x \\ M_x \end{Bmatrix}_i = \begin{bmatrix} A_{11} & B_{11} \\ B_{11} & D_{11} \end{bmatrix}^r_{i,y-axis} \begin{Bmatrix} \varepsilon_x^o \\ k_x^o \end{Bmatrix}_i . \tag{3-5}$$

Here it is noted that all the coupling terms except for B_{11}^r or the extension-bending coupling in the x-direction have been disregarded. This single coupling term is seen in Figure 3.5.

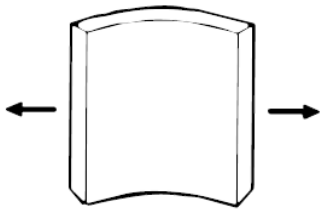

Figure 3.5 Wide Beam Approach only coupling term between extension and bending in the x-direction

This leads to inaccurate centroid and stiffness results for composite cross sections.

CONVERTING ELEMENT ABD INTO A 1D MATRIX: NARROW BEAM APPROACH

To find the centroid about the y-axis, the Narrow Beam assumptions for a laminate are made, where only N_x and M_x loads are considered and all other loads are approximated to be zero. In the I-beam case, M_{xy} was also considered since there was a web to improve torsional stiffness. In the airfoil case, twisting is assumed to occur relatively easily thus M_{xy} is assumed to be zero.

Note that M_x is a moment about the y-axis. By using matrix substitution, the coupling terms are considered since they are included in the simplified 1D stiffness matrix as follows. In these equations, the strains, curvatures, and loads are acting about the midplane of each element, noted by the superscript, $'o'$.

$$\begin{Bmatrix} N_x \\ M_x \\ N_y \\ N_{xy} \\ M_y \\ M_{xy} \end{Bmatrix}_i = \begin{bmatrix} A_{11} & B_{11} & A_{12} & A_{16} & B_{12} & B_{16} \\ B_{11} & D_{11} & B_{12} & B_{16} & D_{12} & D_{16} \\ A_{12} & B_{12} & A_{22} & A_{26} & B_{22} & B_{26} \\ A_{16} & B_{16} & A_{26} & A_{66} & B_{26} & B_{66} \\ B_{12} & D_{12} & B_{22} & B_{26} & D_{22} & D_{26} \\ B_{16} & D_{16} & B_{26} & B_{66} & D_{26} & D_{66} \end{bmatrix}_{i,y-axis}^{r} \bullet \begin{Bmatrix} \varepsilon_x^o \\ k_x^o \\ \varepsilon_y^o \\ \gamma_{xy}^o \\ k_y^o \\ k_{xy}^o \end{Bmatrix}_i \Rightarrow \begin{bmatrix} A_{11} & B_{11} & P \\ B_{11} & D_{11} & \\ & P^T & R \end{bmatrix}_i \quad (3\text{-}6)$$

where: $P = \begin{bmatrix} A_{12} & A_{16} & B_{12} & B_{16} \\ B_{12} & B_{16} & D_{12} & D_{16} \end{bmatrix}$, $R = \begin{bmatrix} A_{22} & A_{26} & B_{22} & B_{26} \\ A_{26} & A_{66} & B_{26} & B_{66} \\ B_{22} & B_{26} & D_{22} & D_{26} \\ B_{26} & B_{66} & D_{26} & D_{66} \end{bmatrix}$. (3-7)

Note that P^T is the transpose of the P matrix. The unknown terms $\varepsilon_y^o, \gamma_{xy}^o, k_y^o$, and k_{xy}^o can be substituted for using the P, P^T, and R matrices. The known cross-sectional loads in the x-direction can now be related to only the strain and curvature in the x-direction and material properties as follows,

$$\begin{Bmatrix} N_x \\ M_x \end{Bmatrix} = \begin{bmatrix} A_{11} & B_{11} \\ B_{11} & D_{11} \end{bmatrix} \begin{Bmatrix} \varepsilon_x^o \\ k_x^o \end{Bmatrix} + P\left(-R^{-1}P^T \begin{Bmatrix} \varepsilon_x^o \\ k_x^o \end{Bmatrix} \right). \quad (3\text{-}8)$$

This yields the following stiffness matrix,

$$\begin{Bmatrix} N_x \\ M_x \end{Bmatrix}_i = \begin{bmatrix} A^* & B^* \\ B^* & D^* \end{bmatrix}_{i,y-axis}^{r} \begin{Bmatrix} \varepsilon_x^o \\ k_x^o \end{Bmatrix}_i . \quad (3\text{-}9)$$

This simplified matrix relates x-direction loads with x-direction strain and curvature thus is a one dimensional equation. Due to use of matrix substitution, the coupling terms, such as extension couplings as illustrated in Figure 3.6, are not disregarded since they are substituted back into the 1D simplified matrix.

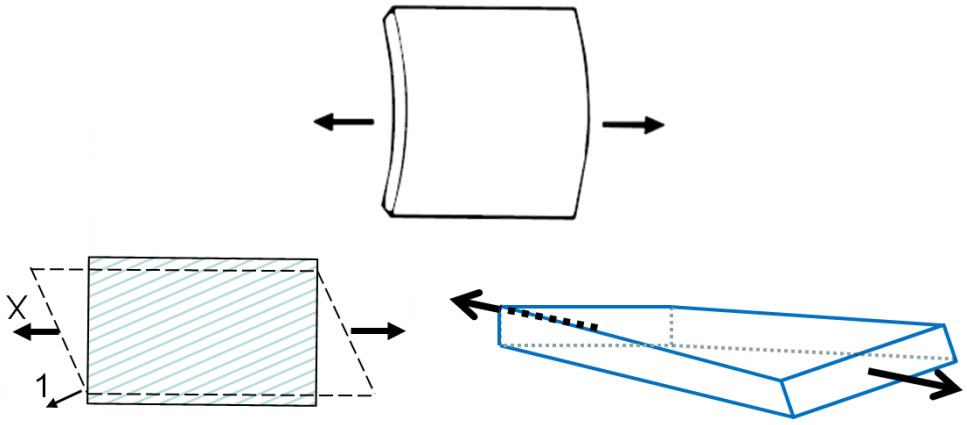

Figure 3.6 Examples of extension coupling included in Narrow Beam Theory. Top is extension-transverse curvature, left is extension–shear, right is extension–twist

AIRFOIL CENTROID

The centroid, or location of the neutral axis, is important because it decouples axial and bending stresses and strains. If an axial load is applied at the centroid, there is no bending and vice-versa. For isotropic material, the centroid is dependent on only the cross-sectional geometry of the beam. For a laminated composite material, the centroid is dependent on the geometry as well as the stacking sequence and material constants.

The centroid can be found by doing a force balance between a normal force acting at the centroid to normal forces acting at each element of the airfoil structure. Instead of finding the normal force and reference distance from only the top and bottom flange and web as with the I-beam, with the airfoil, the normal force and distance from a temporary origin, shown in Figure 3.1, are found for each element and used in equation 3-10 as shown below.

$$Y_c = \frac{\sum_{i=1}^{n} N_{x,i} \cdot b_i \cdot y_i}{\sum_{i=1}^{n} N_{x,i} \cdot b_i} = \frac{\bar{N}_x Y_c}{\bar{N}_x} \quad \text{and} \quad Z_c = \frac{\sum_{i=1}^{n} N_{x,i} \cdot b_i \cdot z_i}{\sum_{i=1}^{n} N_{x,i} \cdot b_i} = \frac{\bar{N}_x Z_c}{\bar{N}_x}, \tag{3-10}$$

and based on equation 3-10, the normal forces of each element can be converted to material properties from equation 3-9 and knowing the curvature is zero with a resultant axial force at the centroid. Thus,

$$N_{x,i} = A_i^{r*} \varepsilon_{x,i}^{o} + B_i^{r*} k_{x,i} = A_i^{r*} \varepsilon_x^{c}. \tag{3-11}$$

'n' is the number of elements on the profile of the airfoil and '$r*$' represents a rotated matrix with NBT applied. y_i and z_i are the distances from the center of each element to the temporary origin as see in Figure 3.7. If an I-beam is used, the elements making up the I-beam are added to the elements of the airfoil.

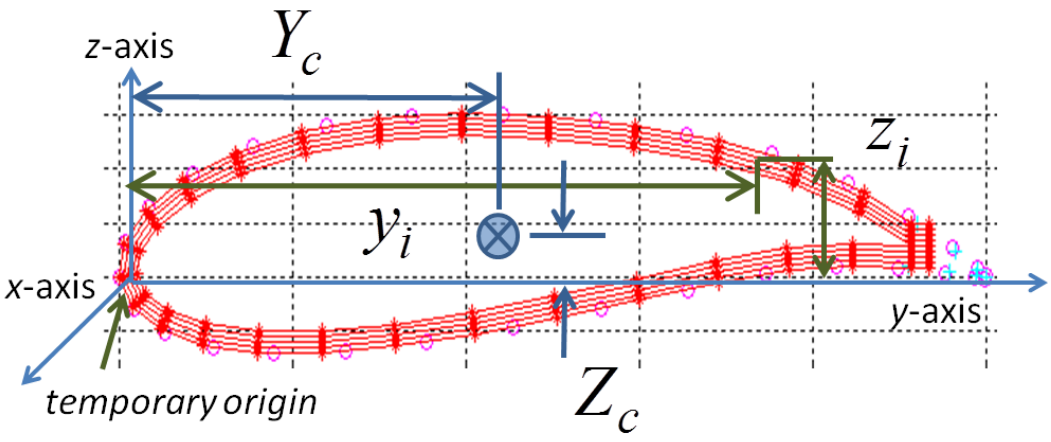

Figure 3.7 Temporary origin

The centroid relative the z-axis, Y_c, and relative to the y-axis, Z_c, are as follows,

$$Y_c = \frac{\bar{N}_x Y_c}{\bar{N}_x} = \frac{\sum_{i=1}^{n} A_i^{r*} \cdot b_i \cdot y_i}{A_i^{r*} b_i} \qquad Z_c = \frac{\bar{N}_x Z_c}{\bar{N}_x} = \frac{\sum_{i=1}^{n} A_i^{r*} \cdot b_i \cdot z_i}{A_i^{r*} b_i} \,. \tag{3-12}$$

AIRFOIL AXIAL STIFFNESS

The equivalent axial stiffness of a structure is defined as the amount of the resultant axial load need to produce a unit of axial strain at the structural centroid as shown below.

$$\overline{EA} = \frac{\bar{N}_x}{\varepsilon_x^c} \tag{3-13}$$

Consider that the resultant axial load, $\overline{N}_x$, is distributed to all airfoil elements. Since the resultant axial load is at the centroid, no resultant moment is produced, thus there is no curvature at the centroid. Since classical lamination theory is applied, curvature is linear thus curvature across the whole airfoil cross-section is constant. With no curvature over the cross section, the axial strain at the centroid is equal to the axial strain over the entire cross-section, therefore $\varepsilon_x^c = \varepsilon_{x,i}^o$.

Applying these assumptions, the 1D equation 3-9 shown below from each element is,

$$\begin{Bmatrix} N_x \\ M_x \end{Bmatrix}_i = \begin{bmatrix} A^* & B^* \\ B^* & D^* \end{bmatrix}_{i,y-axis}^{r} \begin{Bmatrix} \varepsilon_x^c \\ 0 \end{Bmatrix}_i \,. \tag{3-14}$$

The axial force at the centroid for the entire structure can be found by summing the axial forces from all elements as follows,

$$\bar{N}_x = \varepsilon_x^c \sum_{i=1}^{n} A_i^{r*} b_i \,. \tag{3-15}$$

The axial stiffness for the structure, in terms of material properties, is thus,

$$\overline{EA} = \frac{\bar{N}_x}{\varepsilon_x^c} = \sum_{i=1}^{n} A_i^{r*} b_i \,. \tag{3-16}$$

AIRFOIL BENDING STIFFNESS

This method is described in Appendix A for an I-beam and can be applied to a structure composed of discrete elements such as an airfoil as follows.

$$\begin{Bmatrix} \bar{N}_x \\ \bar{M}_x \\ \bar{M}_z \end{Bmatrix} = \begin{bmatrix} \overline{EA} & 0 & 0 \\ 0 & \bar{D}_x & \bar{D}_{xz} \\ 0 & \bar{D}_{xz} & \bar{D}_z \end{bmatrix} \begin{Bmatrix} \varepsilon_x^c \\ k_x^c \\ k_y^{c,XS} \end{Bmatrix} \tag{3-17}$$

Starting from the stiffness matrix for the entire structure that is desired, the general equation used to relate the curvature and bending stiffness is $\bar{M}_x = \bar{D}_x k_x^c + \bar{D}_{xz} k_z^c \approx \bar{D}_x k_x^c$ where the $\bar{D}_{xz} k_z^c$ term is neglected since it is small in comparison to the $\bar{D}_x k_x^c$ term. To determine the structural bending stiffness term in the x-direction with respect to each element, $\overline{D}_{x,i}$, consider a resultant moment at the centroid of the structure, $\overline{M}_x$. This moment consists of loads $N_{x,i}$ and $M_{x,i}$ acting at the midplane of an element 'i'. This equilibrium relation of moments from an element is written mathematically as,

$$\overline{M}_{x,i} = b_i \left(M_{x,i} + z_{i,c} N_{x,i} \right), \tag{3-18}$$

where $\overline{M}_{x,i}$ is the moment produced from element 'i'.

The loads in equation 3-18 can be replaced with material properties from equation 3.9 to find the moment applied to the structure from element 'i',

$$\overline{M}_{x,i} = b_i \left(B_i^{r*} \varepsilon_{x,i}^o + D_i^{r*} k_{x,i}^o + z_{i,c} \left(A_i^{r*} \varepsilon_{x,i}^o + B_i^{r*} k_{x,i}^o \right) \right). \tag{3-19}$$

In finding the axial stiffness, it was determined that $k_{x,i}^o = k_{x,i}^c$ due to the linear curvature assumption. Note that $k_{x,i}^c$ is the curvature about the centroid caused by loads at one element. If a moment about the centroid is produced, then the element midplane strain is only a function of $k_{x,i}^c$ and there is no centroidal strain, thus $\varepsilon_{x,i}^0 = z_{i,c} k_{x,i}^c$. $z_{i,c}$ is the distance from the cross-sectional centroid to the element centroid in the z-direction. So, the equation above can be simplified to,

$$\overline{M}_{x,i} = b_i k_{x,i}^c \left(A_i^{r*} z_{i,c}^2 + 2B_i^{r*} z_{i,c} + D_i^{r*} \right), \tag{3-20}$$

and the structural stiffness term $D_{x,i}$ due to $N_{x,i}$ and $M_{x,i}$ acting on element 'i' is,

$$\overline{D}_{x,i} = b_i \left(A_i^{r*} z_{i,c}^2 + 2B_i^{r*} z_{i,c} + D_i^{r*} \right). \tag{3-21}$$

A similar approach is taken to find $\overline{M}_{z,i}$. This yields,

$$\overline{M}_{z,i} = b_i k_{z,i}^c \left(A_i^{r*} y_{i,c}^2 + 2B_i^{r*} y_{i,c} + D_i^{r*} \right) \tag{3-22}$$

where $\overline{D}_{z,i} = b_i \left(A_i^{r*} y_{i,c}^2 + 2B_i^{r*} y_{i,c} + D_i^{r*} \right)$. (3-23)

For moment coupling terms $\bar{D}_{xz}$, consider an applied moment $\overline{M}_x$ on the structure which causes curvature k_x^c as well as induces k_z^c due to the coupling term $\bar{D}_{xz}$ as follows,

$$\overline{M}_x = \bar{D}_x k_x^c + \bar{D}_{xz} k_z^c . \tag{3-24}$$

Primary interest is on the coupled curvature, k_z^c, so $\bar{M}_x$ can be isolated with the k_z^c term, leaving $\overline{M}_x = \bar{D}_{xz} k_z^c$. $\bar{M}_x$ needs to be converted into material properties to find $\bar{D}_{xz}$. This is done by breaking down $\bar{M}_x$ into loads on discrete elements such as element $'i'$ as follows,

$$\bar{M}_{x,i} = b_i \left(M_{x,i} + z_{i,c} N_{x,i} \right). \tag{3-25}$$

Again, the 1D equation 3-9 from Narrow Beam Theory is used to break down the element loads into material properties using ABD_i^{r*} giving equation 3-26 shown below,

$$\bar{M}_{x,i} = b_i \left(B_i^{r*} \varepsilon_{x,i}^o + D_i^{r*} k_{x,i}^c + z_{i,c} \left(A_i^{r*} \varepsilon_{x,i}^o + B_i^{r*} k_{x,i}^c \right) \right). \tag{3-26}$$

Relating element midplane strain, $\varepsilon_{x,i}^0$, to curvature of the cross-section,

$$\varepsilon_{x,i}^0 = \varepsilon_{x,i}^c + z_{i,c} k_{x,i}^c + y_{i,c} k_{z,i}^c . \tag{3-27}$$

However, only a moment is applied so there is no net axial strain at the centroid and $k_{x,i}^c$ can be neglected since the primary interest is on the coupled curvature $k_{z,i}^c$. Thus,

$$\varepsilon_{x,i}^0 = y_{i,c} k_z^c , \tag{3-28}$$

which is then inserted into equation 3-26, and still neglecting $k_{x,i}^{c}$, yields,

$$\bar{M}_{x,i} = b_i y_{i,c}\left(z_{i,c}A_i^{r*} + B_i^{r*}\right)k_{z,i}^{c} \tag{3-29}$$

where $\bar{D}_{xz,i} = b_i y_{i,c}\left(z_{i,c}A_i^{r*} + B_i^{r*}\right)$. (3-30)

Of course, the equations above found are the bending stiffness terms from one element. To obtain the cross-sectional stiffness of the airfoil structure, the stiffness terms must be summed for all elements as follows:

$$\bar{D}_x = \sum_{i=1}^{n} b_i\left(A_i^{r*}z_{i,c}^2 + 2B_i^{r*}z_{i,c} + D_i^{r*}\right) \tag{3-31}$$

$$\bar{D}_z = \sum_{i=1}^{n} b_i\left(A_i^{r*}y_{i,c}^2 + 2B_i^{r*}y_{i,c} + D_i^{r*}\right) \tag{3-32}$$

$$\bar{D}_{xz} = \sum_{i=1}^{n} b_i y_{i,c}\left(z_{i,c}A_i^{r*} + B_i^{r*}\right). \tag{3-33}$$

With the coupled stiffness moment terms, the stiffness matrix of the entire structure about the centroid due to $\bar{N}_x, \bar{M}_x,$ and $\bar{M}_z$ is given as,

$$\begin{Bmatrix} \bar{N}_x \\ \bar{M}_x \\ \bar{M}_z \end{Bmatrix} = \begin{bmatrix} \overline{EA} & 0 & 0 \\ 0 & \bar{D}_x & \bar{D}_{xz} \\ 0 & \bar{D}_{xz} & \bar{D}_z \end{bmatrix} \begin{Bmatrix} \varepsilon_x^c \\ k_x^c \\ k_y^c \end{Bmatrix}, \tag{3-34}$$

where the resultant loads and strains are acting upon the centroid.

LAMINATE PLY STRAINS AND STRESSES

From the cross-sectional stiffness matrix about the centroid, the axial strain at the midplane of each element in the global x-y direction can be found by,

$$\varepsilon_{x,i}^{o} = \varepsilon_{x}^{c} + z_{i,c}k_{x}^{c} + y_{i,c}k_{y}^{c,XS}, \tag{3-35}$$

where $k_{y}^{c,XS}$ is the curvature about the z-axis in the y-z plane. When dealing with laminates, k_{y} is used to represent the curvature about the x-axis affecting the longitudinal side of the airfoil beam thus this nomenclature is used.

Distances $y_{i,c}$ and $z_{i,c}$ are illustrated in Figure 3.8.

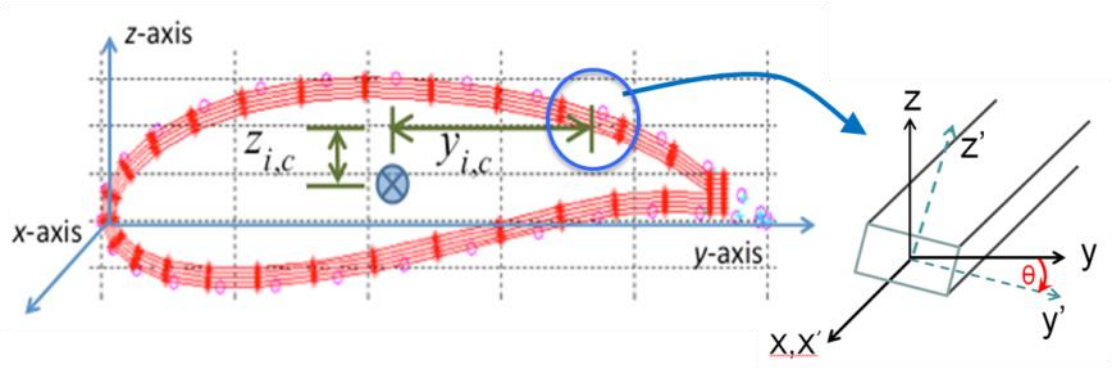

Figure 3.8 Translating and rotating cross-section centroidal strains and curvatures to laminate midplane

Again assuming linear curvature, k_{x}^{c} and $k_{y}^{c,XS}$ are the same for the centroid as well as at each element in the global x-y-z direction. Thus, at the laminate element, the axial strain and curvatures are known in the global x-y-z direction. These strains and curvatures can then be rotated about the x-axis by the transformation matrix to align with the laminate y'-z' plane as follows,

$$\begin{Bmatrix} \varepsilon^o_{x'} \\ k^o_{x'} \\ k^{o,XS}_{y'} \end{Bmatrix}_i = \left[T_\varepsilon(\theta_i)\right] \begin{Bmatrix} \varepsilon^o_x \\ k^c_x \\ k^{c,XS}_y \end{Bmatrix}_i , \tag{3-36}$$

where θ_i is illustrated in Figure 3.7 which in this case is a negative theta.

A key to finding the ply strains and curvatures is to assume twisting is negligible, $k^o_{x'y'} = 0$. This is a valid assumption considering that the material of the airfoil cross-section is a considerable distance away from the shear center, thus the structure is stiff relative to torque.

With these assumptions, the strains and curvatures of each element relative to the laminate's x'-y' coordinate system, or the composite coordinate system, is found as follows,

$$\begin{Bmatrix} \varepsilon^o_{x'} \\ \varepsilon^o_{y'} \\ \gamma^o_{x'y'} \\ k_{x'} \\ k_{y'} \\ k_{x'y'} \end{Bmatrix}_i = \begin{Bmatrix} \boldsymbol{\varepsilon^o_{x'}} \\ \varepsilon^o_{y'} \\ \gamma^o_{x'y'} \\ \boldsymbol{k^o_{x'}} \\ k^o_{y'} \\ \mathbf{0} \end{Bmatrix}_i = \begin{bmatrix} a_{11} & b_{11} & b_{16} \\ a_{12} & b_{12} & b_{26} \\ a_{16} & b_{16} & b_{66} \\ b_{11} & d_{11} & d_{16} \\ b_{21} & d_{12} & d_{26} \\ b_{61} & d_{16} & d_{66} \end{bmatrix}_i \begin{Bmatrix} N_{x'} \\ M_{x'} \\ M_{x'z'} \end{Bmatrix}_i , \tag{3-37}$$

where the bold items, $(\varepsilon^o_{x'}, k^o_{x'}, k^o_{x'y'})$, are known. The 6x3 $[abd]$ matrix is from the compliance matrix of the laminate itself. The loads are acting on the midplane of the laminate. Note that the *b* coupling terms associated with the curvatures are not the same as the *b* coupling terms associated with the strains.

This set of equations can be simplified as follows. First, the 6x3 $[abd]$ matrix is rearranged to separate the known and unknown strains and curvatures;

$$\begin{Bmatrix} \boldsymbol{\varepsilon}^{o}_{x'} \\ \boldsymbol{k}^{o}_{x'} \\ \mathbf{0} \\ \varepsilon^{o}_{y'} \\ \gamma^{o}_{x'y'} \\ k^{o}_{y'} \end{Bmatrix}_i = \begin{bmatrix} a_{11} & b_{11} & b_{16} \\ b_{11} & d_{11} & d_{16} \\ b_{61} & d_{16} & d_{66} \\ a_{12} & b_{12} & b_{26} \\ a_{16} & b_{16} & b_{66} \\ b_{21} & d_{12} & d_{26} \end{bmatrix}_i \begin{Bmatrix} N_{x'} \\ M_{x'} \\ M_{x'z'} \end{Bmatrix}_i = \begin{bmatrix} U \\ V \end{bmatrix}_i \begin{Bmatrix} N_{x'} \\ M_{x'} \\ M_{x'z'} \end{Bmatrix}_i \tag{3-38}$$

$$\text{where: } [U]_i = \begin{bmatrix} a_{11} & b_{11} & b_{16} \\ b_{11} & d_{11} & d_{16} \\ b_{61} & d_{16} & d_{66} \end{bmatrix}_i \text{ and } [V]_i = \begin{bmatrix} a_{12} & b_{12} & b_{26} \\ a_{16} & b_{16} & b_{66} \\ b_{21} & d_{12} & d_{26} \end{bmatrix}_i . \tag{3-39}$$

Now, matrix substitution for the loads can be performed as follows,

$$\begin{Bmatrix} N_{x'} \\ M_{x'} \\ M_{x'z'} \end{Bmatrix}_i = [U]_i^{-1} \begin{Bmatrix} \varepsilon^{o}_{x'} \\ k^{o}_{x'} \\ 0 \end{Bmatrix}_i . \tag{3-40}$$

This is used to find the unknown strain and curvature in terms of known strains and curvatures.

$$\begin{Bmatrix} \varepsilon^{o}_{y'} \\ \gamma^{o}_{x'y'} \\ k^{o}_{y'} \end{Bmatrix}_i = [V]_i [U]_i^{-1} \begin{Bmatrix} \varepsilon^{o}_{x'} \\ k^{o}_{x'} \\ 0 \end{Bmatrix}_i . \tag{3-41}$$

The laminate midplane strains and curvatures can be used to solve for the strains on the surface of each ply as follows,

$$\begin{Bmatrix} \varepsilon_{x'} \\ \varepsilon_{y'} \\ \gamma_{x'y'} \end{Bmatrix}_{i,k} = \begin{Bmatrix} \varepsilon^{o}_{x'} \\ \varepsilon^{o}_{y'} \\ \gamma^{o}_{x'y'} \end{Bmatrix}_i + z' \begin{Bmatrix} k_{x'} \\ k_{y'} \\ k_{x'y'} \end{Bmatrix}_i , \tag{3-42}$$

where z' is the distance from the laminate midplane to the interested ply surface and k is the number of the ply surface starting from the inner ply surface going to the outer surface. Stresses in the laminate global direction (x'-y') at each ply surface can also be found using,

$$\begin{Bmatrix} \sigma_{x'} \\ \sigma_{y'} \\ \tau_{x'y'} \end{Bmatrix}_{i,k} = \left[\overline{Q}_{x'-y'}\right]_k \begin{Bmatrix} \varepsilon_{x'} \\ \varepsilon_{y'} \\ \gamma_{x'y'} \end{Bmatrix}_{i,k} . \tag{3-43}$$

Finally, stresses in the 1-2 material direction at each ply surface are found using,

$$\begin{Bmatrix} \sigma_1 \\ \sigma_2 \\ \tau_{12} \end{Bmatrix}_{i,k} = \left[T_\sigma(\phi)\right]_k \cdot \begin{Bmatrix} \sigma_x \\ \sigma_y \\ \tau_{xy} \end{Bmatrix}_{i,k} . \tag{3-44}$$

The ply stress in the principal material direction can be found for each laminate.

CHAPTER 4

RESULTS OF AIRFOIL UNDER AXIAL LOAD AND BI-DIRECTIONAL MOMENTS

The analytical method discussed in Chapter 3 for an airfoil under axial and bi-directional moments is compared to finite element analysis to determine prediction accuracy. The finite element model will be explained followed by a comparison of the FEA and analytical method results.

AIRFOIL FINITE ELEMENT MODELS

Similar to the I-beam FEA models, SOLID186 elements are used in ANSYS to obtain more accurate FEA results since it includes out of plane stresses. MATLAB is used to create an APDL code which ANSYS runs to create the model and apply constraints and loads. The models created in ANSYS are identical to the models run for the analytical analysis thus direct comparisons can be made. For each model, the outer airfoil shape is the profile of the airfoil modeled. Most models are from the NACA 4-series airfoils.

Four types of airfoils are chosen for study, the NACA 6721, NACA 0030, and NACA 9312 which are shown in Figure 4.1, 4.2, and 4.3 respectively. One other is the airfoil that is used for the experimental section but its designation is unknown. The airfoils were chosen to study a symmetric geometry case, the NACA 0030, a more common airfoil, the NACA 6721, and an extreme case of the NACA 4-series, the NACA 9312. Each beam is studied with and without an I-beam stiffener.

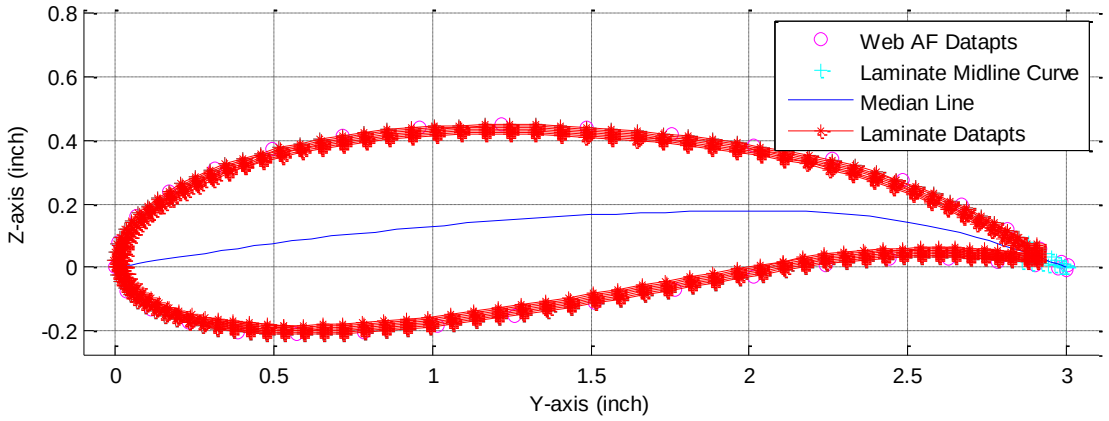

Figure 4.1 MATLAB cross sectional plot of NACA 6721 airfoil

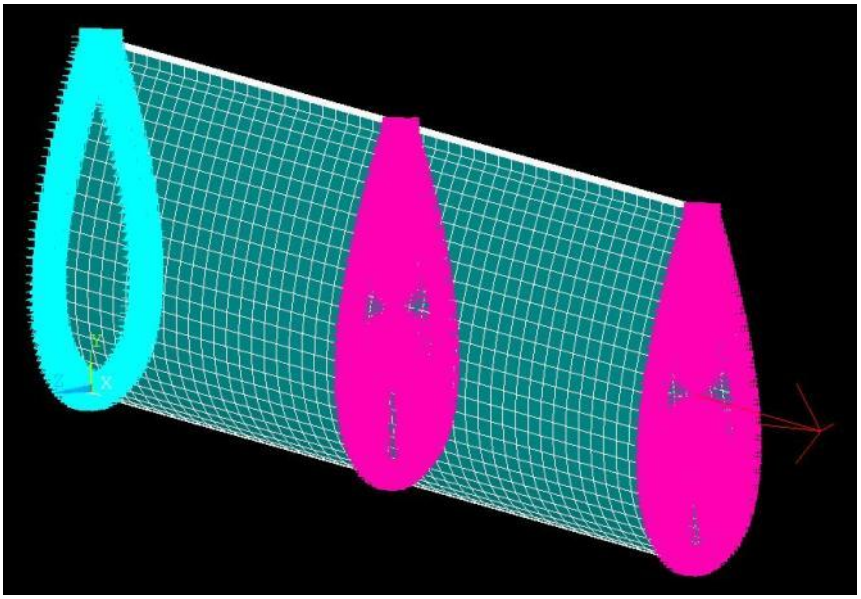

Figure 4.2 NACA 0030 airfoil with constraints and axial load

An ANSYS model of the NACA 0030 airfoil is shown in Figure 4.2. The end at the left is fully constrained at each node. The loaded end on the right has a CERIG constraint applied at all the end nodes. The master node of the CERIG constraint is located at the centroid and is axially loaded in the figure. An RBE3 constraint is used in the middle of the beam to measure deflections and find the centroid. The CERIG and

RBE3 constraints have been described in the I-beam finite element models section. The cross-sectional mesh of the airfoil is denser near the leading edge of the airfoil where there is more curvature to maintain the geometry of the airfoil shape. This is more acute in the NACA 9312 model shown in Figure 4.3 which is generated in MATLAB. Notice that there is a row of elements for each composite ply.

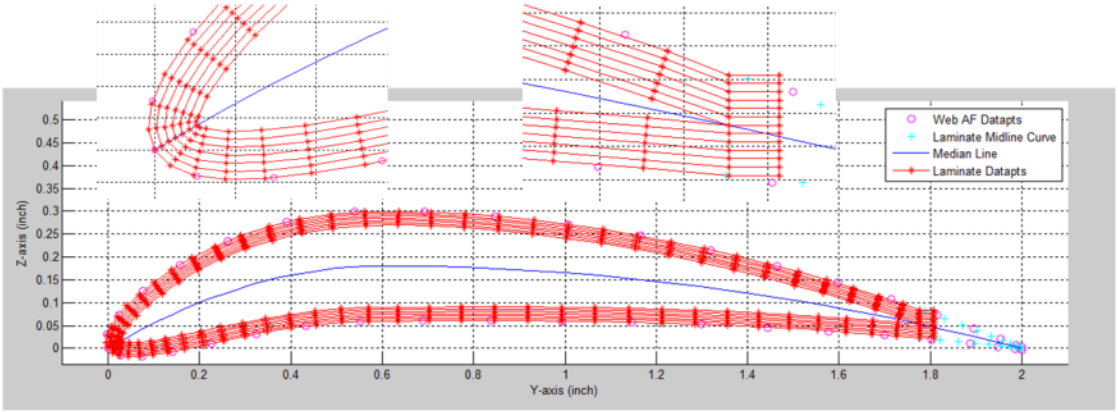

Figure 4.3 NACA 9312 cross-section with close-ups of leading and trailing edges

Airfoil models with I-beam stiffeners are also studied. Figure 4.4 shows a simple cross-section of an FEM with an I-beam. Notice that the trailing edge uses a box-tail instead of a pointy tail. Composite designs of airfoils typically use a box-tail approach. The I-beam has equal lengths for each flange where the web is placed central to each flange. The position of the I-beam has been arbitrarily chosen such that the distance from the leading edge to the edge of each flange is 0.2 times the chord length. The length of each flange is ¼ the length of the chord. These distances can be modified easily in the MATLAB code and optimized but is not done in this research.

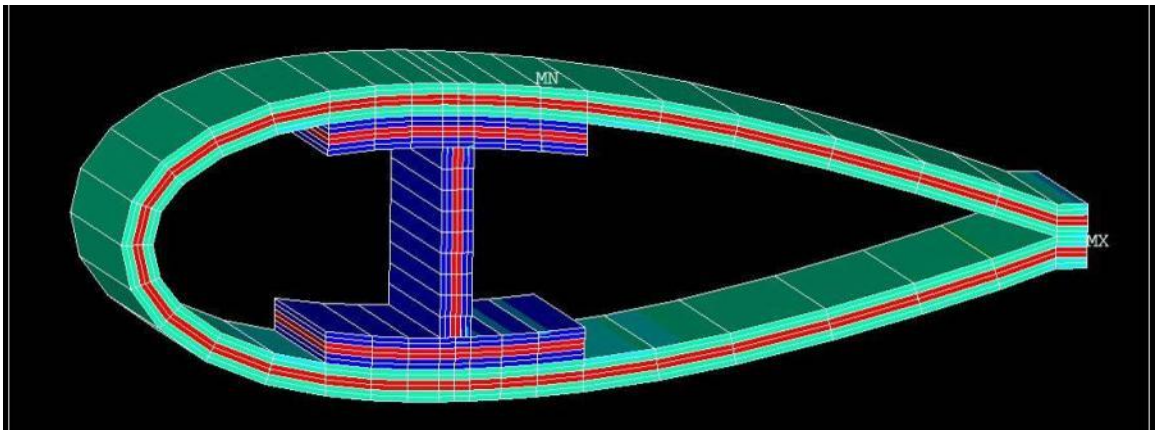

Figure 4.4 Airfoil with I-beam stiffener, axial stress shown

It is important to verify the element coordinate system in ANSYS thus it is checked in various ways. One method is a visual check of the element CSYS in ANSYS as seen in Figure 4.5 which shows the bottom flange of the I-beam. Each color represents a different CSYS. A symmetric layup can be noticed in each element laminate.

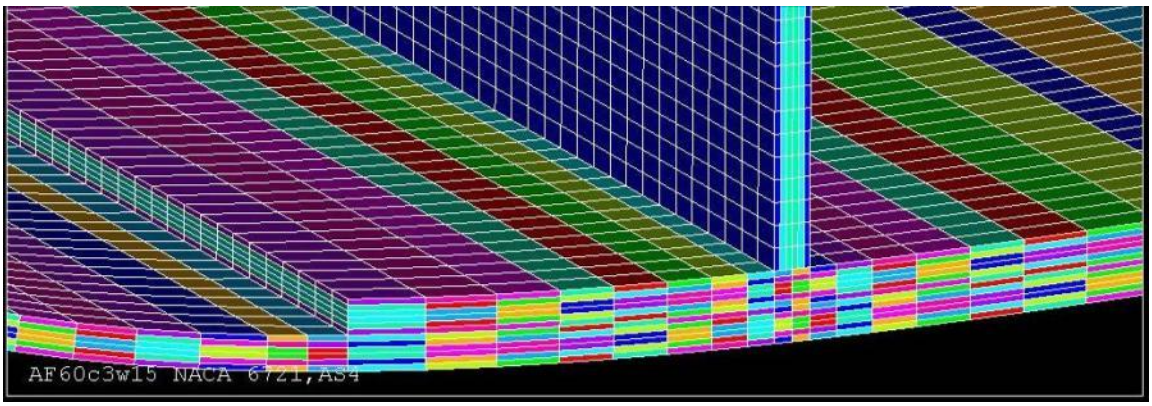

Figure 4.5 Checking element CSYS visually in ANSYS

Another way to check the element CSYS is to show the principle material axes of each element as seen in Figure 4.6. The blue axis represents the out-of-plane or z'

direction and the yellow and white axes represent the in-plane directions.

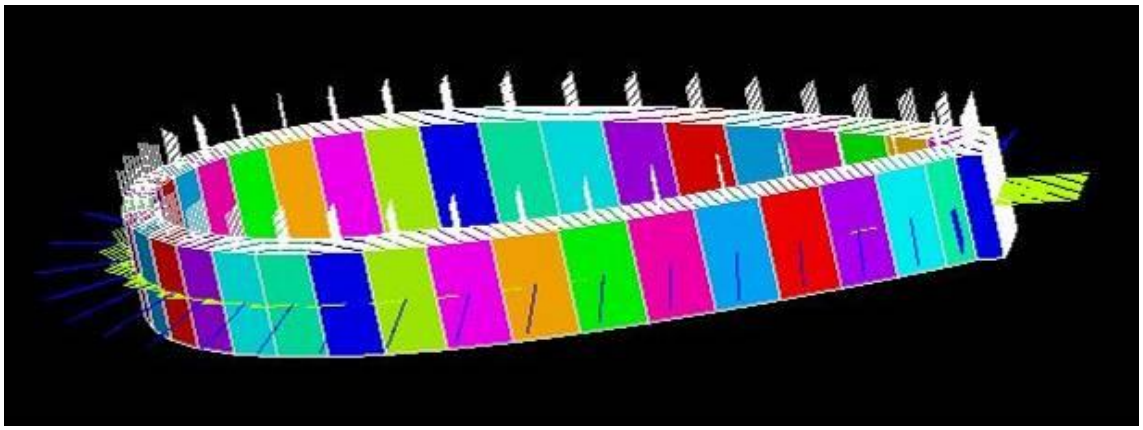

Figure 4.6 Checking element CSYS with principle material axes

For the I-beam model in Chapter 2, the flange mesh matches the web mesh at the interface. However, this creates many very small elements. To reduce the amount of elements and degrees of freedom in the airfoil with I-beam model, a discontinuous mesh is used at the interface of the web and flanges. This is shown in Figure 4.7.

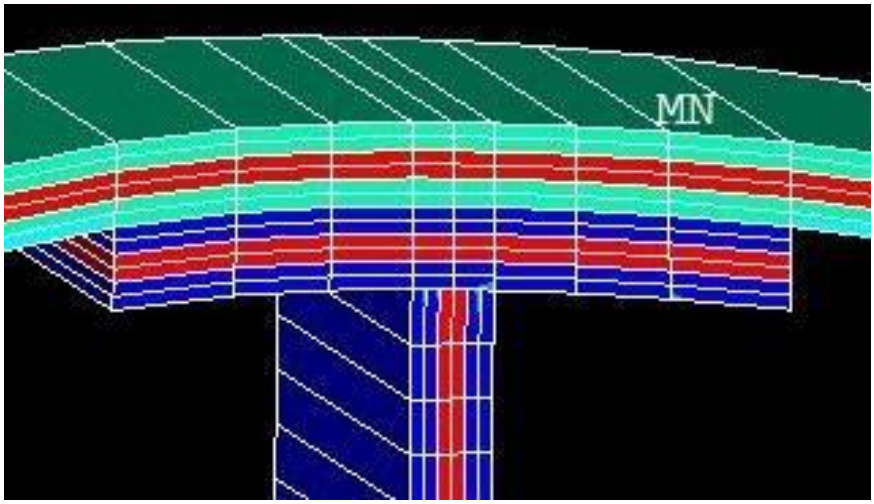

Figure 4.7 Discontinuous mesh at web and flange, axial stress shown

To ensure the dissimilar meshes are attached at the interface, a constraint along adjacent meshes is used in ANSYS. At the interface, the degrees of freedom of the

nodes of the web are interpolated with the degrees of freedom of the flange using the shape functions of the flange. Constraint equations are used to associate the nodes of the web with those of the flange. The constraint at these interfaces is shown in Figure 4.8. The web-flange constraints run the length of the model.

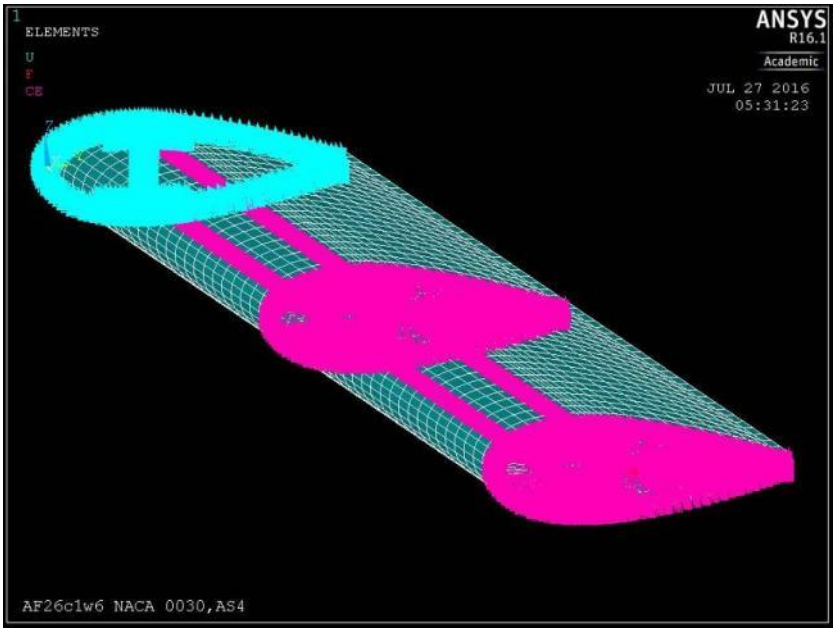

Figure 4.8 Constraints of airfoil with I-beam

ANSYS is able to show and list the stresses in the global x-y coordinate system. However, the stress in each element's material coordinate system is sought. Thus, ANSYS generated stresses in the global material direction about the center cross section of the airfoil are saved into a file. MATLAB is then used to convert these global stresses into elemental material stresses in the 1-2 direction. This is accomplished by rotating the global x-y stresses about the x-axis towards the element x'-y' coordinate system as seen in Figure 4.9 on the left. Next, the elemental x'-y' stresses are rotated about the z' axis to the elemental 1-2 direction as shown at the right. Mathematically,

both these rotations involve the 2D transformation matrix first about the x-axis using θ, then about the z-axis using ϕ.

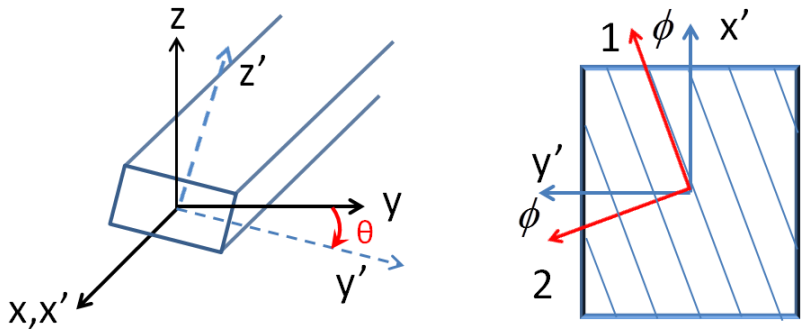

Figure 4.9 Rotating global x-y stress into elemental x'-y' stresses on the left then rotating the elemental x'-y' stresses to the elemental 1-2 direction

Convergence of Finite Element Model

To check on the proper mesh size, a convergence study is performed on a NACA 0030 airfoil without I-beam with a 2 inch chord and 12 inches in length. Element thickness is the smallest element dimension and is determined by the ply thickness which is held constant at 0.005 inches for this study (except for the experimental specimens). Thus, convergence checks are made on length to ply thickness and on width to ply thickness. For the length to ply thickness, 66 elements are used along the perimeter of the airfoil cross-section which yields an average width to thickness aspect ratio of 12.6 with a maximum of 17.1. For the width to thickness check, an aspect ratio of 100:1 is used for length to thickness.

The variable of interest is the bending stiffness term. Figure 4.10 shows the bending stiffness, D_x relation to length to thickness aspect ratio in terms of degrees of freedom. After about 100,000 DOFs, the bending stiffness term is approximately 0.004% away from the converged value.

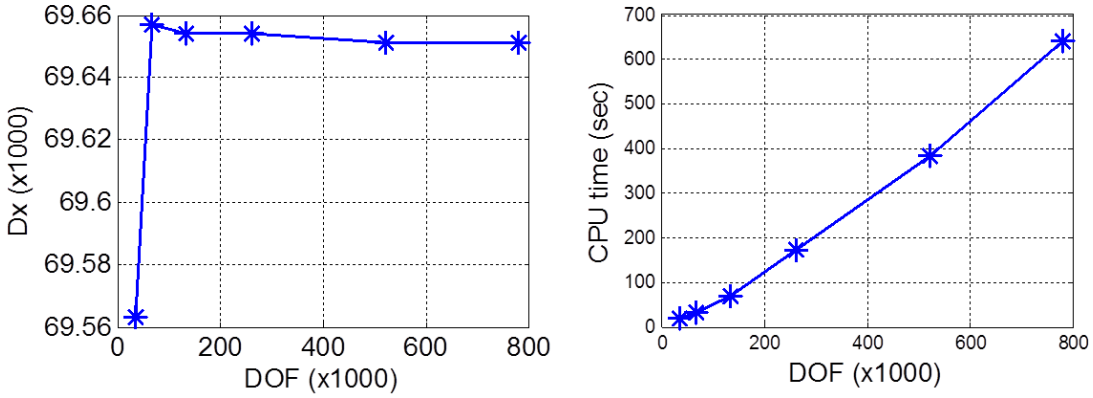

Figure 4.10 Convergence plot of length to thickness to bending stiffness

Table 4.1 Convergence check of length to thickness aspect ratio

L/thk AR	DOF	CPU time (sec)	D_x	% from converge value	σ_1 max, 0 deg	σ_1 max, 30 deg	σ_1 max, -30 deg
400	36,438	18	69,563	0.128%	86.484	42.350	43.223
200	68,874	33	69,657	0.008%	86.760	44.100	43.315
100	133,746	70	69,654	0.004%	86.748	44.105	43.2716
50	263,490	172	69,654	0.004%	86.742	44.107	43.2715
25	522,978	385	69,651	0.000%			
17	782,466	640	69,651	0.000%	86.742	44.108	43.2707

A table of these values including stress in the 1 principle material direction is shown in Table 4.1. Even at a length to thickness aspect ratio of 100:1, there is good agreement between the converged value of D_x (approximately 69,651) and the

converged values of the maximum values of σ_1 in the 0, 30, and -30 degree plies. An aspect ratio of at least 50:1 in length to thickness is chosen to use for this study.

Table 4.2 shows the convergence study for the width to length aspect ratio. At an average width to thickness aspect ratio of 15, there is a 0.2% error in the prediction for D_x as compared to the converged D_x value of 69,749. A check is also made for this aspect ratio between the analytical model's prediction and the converged D_x value of 69,645. As an average ratio of 15, there is only a 0.24% error in the predicted value. Thus, an average width to thickness ratio of 15 is adhered to in this study.

Table 4.2 Convergence check of width to thickness

aspect ratio, XS is cross-section

Avg/Max W / thk AR	Elems in XS	DOF (10^3)	CPU time (sec)	D_x by FEM	% from converge value	D_x by Analyt	% from converge value
30 / 45	28	58	31	68,776	1.40	68,438	1.73
22 / 32	38	78	42	69,311	0.63	69,086	0.80
18 / 24	48	98	53	69,520	0.33	69,347	0.43
15 / 20	58	118	60	69,616	0.19	69,476	0.24
12 / 17	68	138	72	69,668	0.12	69,548	0.14
11 / 15	78	158	84	69,697	0.07	69,593	0.07
9 / 13	90	182	96	69,740	0.01	69,624	0.03
8 / 11	100	202	100	69,749	0.00	69,645	0.00

FEA Centroid Calculation

The centroid is calculated by applying an axial load at an arbitrary point about the cross-section near the center of the airfoil. The cross-sectional coordinates of the master nodes for the loaded end CERIG constraint and the middle RBE3 constraint are

made equal to the arbitrary point's coordinates. The displacements are noted and a second point is arbitrarily chosen and the same procedure followed. This is illustrated in Figure 4.11 where arbitrarily chosen positions are noted by a dot and corresponding displacements caused by an axial load are noted by an asterix.

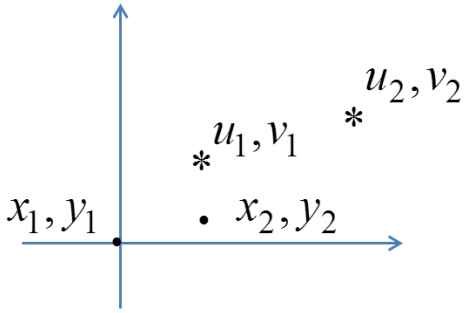

Figure 4.11 Calculating centroid in ANSYS

Taking the differences in the position and displacement changes in the x-direction and assuming linear curvature, the position of zero displacement is,

$$x_o = x_1 - \left(\frac{x_1 - x_2}{u_1 - u_2} \right) u_1 . \tag{4-1}$$

The same is done for the y-direction. However, curvature is not absolutely linear and the neutral axis is not parallel to the x and y axes thus this is an iterative process until the cross-sectional displacements are approximately zero.

FEA Stiffness Calculations

Once the cross-sectional centroid is found, stiffness terms can be calculated. Axial stiffness is found by applying an axial load at the load end centroid and dividing the load by the axial strain found at the middle length centroid using the RBE3 master node. Bending stiffness terms D_x and D_z are found using the Bernoulli-Euler equation

for a cantilever beam with one end fixed and a moment applied at the free end as follows,

$$\begin{aligned} \overline{D}_x &= \overline{EI}_x = -\frac{\overline{M}_x L^2}{2w} \\ \overline{D}_z &= \overline{EI}_z = -\frac{\overline{M}_z L^2}{2v} \end{aligned}, \tag{4-2}$$

where the bars indicate over the entire cross-section, L is the length of the beam, w is displacement in the z-direction, and v is the displacement in the y-direction.

The coupling bending stiffness is found by applying M_x and finding the points along the perimeter of the cross-section at the middle length of the beam where axial stress is zero. There will be 2 points were stress will be zero which are the points that a linear neutral axis will cross. Elemental stresses are actually used and stress will not actually be zero at an element. Thus, the stress along the perimeter is interpolated to find the zero axially stressed points. Once the neutral axis is found, the angle it makes, α, from the y-axis is obtained and the following equation is used to find the coupling stiffness,

$$\begin{aligned} \overline{D}_{xz} &= \overline{D}_z \tan(\alpha) \\ \overline{D}_{zx} &= \overline{D}_x \tan(\beta) \end{aligned}. \tag{4-3}$$

AIRFOIL RESULTS FROM AXIAL LOAD AND BI-DIRECTIONAL MOMENTS

Four symmetric geometry cases are studied from the three main NACA airfoils. These cases are listing in Table 4.3. Each airfoil beam is analyzed as a hollow beam and with an I-beam stiffener. The first cases, C1 and C1ib2, consist of six plies of zero

degree only and have a chord length of 1 inch. The other cases have a symmetric layup of $[\pm 30/0]_S$ and vary in chord length and NACA designation except for case C21 which uses a $[\pm 45]_S$ layup. I-beam stiffeners, other than case C1ib2, use a $[\pm 45/0]_S$ layup for the flanges and web. The aspect ratio of each model made is also shown which applies to both the ANSYS and analytical models studied. All models have a width to thickness (W/thk) ratio of less than 15 and a length to thickness (L/thk) ratio of 50 or less.

Table 4.3 Symmetric Geometry Cases studied

Case	NACA	Layup	Chord Length (inch)	Average Aspect Ratios W/thk, L/thk
C1	AF0030	$[0]_{6T}$	1	8.5 / 25
C1ib2	AF0030 + IB	IB = $[0]_{6T}$	1	7.2 / 25
C2	AF0030	$[30/-30/0]_S$	1	7.5 / 25
C2ib1	AF0030 + IB	IB = $[45/-45/0]_S$	1	7.5 / 25
C21	AF0030	$[45/-45]_S$	1	9.5 / 25
C30	AF6721	$[0]_{6T}$	1	9.5 / 25
C31	AF6721	$[30/-30/0]_S$	1	9.5 / 25
C32	AF6721	$[30/-30/0]_S$	2	15 / 25
C33	AF6721	$[30/-30/0]_S$	3	12 / 50
C33ib1	AF6721 + IB	IB = $[45/-45/0]_S$	3	13 / 50
C4	AF9312	$[30/-30/0]_S$	2	11 / 50
C4ib1	AF9312 + IB	IB = $[45/-45/0]_S$	2	12 / 50

Results for the centroid are found in Table 4.4. The ANSYS model in case C1 is compared to the analytical model as a means for verifying the FEA model. The error between the FEM and the Narrow Beam Theory approach (NBT) is very minimal for the zero degree laminate cases. Cases C1, C1ib2, C2, C2ib1, and C21 are all symmetric thus the centroid along the z-direction, C_z, is approximately zero thus the error is not listed. In all cases, the error between the predicted value and FEA is less than 1.0%

thus there is excellent agreement. In most cases, the presence of the I-beam reduces the error in the predicted centroid value. The worst prediction of centroid is with the [45/-45]s layup which tends to have more nonlinear behavior.

Table 4.4 Verification of Centroid NBT Prediction with FEA

Case	Method	C_y (in)	C_z (in)
C1 N0030c1	FEA	0.455	1.07E-06
	NBT	0.454	-1.00E-06
$[0]_{6T}$	Error	-0.12%	
C1 ib2 N0030c1	FEA	0.421	4.75E-06
	NBT	0.421	4.41E-06
IB $[0]_{6T}$	Error	-0.04%	
C2 N0030c1	FEA	0.455	7.18E-05
	NBT	0.454	1.69E-05
$[\pm30/0]_S$	Error	-0.09%	
C2 ib1 N0030c1	FEA	0.430	3.43E-05
	NBT	0.429	3.01E-06
IB $[\pm45/0]_S$	Error	-0.39%	
C4 N9312c2	FEA	0.892	1.31E-01
	NBT	0.890	1.32E-01
$[\pm30/0]_S$	Error	-0.23%	0.26%
C4 ib1 N9312c2	FEA	0.849	1.40E-01
	NBT	0.847	1.40E-01
IB $[\pm45/0]_S$	Error	-0.24%	0.02%

Case	Method	C_y (in)	C_z (in)
C21 N0030c1	FEA	0.465	1.45E-05
	NBT	0.462	
$[\pm45]_S$	Error	-0.75%	
C30 N6712c1	FEA	0.444	4.32E-02
	NBT	0.444	4.32E-02
$[0]_{6T}$	Error	-0.01%	0.05%
C31 N6712c1	FEA	0.445	4.32E-02
	NBT	0.444	4.32E-02
$[\pm30/0]_S$	Error	-0.07%	0.15%
C32 N6712c2	FEA	0.933	8.37E-02
	NBT	0.932	8.42E-02
$[\pm30/0]_S$	Error	-0.14%	0.57%
C33 N6712c3	FEA	1.421	1.23E-01
	NBT	1.419	1.25E-01
$[\pm30/0]_S$	Error	-0.15%	1.02%
C33 ib1 N6712c3	FEA	1.339	1.25E-01
	NBT	1.333	1.25E-01
IB $[\pm45/0]_S$	Error	-0.44%	0.21%

All stiffness results are tabulated in Table 4.5 where orange highlights indicated predictions off by more than 5%. Stiffness results for NACA 0030 models with the symmetric geometry are in very good agreement between the FEA and Narrow Beam Theory Approach. Error in axial and bending stiffness in the flapwise direction, D_x, and chord-wise direction, D_z, are less than 4%. However, predictions for the bending coupling terms D_{xz} with the NACA 9312 and the 3 inch chord NACA 6712 without I-

beam have fairly high errors. All other cases have D_{xz} predictions under 5.3%. The presence of an I-beam stiffener results in much lower errors in the D_{xz} term. Note that the D_{xz} term is actually an average of the calculated D_{xz} and D_{zx} terms found with FEA. NBT predicts only D_{xz} and assumes D_{zx} is equal.

Table 4.5 Verification of Axial and Bending Stiffness NBT Predictions with FEA

Case	Method	AE (lb-in)	D_x (lb-in^2)	D_z (lb-in^2)	D_{xz} (lb-in^2)
C1 N0030c1	FEA	1,268,875	12,312	98,217	~0
	NBT	1,271,555	12,341	98,735	
$[0]_{6T}$	Error	0.21%	0.23%	0.53%	
C1 ib2 N0030c1	FEA	1,702,321	16,012	105,367	~0
	NBT	1,705,584	16,013	105,784	
IB = $[0]_{6T}$	Error	0.19%	0.01%	0.40%	
C2 N0030c1	FEA	784,745	7,636	60,277	~0
	NBT	779,426	7,570	60,612	
$[\pm30/0]_S$	Error	-0.68%	-0.87%	0.55%	
C2 ib1 N0030c1	FEA	980,937	9,521	63,933	~0
	NBT	972,376	9,179	63,929	
IB $[\pm45/0]_S$	Error	-0.87%	-3.59%	-0.01%	
C21 N0030c1	FEA	143,423	1,505	11,711	~0
	NBT	140479	1.45E+03	1.16E+04	
$[\pm45]_S$	Error	-2.05%	-3.84%	-1.16%	
C4 N9312c2	FEA	1,468,249	12,098	406,872	6,518
	NBT	1,457,337	12,041	408,127	4,638
$[\pm30/0]_S$	Error	-0.74%	-0.47%	0.31%	-28.8%
C4 ib1 N9312c2	FEA	1,793,400	14,416	427,493	8,460
	NBT	1,775,408	14,129	429,161	7,383
IB $[\pm45/0]_S$	Error	-1.00%	-1.99%	0.39%	-12.7%
C30 N6712c1	FEA	1,182,080	5,502	78,857	3,749
	NBT	1,183,571	5,689	81,817	3,913
$[0]_{6T}$	Error	0.13%	3.38%	3.75%	4.38%
C31 N6712c1	FEA	730,727	3,399	48,296	2,276
	NBT	724,988	3,465	50,116	2,397
$[\pm30/0]_S$	Error	-0.79%	1.95%	3.77%	5.30%
C32	FEA	1,566,989	33,205	482,096	16,983

Case	Method	AE (lb-in)	D_x (lb-in^2)	D_z (lb-in^2)	D_{xz} (lb-in^2)
N6712c2	NBT	1,555,492	33,629	493,112	17,682
$[\pm 30/0]_S$	Error	-0.73%	1.28%	2.29%	4.12%
C33 N6712c3	FEA	2,406,005	119,189	1,741,702	46,093
	NBT	2,386,208	121,046	1,777,674	56,108
$[\pm 30/0]_S$	Error	-0.82%	1.56%	2.07%	21.7%
C33 ib1 N6712c3	FEA	2,990,192	156,703	1,873,002	55,480
	NBT	2,957,515	154,242	1,888,476	57,273
IB $[\pm 45/0]_S$	Error	-1.09%	-1.57%	0.83%	3.23%

Stress results are much more agreeable in these cases. The stress results shown are the stress in the 1-2 material direction for each ply of a chosen laminate. In plots showing the airfoil skin, the upper and lower skin are shown in the same plot with the upper surface starting at the leading edge at a value of zero. A vertical black line indicates the location of the trailing edge where the lower surface stress plot starts and ends to the right which is back at the leading edge. The x-axis is the distance relative to the chord. Only unique ply angles are shown in the legend however all ply stresses are present in the plot. Typically, plies with the same angle in a laminate will have similar stresses.

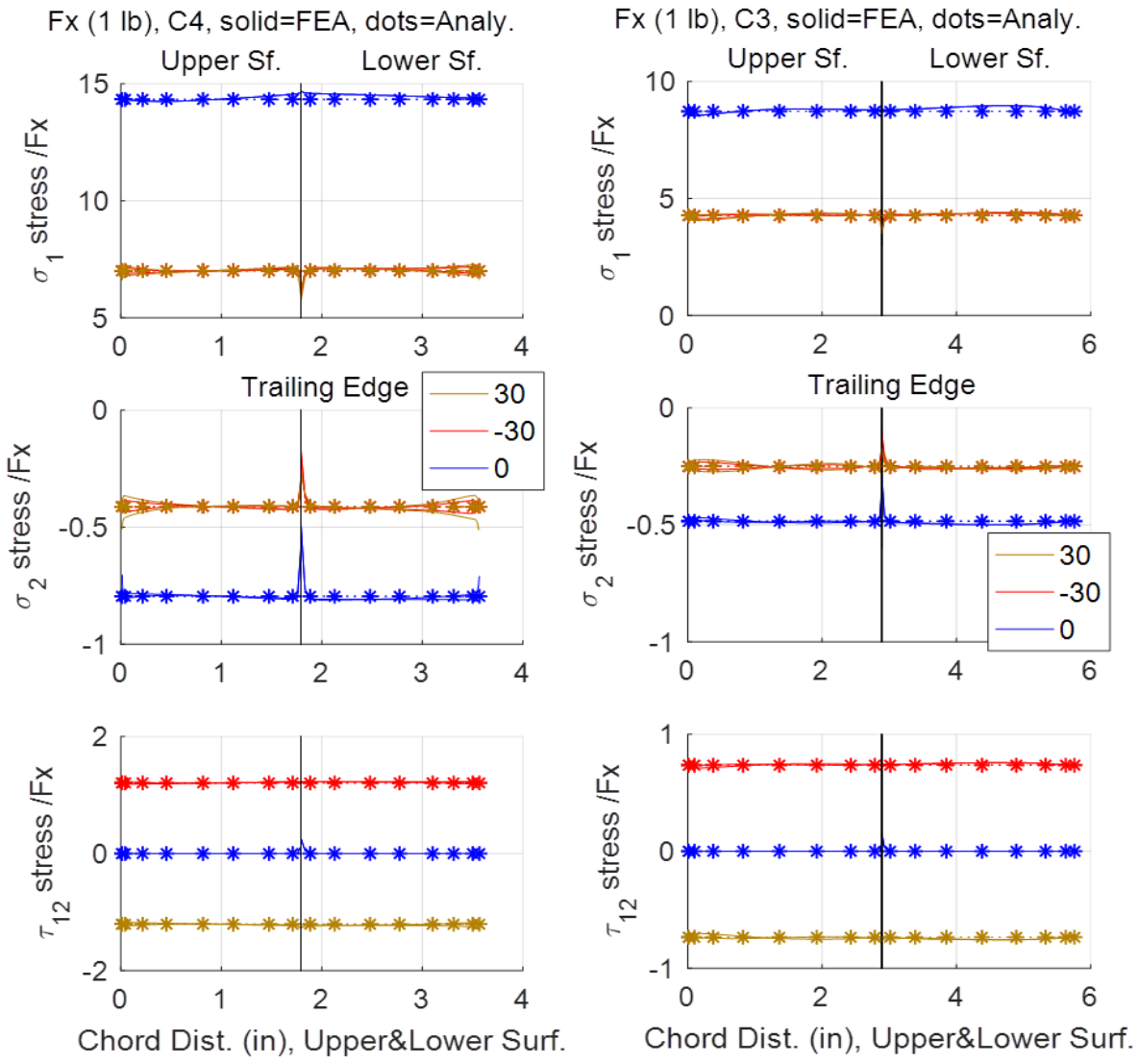

Figure 4.12 Stress Comparisons of cases C33 and C4 under an applied axial load, F_x

Figure 4.12 shows a comparison of cases C33 (NACA 6721, $[\pm 30/0]_S$, chord 3") and C4 (NACA 9312, $[\pm 30/0]_S$, chord 2") under an applied axial load of 1 lb. The solid curves are the FEM stresses and the dotted curves with the asterix markers are created from the analytical theory. It is evident that there is very good agreement in the $\sigma_1, \sigma_2,$

and τ_{12} in-plane stresses when considering axial loading for these cases. This is typical for all axial loaded cases with unstiffened beams.

For beams with I-beam stiffeners, there is a decrease in the FEM airfoil stress over the skin-I-beam interface. This is most noticeable in the transverse direction, σ_2, with an axial load as shown in case C2ib1 (NACA 6721, $[\pm 30/0]_S$, chord 1") on the left in Figure 4.13. The pink regions show the location of the I-beam where the width represents the span of the flanges. The analytical results did not compensate for this stress change. However, the transverse stress case has the highest prediction error but the transverse stress is almost negligible compared to the longitudinal stress.

In other loading cases, the change in stress over the airfoil skin, I-beam interface is not as pronounced. This is shown on the right in Figure 4.13 which shows C33ib1 case (NACA 6721, $[\pm 30/0]_S$, chord 3") under an M_x applied load.

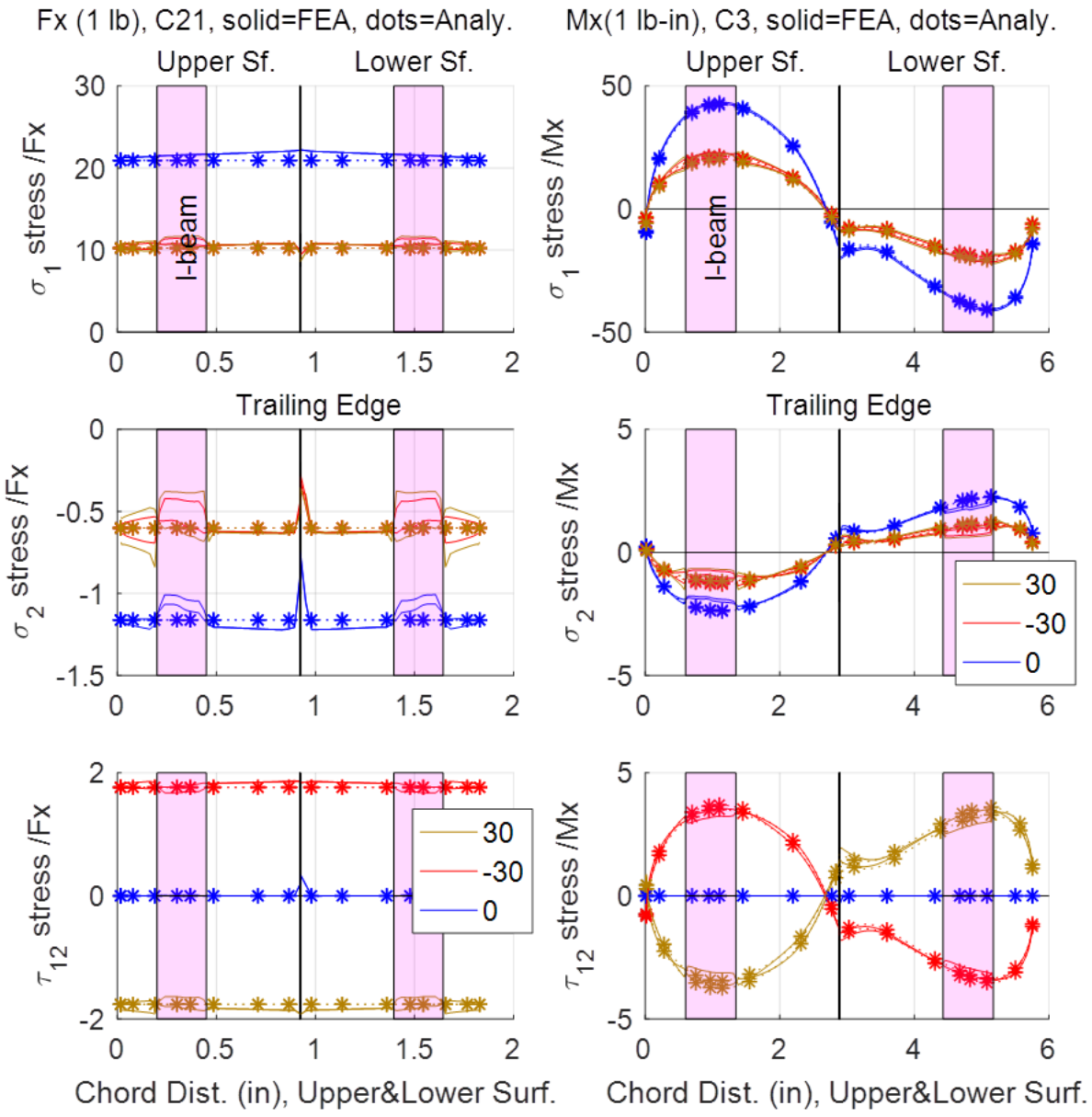

Figure 4.13 Stress discrepancies occurring over I-beam interface with airfoil

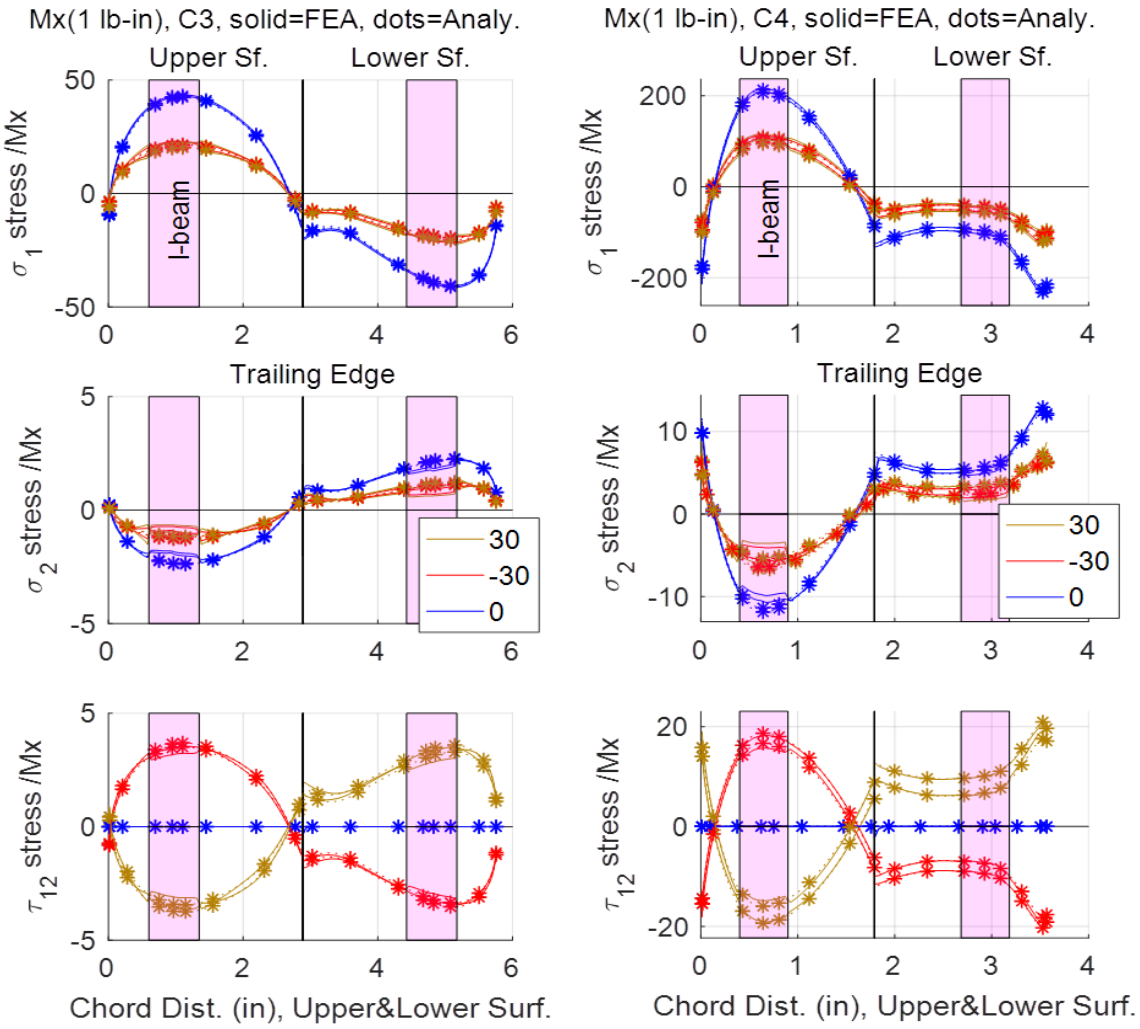

Figure 4.14 Comparing flap-wise moment induced stresses

between cases C33ib1 and C4ib1

There is good agreement between the NBT and FEA stress results considering M_x loading in cases C33ib1 (NACA 6721, $[\pm 30/0]_S$, chord 3") and C4ib1 (NACA 9312, $[\pm 30/0]_S$, chord 2"). Again, there are slight prediction errors over the I-beam, airfoil skin interface but mainly with the transverse stress which is significantly lower than the longitudinal stress.

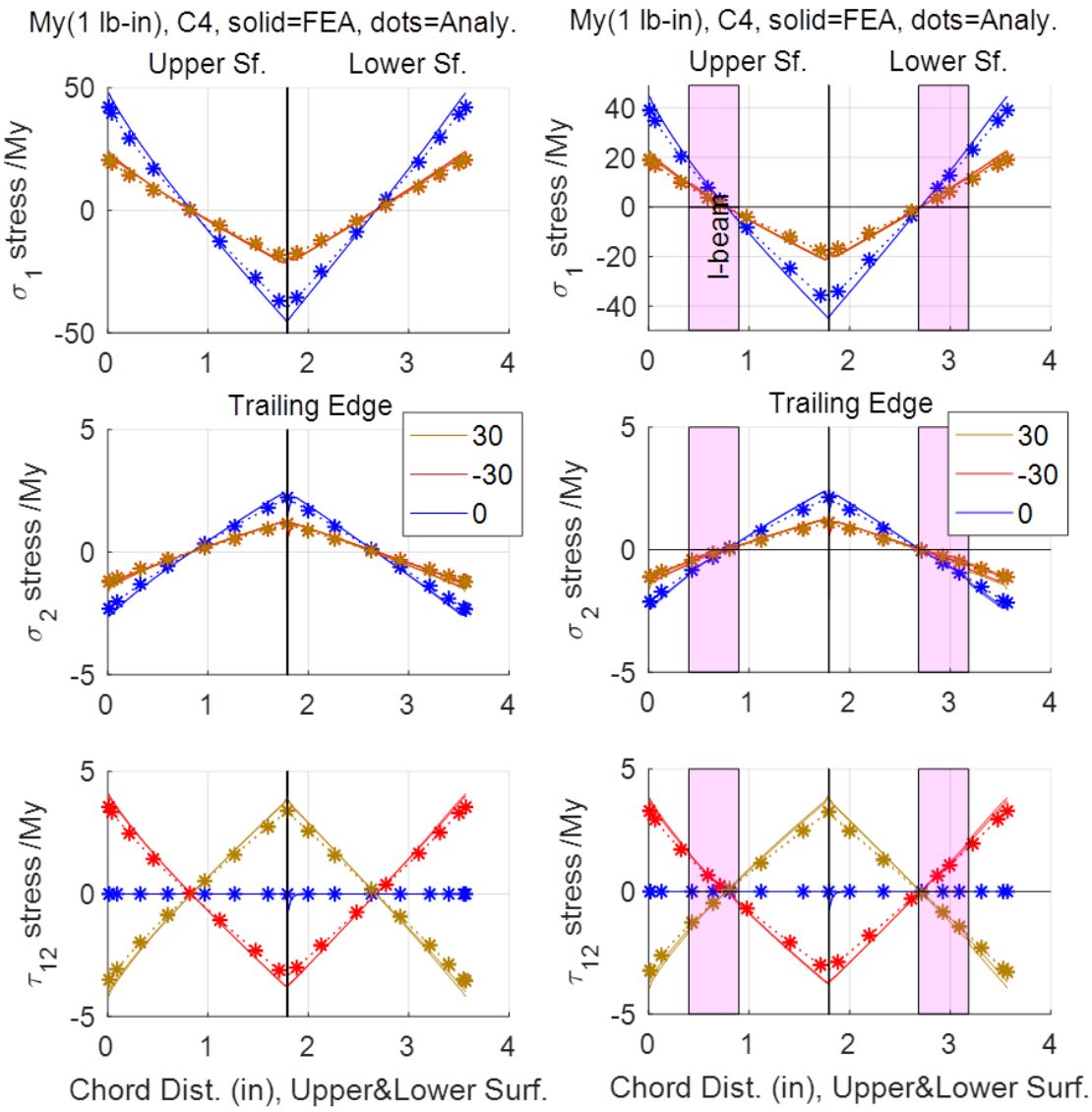

Figure 4.15 Comparing chord-wise moment induced stresses between cases C4 and C4ib1

Considering a load of M_z, NBT predictions of stress are in good agreement with FEA stress results. By comparing the same model with and without an I-beam stiffener, stress level reductions can be noticed primarily in the primary material direction (σ_1) when using an I-beam.

For design purposes, considering axial and bi-directional moment loads, an optimal location for the I-beam stiffener would be where there is maximum stress which is due to the M_x load as seen in Figure 4.14. In this research however, the I-beam location was arbitrarily chosen and not optimized.

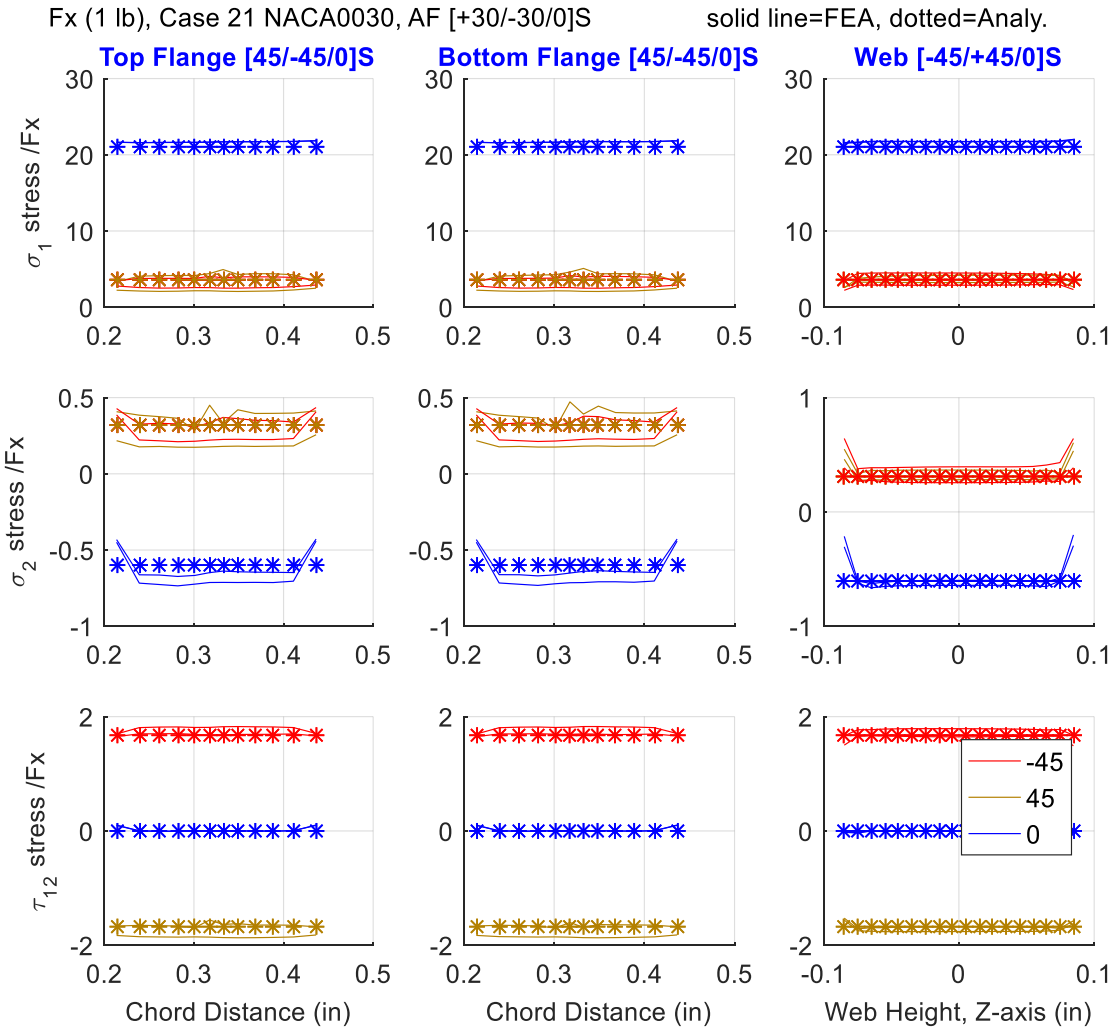

Figure 4.16 I-beam stresses for case C2ib1 under axial applied load

Considering stress of the I-beam stiffener, there are good predictions by NBT in the longitudinal and shear stress states for top, bottom, and web members of the

stiffener under axial loading as in Figure 4.16. Prediction errors are evident in the transverse direction but again, theses stresses are negligible as compared to the longitudinal stress.

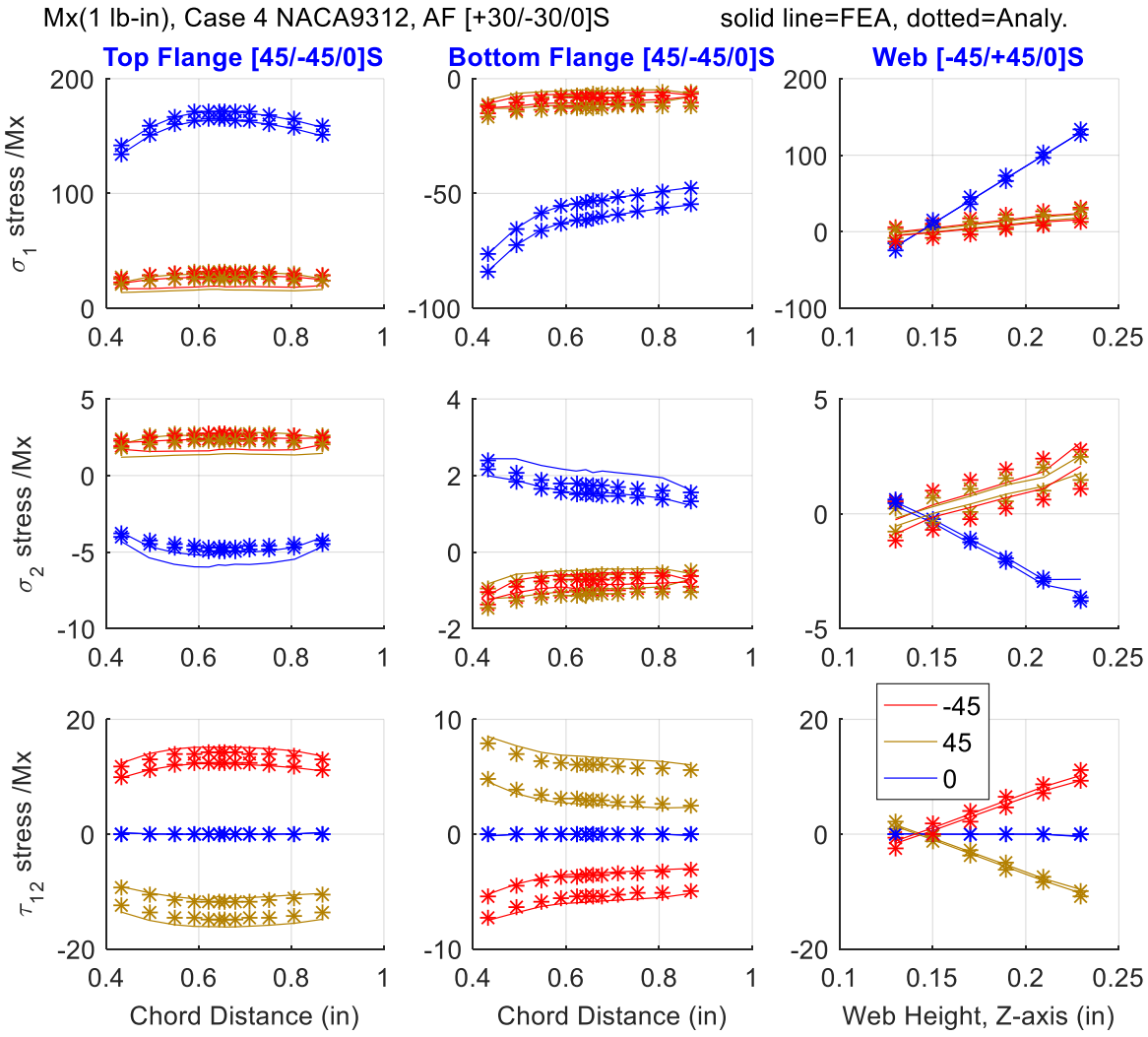

Figure 4.17 I-beam stresses for case C4ib1 under applied flap-wise moment

The prediction errors are again only notable in the transverse direction under a flap-wise applied moment as in Figure 4.17.

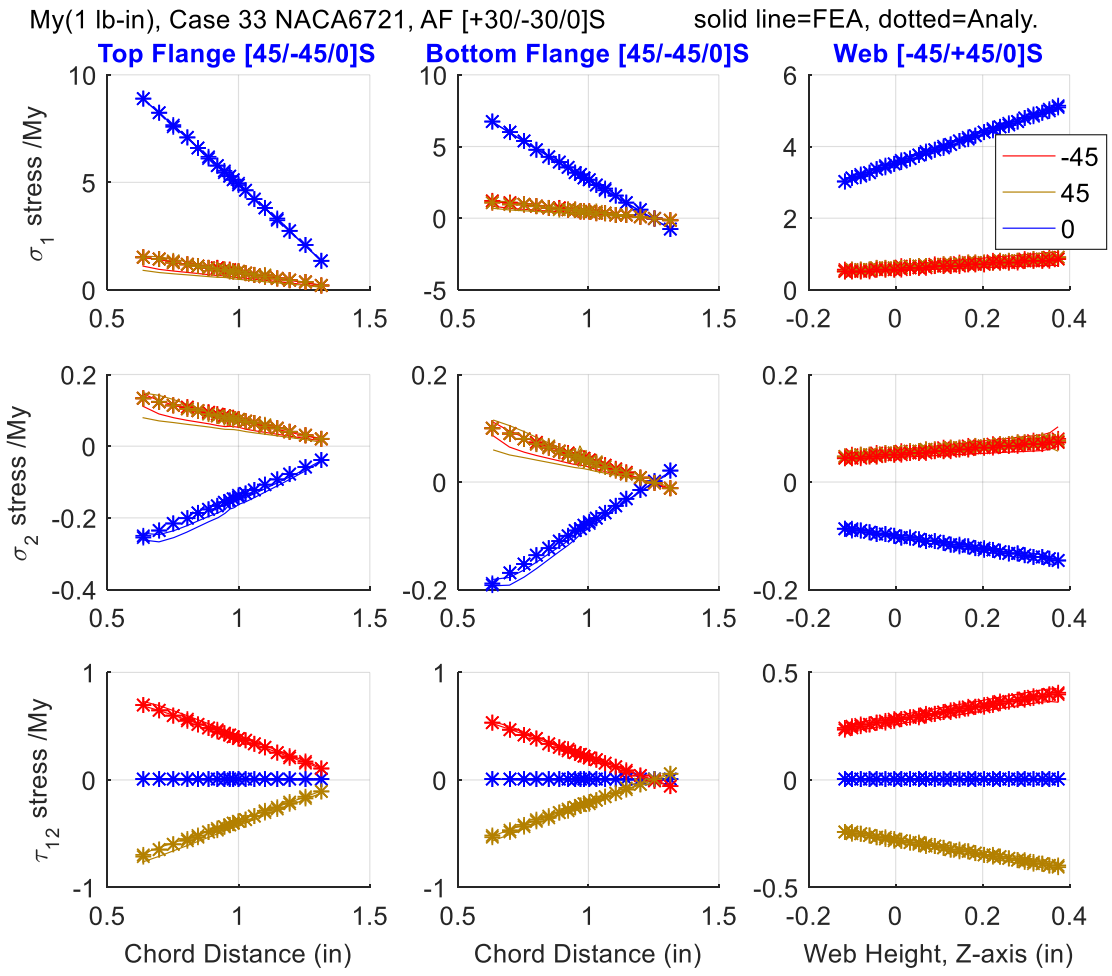

Figure 4.18 I-beam stresses for case C33ib1 under applied chord-wise moment

For I-beam stiffeners under a flap-wise applied moment as in Figure 4.18, prediction errors are again only notable in the transverse direction.

CHAPTER 5

EXPERIMENTAL STUDY

This chapter describes the fabrication of airfoil beam structures for bending test. Descriptions of test setup, test fixture and load application as well as data acquisitions are also included. The main purpose of this experimental study is used to validate the flapwise bending stiffness/ply stress of the composite airfoil that were obtained by the present method. This test is chosen since it is the primary load for wind turbine blades. Fabrication of coupons for material characterization and description of coupon test procedures as well as test results are given in Appendix C.

The test to be performed on the experimental specimens is the flapwise bending test. This test is chosen since it is the primary load for wind turbine blades.

FABRICATION OF COMPOSITE WINGS

Material Used

The label on the prepreg roll used for the airfoil skin of the first specimen is IM7-G/8552, 35%, 380AW, 12", FM 00. IM7 is a carbon fiber, 8552 is an epoxy which cures at 350^{o}F, and 35% is the percent resin content in the prepreg thus there is 65% fiber content. The '380AW' indicates the thickness and application of the composite. 'AW' most likely means All-Weather and the 380 represents a thickness of 14.6/1000 inches. The 'FM 00' indicates it is 2 plies of unidirectional plies. 12" is the width of the prepreg roll used. The manufacture date on the roll is Jan, 2010 thus a material characterization, which is described in Appendix C, was performed to check the properties.

Cutting Prepreg Material

To avoid aging the prepreg material, 4 kits were cut at one time to minimize the time the roll is out of the freezer. When a kit comes out, it can defrost in about 1 hour when left outside the freezer. In comparison, a full prepreg reel can take 8 to 10 hours to defrost.

Not all cuts were made for each kit thus allowing for changes if needed. For each kit, the 0, 90, and ±45 degree plies must be cut. Also, the $\pm 45^{o}$ leading edge strip must be cut, width = 2 inches. In fact, some of the kits were used to make test coupons since only 2 wings were made.

The roll used was opened recently and each layer is two plies of 0 degrees at a one foot width. Material was pliable and in good condition. The zero degree plies are cut in 3 foot lengths.

For specimen 1, the $-+45^{o}$ and 90^{o} plies cut are in about 1 foot lengths so 3 cuts are placed together on the wing to make up one ply. The layup with $-+45^{o}$ plies is shown in Figure 5.1.

For specimen 2, the 45^{o} plies were left in 3 foot sections. Thus, the layup could not be a symmetric $[\pm 45/0]_S$ since there is only one roll of $\pm 45^{o}$ and a 3 foot section of $-+45^{o}$ cannot be made with it. Also 3 foot sections of $-+45^{o}$ or 90^{o} plies cannot be made from the 0^{o} roll since it is one foot wide. Thus, specimen 2 uses an unsymmetric layup however each layer is continuous.

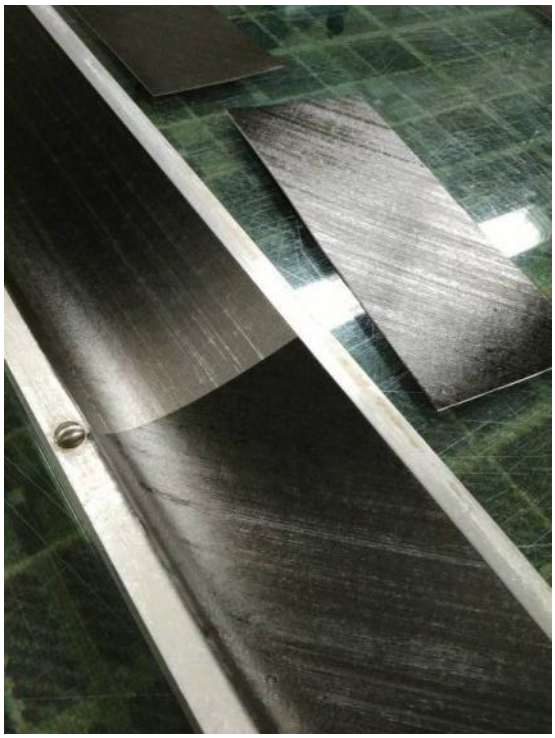

Figure 5.1 Layup of -+45 degree plies for specimen 1

Mold Preparation

The mold utilized is from the UTA Formula Car Team. The wing mold comes in 2 halves, an upper and lower ‘clam-shell’ half. Each half is made out of aluminum. The length of the mold is 36.0 inches and the chord of the airfoil to be made is 4.88 inches. Material for top and bottom surface is 5 inch width for butted up ends at the leading edge.

Mold surfaces which contact the composite must be wet-sanded smooth down to 900 grit sand-paper although this is not done every time the mold is used. Mold surfaces are treated with a release agent. The release agent is similar to wax and helps the wing pop off the mold.

Layup Prior to Cure

The top and bottom halves of the wing are laid up separately. Each wing half is laid up by placing prepreg plies against the shoulder at the trailing edge then working material to match the contour of the airfoil. Plastic tools are used to help eliminate voids.

When laying up -+45^{o} and 90^{o} prepreg plies for specimen 1, 3 prepreg pieces are butted up together by overlapping them slightly. A major problem of voids comes from the overlapped 45 and 90 degree plies which necessitates that preceding layers are worked extra at these overlaps to create a smooth surface with minimal voids.

Most material went over the leading edge plane so excess material is cut off by a razor blade. Some material is excess at the ends of the 3 foot length and this excess is also cut off by a razor blade. This finalizes the layup of each half of the airfoil.

After laying up each half of the mold, a 2 inch wide leading edge strip was applied as seen in Figure 5.2. One inch of the leading edge strip is adhered to the leading edge of the top half or surface of the airfoil. Also on the top half, the Cytec FM 300, a 350^{o}F cure temperature film adhesive, is placed on the end of the trailing edge. This film adhesive helps to bond the two wing halves together at the trailing edge. A bag is made with double sided tape and placed in the top mold down the inner channel of the wing. This bag is wrapped with release film to help extract the bag once cured.

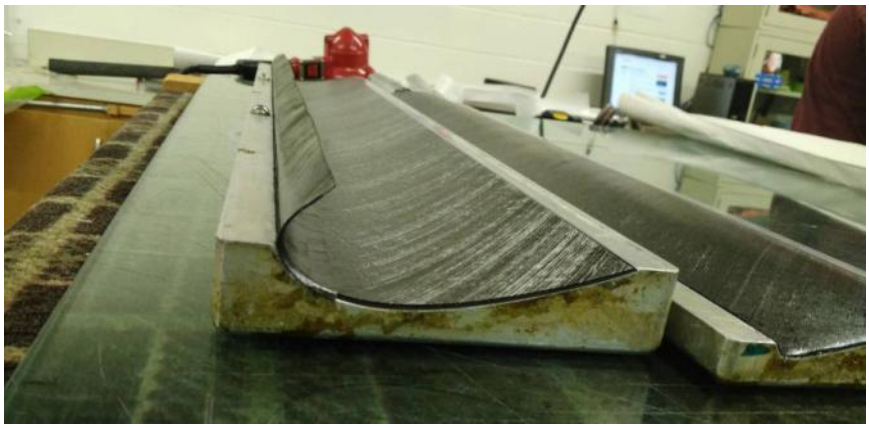

Figure 5.2 Leading edge strip used to attach the upper and lower surfaces

The lower mold is placed on top of the top mold while making sure the other half of the leading edge strip is inside the 2 molds. Once the molds are placed together, the other half of the leading edge strip is adhered to the bottom half of the mold by use of a long ruler. Thus, the leading edge strip attaches the 2 mold together at the leading edge.

Breather cloth is wrapped around the mold to allow excess resin to be soaked up and for pressure to access all areas of the bag. An outer bag is made which encloses the whole wing mold and breather cloth and makes a seal with the inner channel bag. Thus, the inner channel bag is open to the pressure inside the autoclave which then puts pressure on the leading edge strip to conform to the contour of the inner leading edge.

During and After Cure

The cure process is the same as used for the test coupons as described above. After cure, edges are wet sanded with 180 or 220 grit, then 320 grit sand-paper. Finer

grit is good to use but aesthetics is not a concern, rather safety in handling the wing is critical. There are many sharp edges due to flash after curing that can easily cut hands or leave long composite splinters. Care is taken to not sand down resin covering fibers. Care is also taken when wet sanding to not scratch or damage the surface of the wing as the wing is positioned in a sink over running water to wet-sand.

Inspection

Visual inspections were conducted to see if any surface wrinkle, fiber fraying or other defects occur. No delamination inspection was conducted since the lab has the limited facility for detail damage inspection.

After cure, warping is checked that is likely due to thermal stress caused by the difference in the stress free temperature (slightly below the cure temperature of 350^{o}F) and the ambient temperature of 70^{o}F. Warping of the specimens is measured by placing the wing on a flat surface, making contact with one end and one side edge. One corner will be raised. The raised distance is measure and divided by the length of 3.0 feet.

SPECIFICS FOR EACH WING MADE

General Notes

After cure, warping is present which is likely due to thermal stress caused by the difference in the stress free temperature (slightly below the cure temperature of 350^{o}F) and the ambient temperature of 70^{o}F. Warping of the specimens is measured by placing the wing on a flat surface, making contact with one end and one side edge. One corner will be raised. The raised distance is measure and divided by the length of 3.0 feet.

The inner bag and release film is difficult to pull out thus is left in the wing since weight is not a concern. The inner bag and release film seems to be bonded inside the wing at the trailing edge and does not come free easily. The bag and film are cut back so they are not hanging out of the wing.

The leading edge strip is $[\pm 45^{o}]_{T}$ and is the same material as the skin. Plies for the top and bottom molds are cut to 5 inches width.

The width of the specimen is measured from the leading edge to the end of the curvature at the trailing edge which forms a corner where some extra material comes out.

Summary of Specimens

Table 5.1 shows a summary of critical dimensions for each specimen. The details of each specimen will be described in the sections below.

Table 5.1 Summary of Critical Dimensions for Specimens

Specimen	Skin Layup	# of plies	Width (in)	Angle of twist (radians per foot)	Average ply thickness (in)
1	$[\pm 45/0_2/90]_S$	10	4.635	1.86	0.00695
2	$[+45/-45/0_2/+45/-45]_T$	6	4.637	0.0	0.00689

Composite Wing #1

Most plies had enough width to create a butted-end at leading edge between the 2 halves. One 45^{o} ply did not reach butted-end since it was cut probably not quite at 45^{o}. One 0^{o} ply was miss cut by about an 1/8 inch at the end but the errant cut did cut

the material complete away so the small ‘sliver’ cut on the material was kept. However, when cured, the ‘sliver’ cut went between the 2 mold halves at the trailing edge and were present when the edge were sanded down and became deeply imbedded into my finger. Better to cut any hanging edges off the prepreg I think.

Wing #1 shows small visible scratches on its surface after the wet sanding process.

Prior to cure, the mold could not be pressed together. There was approximately a 0.10 inch gap at the trailing edge and a 0.05 inch gap at the leading edge. After cure, the film adhesive had oozed out at the trailing edge and resin had escaped thru the leading edge gap which was only approximately 0.010 inches. The gap was likely due to the use of too many plies for the mold. Also, the internal vacuum bag could not be taken out from the cavity of the airfoil.

The angle of twist per foot is 0.033 degrees or 1.86 radians.

The average ply thickness for the skin away from the leading edge strip is 0.0139 inches. Thickness was measured at either end of the beam with average measurements of 0.0137 and 0.0141 inches for each end. Since the manufacturer’s cured thickness specification is 0.0146 inches, it appears some excess resin came out of the cure. After testing, the samples will be cut in 3 pieces and the thickness will be measured for each piece to check if the thickness is thin only at the ends of the 3 foot beam.

The trailing edge exhibits some cured plies where the gap between the 2 molds existed. This could be cut away with a Dremel diamond cutter. However, since the specimen will undergo a flapwise bending test and this extra material is located near the neutral axis thus won’t contribute much to the stiffness of the beam. Also, the airfoil

maybe weak at the trailing and leading edge so a little extra material at the trailing edge may help the wing stay together under load.

Composite Wing #2

Some plies did not reach the edges length-wise of the 3 foot mold by approximately 1/8 inch. This is not deemed important since the ends of the beam are clamped. The material was laid up and sat in the mold out of the cooler for 2 days.

The leading edge strip consisted of 2 layers of $\pm 45^{o}$ strips, one 2.0 inches wide, the other 1.5 inches wide. They were laid up by tapering the plies with the 2.0 inch wide applied first.

The 2 mold halves fit together with little gap. After cure, the gap between the mold halves was almost nonexistent. There was little excessive resin out-flow noticeable. The internal vacuum bag could be taken out.

FLAPWISE BENDING TEST FOR SPECIMENS

To conduct the bending test, fixtures were fabricated to fix the beam at one end and enable loading at the other. Also, an apparatus was made to load the cantilevered beam.

Test Preparation, Fixtures

To save on time and money, the fixtures for are made out of ABS by a 3D printer. The airfoil shape that the mold creates is confidential information to the UTA Formula Car Team. Thus, the airfoil designation is unknown. The airfoil shape then is determined

by tracing the airfoil cross-section of specimen 1 on to paper and scanning it into a jpeg file, converting it to data points, then use MATLAB to convert the data points to an airfoil curve again to enable changes to the data. MATLAB was used to separate the airfoil cross-section into 2D upper and lower clamps. Also, since ABS is chosen as the material, there will be little friction to hold the beam in the fixtures. Thus, for specimen 1, a silicon gasket is used to fit between the composite airfoil and the fixtures. MATLAB is then also used to provide room for the silicon gasket material. For specimen 2, thin double sided tap was placed on the lower half of the fixed clamp.

Once the general clamp was formed in MATLAB, CATIA is used to make the clamps in 3D with bolt holes. Thin prototypes are then made to check the fit of the clamp and the airfoil specimen. Figure 5.3 on the left shows a prototype of the bottom clamp ready to be made on a Makerbot 3D printer. The prototypes were made at a 10% to 50% fill as shown in Figure 5.2 on the right.

Figure 5.3 Prototype model of lower clamp on left and start of 3D build using 50% fill on the right

The prototypes were fit checked mainly by using pieces of paper, each at a thickness of 0.004 inches, to estimate the gap between the clamp and airfoil profile. This process is shown in Figure 5.4. Changes were made in CATIA and a new prototype would be made and again fit checked. In total, for specimen 1,about 7 prototypes were made to ensure an even fit along the contour. Since specimen 2's fixed clamp use a thin adhesive instead of silicon, the initial prototype was already a close fit to the airfoil and less prototypes were made.

Figure 5.4 Checking specimen 1fixture prototype fit with paper shims

The fixed end clamp is mounted to a wood panel to allow it to be firmly clamped to a table as seen in Figure 5.5. Figure 5.6 shows how the fixed end clamp is mounted to a table top.

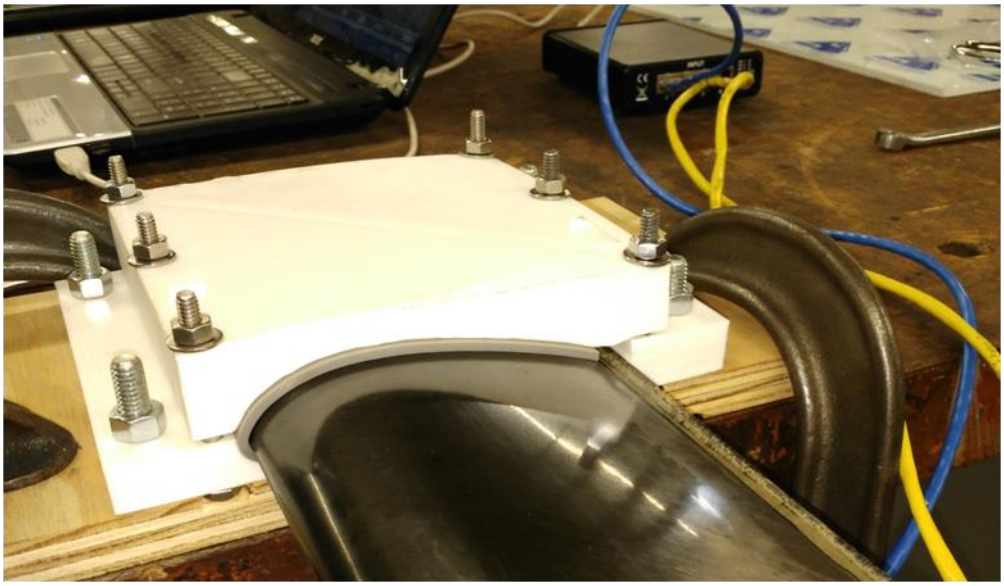

Figure 5.5 Fixed end clamp

Figure 5.6 Fixed end clamped to table top

The load fixture is shown in Figure 5.7 where the beam with the vacuum bag and silicon gasket are shown. Both wing specimens used the same load clamp. In this fixture, the upper clamp is made to extend 3/4 of an inch past the lower clamp. The beam extends to the length of the lower clamp, thus allowing an overhang of the upper

clamp. On the top of the upper clamp is a 2 inch long and 1/4 inch wide slot to allow a cable to pass through which is used to attach weight as seen in Figure 5.8. The steel cable, 3/16 inch diameter, runs just in front of the beam thus applying a vertical shear force to the beam. Notice that the washer making contact with the fixture is knurled and fixture is scratched up around the slot to create friction at their interface to prevent slippage.

Figure 5.7 Load fixture

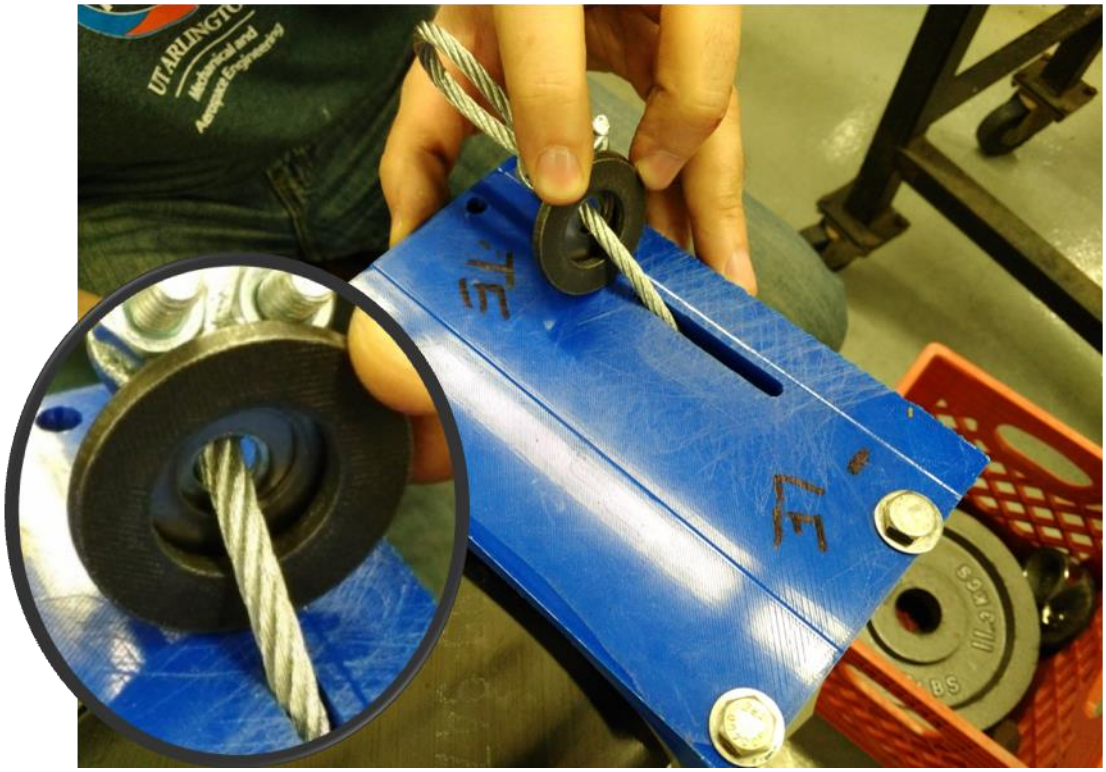

Figure 5.8 Load fixture, upper clamp

The cable ends are clamped with a type of u-bolt. The lower end of the cable runs through the center of a 2 inch pipe as seen in Figure 5.9. Weights can be added onto the pipe to exert a vertical shear load on the beam.

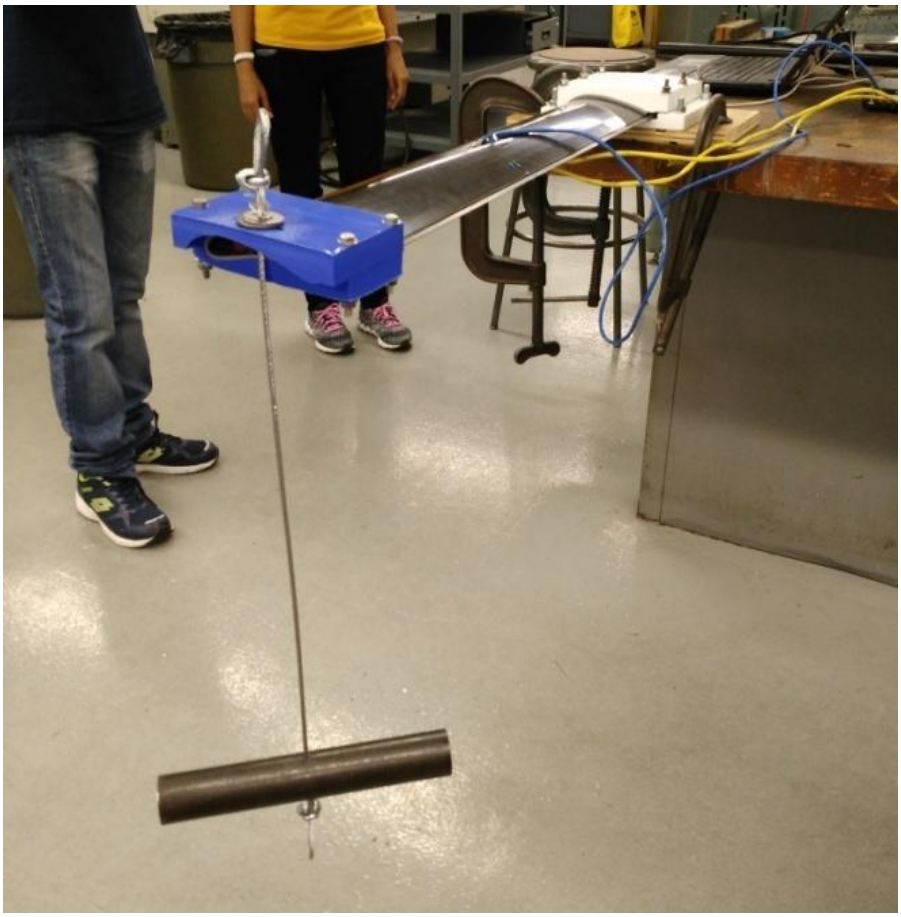

Figure 5.9 Test setup

Test Preparation, Measuring Devices

Strain is measured from the beam with linear strain gages. 3 strain gages are used with wing 1, one on the top side of the airfoil and the other 2 located on the bottom side of the airfoil. Figure 5.10 shows these strain gages. Wing 2 used 2 strain gages on the top and bottom surface of the wing.

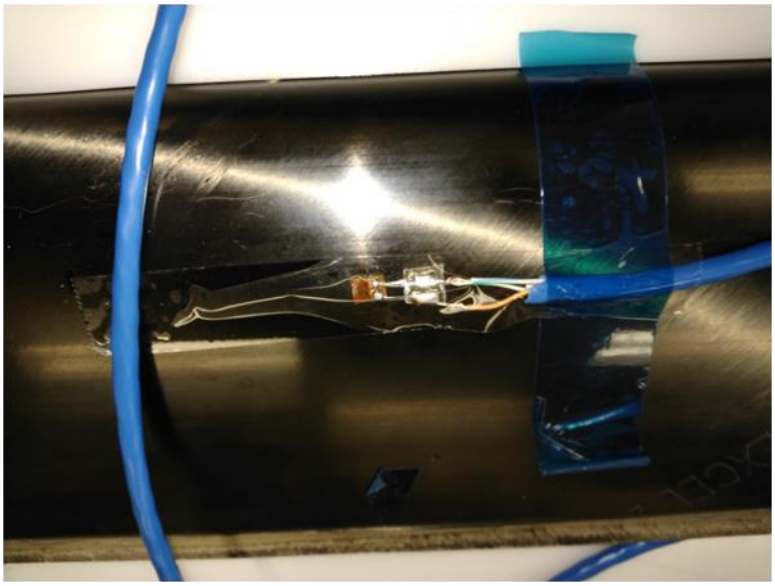

Figure 5.10 Strain gages used on specimen 1

The strain gages are attached to a D4 Data Acquisition Conditioner which is then fed to a computer to Micro-Measurements software to read the strain gages.

The end displacement is also measured at either side of the load fixture by use of spring loaded dial gages. The setup with these dial gages is seen in Figure 5.11.

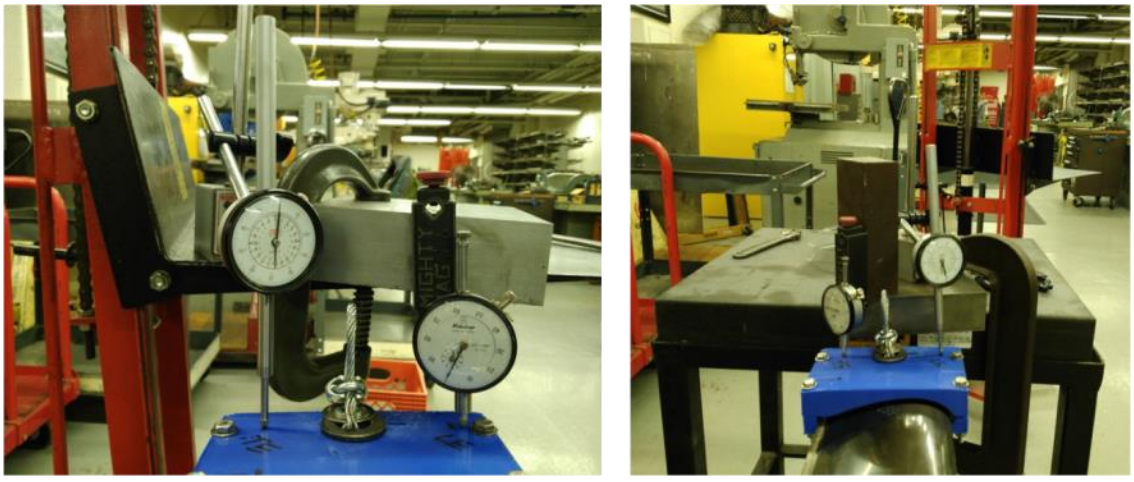

Figure 5.11 End displacement dial gages

The setup on the left of Figure 5.11 was used at first with specimen 1. However it was noticed that the pneumatic platform that the gages were attached to was causing sudden increases of deflection as measured by the gages. Thus, the gages were mounted on a fixed table which gave more reliable readings however a slight strain rate effect was still noticed which caused an approximate deflection of 0.005 inches per minute. The silicon gasket was suspect to produce this deflection thus a new fixed end bracket was made for specimen 2. Also for specimen 2, the dial gages were placed directly on the composite wing at 20 inches from the fixed end of the beam which is nearest the fixed clamp. This can be seen in Figure 5.12.

Figure 5.12 Placement of dial gages for specimen 2

Flapwise Bending Test of Specimens

Load was applied in 2.5 pound increments by placing weight lifting plates on the pipe on either side of the cable. Figure 5.13 shows the maximum applied load for

specimen 1. The total load is the plate weight plus the weight of the load fixture with cable and pipe which is 5.48 lbs. The weight of the wing specimen and half of the strain cables is 1.75 lbs and its resultant acts at the center length of the beam thus half this weight is added to the end of the beam load since a flapwise bending moment is considered. Although the vertical load applies a shear force and moment to the beam, the maximum shear load is 66.4 lbs and the maximum moment is 1,991 in-lb thus the shear load is considered to be negligible.

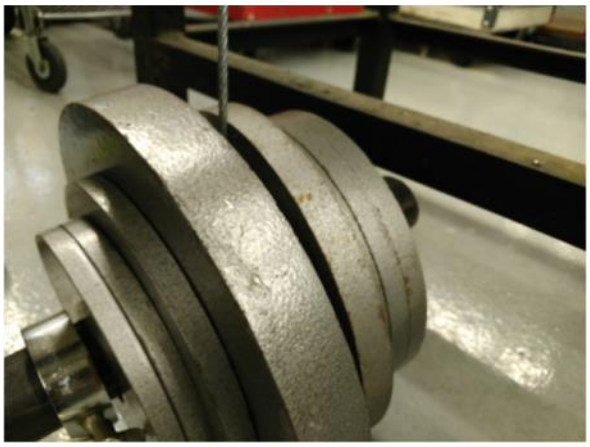

Figure 5.13 Maximum applied load to specimen 1

During the test a few issues were noticed that could affect the bending rigidity calculations. The main issue is the compression of the silicon gasket. The design of the fixed end fixture did not allow one to tighten the bolts very much thus the silicon gasket was not compressed much. This allows the blade to start curvature inside the fixed end fixture as seen in Figure 5.14. The second end clamp design corrected this problem and was used on specimen 2.

Even after using a fixed table to mount the dial gages, a slight strain rate effect was noticed which may have resulted in displacement varying down with time. When

running the second sample, a strain rate effect of approximately 0.004 inch/1000 was still noticed even though no silicon was used on the fixed end. Thus, a second run was made with the second wing where measurements were taken more quickly and the time between load intervals was decreased.

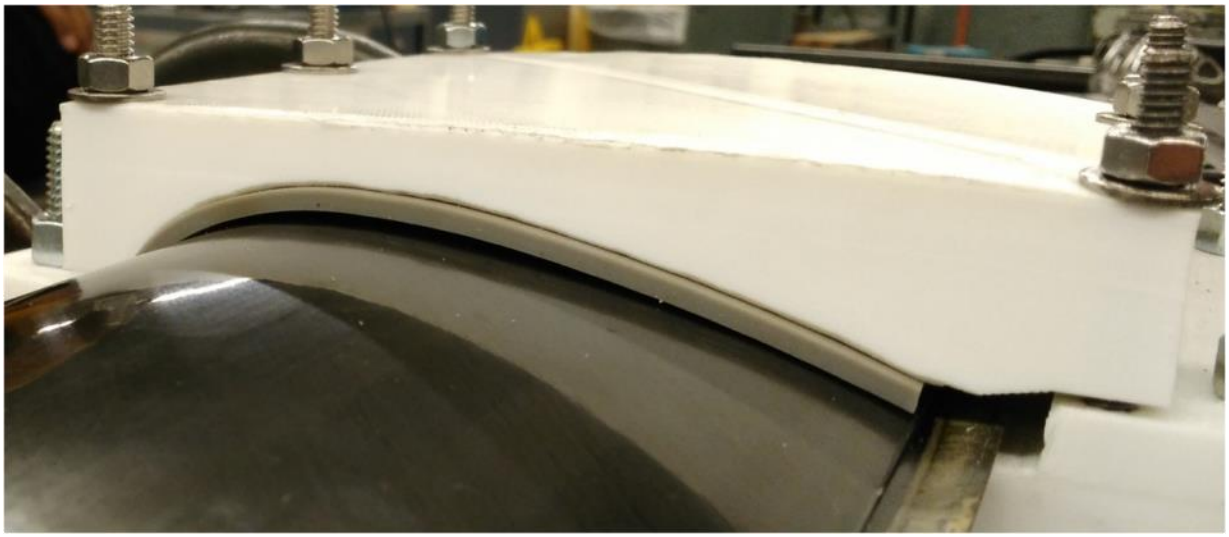

Figure 5.14 Fixed end allowing curavture of the wing

Another issue included a slight curvature of the fixed end fixture which probably affected the deflection readings on the dial gages. To improve on this, specimen 2 used a tight fitting fixed clamp with only a thin layer of double sided tape on one surface. Also, inserts were placed into specimen 2 to fill the cavity of the airfoil which is inside the fixed clamps. These inserts can be seen in Figure 5.15. The inserts consisted of 3 pieces which were fitted tightly inside the airfoil.

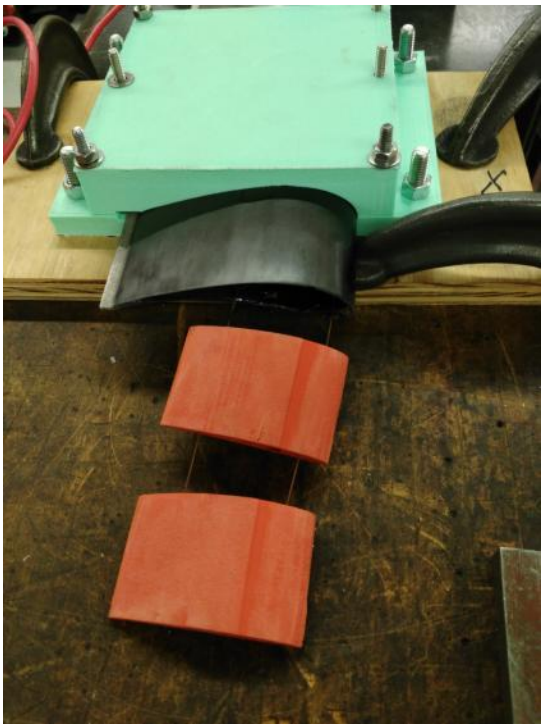

Figure 5.15 End inserts used for specimen 2

COMPARISON OF EXPERIMENTAL RESULTS TO ANALYTICAL AND FEA RESULTS

Flap-wise Bending Stiffness

Sample 1 produced the flap-wise bending stiffness results as shown in Figure 5.16. The bending stiffness is in increments based on the step-wise loading. D_x is calculated for every 2.5 lbs loaded. The beginning of the loading produced very irregular D_x values thus the 3rd D_x value to the end is averaged and compared to the analytical values.

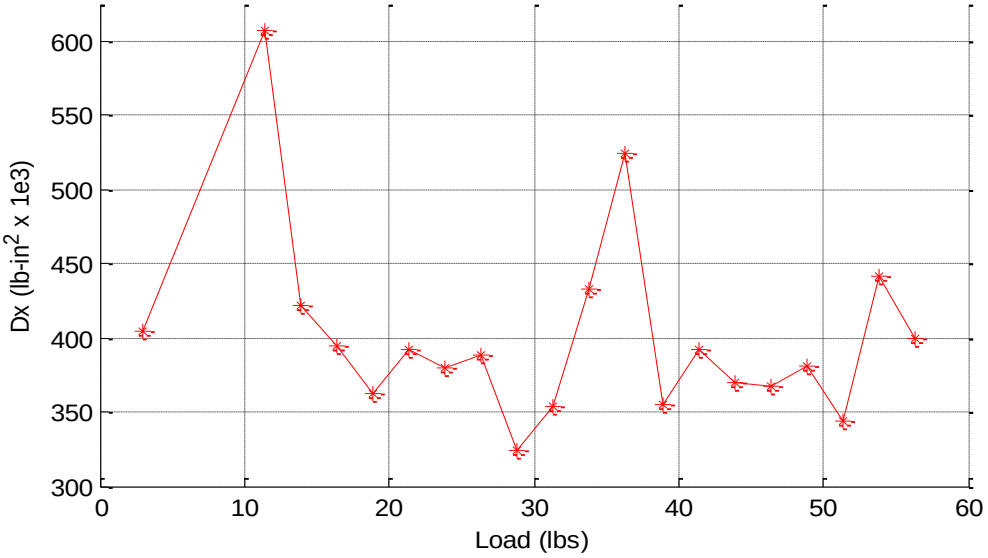

Figure 5.16 Incremental flap-wise bending stiffness plot of sample 1

Figure 5.17 shows the D_x plot for 2 runs of sample 2. All data points from both runs are used to find an average D_x value. Note that run 2 was made at a faster pace than run 1 to try to alleviate any strain rate effects.

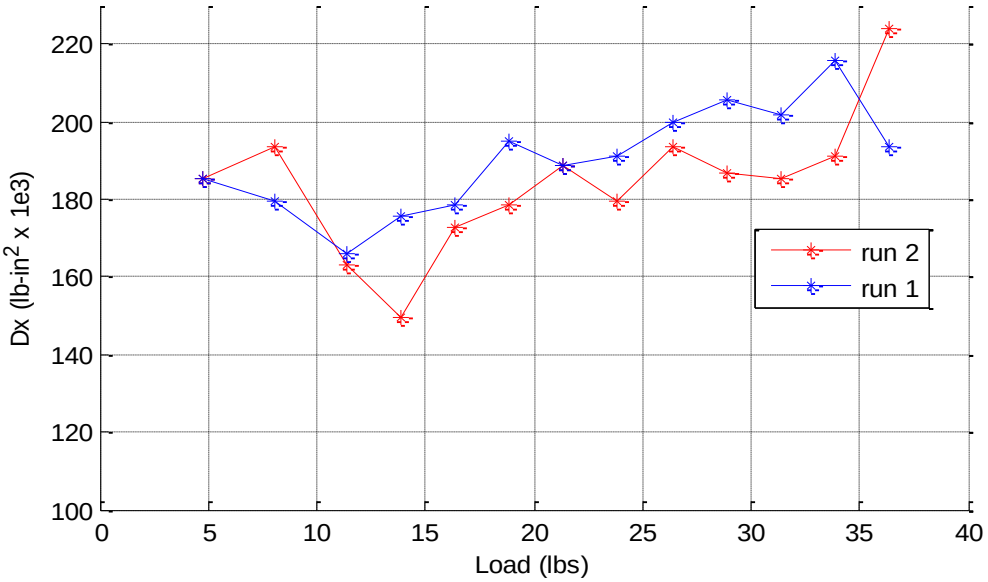

Figure 5.17 Incremental flap-wise bending stiffness plot of sample 2

Table 5.2 shows the comparison of the experimental D_x results with the D_x found with the analytical method. For the NBT analysis, material properties used are presented in Table C.4 which are from volumetric averaging.

Table 5.2 Comparison of Flap-wise Bending Findings

Results of Flap-wise Bending, D_x		
Method	Wing 1	Wing 2
NBT	687,194	286,801
Experimental, run 1	390,334	184,941
Differ from FEM	-43.2%	-35.5%
Experimental, run 2		190,044
Differ from FEM		-33.6%

The experimental results of flap-wise bending stiffness of specimen 1 and specimen 2 are very poor.

Despite the quicker pace run for specimen 2, run 2, the bending stiffness only increased 3.0%. Thus, the strain rate effect does not appear to affect the bending stiffness results with specimen 2 much. However, specimen 1 is probably affected by the use of the silicon gasket. The use of wood for the bottom bracket at the fixed end could be a reason for the strain rate effect also. The bolts that held the clamp to the wood noticeably compressed the wood, allowing the wing to curve down more.

Improved D_x experimental results using Wing 2 are probably due to the continuous layup used, not using the silicon gasket in the fixed end clamp, and using 3D printed ABS inserts in the airfoil at the fixed end. Further improvements could be to replace the wood base with an ABS plastic or aluminum material. Also, the airfoil at the fixed end should be potted to make the fixed end of the airfoil specimen more rigid.

Analysis of Longitudinal Strain on Select Points on Outer Surface of Airfoil

Outer ply longitudinal strain was measured by the strain gages on the outer surface of the airfoils close to points which yield maximum strain. Gage locations were measured and longitudinal strain predictions were obtained from approximately the same positions.

Specimen 2 results are compared to results obtained from Narrow Beam Theory using the same airfoil cross-section and material properties obtained from Table C.4. Figure 5.18 compares the longitudinal strain on the upper surface of wing specimen 2 near the highest point relative to the chord where the strain gage is located. As shown, NBT predicts a higher longitudinal strain than found experimentally. These curves are nearly identical with run 1 and run 2 for specimen 2.

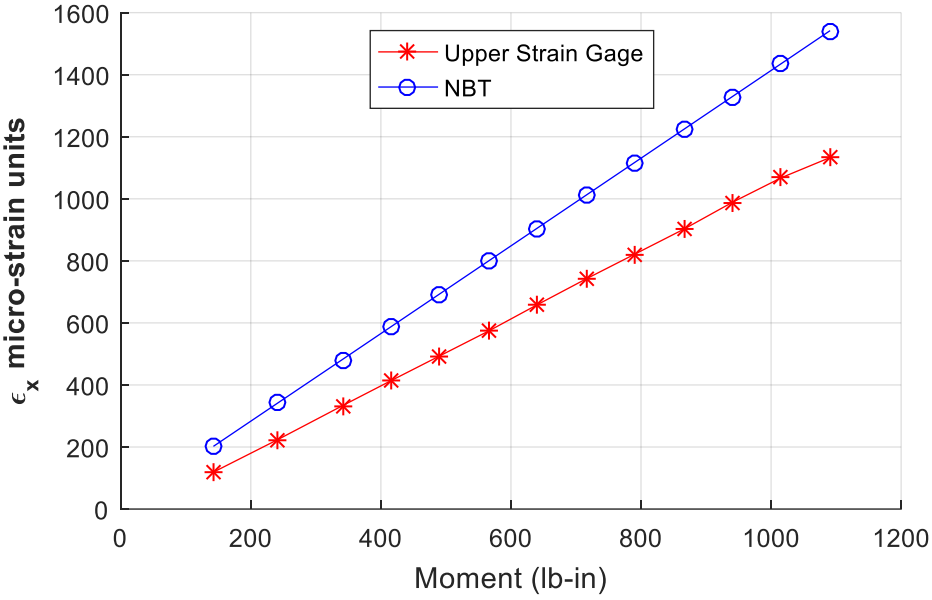

Figure 5.18 Longitudinal strain readings from the upper airfoil surface strain gage and NBT predictions, specimen 2, run 1

Figure 5.19 compares the longitudinal strain on the lower surface of wing specimen 2 near the lowest point relative to the chord where the strain gage is located. As shown, NBT again predicts a higher longitudinal strain than found experimentally. These curves are nearly identical with run 1 and run 2 for specimen 2. Note that strain gage data is much more consistent than the dial gage data used to determine the flap-wise bending stiffness.

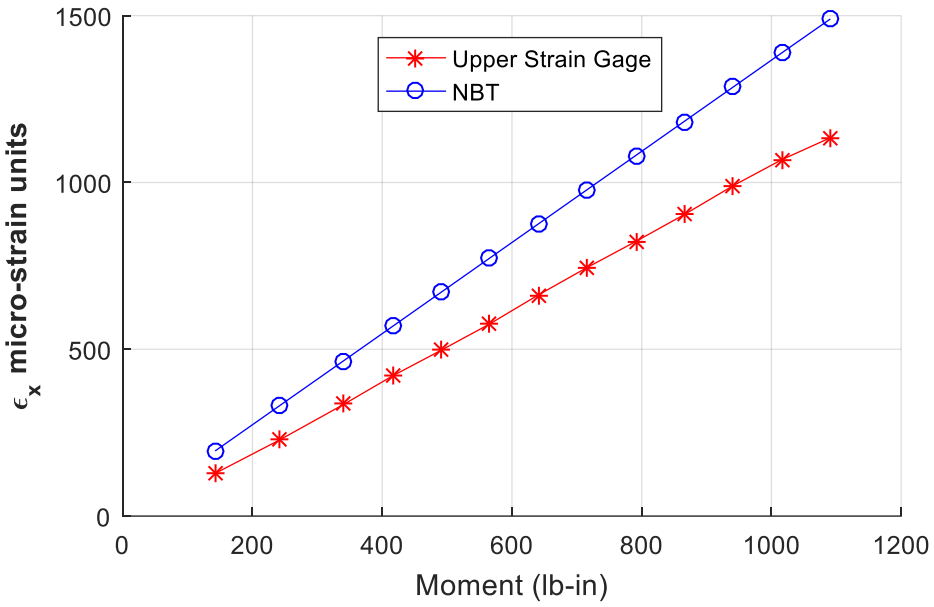

Figure 5.19 Longitudinal strain readings from the lower airfoil surface strain gage and NBT predictions, specimen 2, run 2

Table 5.3 gives the percentage difference between the experimental longitudinal strain readings and those calculated by NBT. All reading in Table 5.3 come from specimen 2. For example, at the moment of 1091 in-lbs, NBT predictions for longitudinal strain are 36% greater than the experimental readings.

Table 5.3 Longitudinal strain comparisons between experimental readings and NBT predictions on bending test of specimen 2

Specimen 2	run 1	run 2	run 2
Moment (lb-in)	Upper surface	Upper surface	Lower surface
143	70%	54%	53%
242	53%	48%	45%
341	45%	42%	39%
416	42%	38%	35%
491	40%	38%	35%

Specimen 2	run 1	run 2	run 2
Moment (lb-in)	Upper surface	Upper surface	Lower surface
566	39%	37%	34%
641	37%	35%	32%
716	36%	35%	31%
791	36%	35%	31%
866	36%	35%	31%
941	34%	34%	30%
1016	34%	34%	30%
1091	36%	36%	31%

The differences between NBT and the experimental data on the longitudinal strain are similar to the differences in the flap-wise bending results. An FEA model was run using the experimental beam model with manufacturer's properties and there was good agreement with NBT on bending stiffness. Also, the airfoil cases run in this research show that NBT is in close agreement with FEA results. Thus, it is suspected that the experimental wing is giving inaccurate results. Some experimental test issues have been identified such as the wood base and the fixed end inserts. Other issues could be that the composite material is old and the wing design is made in two parts.

CHAPTER 6

CONCLUSION AND FUTURE RECOMMENDATIONS

A semi-closed form solution is developed based on Narrow Beam Theory to analyze airfoil cross-sectional beams with and without an I-beam stiffener under axial and bi-directional moments. The solution is based on a discrete element approach which can be applied to any airfoil profile. Only a single line profile is needed to conduct this analysis thus is advantageous over the Finite Element Method especially in an early design phase of a project. Despite the simplicity of this method, accurate ply stresses over approximately the full cross-sectional field can be obtained. Centroid, axial stiffness, and flap-wise and chord-wise bending stiffnesses are accurately determined for symmetric laminates and symmetric and non-symmetric airfoil geometries. The bending coupling stiffness term is also obtained with some prediction errors for airfoils without stiffeners. However, with the use of stiffeners in these airfoils, the bending coupling term prediction is mostly acceptable.

An experimental test was fabricated and conducted to measure flap-wise bending tests and take strain readings on an approximately 5 inch chord airfoil beam. Two good quality airfoil samples were manufactured and tested. Results were obtained and compared to analytical predictions made by this modified Narrow Beam Theory. Differences of 30% or more were found for both flap-wise bending stiffness and longitudinal strain. Possible reasons for these discrepancies are the manufacture of the experimental wing and the age of the material used. The wing is laid up in 2 sections and cured together with adhesive on the trailing edge and composite leading edge

strips. The material is 5.5 years old so a material characterization study was made but did not yield dependable data. NBT results have good agreement with FEA thus the experimental data seems suspect.

An analysis of equivalent properties for lamina, laminate and I-beams is conducted to gain an understanding of Narrow Beam Theory and develop MATLAB code to conduct analyses, facilitate creating, running, and post processing of ANSYS models. An approximate full-field cross-sectional stress analysis in the material's principal coordinate system is created and a thorough I-beam analysis of symmetric, unsymmetric, and unbalanced layups composed of 0^o, 90^o, and 45^o plies was performed. Centroid and axial and bending stiffnesses are determined with Narrow Beam Analyses which outperforms conventional analyses. Stress predictions from NBT are very accurate under applied loads with rigid cross-sections with few exceptions. Stress predictions from applied loads on a free end with the RBE3 constraint are more challenging especially concerning M_z moments and some poor predictions were noted. A detailed summary of equivalent property modified method and the I-beam analysis is found at the end of Chapter 2.

It is concluded that the developed novel analytical method can be used in the evaluation of axial and bi-directional bending stiffness of composite beams with airfoil cross-section with and without stiffeners, performing parametric study in preliminary design stage, as well as optimize designs.

FUTURE RECOMMENDATIONS

Based on this research and the success of the modified Narrow Beam Theory, the following work is recommended as a continuation of this research.

Airfoil Analyses

- A closed form solution could be developed by considering the airfoil profile as a curve and integrating over the length of the curve.
- Various stiffeners could be explored to be coupled with airfoils to compare which performs better in defined conditions.
- Stiffener position and layups could be optimized.
- Torsion should be studied first at the shear center to decouple it from moments then at the centroid to merge it with axial, and bi-directional moment loads.
- Airfoils with various laminates could be studied such as using a different laminate for the upper and lower surface or making a fiberglass beam with carbon-epoxy flange I-beams.
- An analysis of a tapered and rotated airfoil beam could be conducted. Different thicknesses could be modeled considering a long beam such as a wind turbine blade. A method to couple cross-section analyses would need to be developed such as treating attachments to sections as springs and dampeners.
- Thermal analyses could be performed using NBT on airfoil beams.

- Larger chord beams should be studied and compared to literature. FEA comparisons could also be made by using shell elements. If shell elements are used, an analysis could be made to see if it yields similar stress and strains to brick elements.
- Consider using layered brick elements to reduce the size of the FEA model.

Experimental Study

- Make an aluminum base to mount the fixed end to the table. The wood base use in this research seemed to cause problems.
- Consider constructing a one piece airfoil with a removable inner mold. This may allow a better comparison to the analytical analysis.
- Narrow Beam Theory appears to yield better predictions with stiffened airfoils. An airfoil with a stiffener could be tested.
- A torsion test could be conducted perhaps with use of a torque wrench.

APPENDIX A

REVIEW OF NARROW BEAM THEORY FOR I-BEAMS

This method applies to I-beams made of straight members. The I-beam is composed of 3 laminate members as shown in Figure A.1, labeled ‘f1’ for the top flange, ‘w’ for the web, and ‘f2’ for the bottom flange. The ABD matrix is found in each laminate member by use of Classical Lamination Theory then Narrow Beam Theory is used to find the centroid, stiffnesses, and strains and stresses of the entire I-beam as discussed below.

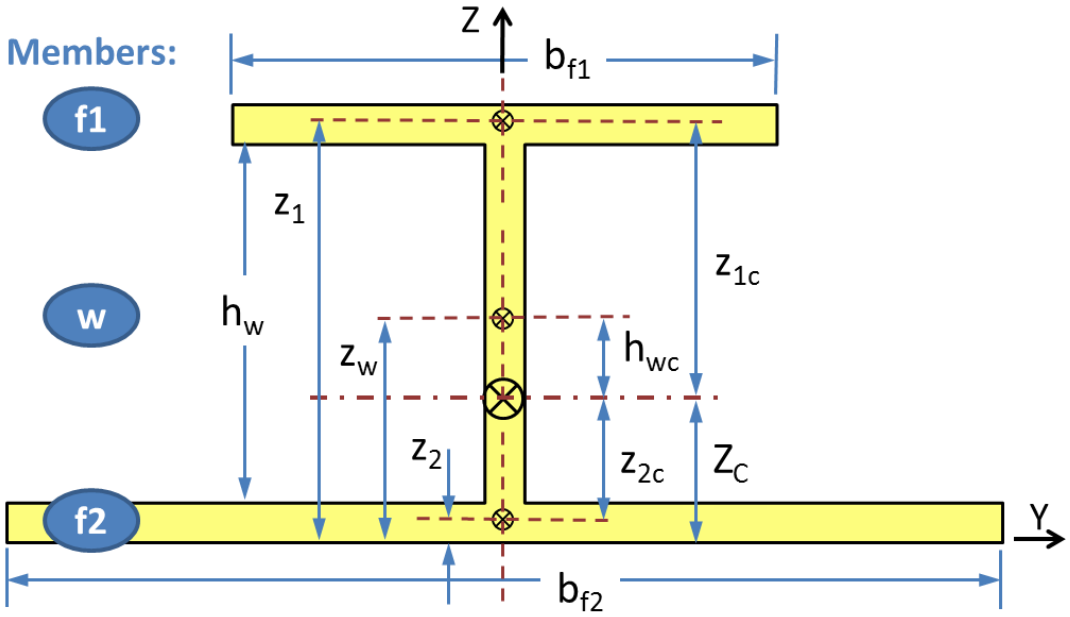

Figure A.1 Composite I-beam cross-section geometry with straight members. Member ‘f1’ is the top flange, ‘w’ is the web, and ‘f2’ is the bottom flange.

To analyze a composite I-beam, the Narrow Beam assumption is made which was developed by Parambil and Chan in 2011 (33). In this assumption, the beam is treated as one-dimensional in the x-direction. Normally, the narrow beam assumption is valid when the depth (z-direction) over width (y-direction) ratio is 6 or greater.

An illustration of a narrow beam, first undeformed, then under a bending load, M_x, is shown in Figure 2.13. A reduced 2x2 stiffness matrix is obtained using Narrow Beam Assumptions for each member of the I-beam as shown in Chapter 2 with equations 2-52 through 2-57. The reduced stiffness matrix is thus:

$$\begin{bmatrix} A^* & B^* \\ B^* & D^* \end{bmatrix}_i = \begin{bmatrix} a^* & b^* \\ b^* & d^* \end{bmatrix}_i^{-1} = \begin{bmatrix} a_{11} - \dfrac{b_{16}^2}{d_{66}} & b_{11} - \dfrac{b_{16}d_{16}}{d_{66}} \\ b_{11} - \dfrac{b_{16}d_{16}}{d_{66}} & d_{11} - \dfrac{d_{16}^2}{d_{66}} \end{bmatrix}_i^{-1} \qquad \text{(A-1)}$$

$$\begin{Bmatrix} N_x \\ M_x \end{Bmatrix}_i = \begin{bmatrix} A^* & B^* \\ B^* & D^* \end{bmatrix}_i \begin{Bmatrix} \varepsilon_x^o \\ k_x^o \end{Bmatrix}_i .$$

CENTROID OF I-BEAM

The centroid, or location of the neutral axis, is important because it decouples axial and bending stresses and strains. If an axial load is applied at the centroid, there is no bending and vice-versa. For isotropic material, the centroid is dependent on only the cross-sectional geometry of the beam. For a laminated composite material, the centroid is dependent on the geometry as well as the stacking sequence and material constants.

The centroid is the location where a resultant axial force will be equal to distributed axial forces applied to each laminate member. Figure A.2 illustrates this concept where the axial loads acting at the centroid of each laminate are noted by $N_{x,i}$ which are load per unit length of laminate $'i'$. The magnitude of the resultant force, $\bar{N}_x$,

over the whole I-beam structure (as noted by the bar over the N) is the sum of each $N_{x,i}$ times the respective laminate width.

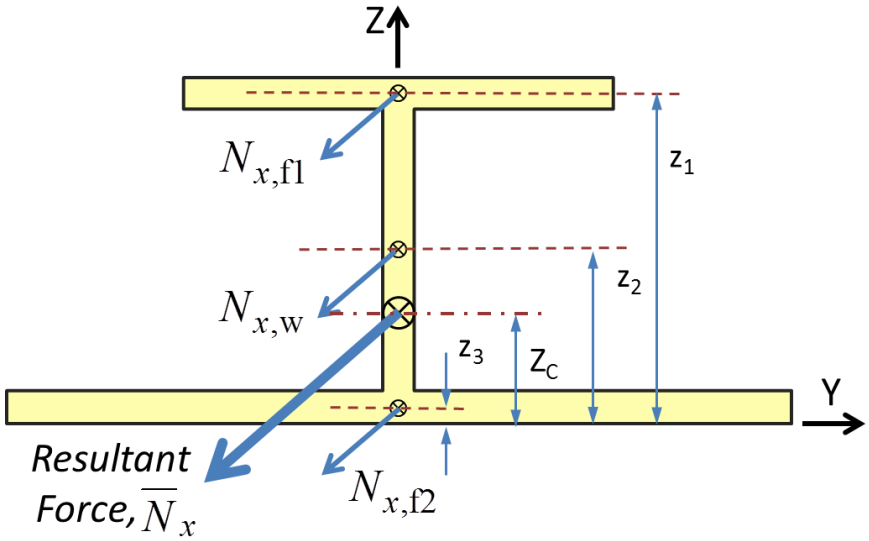

Figure A.2 Net forces acting on the centroid of each member

The distances z1, z2, and z3 are from the centroid of each laminate member to the y-axis. To find the centroid of each laminate, set $M_{x,i}=0$ and apply $N_{x,i}$ at the midplane of laminate 'i'. Equation A-1, which finds the strains about the midplane, is applied yielding,

$$\begin{aligned}\varepsilon_x^o &= a*N_x \\ k_x &= b*N_x\end{aligned}. \qquad \text{(A-2)}$$

Considering the strain about the centroid of the laminate, ε_x,

$$\begin{aligned}\varepsilon_x = 0 &= \varepsilon_x^o + \rho k_x \\ \rho &= -\varepsilon_x^o / k_x = -a_{11} / b_{11}\end{aligned}, \qquad \text{(A-3)}$$

where ρ is the distance from the midplane to the centroid for a laminate member.

Note that for this I-beam, there is symmetry about the z-axis. Thus, only the centroid in the z-direction needs to be determined, defined by Z_c. The centroid is found by taking a moment equilibrium about the y-axis as follows:

$$Z_c = \frac{\sum_{i=1}^{\text{f1,f2,w}} N_{x,i} \cdot b_i \cdot z_i}{\sum_{i=1}^{\text{f1,f2,w}} N_{x,i} \cdot b_i} = \frac{\bar{N}_x z_c}{\bar{N}_x} \tag{A-4}$$

where b_i is the width of each laminate (for the web (h_w), this is in the z-direction), and z_i is the distance from the bottom of the lower flange (y-axis) to the centroid of each laminate member as seen in Figure A.2.

The forces, $N_{x,i}$, can be written in terms of the strain and curvature using the ABD_i^* matrix in equation A-1. Note that the forces $N_{x,i}$ are applied to the centroid of each laminate thus there is no curvature about that individual laminate so $k_{x,i}^o = 0$, as shown in equation A-5. Expanding equation A-4 by subbing in equation A-5, Z_c is found in equation A-6.

$$N_{x,i} = A_{x,i}^* \varepsilon_{x,i}^o + B_{x,i}^* k_{x,i} = A_{x,i}^* \varepsilon_x^c \tag{A-5}$$

$$Z_c = \frac{\bar{N}_x z_c}{\bar{N}_x} = \frac{\varepsilon_x^c (A_{x,\text{f1}}^* b_{\text{f1}} z_1 + A_{x,\text{f2}}^* b_{\text{f2}} z_2 + A_{x,\text{w}}^* \text{h}_\text{w} z_\text{w})}{\varepsilon_x^c (A_{x,\text{f1}}^* b_{\text{f1}} + A_{x,\text{f2}}^* b_{\text{f2}} + A_{x,\text{w}}^* \text{h}_\text{w})} = \frac{A_{x,\text{f1}}^* b_{\text{f1}} z_1 + A_{x,\text{f2}}^* b_{\text{f2}} z_2 + A_{x,\text{w}}^* \text{h}_\text{w} z_w}{A_{x,\text{f1}}^* b_{\text{f1}} + A_{x,\text{f2}}^* b_{\text{f2}} + A_{x,\text{w}}^* \text{h}_\text{w}}. \tag{A-6}$$

Note that the centroid relative to the z-axis can also be obtained for unsymmetric I-beam geometries using a similar approach with Z_c. The resulting equation is:

$$Y_c = \frac{\bar{N}_x y_c}{\bar{N}_x} = \frac{A^*_{x,\mathrm{f1}} b_{\mathrm{f1}} y_1 + A^*_{x,\mathrm{f2}} b_{\mathrm{f2}} y_2 + A^*_{x,\mathrm{w}} \mathrm{h_w} y_w}{A^*_{x,\mathrm{f1}} b_{\mathrm{f1}} + A^*_{x,\mathrm{f2}} b_{\mathrm{f2}} + A^*_{x,\mathrm{w}} \mathrm{h_w}}. \quad \text{(A-7)}$$

EQUIVALENT STIFFNESS OF I-BEAM

Stiffness is important since stiffness can be used to derive the stress and strain of the material. Using the narrow beam assumption to relate stress to strain, an equivalent stiffness for the entire structure can be found. Stiffness or rigidity is a measure of a material's resistance to various deformations. A material exhibits axial, bending, shear and torsional stiffness depending on the loading condition. Here, only loads $\bar{N}_x, \bar{M}_x,$ and $\bar{M}_z$ are considered.

Axial stiffness of the entire structure, $\overline{EA}$, relates a pure axial load located at the centroid of the structure, $\bar{N}_x$, to axial strain that is produced. A pure axial load is placed at the structure's centroid where no moment is induced. Structural bending stiffnesses, $\bar{D}_x$ and $\bar{D}_z$, relate a pure moments, $\bar{M}_x$ or $\bar{M}_z$, with curvature in that direction. Structural bending coupling, $\bar{D}_{xz}$, is also considered.

Loads are shown in Figure A.3. The orientation of the moments using composite lamination theory is such that the resultant tensile stresses produced are on the positive side of the respective axis. For example, $\bar{M}_z$ is oriented in the negative z-direction since it produces a tensile stress in the positive y-direction. $\bar{M}_x$, which is in the positive direction about the y-axis, produces tensile loads in the positive z-direction.

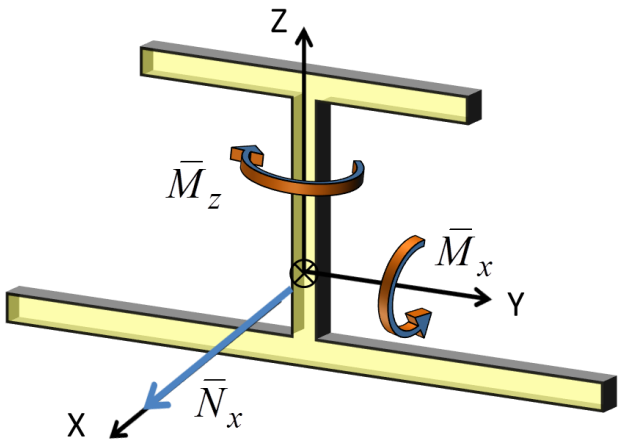

Figure A.3 Loads considered for structural stiffness

The governing equation for the structure relating the considered loads to strains and curvatures is:

$$\begin{Bmatrix} \bar{N}_x \\ \bar{M}_x \\ \bar{M}_z \end{Bmatrix} = \begin{bmatrix} \overline{EA} & 0 & 0 \\ 0 & \bar{D}_x & \bar{D}_{xz} \\ 0 & \bar{D}_{xz} & \bar{D}_z \end{bmatrix} \begin{Bmatrix} \varepsilon_x^c \\ k_x^c \\ k_z^c \end{Bmatrix}. \tag{A-8}$$

EQUIVALENT AXIAL STIFFNESS

The equivalent axial stiffness of an I-beam relates a centroid located axial load to axial strain. Only an axial load applied at the centroid is used to find the axial stiffness. Pure moments do not produce axial strains. The relationship was utilized in equation A-5 and is displayed again in equation A-9.

$$\begin{aligned} \bar{N}_x &= \varepsilon_x^c (A_{x,\mathrm{f1}}^* b_{\mathrm{f1}} + A_{x,\mathrm{f2}}^* b_{\mathrm{f2}} + A_{x,\mathrm{w}}^* \mathrm{h_w}) \\ \overline{EA} &= \frac{\bar{N}_x}{\varepsilon_x^c} = A_{x,\mathrm{f1}}^* b_{\mathrm{f1}} + A_{x,\mathrm{f2}}^* b_{\mathrm{f2}} + A_{x,\mathrm{w}}^* \mathrm{h_w} \end{aligned}. \tag{A-9}$$

EQUIVALENT BI-DIRECTIONAL BENDING STIFFNESS

From equation A-8, bending stiffness $\bar{D}_x$ can be written as follows,

$$\bar{M}_x = \bar{D}_x k_x^c + \bar{D}_{xz} k_z^c \approx \bar{D}_x k_x^c . \tag{A-10}$$

When $\bar{M}_x$ is applied, it is assumed that curvature about the z-axis, k_z^c, is very small as compared to curvature about the y-axis, k_x^c. Thus, k_z^c is assumed to be equal to zero in equation A-10. The goal from equation A-10 is to find a relationship between $\bar{M}_x$ and k_x^c in terms of material properties found in the ABD_i^* matrix to find the stiffnesses.

$\bar{M}_x$ is the resultant moment on the structure. This can be broken down into moments from each member about the y-axis passing. Thus, for each member, the total moment and normal force times moment arm to the centroid affects the moment about the centroid of the structure. Considering both $M_{x,i}$ and $N_{x,i}$ on only the flanges, the following equation can be obtained for the resultant moment about the I-beam centroid.

$$\bar{M}_{x,\mathrm{f1,f2}} = b_{\mathrm{f1}}\left(M_{x,\mathrm{f1}} + z_{1c} N_{x,\mathrm{f1}}\right) + b_{\mathrm{f2}}\left(M_{x,\mathrm{f2}} + z_{2c} N_{x,\mathrm{f2}}\right). \tag{A-11}$$

Now considering only the top flange member, using equation A-1 from Narrow Beam Theory, $M_{x,f1}$ and $N_{x,f1}$ can be written in terms of material properties and substituted in equation A-11 as follows,

$$\bar{M}_{x,\mathrm{f1}} = b_{\mathrm{f1}}\left(B_{\mathrm{f1}}^* \varepsilon_{x,\mathrm{f1}}^o + D_{\mathrm{f1}}^* k_{x,\mathrm{f1}} + z_{1c}\left(A_{\mathrm{f1}}^* \varepsilon_{x,\mathrm{f1}}^o + B_{\mathrm{f1}}^* k_{x,\mathrm{f1}}\right)\right). \tag{A-12}$$

(0-1)

where z_{1c} is the distance from the top flange centroid to the centroid of the I-beam as seen in Figure A-1.

Using Classical Lamination Theory, strain and curvature are related through a first order, or linear, warping. About the mid-plane of the top flange, this relationship is:

$$\varepsilon_{x,\mathrm{f1}}^{0} = \varepsilon_{x}^{c} + z_{1c}k_{x}^{c} + y_{1c}k_{z}^{c}. \tag{A-13}$$

where y_{1c} is the distance from the mid-width of the flange to the centroid of the I-beam as seen in Figure A-1. However, after applying only a resultant $M_{x,\mathrm{f1}}$ about the midplane of flange 1, there is no axial strain at the centroid of the I-beam, $\varepsilon_{x}^{c} = 0$. As stated above, curvature about the z-axis is neglected so $k_{z}^{c} = 0$. Note that curvature k_{x}^{c} is linear (in the y-direction) over the whole cross section. Applying these conditions to equation A-13,

$$\varepsilon_{x,\mathrm{f1}}^{0} = z_{1c}k_{x}^{c}. \tag{A-14}$$

and plugging into equation A-12,

$$\begin{aligned} \bar{M}_{x,\mathrm{f1}} &= b_{\mathrm{f1}}\left(B_{\mathrm{f1}}^{*}z_{1c}k_{x}^{c} + D_{\mathrm{f1}}^{*}k_{x}^{c} + z_{1c}\left(A_{\mathrm{f1}}^{*}z_{1c}k_{x}^{c} + B_{\mathrm{f1}}^{*}k_{x}^{c}\right)\right) \\ \bar{M}_{x,\mathrm{f1}} &= b_{\mathrm{f1}}k_{x}^{c}\left(A_{\mathrm{f1}}^{*}z_{1c}^{2} + 2B_{\mathrm{f1}}^{*}z_{1c} + D_{\mathrm{f1}}^{*}\right). \end{aligned} \tag{A-15}$$

Note that the term in the parentheses in equation A-15 is similar to the parallel axis theorem. This is true for a laminate that is aligned horizontally with the centroidal axes.

Similarily, for the bottom flange,

$$\bar{M}_{x,\mathrm{f2}} = b_{\mathrm{f2}} k_x^c \left(A_{\mathrm{f2}}^* z_{2c}^2 + 2B_{\mathrm{f2}}^* z_{2c} + D_{\mathrm{f2}}^* \right). \tag{A-16}$$

Bending of the web, $\bar{M}_{x,\mathrm{w}}$, only considers the normal force, $N_{x,\mathrm{w}}$, acting on the centroid of the web. The normal force on the web though is treated as a distributed load along the length of the web in equation A-17.

$$\bar{M}_{x,\mathrm{w}} = \int_{-\mathrm{h_w}/2+\mathrm{h_{wc}}}^{\mathrm{h_w}/2+\mathrm{h_{wc}}} z \cdot N_{x,\mathrm{w}} dz \,. \tag{A-17}$$

The limits on the integral represent the moment arms of $N_{x,\mathrm{w}}$ about the centroid of the I-beam. Figure A-4 illustrates these moment arms.

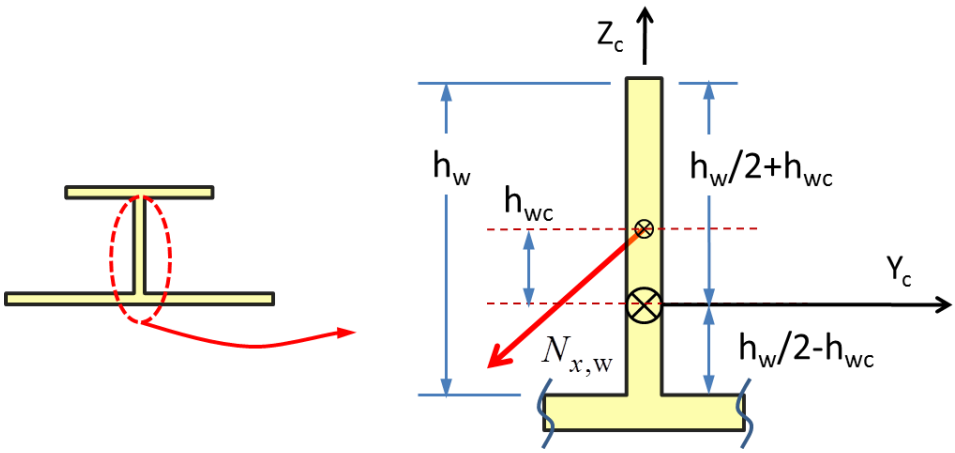

Figure A.4 Moment arms for web normal force $N_{x,\mathrm{w}}$ about I-beam centroid

Integrating and converting $N_{x,\mathrm{w}}$ to strain and curvature using the ABD_w^* matrix shown in equation A-1, the following equation is obtained.

$$\bar{M}_{x,\mathrm{w}} = A_{\mathrm{w}}^* \left(\mathrm{h_w^3}/_{12} + \mathrm{h_w h_{wc}^2} \right) k_x^c \,. \tag{A-18}$$

Summing up equations A-15, A-16, and A-18, the total moment, $\bar{M}_x$, about the I-beam centroid is:

$$\bar{M}_x = \left[\begin{array}{c} b_{\mathrm{f1}}\left(A^*_{\mathrm{f1}} z^2_{1c} + 2B^*_{\mathrm{f1}} z_{1c} + D^*_{\mathrm{f1}} \right) + b_{\mathrm{f2}}\left(A^*_{\mathrm{f2}} z^2_{2c} + 2B^*_{\mathrm{f2}} z_{2c} + D^*_{\mathrm{f2}} \right) \\ + A^*_{\mathrm{w}}\left(\mathrm{h}^3_{\mathrm{w}} \big/ 12 + \mathrm{h}_{\mathrm{w}} \mathrm{h}^2_{\mathrm{wc}} \right) \end{array} \right] k^c_x . \qquad \text{(A-19)}$$

Applying equation A-10, the bending stiffness $\bar{D}_x$ is found to be:

$$\begin{array}{c} \bar{D}_x = b_{\mathrm{f1}}\left(A^*_{\mathrm{f1}} z^2_{1c} + 2B^*_{\mathrm{f1}} z_{1c} + D^*_{\mathrm{f1}} \right) \\ + b_{\mathrm{f2}}\left(A^*_{\mathrm{f2}} z^2_{2c} + 2B^*_{\mathrm{f2}} z_{2c} + D^*_{\mathrm{f2}} \right) + A^*_{\mathrm{w}}\left(\mathrm{h}^3_{\mathrm{w}} \big/ 12 + \mathrm{h}_{\mathrm{w}} \mathrm{h}^2_{\mathrm{wc}} \right) \end{array} . \qquad \text{(A-20)}$$

Bending stiffness about the z-axis, $\bar{D}_z$, is found in a similar manner by applying $M_{z,i}$ and $N_{x,i}$ at each member and finding the resultant moment, $\bar{M}_z$. The resulting equation is shown below.

$$\begin{array}{c} \bar{D}_z = \dfrac{\bar{M}_z}{k^c_z} = A^*_{\mathrm{f1}}\left(b^3_{\mathrm{f1}} \big/ 12 + b_{\mathrm{f1}} y^2_{1c} \right) + A^*_{\mathrm{f2}}\left(b^3_{\mathrm{f2}} \big/ 12 + b_{\mathrm{f2}} y^2_{2c} \right) . \\ + \mathrm{h}_{\mathrm{w}}\left(A^*_{\mathrm{w}} y^2_{\mathrm{wc}} + 2B^*_{\mathrm{w}} y_{\mathrm{wc}} + D^*_{\mathrm{w}} \right) \end{array} \qquad \text{(A-21)}$$

EQUIVALENT BENDING STIFFNESS, $\bar{D}_{xz}$

$\bar{D}_{xz}$ is the coupling between moments in the *x* and *z* direction. Equation A-8 can be used to derive $\bar{D}_{xz}$ starting with:

$$\bar{D}_{xz} = \frac{\bar{M}_x - \bar{D}_x k_x^c}{k_z^c}, \tag{A-22}$$

$$\bar{D}_{xz} = b_{f1}\left(A_{f1}^* z_{f1} + B_{f1}^*\right) y_{f1} + b_{f2}\left(A_{f2}^* z_{f2} + B_{f2}^*\right) y_{f2} + \left(A_w^* y_w + B_w^*\right) h_w z_w . \tag{A-23}$$

STRAINS AND STRESSES

Once the stiffness components of the I-beam are known, the strain and curvature at the I-beam's centroid can be found using equation A-8 as follows:

$$\begin{Bmatrix} \varepsilon_x^c \\ k_x^c \\ k_z^c \end{Bmatrix} = \begin{bmatrix} \overline{EA} & 0 & 0 \\ 0 & \bar{D}_x & \bar{D}_{xz} \\ 0 & \bar{D}_{xz} & \bar{D}_z \end{bmatrix}^{-1} \begin{Bmatrix} \bar{N}_x^{total} \\ \bar{M}_x^{total} \\ \bar{M}_z^{total} \end{Bmatrix} \text{ where}$$

$$\begin{Bmatrix} \bar{N}_x^{total} \\ \bar{M}_x^{total} \\ \bar{M}_z^{total} \end{Bmatrix} = \begin{Bmatrix} \overline{N}_x + \overline{N}_x^T + \overline{N}_x^H \\ \overline{M}_x + \overline{M}_x^T + \overline{M}_x^H \\ \overline{M}_z + \overline{M}_z^T + \overline{M}_z^H \end{Bmatrix}. \tag{A-24}$$

The force and moments are actually summations of the mechanical and hygrothermal loads on the structure thus the superscript '$total$'. Note, the bar represents something applied to the whole structure. For example, in the case of the thermal load on the structure in the x-direction, $\overline{N}_x^T = N_{x,f1}^T + N_{x,f2}^T + N_{x,w}^T$.

The superscript 'T' indicates thermally induced loads and 'H' indicates hygroscopic or moisture induced loads. Thermally induced loads occur when there is a temperature difference (dT) between the service temperature and the stress free temperature which for composites is slightly less than the curing temperature.

Hygroscopic induced loads are caused by moisture absorption after the curing process (dC) which causes the composite to expand. Thus, the strain and curvature at the centroid of the I-beam represents the deformation due to the combined mechanical and hygrothermal loading. However, provided that the structure is free to deform, the hygrothermal loads do not cause additional stress due to hygrothermal induced deformation. Hygrothermal loads do induce stresses within the laminate caused by adjacent ply hygrothermal expansion differences.

The structural strain and curvature can then be translated to each laminate member. First, the axial strain in the x-direction of each laminate is found using,

$$\varepsilon_{x,i}^{o} = \varepsilon_{x}^{c} + z_{i,c}k_{x}^{c} + y_{i,c}k_{z}^{c} . \qquad \text{(A-25)}$$

For the case of a geometrically symmetric I-beam, $y_{i,c} = 0$. Since curvature is assumed to be linear, $k_{i,x} = k_{x}^{c}$ for each laminate member. Also, it is assumed that twisting curvature is negligible, thus $k_{i,xy} = 0$. This is assumed because the web supports the flanges and inhibits twisting of the I-beam. Equation A-25 applies to laminates in structures that are horizontally oriented as the case with the two flanges of an I-beam. The web of the I-beam however is vertically oriented and requires switching $z_{w,c}$ with $y_{w,c}$ in equation A-25. Thus, the mid-plane strain, curvature, and loads on each laminate of the symmetric I-beam structure can be found using,

$$\begin{Bmatrix} \varepsilon_x^o \\ \varepsilon_y^o \\ \gamma_{xy}^o \\ k_x \\ k_y \\ k_{xy} \end{Bmatrix}_i = \begin{Bmatrix} \boldsymbol{\varepsilon_x^o} \\ \varepsilon_y^o \\ \gamma_{xy}^o \\ \boldsymbol{k_x^c} \\ k_y \\ \mathbf{0} \end{Bmatrix}_i = \begin{bmatrix} a_{11} & b_{11} & b_{16} \\ a_{12} & b_{21} & b_{26} \\ a_{16} & b_{61} & b_{66} \\ b_{11} & d_{11} & d_{16} \\ b_{12} & d_{12} & d_{26} \\ b_{16} & d_{16} & d_{66} \end{bmatrix}_i \begin{Bmatrix} N_x \\ M_x \\ M_{xz} \end{Bmatrix}_i , \tag{A-26}$$

where the bolded variables, $\varepsilon_{x,i}^o, k_x^c, k_{xy,i}$, are known values and i= f1,f2, and w (top flange, bottom flange, and web). Thus, there are six equations and six unknowns so the unknowns can be solved for.

Strains on the surface of each ply of each laminate member can be found using,

$$\begin{Bmatrix} \varepsilon_{x,i} \\ \varepsilon_{y,i} \\ \gamma_{xy,i} \end{Bmatrix}_k = \begin{Bmatrix} \varepsilon_{x,i}^o \\ \varepsilon_{y,i}^o \\ \gamma_{xy,i}^o \end{Bmatrix} + z \begin{Bmatrix} k_{x,i} \\ k_{y,i} \\ k_{xy,i} \end{Bmatrix}. \tag{A-27}$$

Stresses in the global direction (x-y) at each ply surface can also be found using,

$$\begin{Bmatrix} \sigma_{x,i} \\ \sigma_{y,i} \\ \tau_{xy,i} \end{Bmatrix}_k = \left[\overline{Q}_{x-y}\right]_k \begin{Bmatrix} \varepsilon_{x,i} - \alpha'_{x,i} \cdot \Delta T - \beta'_{x,i} \cdot \Delta C \\ \varepsilon_{y,i} - \alpha'_{y,i} \cdot \Delta T - \beta'_{y,i} \cdot \Delta C \\ \gamma_{xy,i} - \alpha'_{xy,i} \cdot \Delta T - \beta'_{xy,i} \cdot \Delta C \end{Bmatrix}_k . \tag{A-28}$$

The CTE and CHE's come from the Modified Method, equations 2-49. The hygrothermal effects are subtracted from the strains at each ply surface since these strains are due to both mechanical and hygrothermal loads. In effect, if there are no mechanical loads, hygrothermal effects would cause ply stresses based on the

difference between the structural deformation minus the hygrothermal expansion at that point in the laminate. These equations find strains and stresses at the ply surface only.

Stress can then be found in the material direction (1-2) as follows,

$$\begin{Bmatrix} \sigma_1 \\ \sigma_2 \\ \tau_{12} \end{Bmatrix}_{i,k} = \left[T_\sigma(\theta_i)\right]_k \cdot \begin{Bmatrix} \sigma_x \\ \sigma_y \\ \tau_{xy} \end{Bmatrix}_{i,k} . \tag{A-29}$$

APPENDIX B

STRESS PLOTS OF I-BEAM MODELS

The following plots are the stress plots of all I-beam cases studied with a length of 6 inches. In all plots, the solid stress curves are from the FEA analysis and the dotted stress curves are from Narrow Beam Theory. Note that theses plots use the term "Modified" which refers to the NBT. There are 3 columns in each plot to show the stress in each I-beam member, from top flange, web, and bottom flange. The 3 rows in each plot are the principal material stresses starting with σ_1, then σ_2, and τ_{12}. Note that the stress range on the y-axis varies for each member. The x-axis shows the width of the corresponding member. For the web, the x-axis is zero at the bottom flange interface and increases to the top flange interface.

The legend gives a unique color to each ply angle used in the laminate member. Note that the ply angle often occurs more than once in a layup such as for $[\pm 45/0/90]_S$ and there are separate curves for each layer. However, these plots do not distinguish which ply a certain curve is from. In many cases, the stress from one angle ply is very similar to the stress of the same ply angle but at a different height in the layup.

The title to the left indicates the load (F_x, M_x, M_z, and $F_x M_x M_z$), I-beam model, tall (L112) or short (L1052) model, the aspect ratio for width to thickness (i.e. A20) and length to thickness (i.e. R25), and the constraint type for the load. The loads used are F_x = 1 lb, M_x = 1 lb-in, and M_z = 1 lb-in.

The plots are grouped first by web height (tall then short model), then by constraint (CERIG then RBE3), then by load (F_x, M_x, M_z, and $F_x M_x M_z$), and finally by layup type (sym&bal, unsym&bal, sym&unbal, and unsym&unbal).

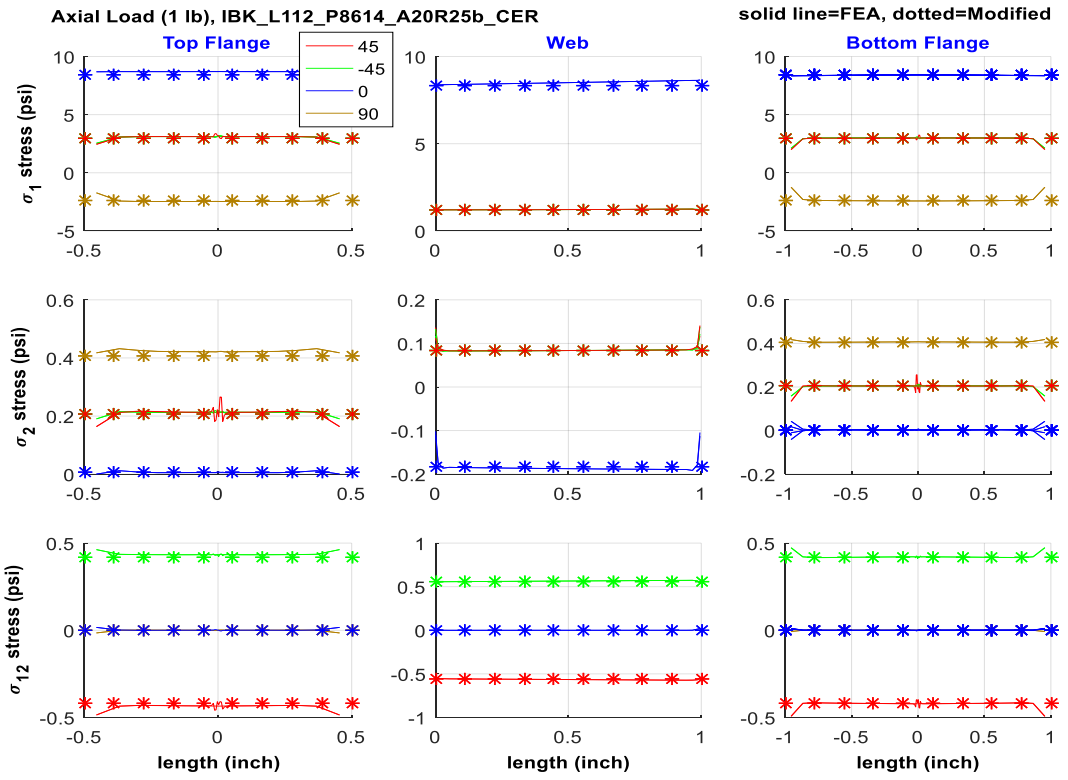
Axial Load (1 lb), IBK_L112_P8614_A20R25b_CER
solid line=FEA, dotted=Modified
Top Flange
Web
Bottom Flange
45
-45
0
90
σ1 stress (psi)
σ2 stress (psi)
σ12 stress (psi)
length (inch)

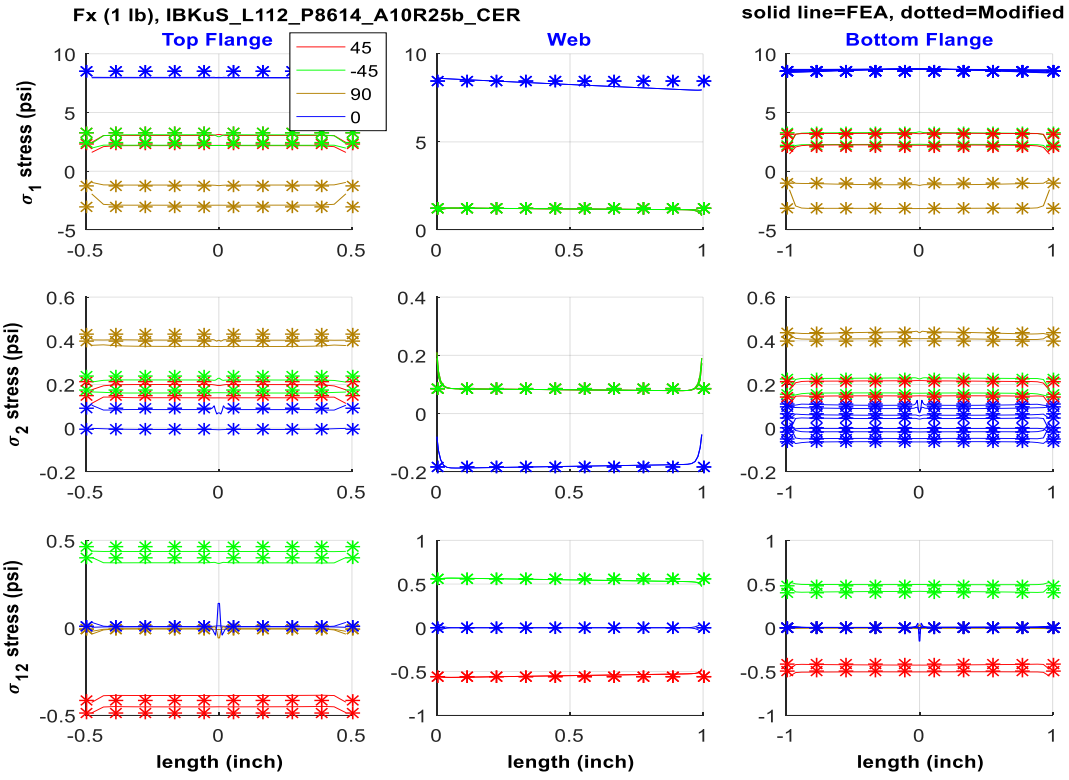
Fx (1 lb), IBKuS_L112_P8614_A10R25b_CER
solid line=FEA, dotted=Modified
Top Flange
Web
Bottom Flange
45
-45
90
0
σ1 stress (psi)
σ2 stress (psi)
σ12 stress (psi)
length (inch)

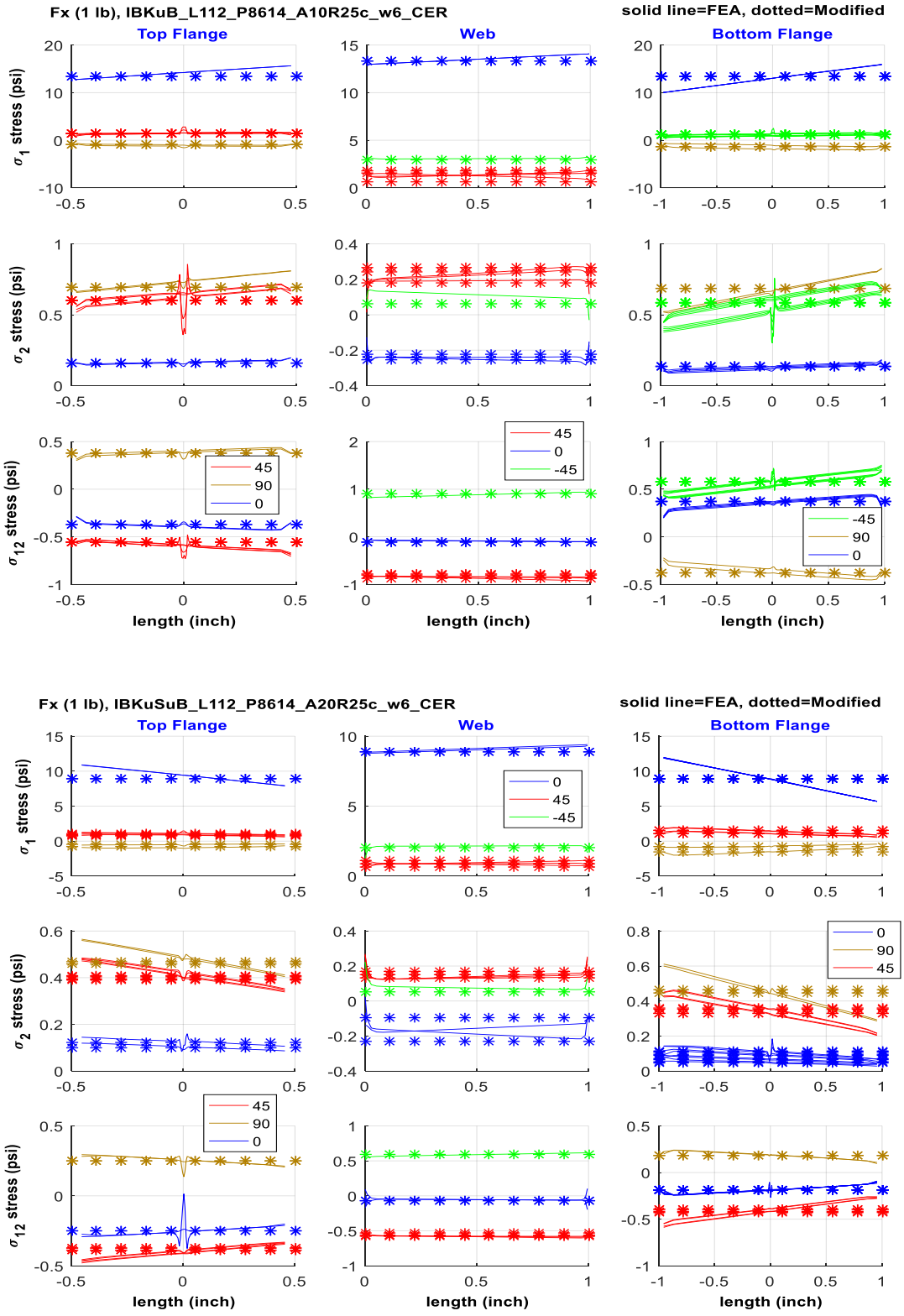

Figure B.1 Stress plots of tall, CERIG model under axial load

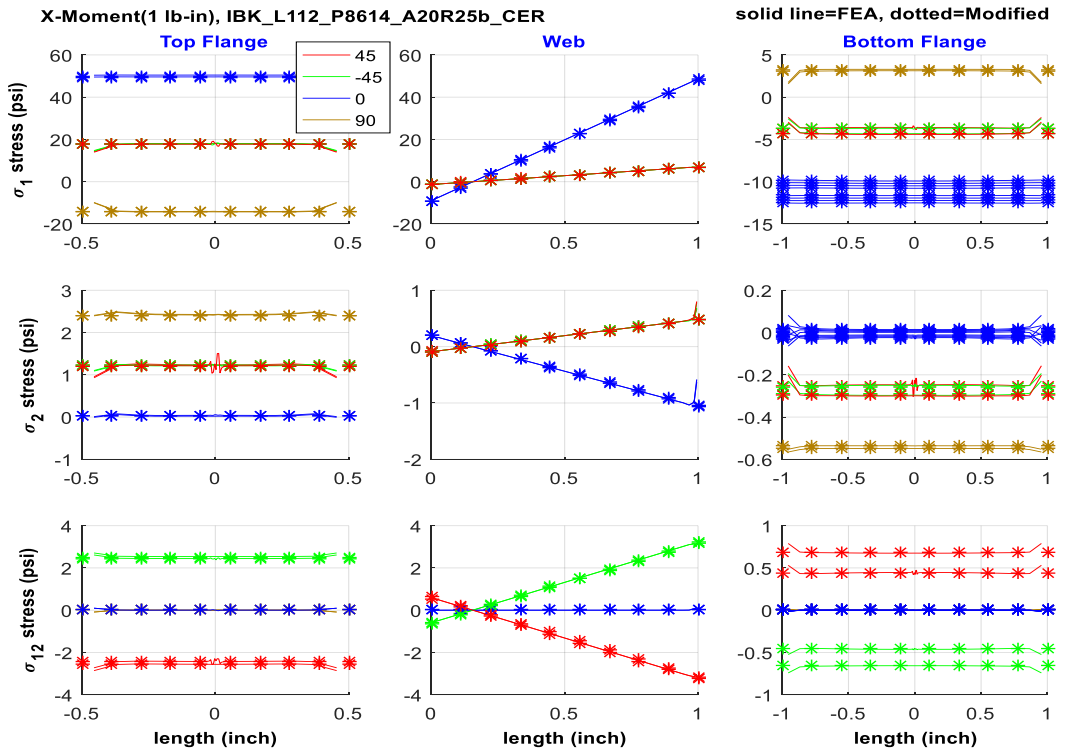
X-Moment(1 lb-in), IBK_L112_P8614_A20R25b_CER
solid line=FEA, dotted=Modified
Top Flange
Web
Bottom Flange
45
-45
0
90
σ1 stress (psi)
σ2 stress (psi)
σ12 stress (psi)
length (inch)

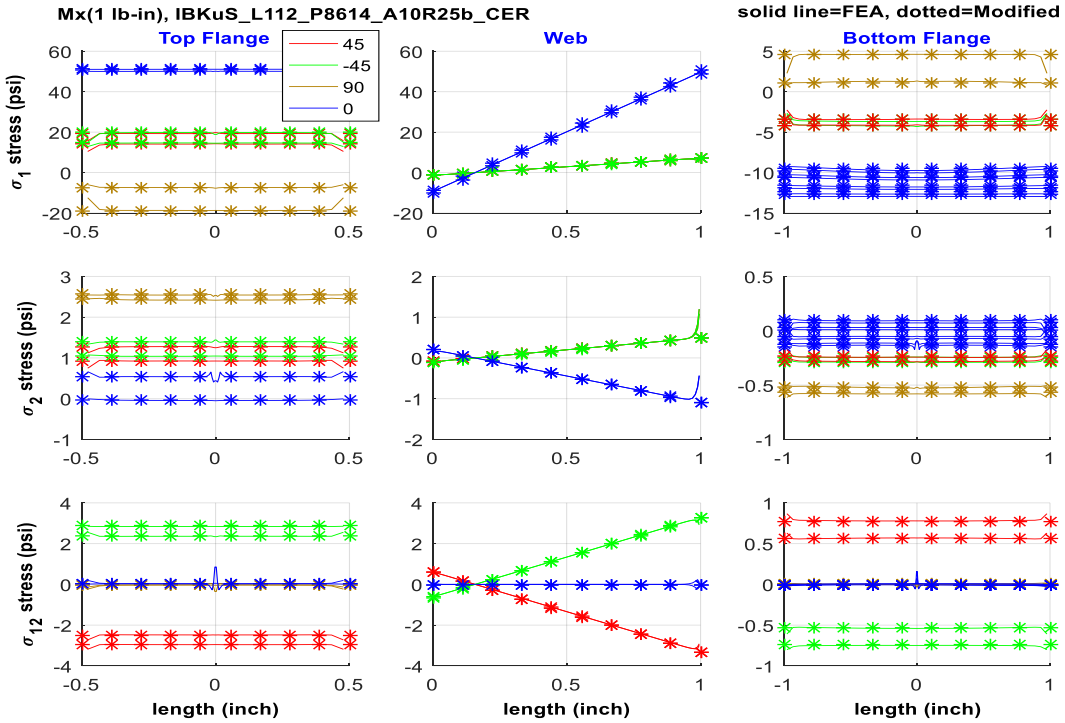
Mx(1 lb-in), IBKuS_L112_P8614_A10R25b_CER
solid line=FEA, dotted=Modified
Top Flange
Web
Bottom Flange
45
-45
90
0
σ1 stress (psi)
σ2 stress (psi)
σ12 stress (psi)
length (inch)

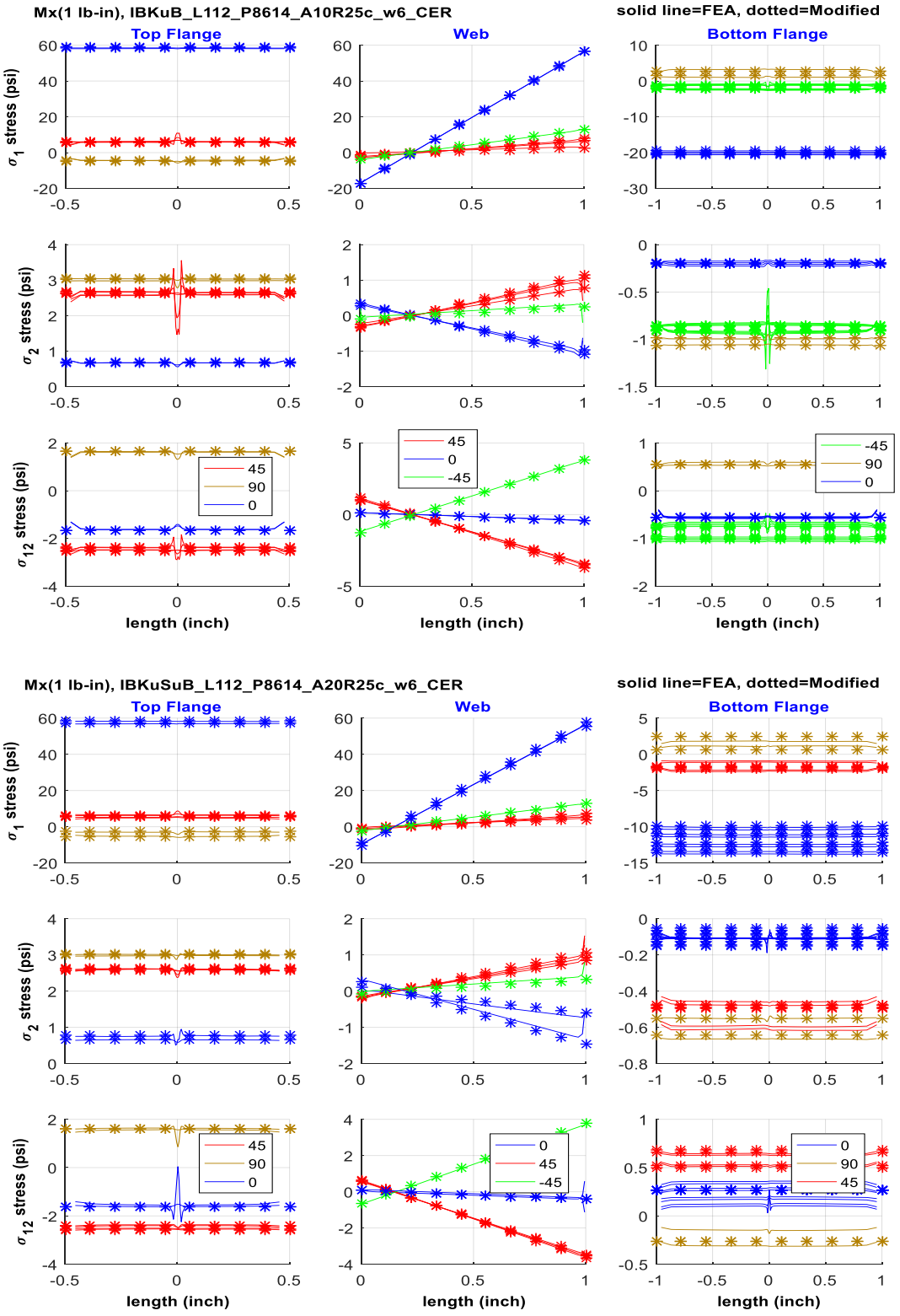

Figure B.2 Stress plots of tall, CERIG model under M_x load

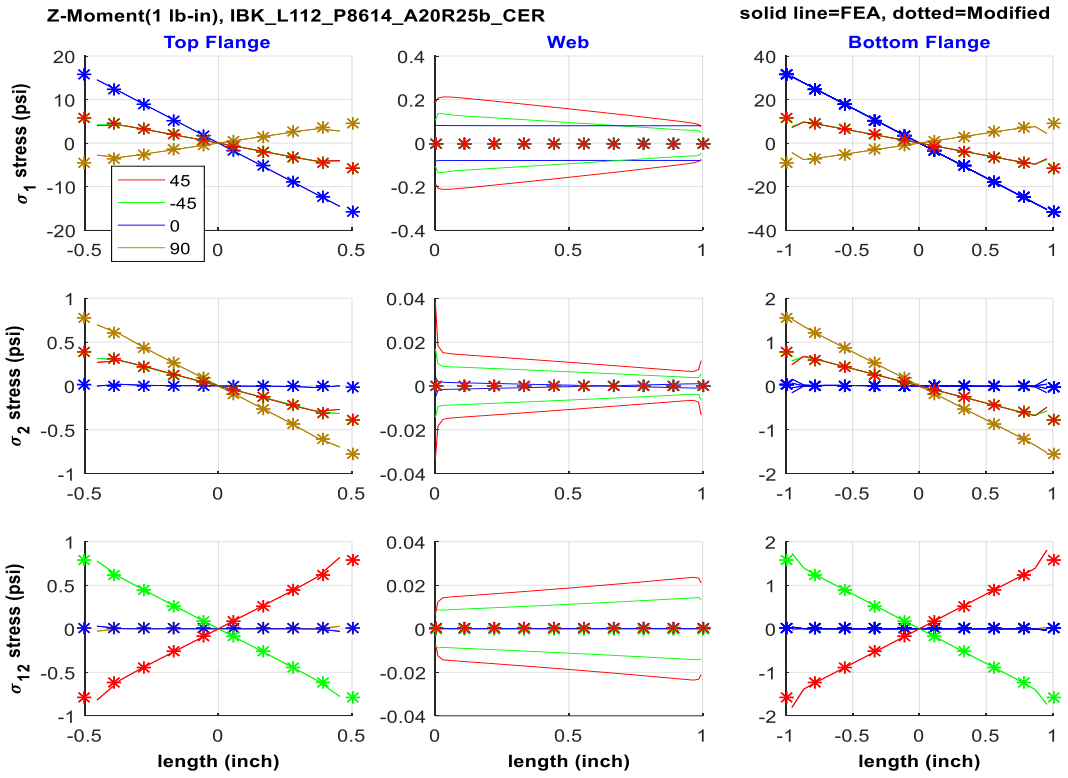
Z-Moment(1 lb-in), IBK_L112_P8614_A20R25b_CER
solid line=FEA, dotted=Modified
Top Flange
Web
Bottom Flange
σ1 stress (psi)
σ2 stress (psi)
σ12 stress (psi)
45
-45
0
90
length (inch)

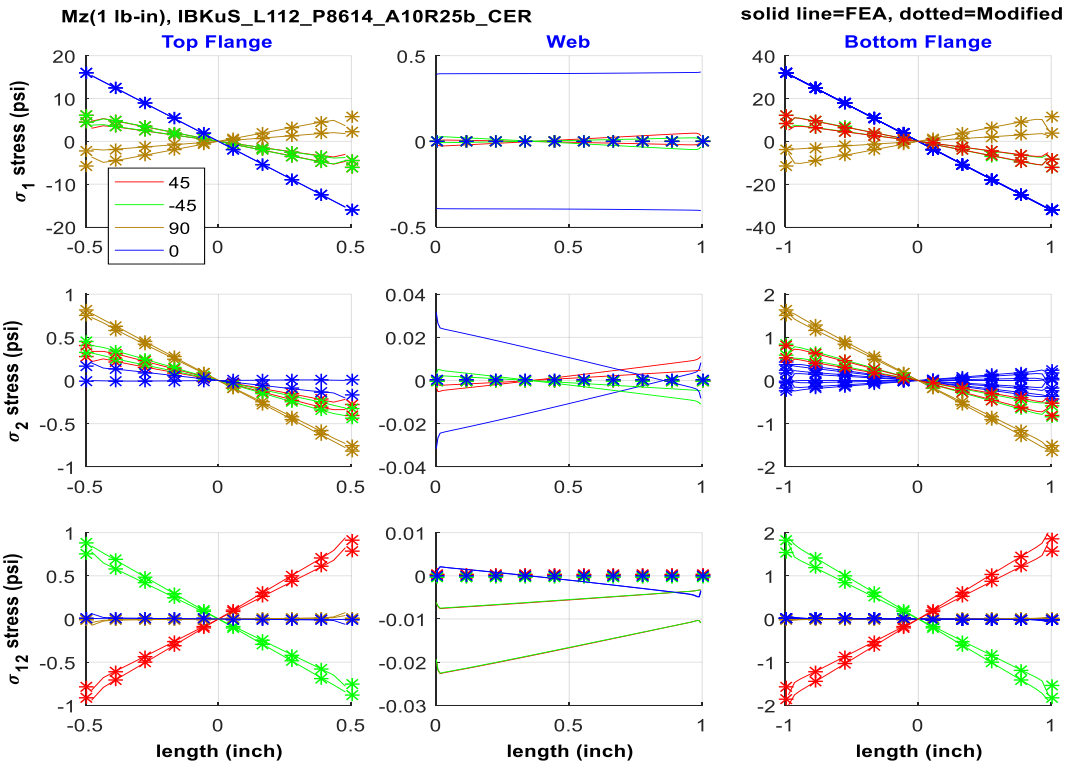
Mz(1 lb-in), IBKuS_L112_P8614_A10R25b_CER
solid line=FEA, dotted=Modified
Top Flange
Web
Bottom Flange
σ1 stress (psi)
σ2 stress (psi)
σ12 stress (psi)
45
-45
90
0
length (inch)

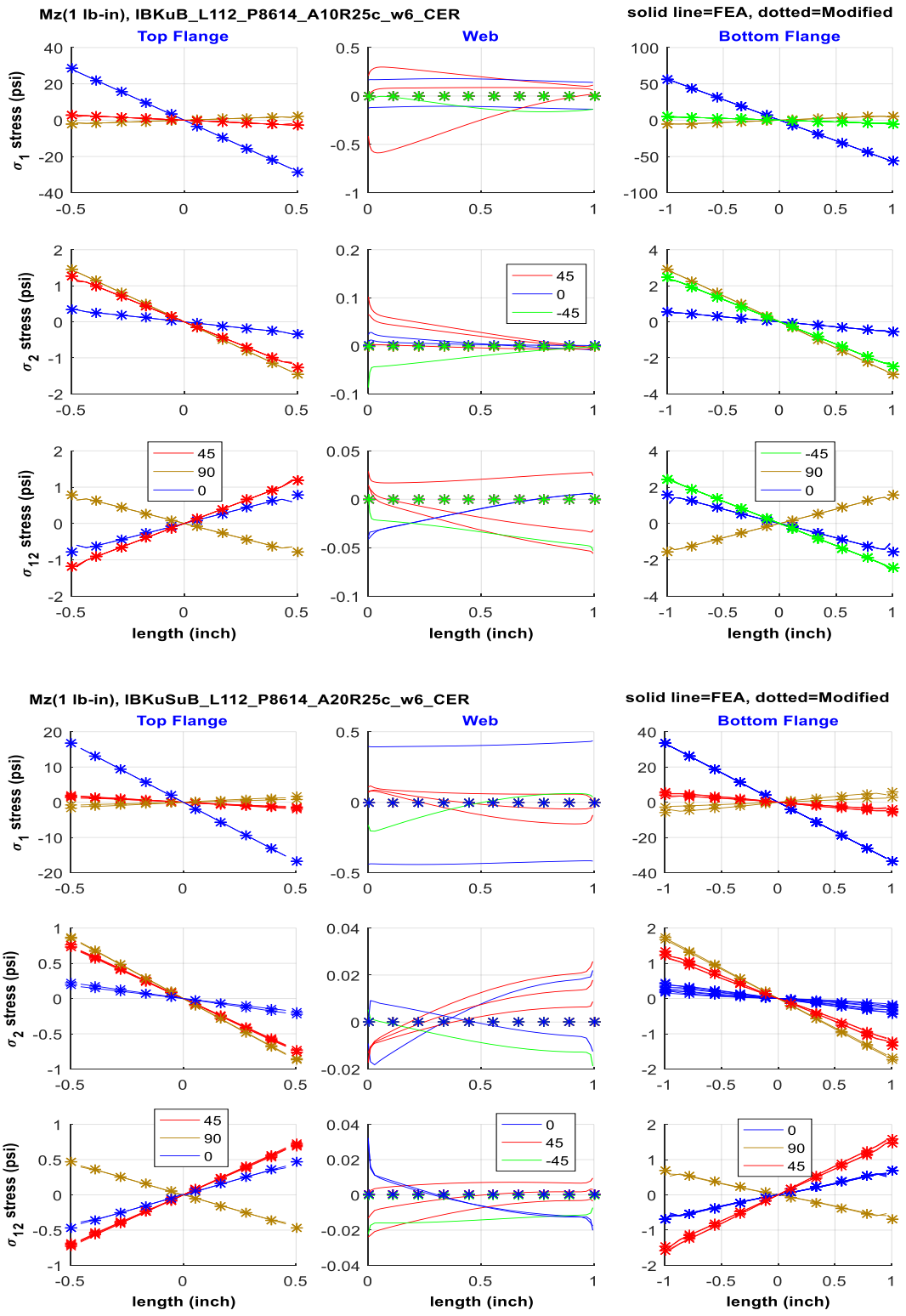

Figure B.3 Stress plots of tall, CERIG model under M_z load

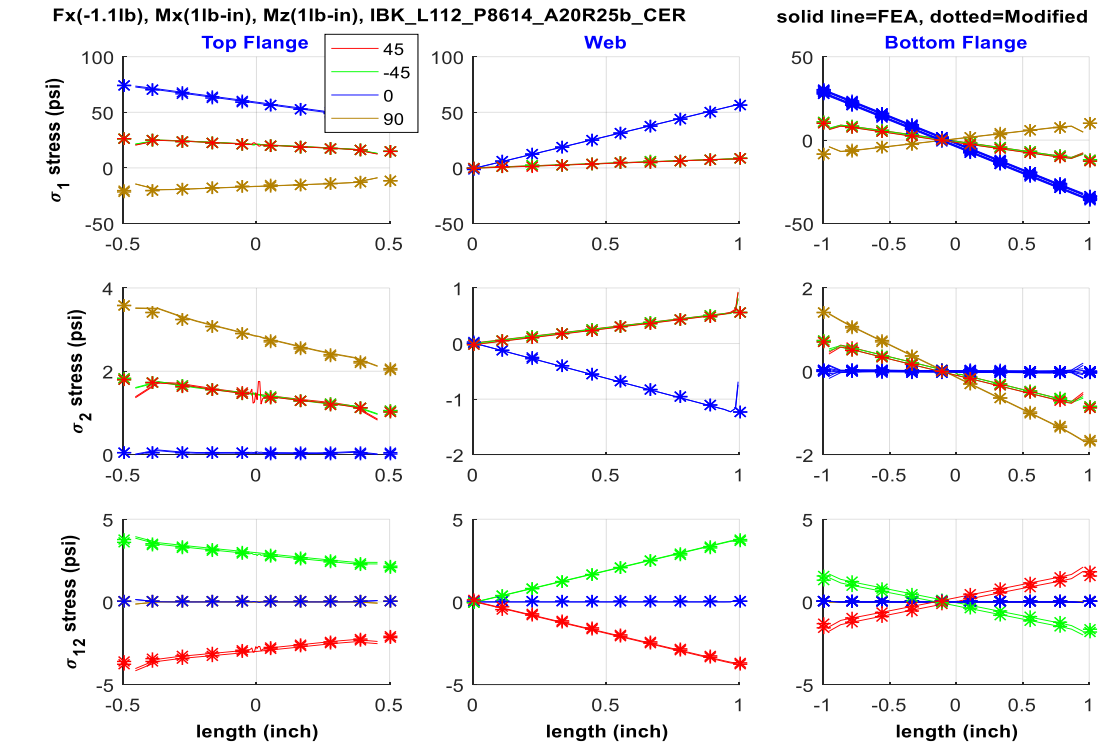
Fx(-1.1lb), Mx(1lb-in), Mz(1lb-in), IBK_L112_P8614_A20R25b_CER
solid line=FEA, dotted=Modified
Top Flange
Web
Bottom Flange
45
-45
0
90
σ1 stress (psi)
σ2 stress (psi)
σ12 stress (psi)
length (inch)

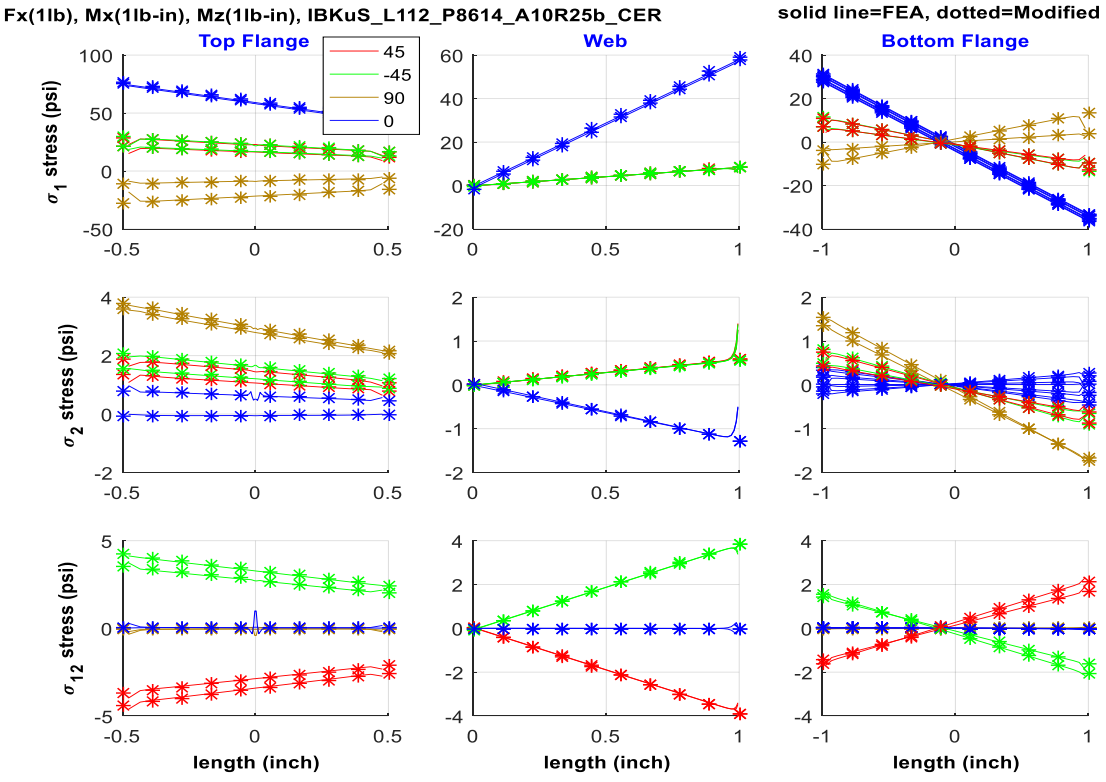
Fx(1lb), Mx(1lb-in), Mz(1lb-in), IBKuS_L112_P8614_A10R25b_CER
solid line=FEA, dotted=Modified
Top Flange
Web
Bottom Flange
45
-45
90
0
σ1 stress (psi)
σ2 stress (psi)
σ12 stress (psi)
length (inch)

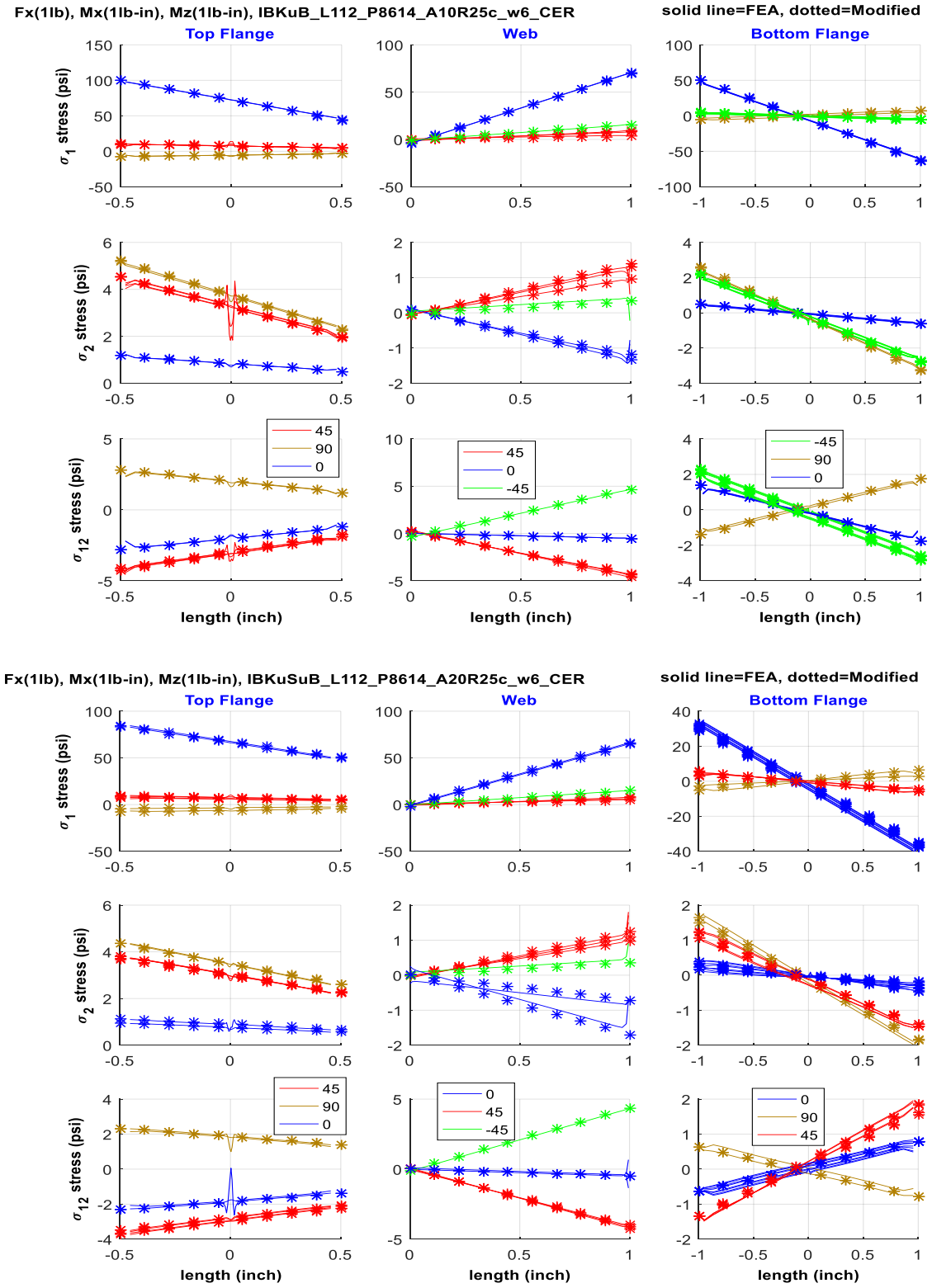

Figure B.4 Stress plots of tall, CERIG model under combined load

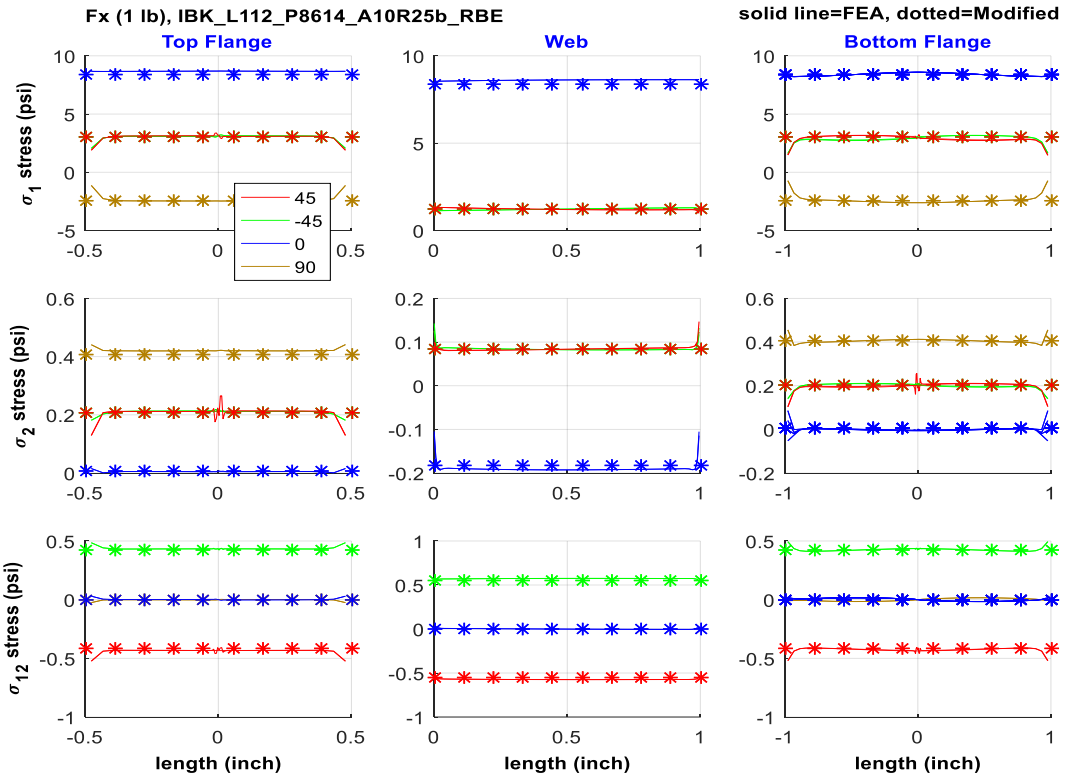
Fx (1 lb), IBK_L112_P8614_A10R25b_RBE
solid line=FEA, dotted=Modified
Top Flange
Web
Bottom Flange
σ1 stress (psi)
σ2 stress (psi)
σ12 stress (psi)
45
-45
0
90
length (inch)

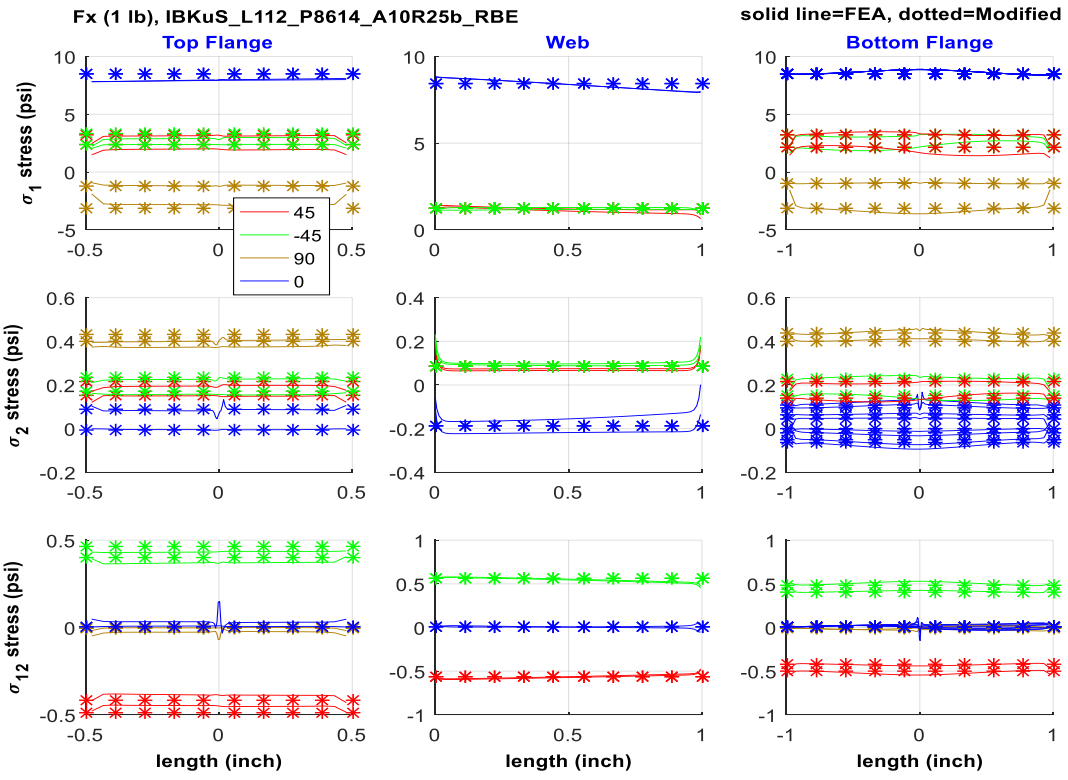
Fx (1 lb), IBKuS_L112_P8614_A10R25b_RBE
solid line=FEA, dotted=Modified
Top Flange
Web
Bottom Flange
σ1 stress (psi)
σ2 stress (psi)
σ12 stress (psi)
45
-45
90
0
length (inch)

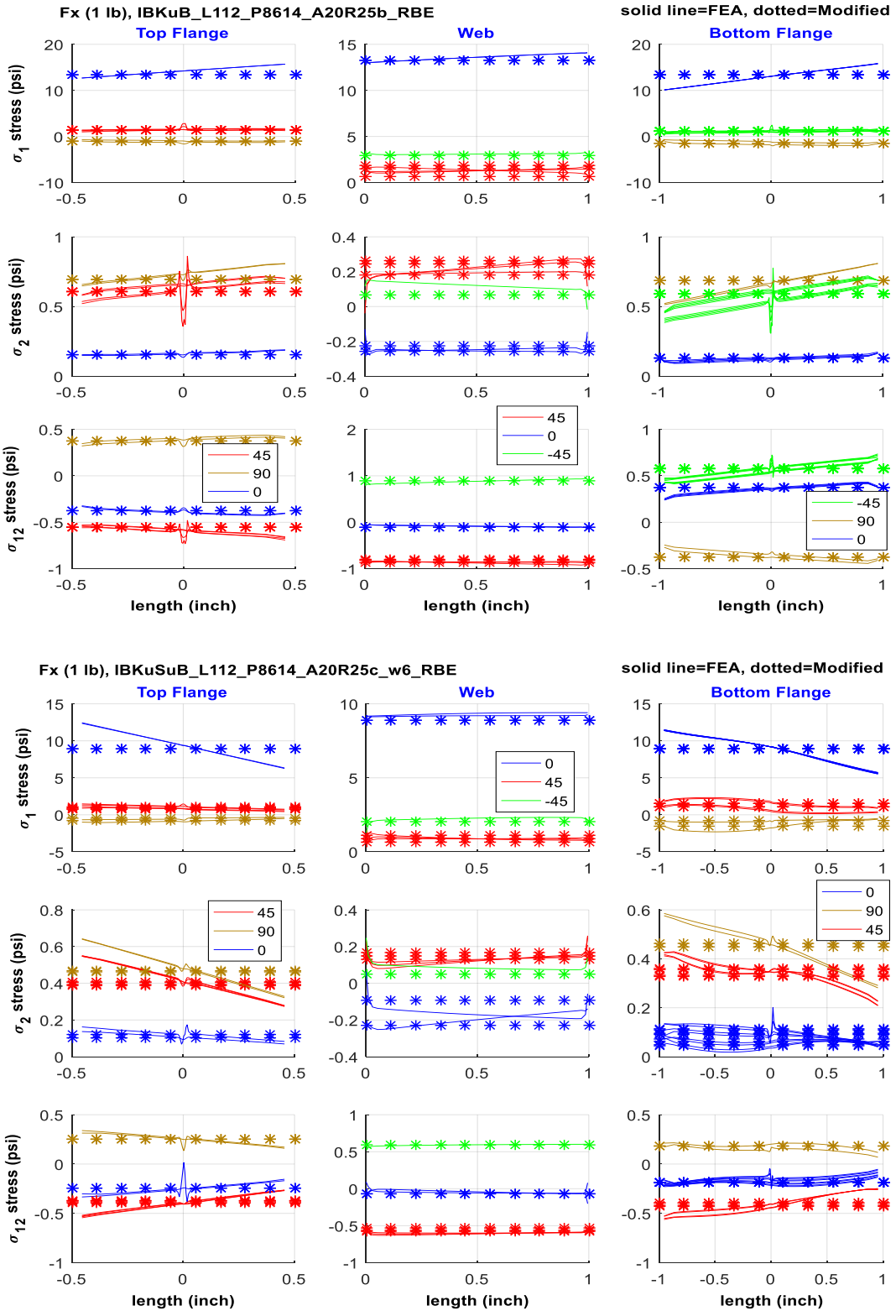

Figure B.5 Stress plots of tall, RBE3 model under axial load

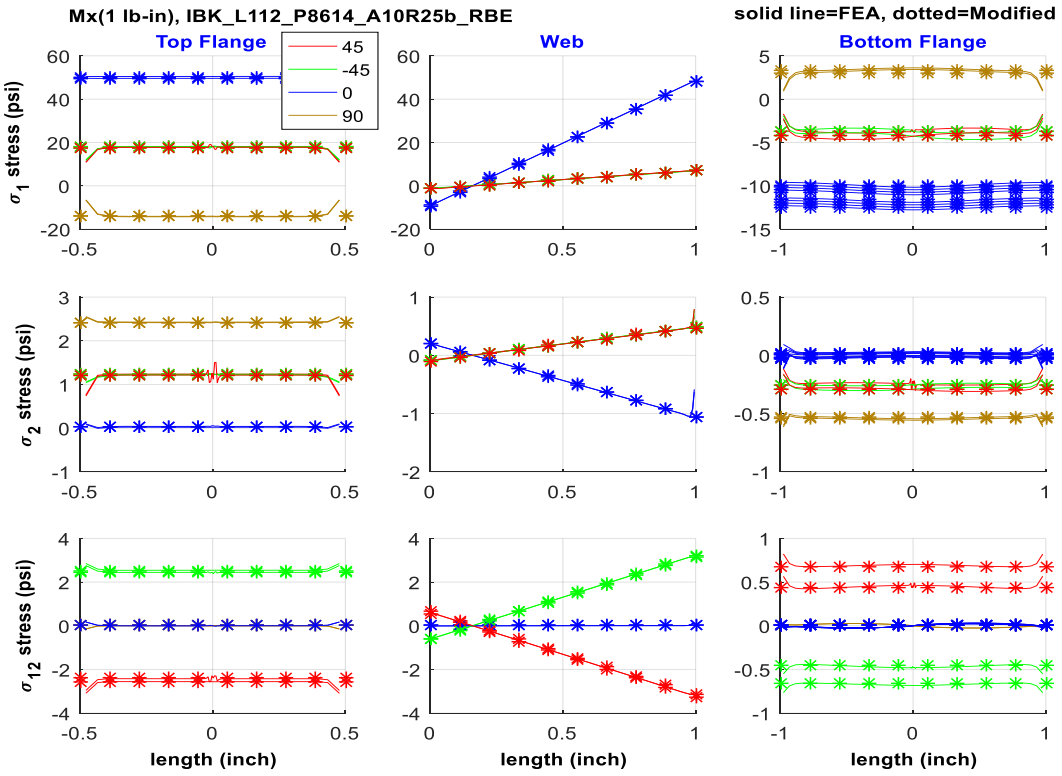
Mx(1 lb-in), IBK_L112_P8614_A10R25b_RBE
solid line=FEA, dotted=Modified
Top Flange
Web
Bottom Flange
45
-45
0
90
σ1 stress (psi)
σ2 stress (psi)
σ12 stress (psi)
length (inch)
length (inch)
length (inch)

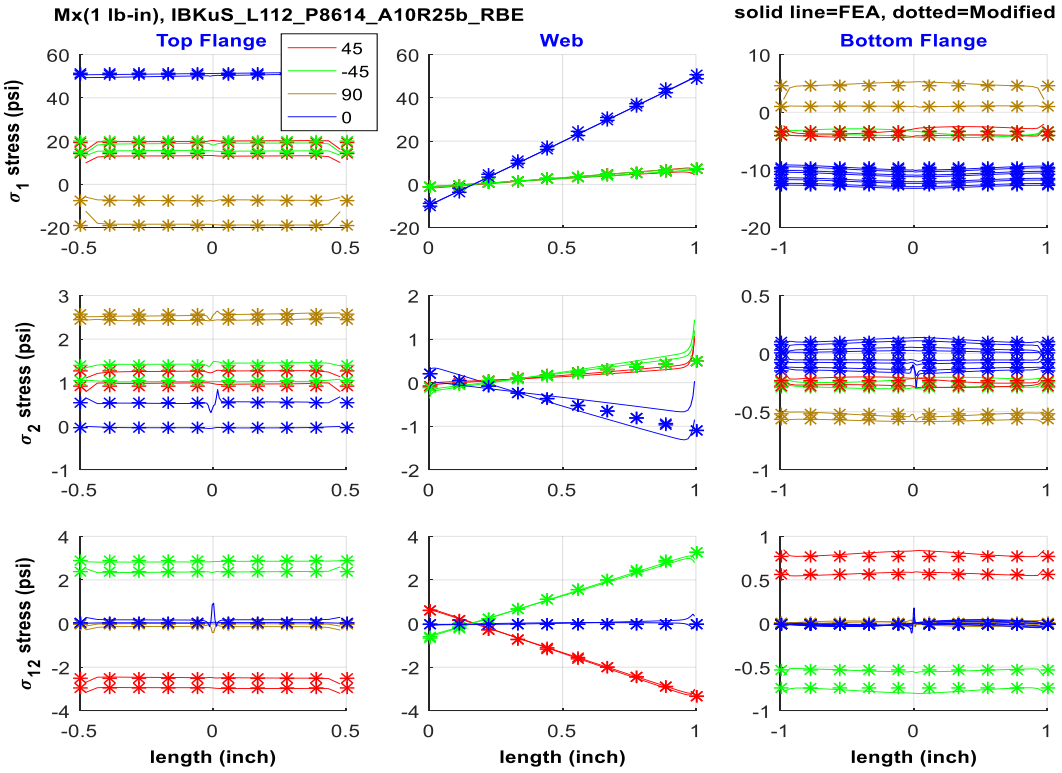
Mx(1 lb-in), IBKuS_L112_P8614_A10R25b_RBE
solid line=FEA, dotted=Modified
Top Flange
Web
Bottom Flange
45
-45
90
0
σ1 stress (psi)
σ2 stress (psi)
σ12 stress (psi)
length (inch)
length (inch)
length (inch)

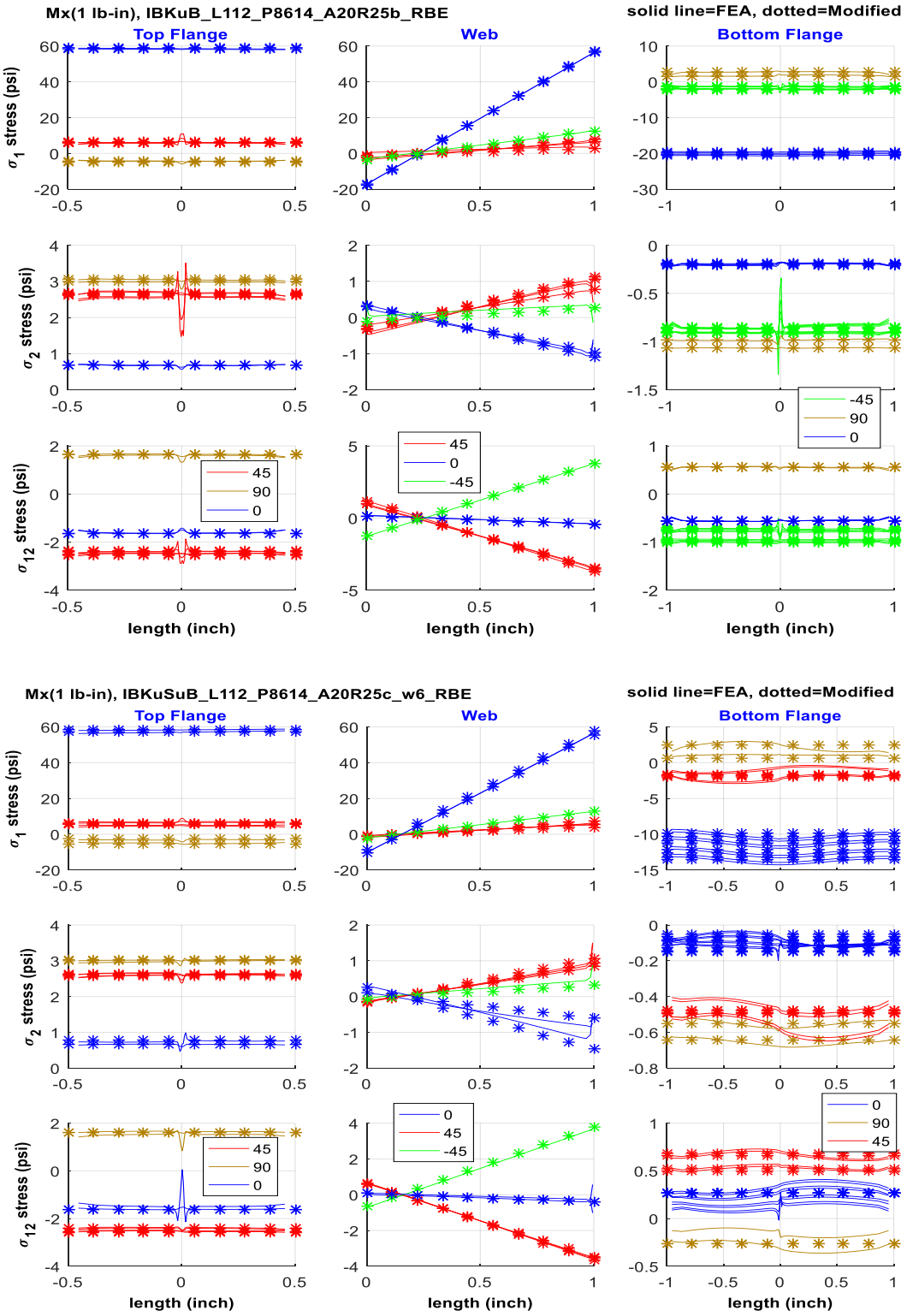

Figure B.6 Stress plots of tall, RBE3 model under M_x load

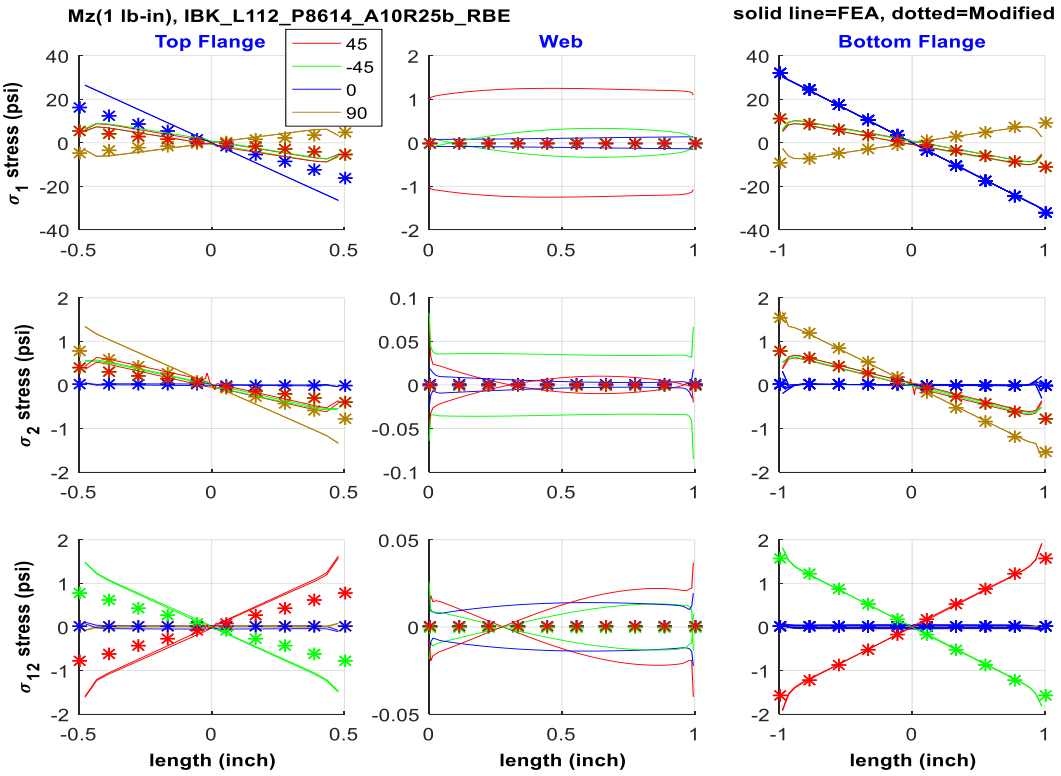
Mz(1 lb-in), IBK_L112_P8614_A10R25b_RBE
solid line=FEA, dotted=Modified
Top Flange
Web
Bottom Flange
45
-45
0
90
σ1 stress (psi)
σ2 stress (psi)
σ12 stress (psi)
length (inch)

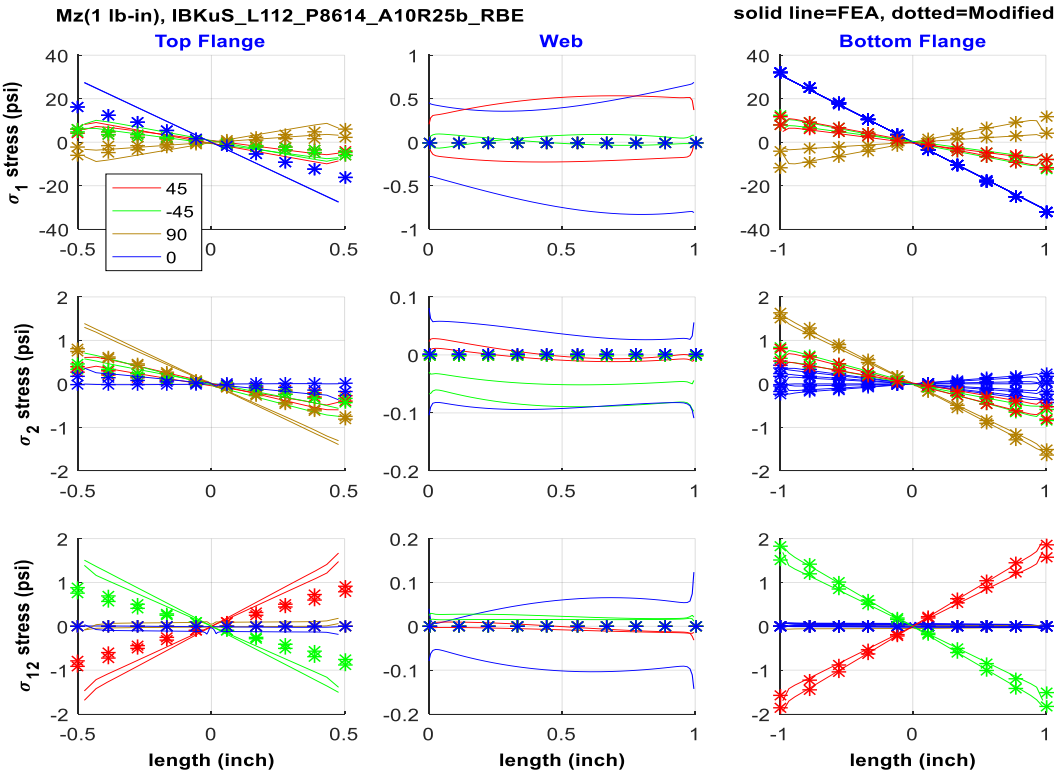
Mz(1 lb-in), IBKuS_L112_P8614_A10R25b_RBE
solid line=FEA, dotted=Modified
Top Flange
Web
Bottom Flange
45
-45
90
0
σ1 stress (psi)
σ2 stress (psi)
σ12 stress (psi)
length (inch)

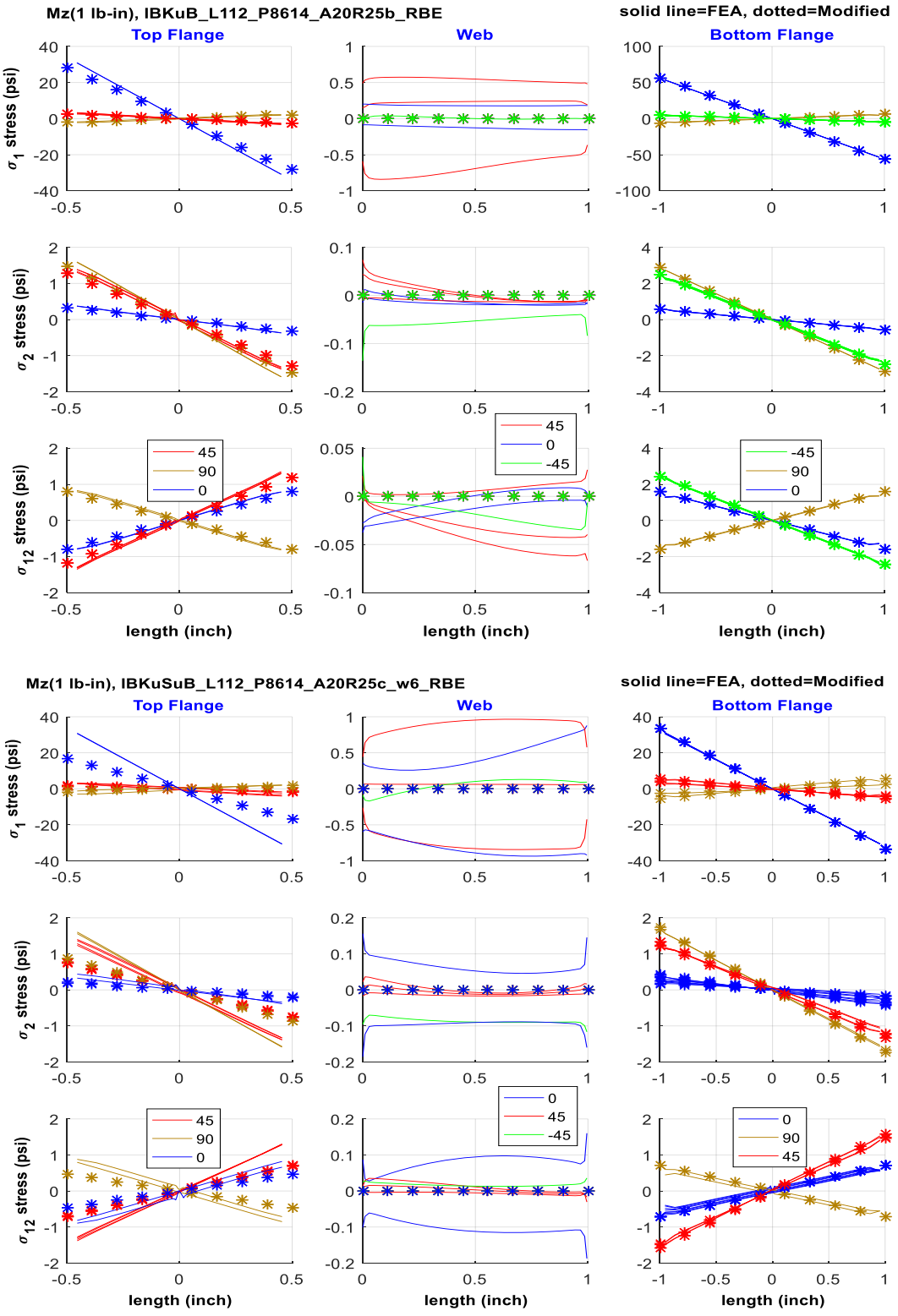

Figure B.7 Stress plots of tall, RBE3 model under M_z load

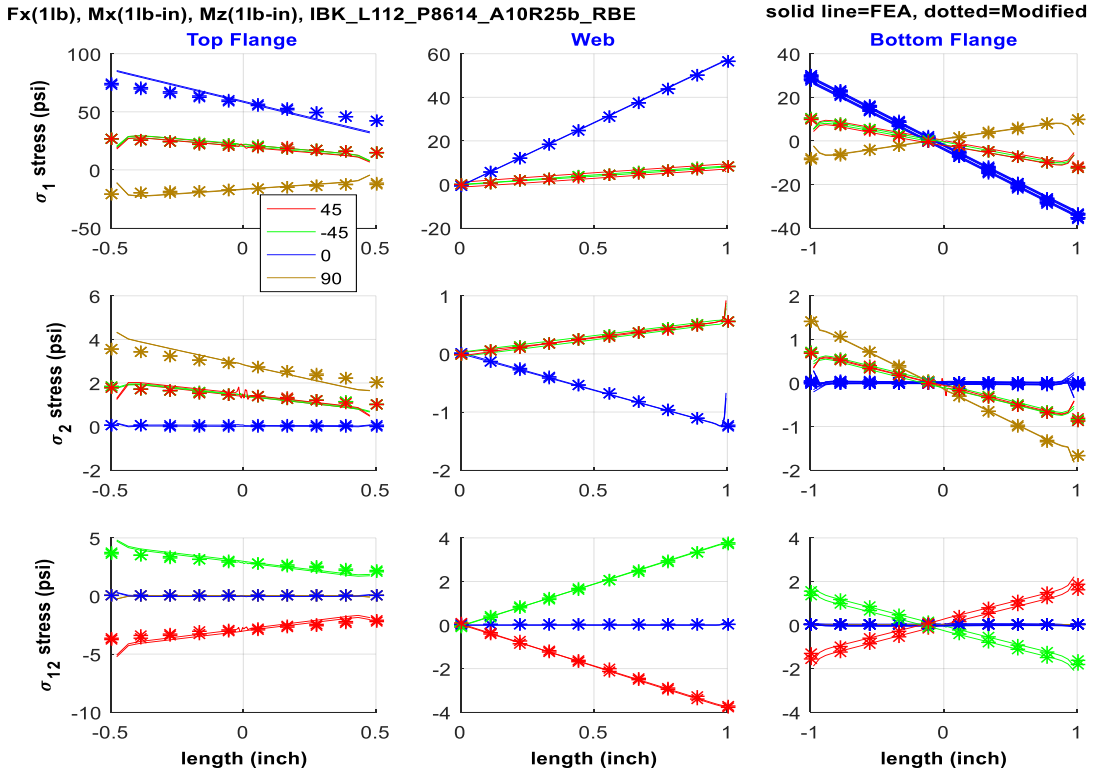
Fx(1lb), Mx(1lb-in), Mz(1lb-in), IBK_L112_P8614_A10R25b_RBE
solid line=FEA, dotted=Modified
Top Flange
Web
Bottom Flange
σ1 stress (psi)
σ2 stress (psi)
σ12 stress (psi)
45
-45
0
90
length (inch)

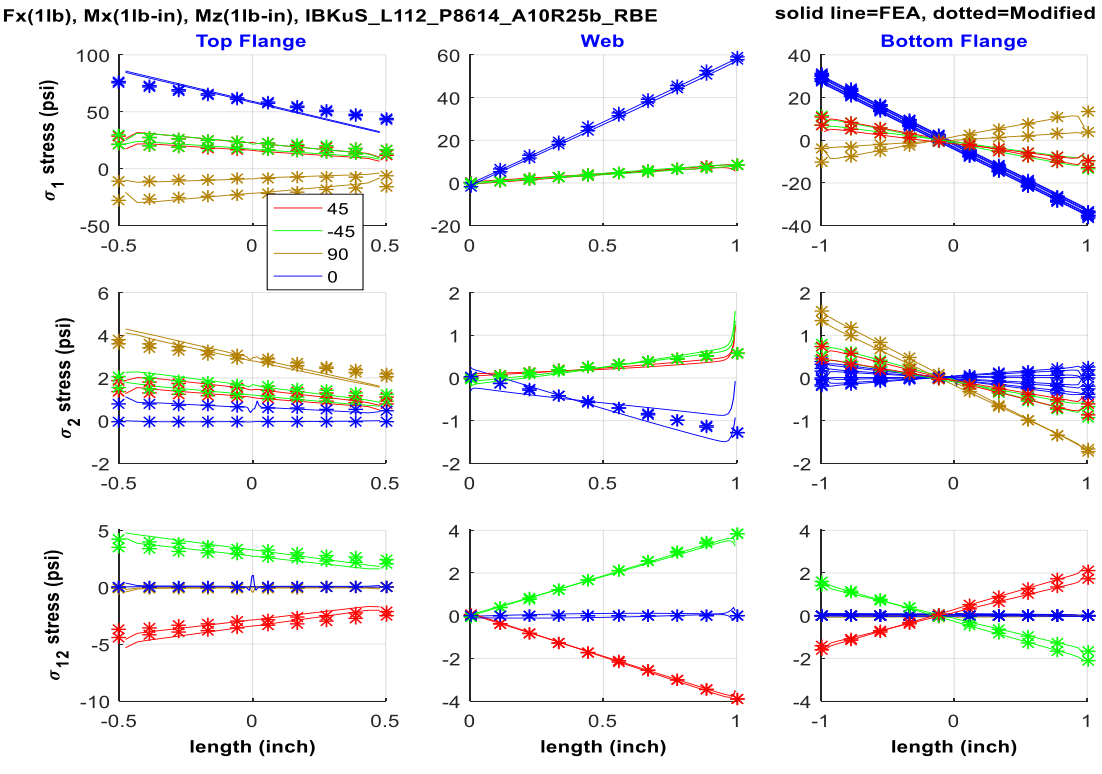
Fx(1lb), Mx(1lb-in), Mz(1lb-in), IBKuS_L112_P8614_A10R25b_RBE
solid line=FEA, dotted=Modified
Top Flange
Web
Bottom Flange
σ1 stress (psi)
σ2 stress (psi)
σ12 stress (psi)
45
-45
90
0
length (inch)

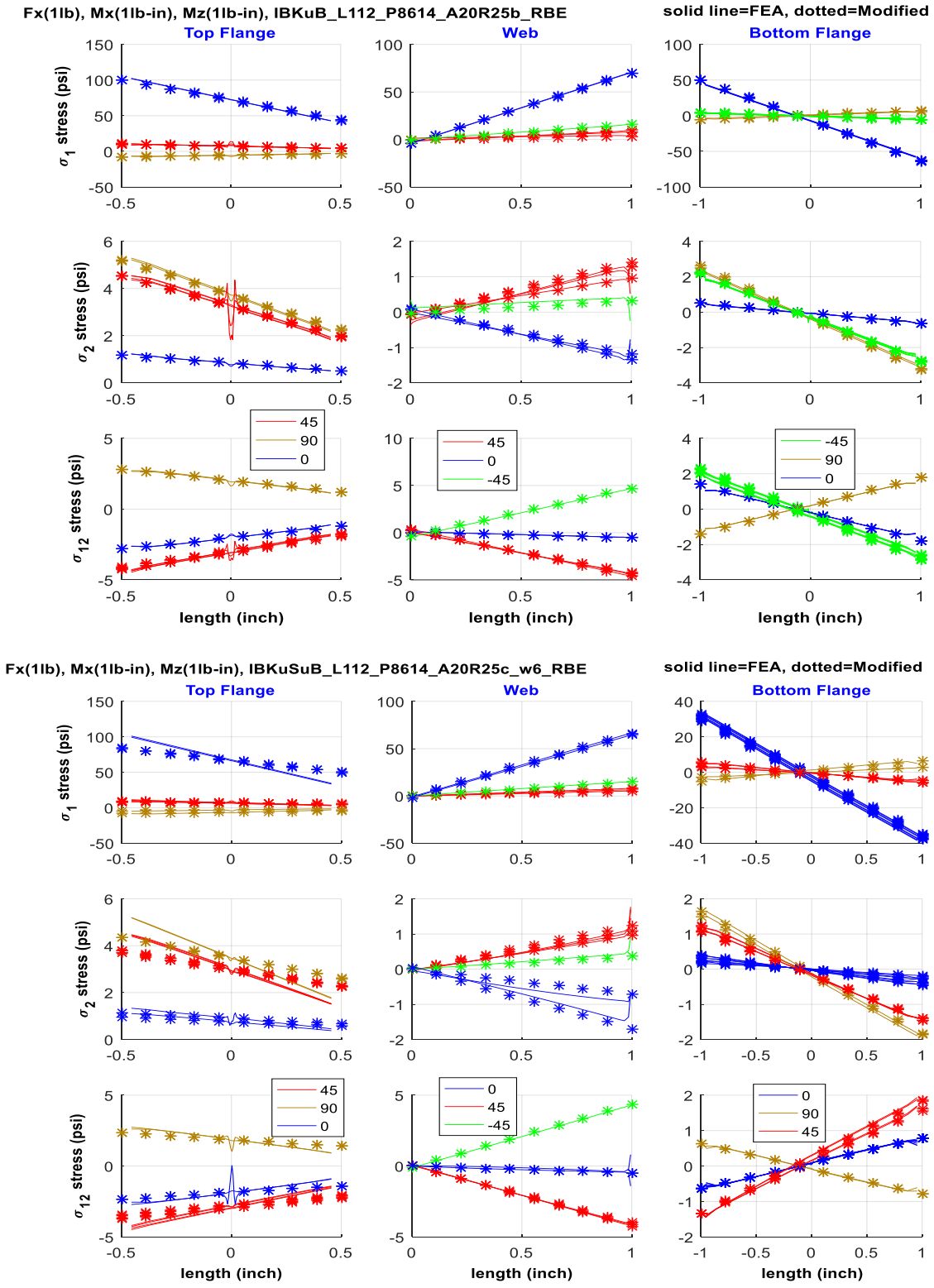

Figure B.8 Stress plots of tall, RBE3 model under axial load

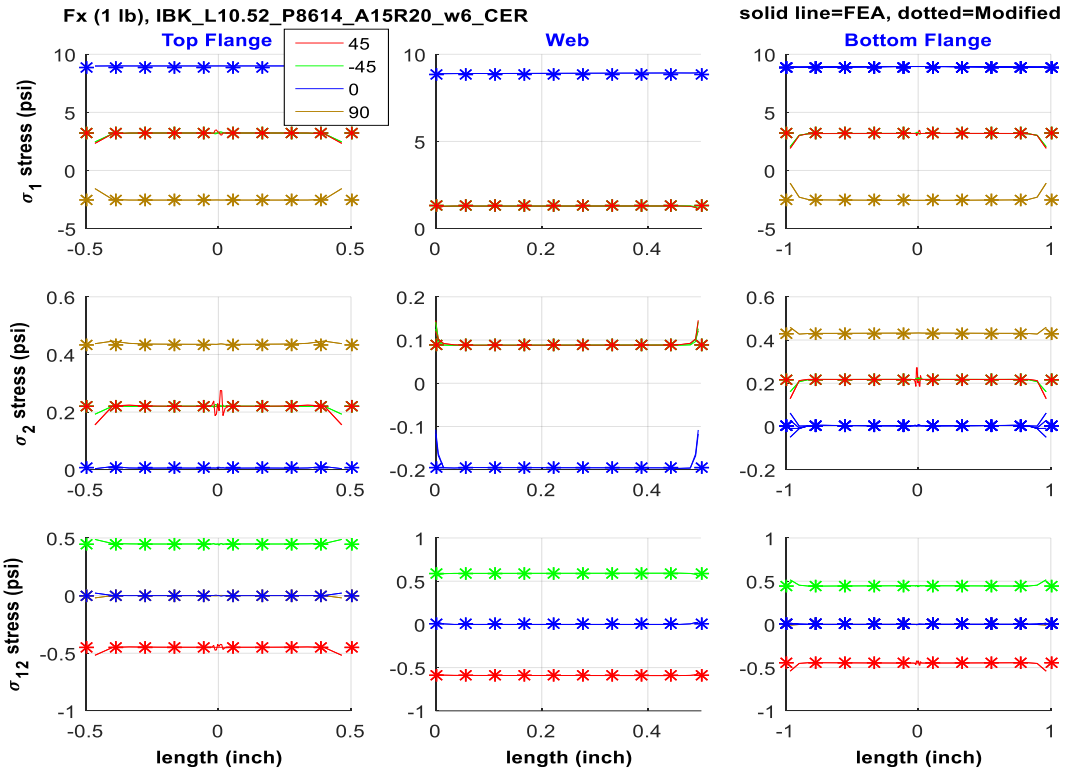
Fx (1 lb), IBK_L10.52_P8614_A15R20_w6_CER
solid line=FEA, dotted=Modified
Top Flange
Web
Bottom Flange
45
-45
0
90
σ1 stress (psi)
σ2 stress (psi)
σ12 stress (psi)
length (inch)

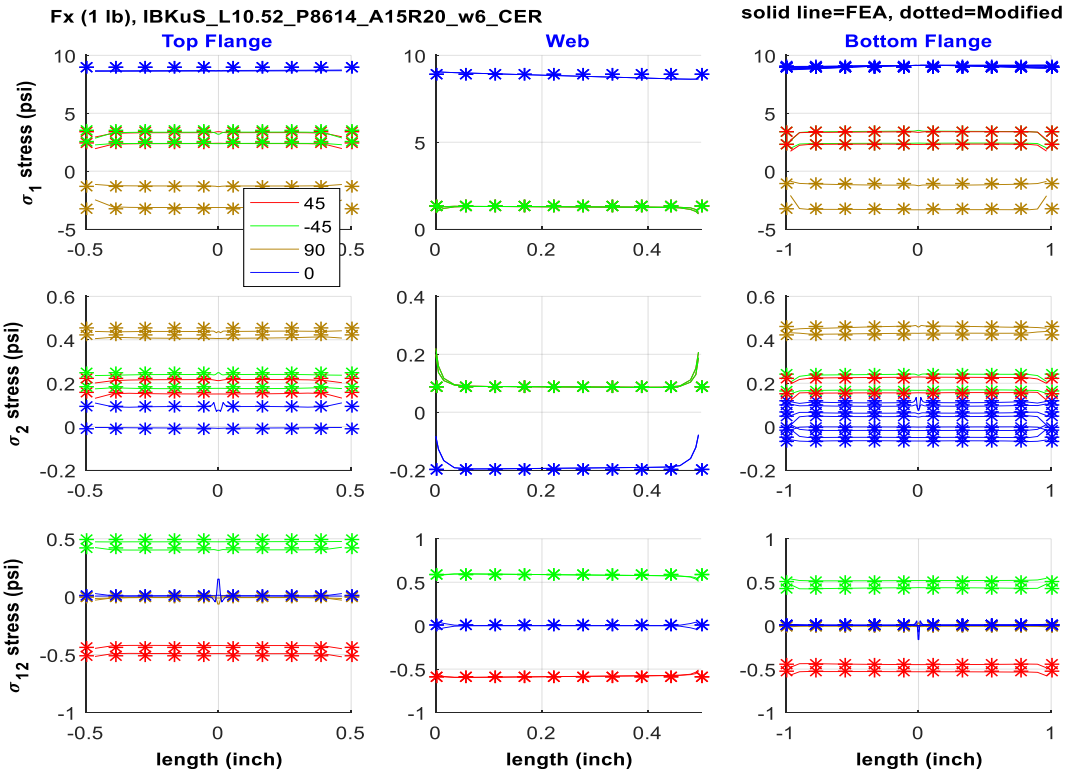
Fx (1 lb), IBKuS_L10.52_P8614_A15R20_w6_CER
solid line=FEA, dotted=Modified
Top Flange
Web
Bottom Flange
45
-45
90
0
σ1 stress (psi)
σ2 stress (psi)
σ12 stress (psi)
length (inch)

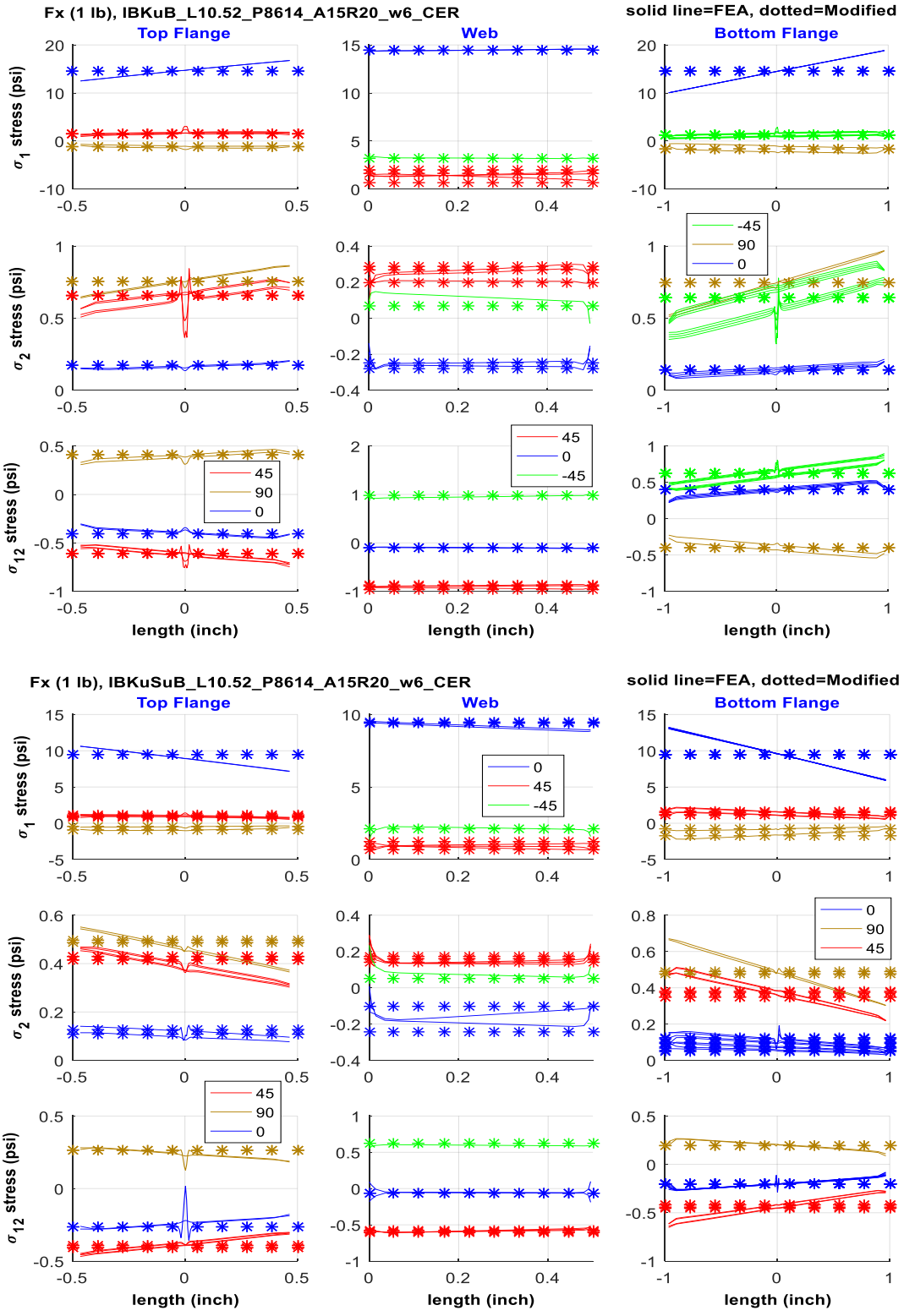

Figure B.9 Stress plots of short, CERIG model under axial load

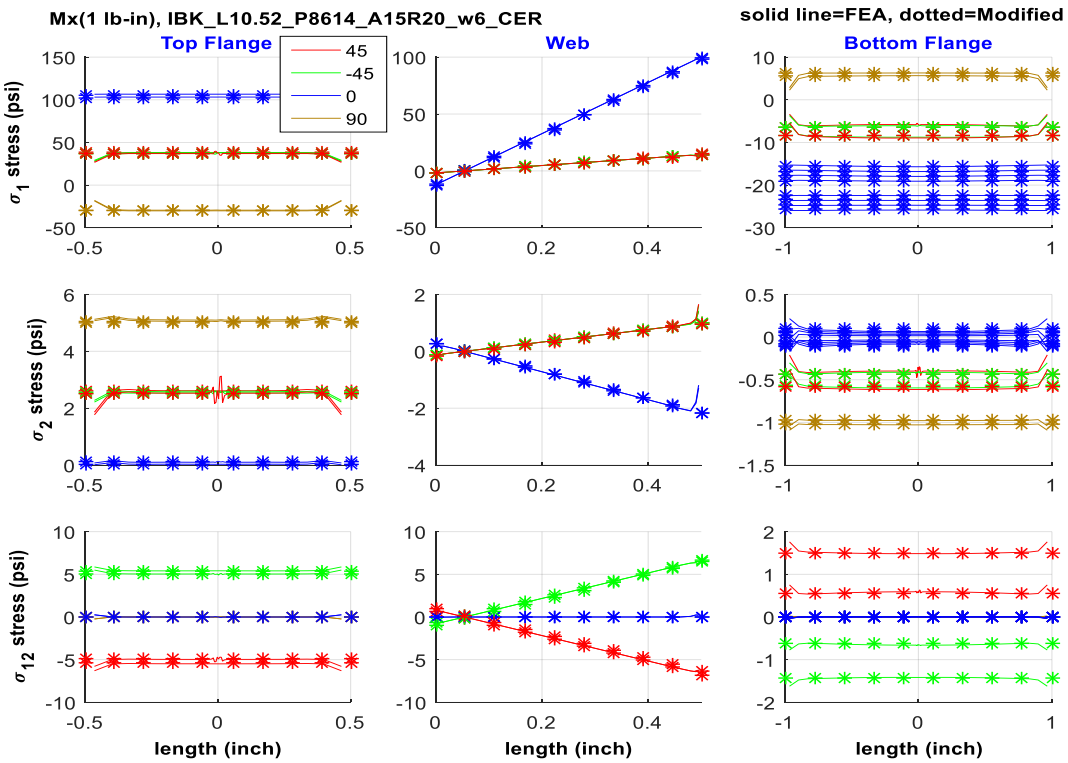
Mx(1 lb-in), IBK_L10.52_P8614_A15R20_w6_CER
solid line=FEA, dotted=Modified
Top Flange
Web
Bottom Flange
45
-45
0
90
σ1 stress (psi)
σ2 stress (psi)
σ12 stress (psi)
length (inch)

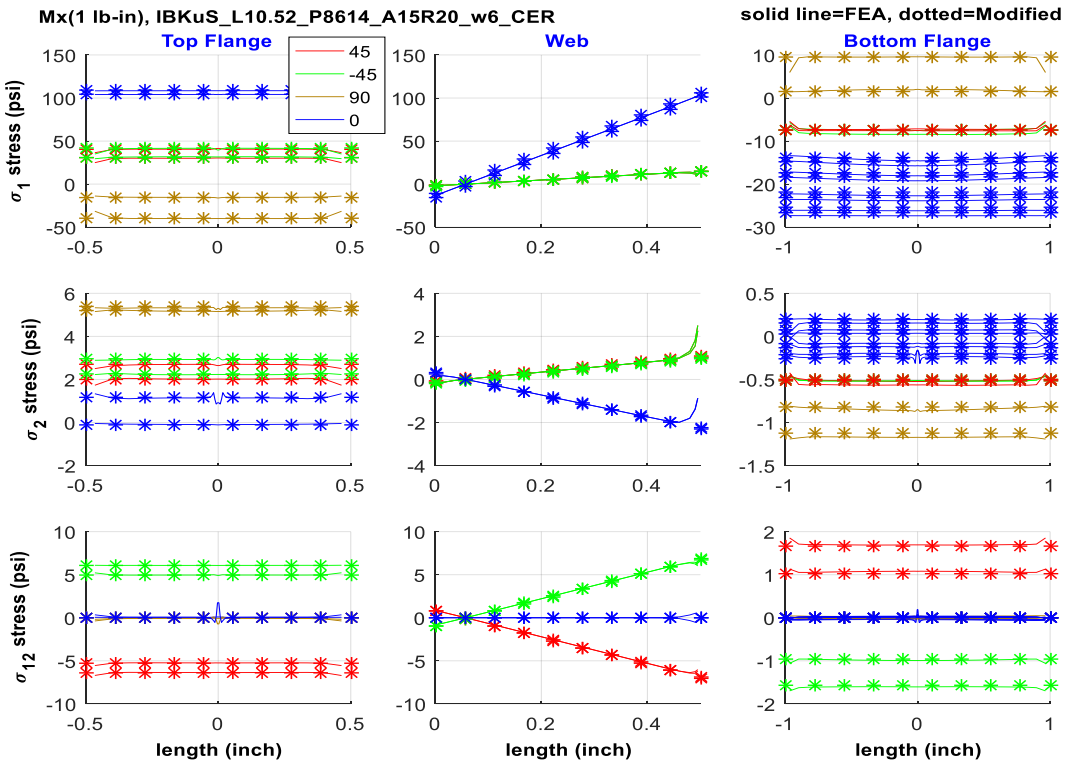
Mx(1 lb-in), IBKuS_L10.52_P8614_A15R20_w6_CER
solid line=FEA, dotted=Modified
Top Flange
Web
Bottom Flange
45
-45
90
0
σ1 stress (psi)
σ2 stress (psi)
σ12 stress (psi)
length (inch)

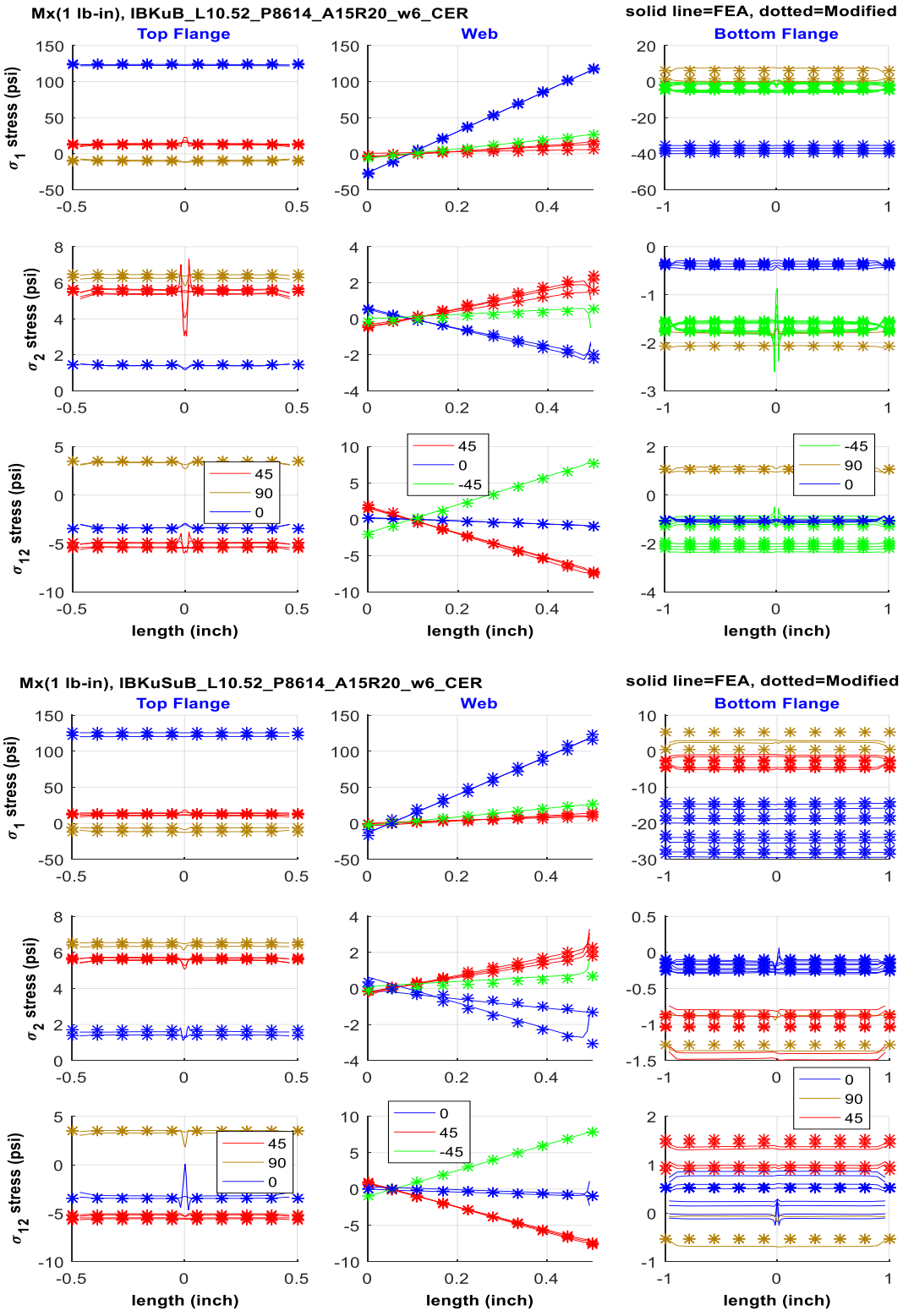

Figure B.10 Stress plots of short, CERIG model under M_x load

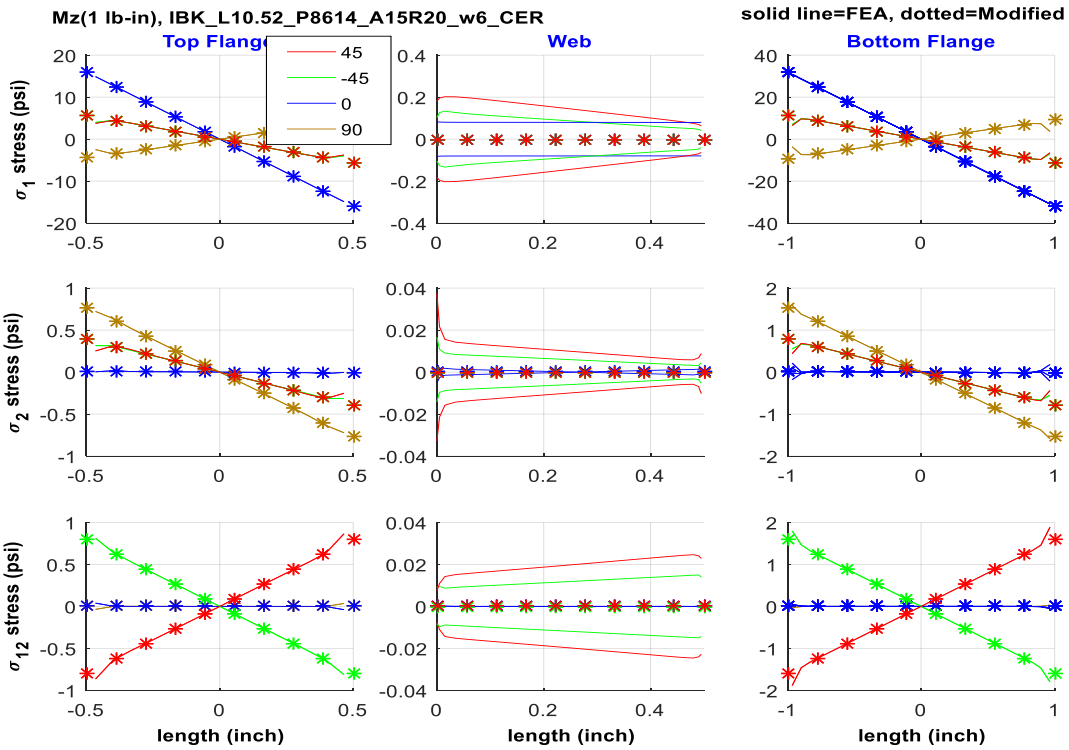
Mz(1 lb-in), IBK_L10.52_P8614_A15R20_w6_CER
solid line=FEA, dotted=Modified
Top Flange
Web
Bottom Flange
45
-45
0
90
σ1 stress (psi)
σ2 stress (psi)
σ12 stress (psi)
length (inch)

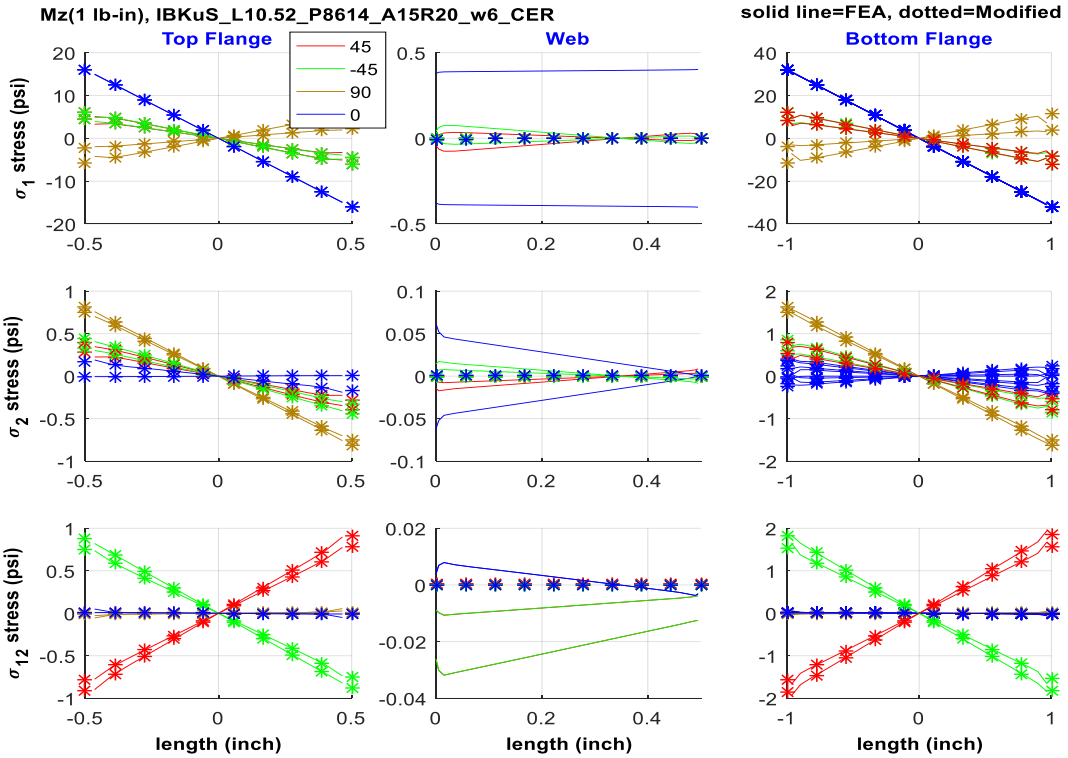
Mz(1 lb-in), IBKuS_L10.52_P8614_A15R20_w6_CER
solid line=FEA, dotted=Modified
Top Flange
Web
Bottom Flange
45
-45
90
0
σ1 stress (psi)
σ2 stress (psi)
σ12 stress (psi)
length (inch)

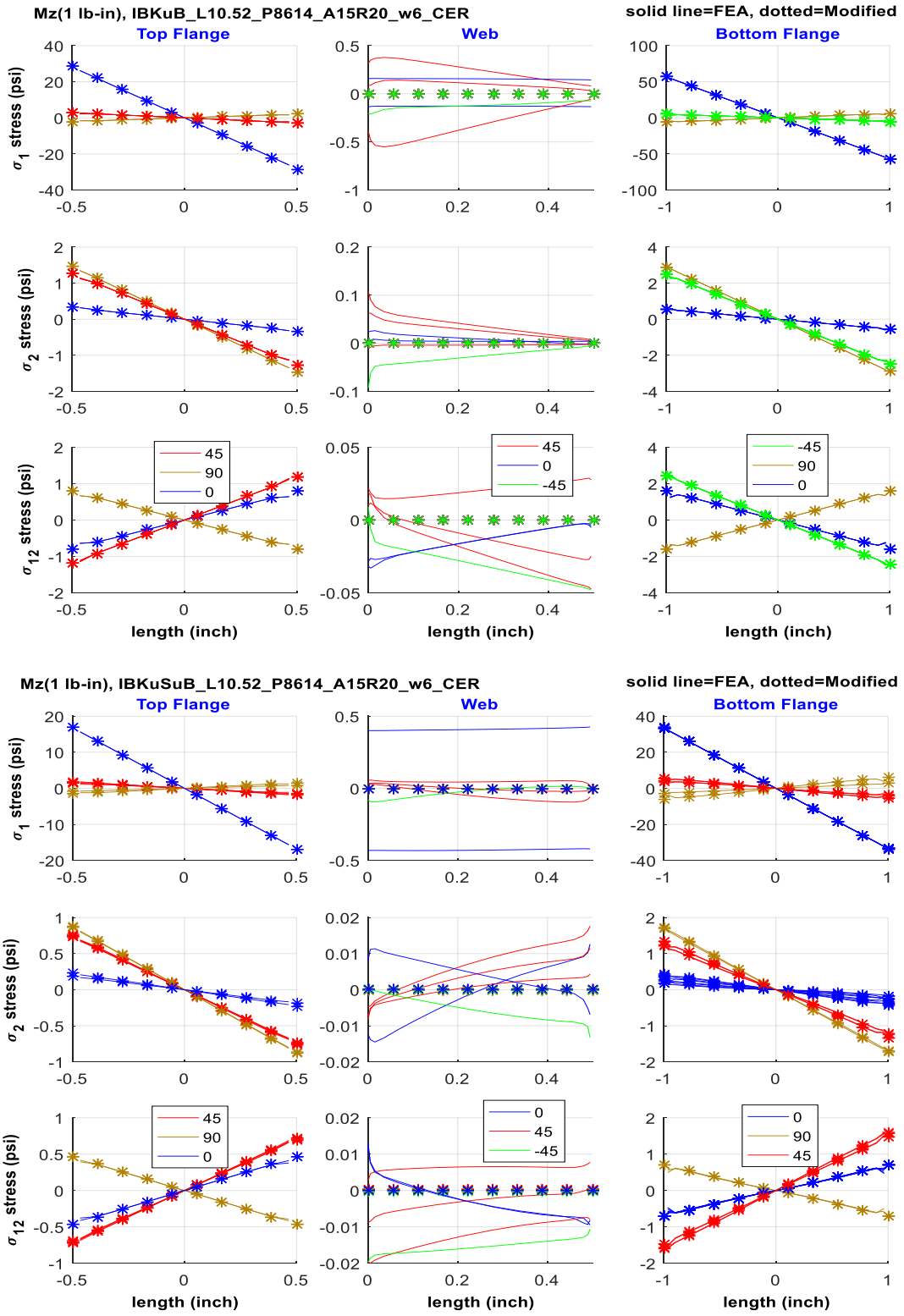

Figure B.11 Stress plots of short, CERIG model under M_z load

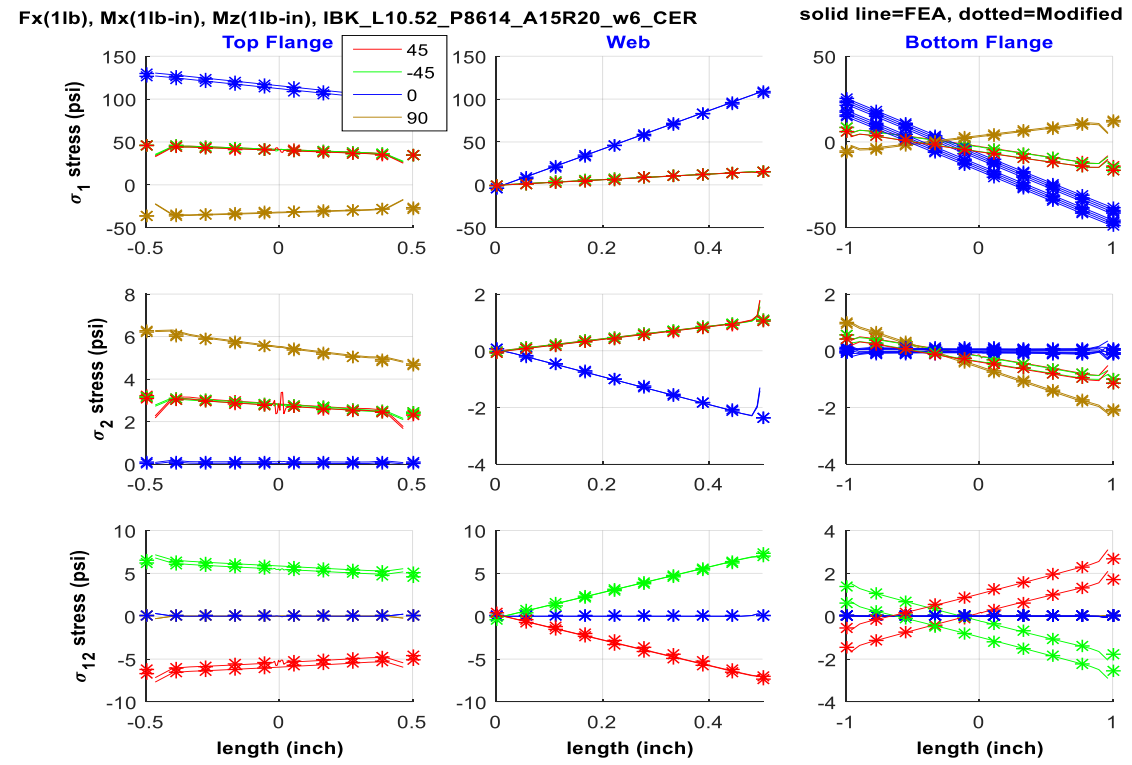
Fx(1lb), Mx(1lb-in), Mz(1lb-in), IBK_L10.52_P8614_A15R20_w6_CER
solid line=FEA, dotted=Modified
Top Flange
Web
Bottom Flange
45
-45
0
90
σ1 stress (psi)
σ2 stress (psi)
σ12 stress (psi)
length (inch)

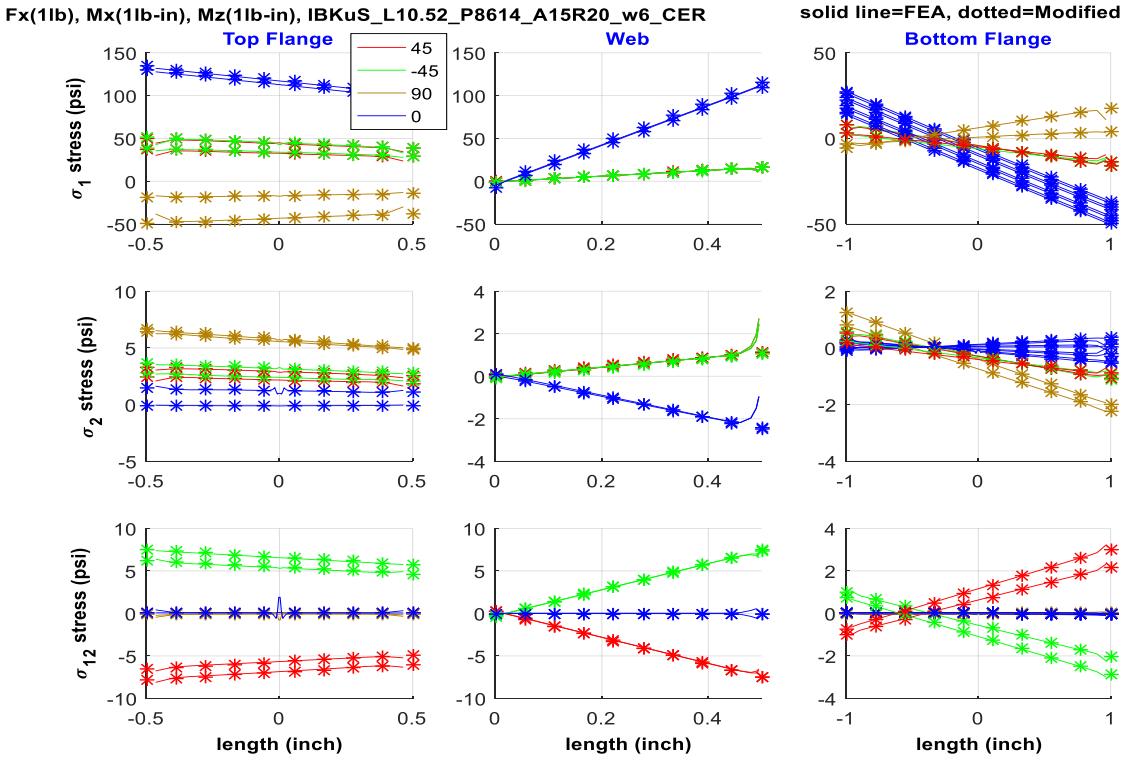
Fx(1lb), Mx(1lb-in), Mz(1lb-in), IBKuS_L10.52_P8614_A15R20_w6_CER
solid line=FEA, dotted=Modified
Top Flange
Web
Bottom Flange
45
-45
90
0
σ1 stress (psi)
σ2 stress (psi)
σ12 stress (psi)
length (inch)

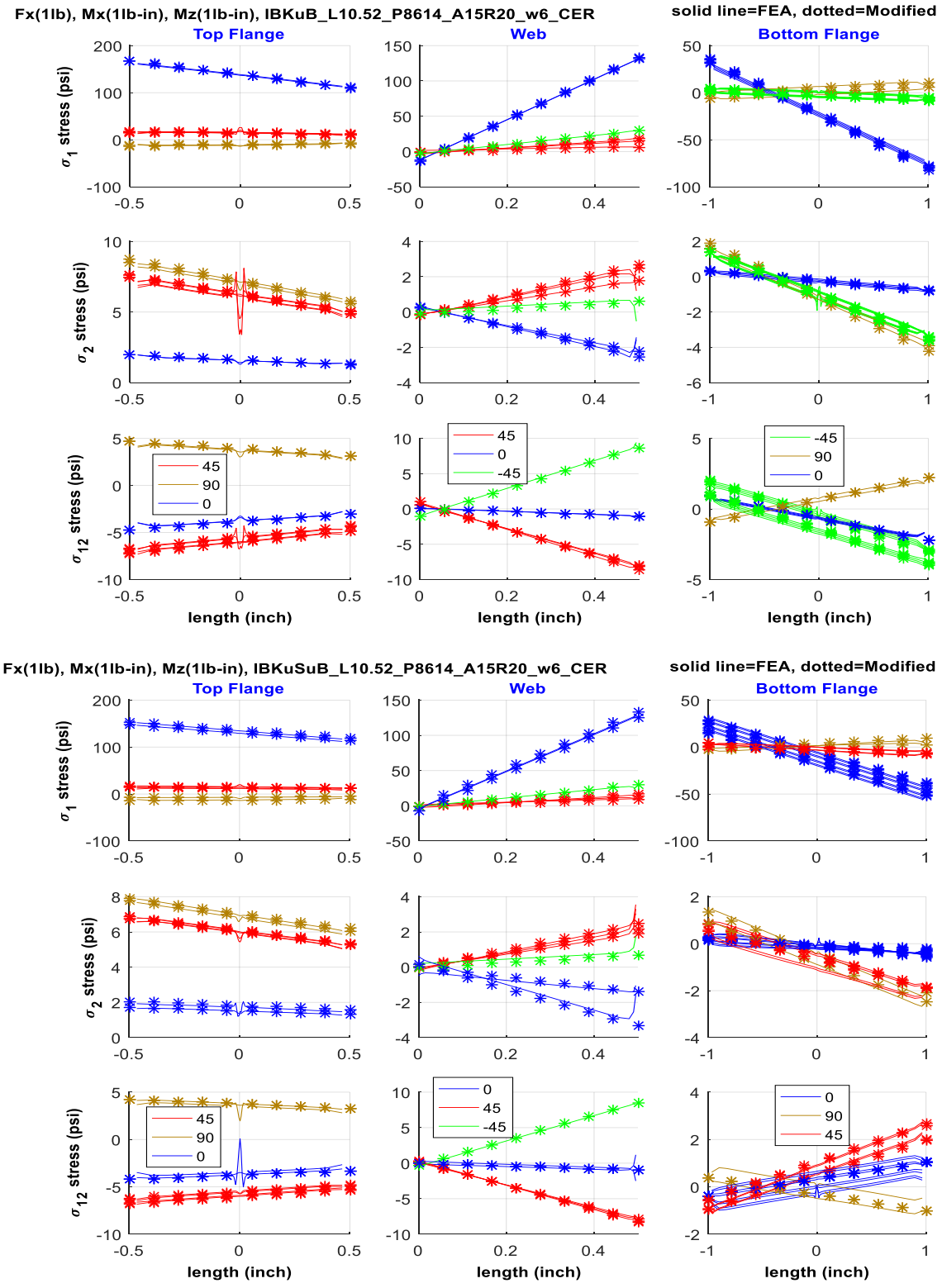

Figure B.12 Stress plots of short, CERIG model under combined load

APPENDIX C

MATERIAL CHARACTERIZATION FOR EXPERIMENTAL STUDY

Material used for the experimental study is characterized to check its properties against published data. The goal is to use the current properties found with the material characterization in the analytical and FEA analysis to conduct a correct comparison of flap-wise bending results with the experimental study.

FABRICATION OF COMPOSITE MATERIAL SAMPLES

Basic material properties are sought after which are the in-plane longitudinal and transverse elastic modulus, Poisson's ratio, and in-plane shear modulus. To test for these, the following coupons were made per ASTM standards. Material used was IM7-G/8552 which has a date of manufacture of January 2010. The manufacturer's prepreg storage life in freezer conditions for 8552 epoxy is 12 months [46].

2 rolls were used, one unidirectional and one [$\pm 45^{o}$]. Each roll was 1 foot in width. The same rolls are used for the wing fabrication and are discussed in more detail in that section.

Table C.1 Samples Tested for Material Characterization

Property	Layup	# samples	Width (in)	Length (in)
E_1, v_{12}	$[0]_{8T}$	3	0.5	9
E_2	$[90]_{8T}$	3	1	9
G_{12}	$[\pm 45]_{4S}$	3	1	9

Dimensions for each sample were checked and results are in Table C.2.

Table C.2 Measurement of Samples

Sample	Width	(in/k)			Thick	(in/k)		
measurement#	1	2	3	Avg	1	2	3	Avg
0 deg A	486	489	487	487.3	56	55	55.5	55.5
0 deg B	488	489	487.5	488.2	58	57	56.5	57.2
0 deg C	486	488	487.5	487.2	57.5	57.5	58	57.7
45 deg A	1007	1011	1008	1008.7	55	54.5	54	54.5
45 deg B	1014	1009	1009	1010.7	58	58.5	58	58.2
45 deg C	1003	1002	1003	1002.7	58	58	58.5	58.2
90 deg A	1013	1019	1022	1018.0	57	55.5	57.5	56.7
90 deg B	1014	1014	1015.5	1014.5	56.5	57	57	56.8
90 deg C	1018	1015	1015.5	1016.2	56.5	57	57	56.8

12x12 inch sample panels were laid up on one 3x1 foot aluminum panel which was 3/8 inch thick. A thin release film is first placed on the aluminum mold panel and wrapped over the composite panels after laid up. This is used so the composite panels do not stick to the mold or other material. The sample panels were placed side by side to fit on the panel. Once laid up, breather cloth is placed on top and a vacuum bag is placed and sealed around the whole mold with an air valve place on top where there is extra padding.

An autoclave is used to cure the samples. Program 3 is selected on the autoclave which is preprogrammed to cure the 8552 epoxy. The cure cycle is shown in Figure C.1 below. This includes a pre-soak temperature at 225^{o}F, a 2 hour constant temperature at 350^{o}F. The entire cycle takes approximately 5 hours.

Once the mold is placed into the autoclave, an air pressure line is connected from the autoclave to the vacuum bag to maintain a vacuum. This is until the pressure in

the autoclave reaches 30 psig. The autoclave applies a pressure on the mold during the whole cure.

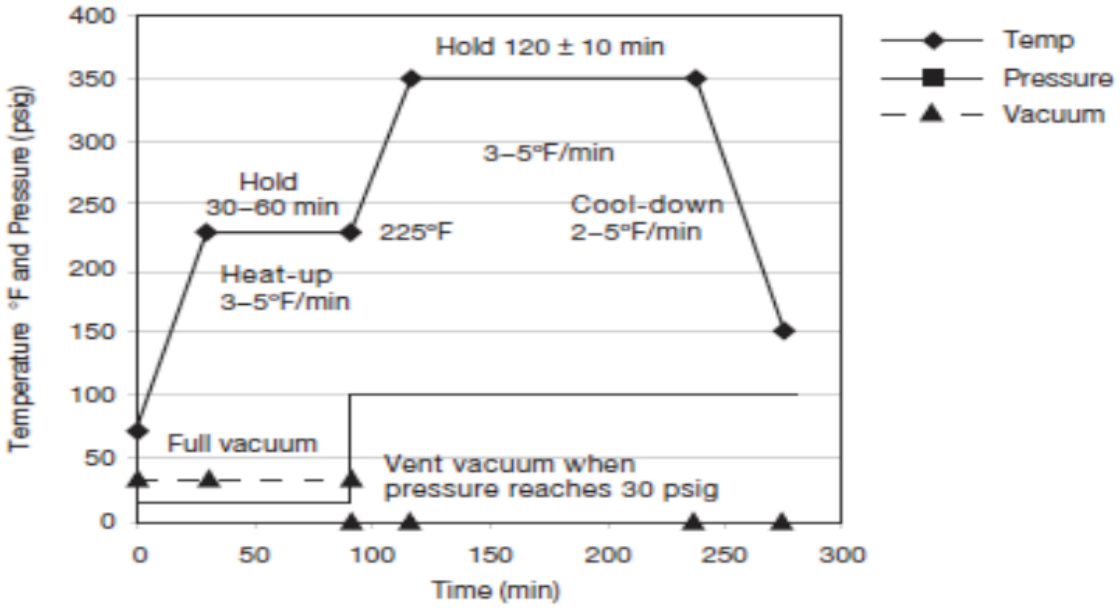

Figure C.1 Cure cycle for 8552 Epoxy

After the panels cured, resin flowed between them thus adhering the 12x12 inch panels together. A band saw was used to cut the 3 samples apart. A diamond embedded wet saw was then used on each 12x12 inch panel to cut the samples to the proper dimensions noted in Table C.1.

After cutting the composite samples, aluminum end tabs, 1.5 inches in length, were made and adhered to the ends of the samples with room temperature cure film adhesive. Next, Micro-Measurement strain gages were adhered to each of the $[0]_{8T}$ and $[\pm 45]_{4S}$ samples in the transverse direction. Cables were attached to the gages with solder pads to provide a stress relief. For longitudinal strain, an Epsilon extensometer is used. Prior to testing the samples a visual inspection is made of the samples and

crease marks were mainly noticed on the samples due to creasing of the release film during curing. Figure C.1b shows the samples that were tested.

Figure C.2 Coupons tested

TESTING OF COMPOSITE MATERIAL SAMPLES

A Shimadzu tensile test machine with a 5000 Newton load cell is used to test the samples. Each sample is loaded to approximately 4800 Newtons. The $[90]_{8T}$ samples experienced a brittle transverse fracture around 2000 Newtons though as seen in Figure C.2. The entire test setup is shown in Figure C.3.

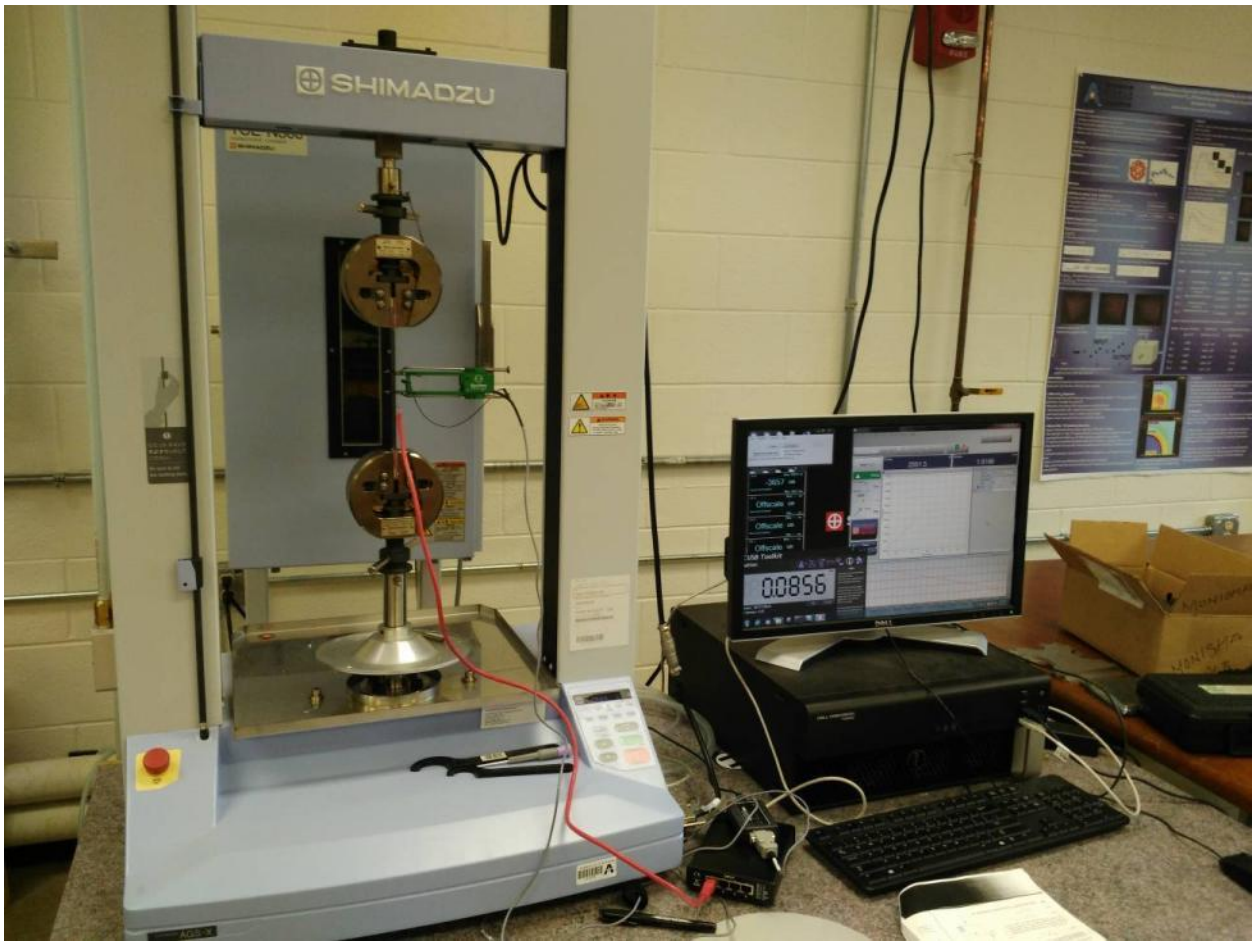

Figure C.3 Test setup for coupon specimens

Data was taken from the strain gages via a Micro-Measurements D4 Data Acquisition Conditioner and software. To record the data, a sample rate of 1 per 1/8 second was selected. The extensometer was connected to a DSCUSB-UL Conditioner then to Epsilon software. The sampling rate for the extensometer was 100 samples per second. Tensile test data was also recorded with Trapezium software in which a sampling rate of 100 samples per second was recorded. The strain gage software did not allow for a sampling rate of 100/second. A close-up view of the strain gages is shown in Figure C.4.

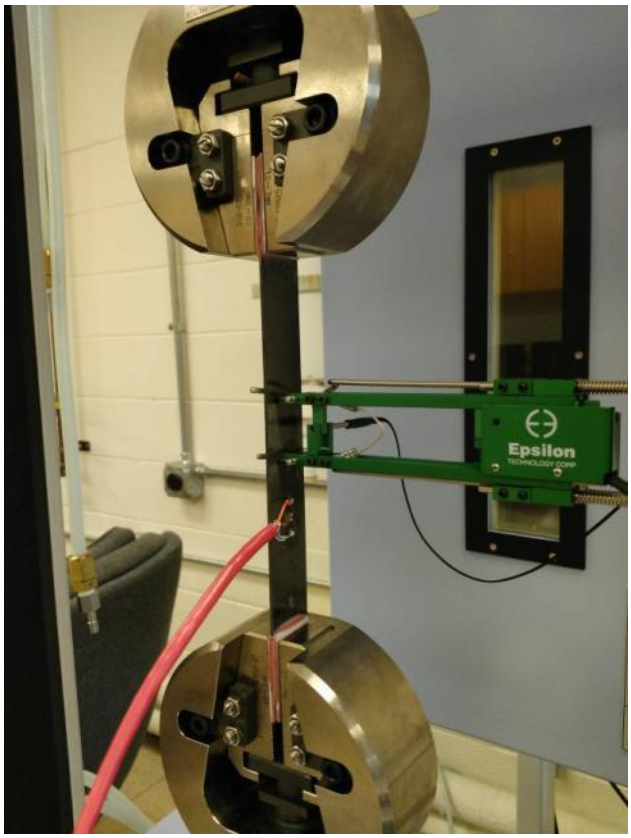

Figure C.4 Strain gages used in coupon tests

Readings of load, longitudinal and transverse strain were collected in Excel spreadsheets with time in seconds. MATLAB was used to merge the data together based on the time stamps. It is noted that although strain sampling rates were chosen, the actual interval between sampling varied and sometimes skipped samplings. Load sampling frequency was consistent at 100/second thus strain data was interpolated to the same rate. The strain and load data were not synchronized so the starting point was determined for each dataset by the end of the load. Strain data was stopped only after the load was stopped and held constant.

On one sample test, a slip of the extensometer was noticed after processing the data thus the test was run again. Figure C.5 shows the processed data illustrating the slip.

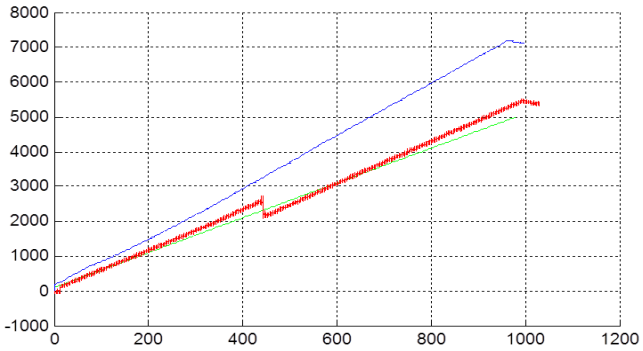

Figure C.5 Extensometer data in red showing a slip

Typical stress-strain curves are shown in Figure C.6.

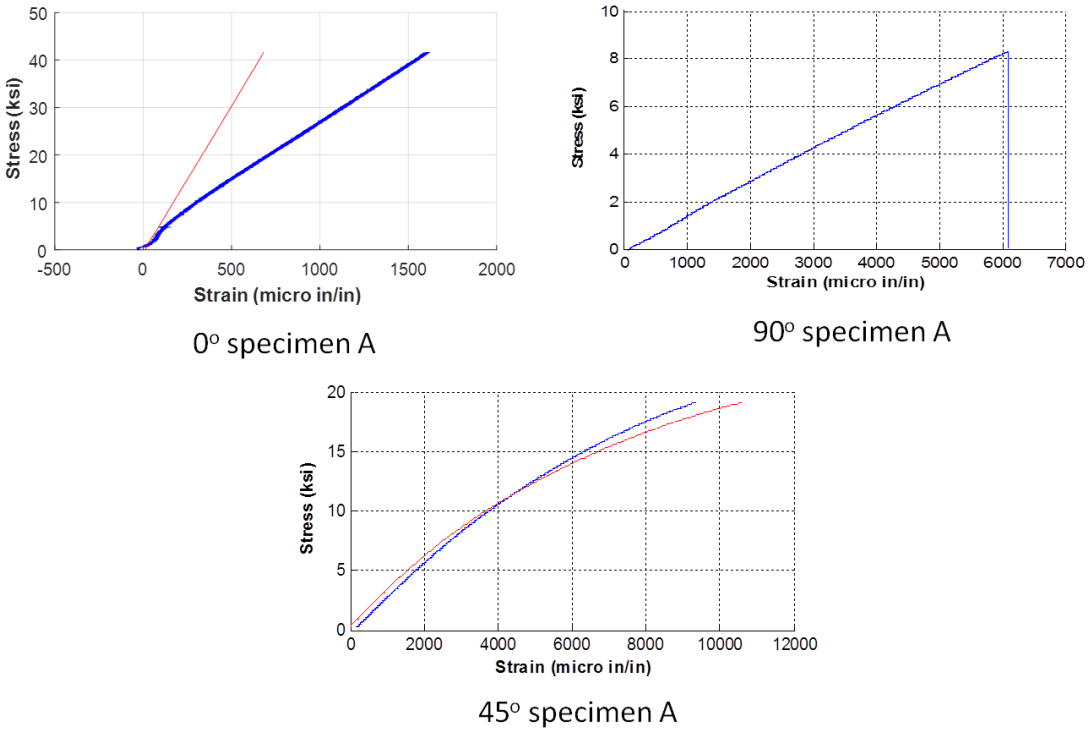

Figure C.6 Typical stress strain curves from each sample type

Figure C.3 Typical stress strain curves from each sample type

RESULTS OF COMPOSITE CHARACTERIZATION TESTING

Results for each property are found in Table C.3. The published properties are from Hexcel [46].

Table C.3 Material Property Results

Measured	0^o Layup		+-45 ^{o} Layup	90 ^{o} Layup
	E1 (Msi)	v12	G12 (Msi)	E2 (Msi)
Test 1	23.95	0.4607	0.787	1.42
Test 2	23.97	0.3716	0.763	1.47
Test 3	23.10	0.37797	0.814	1.35
Avg	23.67	0.403	0.788	1.413
Manufacturer Data	23.80	0.316	0.77	1.70
Difference	-0.5%	27.5%	2.34%	-16.9%

The E1 property is very accurate probably since this property is determined by the condition of the fibers and the fibers probably do not degrade much in the freezer. E2 has a drop of 17% probably partially due to the matrix being 6 years old.

Data and the data processing method were checked but no errors could be found to explain why the Poisson's Ratio is 34% greater and E2 is 17% less than manufacturer's data. Other published data [47] reports E2 values around 1.3 Msi which would then yield an error of 9%.

Due to of the limited amount of coupons tested, no volume fraction tests were performed. Since the material characterization yielded questionable property values, the manufacturer's data will be used for analysis considering the fiber volume fraction by

accounting for the ply thickness difference for obtaining estimated properties of the specimens made.

CALCULATION OF EXPERIMENTAL COMPOSITE PROPERTIES CONSIDERING FIBER VOLUME FRACTION

To compare the fiber volume fraction between the experimental wings and the standard material per specifications given by the manufacturer, The Rule of Mixtures approach is utilized. This will calculate the experimental $E_1^{\exp}, E_2^{\exp}, \nu_{12}^{\exp},$ and $G_{12}^{\exp}$ properties based on the change in volume, which is defined by the ply thickness, between the experimental and standard material. In Figure C.7, the standard material has a thickness of t_{ply}. The wing samples have the same amount of fibers per ply but the thickness is $t_{ply}^{\exp}$ and the matrix portion shown in Figure C.7 is no longer present in the fiber and matrix composite.

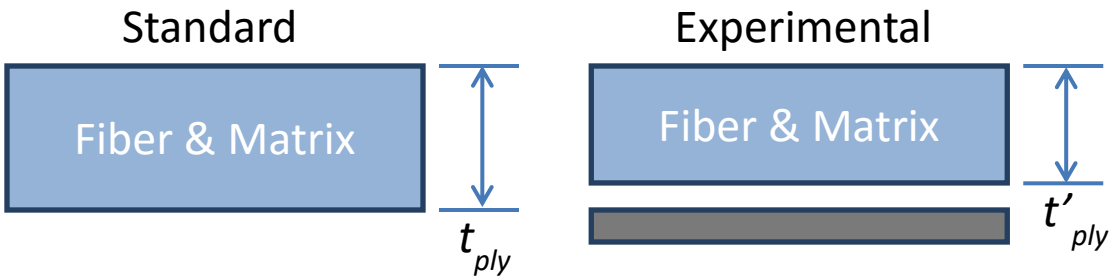

Figure C.7 Volumes of Standard and Experimental Composite

The properties of the experimental specimens can be found as follows where the standard properties are noted without use of a superscript, for example, E_1.

$$R = {t_{ply}}/{t_{ply}^{\exp}} \tag{C-1}$$

$$E_1^{\exp} = E_1 R + E_m(1-R) \tag{C-2}$$

$$E_2^{\exp} = 1\Big/\left(\frac{R}{E_1} + \frac{1-R}{E_m}\right) \tag{C-3}$$

$$\nu_{12}^{\exp} = \nu_{12} R + \nu_m(1-R) \tag{C-4}$$

$$G_{12}^{\exp} = 1\Big/\left(\frac{R}{G_{12}} + \frac{1-R}{G_m}\right) \tag{C-5}$$

where $G_m = \dfrac{E_m}{2(1+\nu_m)}$. (C-6)

Properties used and calculated are shown in Table C.4. The standard properties are from Hexcel, HexPly 8552 Epoxy Matrix Product Data sheet [46]. ν_m is found from similar epoxy material [48].

Table C.4 Experimental wing material properties based on fiber volume fraction analysis

Property	Standard Material	Experimental Wing Material	Units
E_m	0.677	-	Msi
ν_m	0.35	-	
t_{ply}	7.3	6.919	inch/1000
E_1	23.8	25.07	Msi
E_2	1.7	1.03	Msi
ν_{12}	0.316	0.314	
G_{12}	0.77	0.869	Msi

Properties used and calculated are shown in Table C.4. Since the wing ply thickness is less than the standard ply thickness, the experimental material has more fibers per unit volume thus $E_1^{\exp}$ is greater than E_1. Since there is less matrix or epoxy material per unit volume, $E_2^{\exp}$ is less than E_2. Thus, the experimental wing material properties listed in Table C.4 are used in the analytical analysis to compare flap-wise bending stiffness and axial strain with those from the experimental wing bending tests.

REFERENCES

1. Department of energy (DOE), “2013 Distributed Wind Market Report”, PNNL-23484, Washington, D.C.: U.S. Department of Energy, 2013.
2. European Wind Energy Association, “WINDFORCE 12: A Blueprint to Achieve 12% of the World's Electricity from Wind Power by 2020,” 2003.
3. Mishnaevsky, L., Brøndsted, P., Nijssen, R., Lekou, D., Philippidis, T., “Materials of large wind turbine blades: Recent results in testing and modeling,” Wind Energy, 15(1):83-97, 2012.
4. Griffith D.T., “The SNL 100-01 Blade: Carbon Design Studies for the Sandia 100-meter Blade,” Sandia National Laboratories, Albuquerque, Report No. SAND2013-1178, 2013.
5. Griffith D.T., Ashwill TD., “The Sandia 100-meter all-glass baseline wind turbine blade: SNL100-00,” Sandia National Laboratories, Albuquerque, Report No. SAND2011-3779, 2011.
6. Hoogenboom, P., Borgart, A., “Method for including restrained warping in traditional frame analyses,” Heron 50 (1), 2005.
7. Librescu, L., Song, O., “Behavior of Thin-Walled Beams Made of Advanced Composite Materials and Incorporating Non-Classical Effects,” Appl. Mech. Rev 44(11S),S174-S180, 1990.
8. Jung, S.N., Nagaraj, V.T., Chopra I., “Assessment of composite rotor blade modeling techniques,” J Am Helicopter Soc 44(3):188–205, 1999.

9. Sapountzakis, E. J., Dikaros, I. C., “Advanced 3D beam element of arbitrary composite cross section including generalized warping effects,” Int. J. Numer. Meh. Engng, 102:4-78, 2015.
10. Vlasov, V.Z., “Thin Walled Elastic Beams,” Fizmatgiz, Moscow, Translated by the Israel Program for Scientific Translations, 1959.
11. Libove, C., "Stresses and Rate of Twist in Single Cell Thin-Walled Beams with Anisotropic Walls,” AIAA Journal,Vol. 26, No. 9, Sept. 1988, pp. 1107-1118.
12. Gjelsvik, A., *The Theory of Thin-Walled Bars*, John Wiley & Sons, 1981.
13. Mansfield, E. H. and Sobey, A. J., “The fiber composite helicopter blade, Part 1 : Stiffness properties, Part 2: Prospects of aeroelastic tailoring,” Aeronaut. Q. 30, 413-449, 1979.
14. Bauld, N. R. and Tzeng, L., "A Vlasov Theory for Fiber-Reinforced Beams with Thin-Walled Open Cross Sections," International Journal of Solids and Structures, Vol. 20, No. 3, pp. 277-297, 1984.
15. Bauchau. O.A., Coffenberry, B.S., and Rehfield, L.W., "Composite Box Beam Analysis: Theory and Experiments," Journal of Reinforced Plastics and Composites, Vol. 6, pp. 25-35, 1987.
16. Bank, L. C. and Melehan, T. P., “Shear Coefficients for Multicelled Thin-Walled Composite Beams,” Composite Structures, Vol. 11, No. 4, pp. 259-276, 1989.
17. Chandra R, Chopra I., “Structural behavior of two-cell composite rotor blades with elastic couplings,” AIAA J. 1992; 30(12):2914-2921.
18. Smith, E.C., Chopra, I., “Formulation and evaluation of an analytical model for composite box-beams,” J Am Helicopter Soc 1991; 36(3):23–35.

19. Wu, X. X. and Sun, C. T., “Simplified theory for composite thin-walled beams,” AIAA J. 30, 2945-2951, 1992.
20. Kim, C., White, S.R., “Thick-walled composite beam theory including 3-D elastic effects and torsional warping,” Int J Solids Structures. 1997;34(31):4237-4259.
21. Librescu L., Song O., *Thin-walled composite beams: Theory and application*, Springer Science & Business Media, The Netherlands; 2006.
22. Song, O., “Modeling and Response Analysis of Thin-Walled Beam Structures Constructed of Advanced Composite Materials,” Ph.D. dissertation, Virginia Polytechnic Institute and State University, Nov. 1990.
23. Jung, S. N., Nagaraj, V. T., Chopra, I., “Assessment of Composite Rotor Blade Modeling Techniques,” AHS International Meeting on Advanced Rotorcraft Technology and Disaster Relief, Gifu. Japan, April 21-23, 1998.
24. Park I., Jung S.N., Kim D., Yun C.Y., “General purpose cross-section analysis program for composite rotor blades,” International Journal of Aeronautical and Space Sciences. 2009;10(2):77-85.
25. Wang, L., Liu, X., Guo, L., Renevier, N., Stables, M., “A mathematical model for calculating cross-sectional properties of modern wind turbine composite blades,” Renewable Energy. 2014;64:52-60.
26. Chen, H., Yu, W., Capellaro, M., “A critical assessment of computer tools for calculating composite wind turbine blade properties,” Wind Energy. 2010;13(6):497-516.
27. Bir, G., “Computerized Method for preliminary structural design of composite wind turbine blades,” Journal of Solar Energy Engineering 2001; 123: 372–381.

28. Hodges, D.H., Yu, W., “A rigorous, engineering-friendly approach for modeling realistic, composite rotor blades,” Wind Energy 2007; 10: 179–193.
29. Berdichevsky, V. L., “Variational-Asymptotic Method of Constructing a Theory of Shells,” PMM, Vol. 43, No. 4, 1979, pp. 664 –687.4Le.
30. Syed, K. A. and Chan, W. S., “Analysis of Hat-Sectioned Reinforced Composite Beams”, Proceedings of American Society of Composites, Sept. 2006.
31. Rios, G., “A Unified Analysis of Stiffener Reinforced Composite Beams With Arbitrary Cross-Section”, Ph.D. dissertation, Department of Mechanical and Aerospace Engineering, University of Texas at Arlington, Dec. 2009.
32. Parambil, J. C., and W. S. Chan, Lawrence, K. L., and Sanghavi, V. M., “ Stress Analysis for Composite I-beams by a Non-Conventional Method” Proceedings of the American Society for Composites 26th Technical Conference, Montréal, Canada, September26-28, 2011.
33. Sanghai, V. and Chan, W.S., “Torsional Analysis of a Composite I-beam”, Proceedings of the American Society for Composites 28th Technical Conference, 2013.
34. Kora, M., “Analysis of a Composite Beam with Unsymmetrical C Cross Section,” Master’s Thesis, Department of Mechanical and Aerospace Engineering, University of Texas at Arlington, Dec. 2015.
35. Christen, R. M., *Mechanics of Composite Material,* John Wiley &Sons, Inc. Chapter 2, 1979.

36. Pagano, N. J., “Exact Moduli of Anisotropic Laminates,” in Composite Materials, L. J. Broutman and R. H. Krock, eds., Vol.2, Mechanics of Composite Materials, G. P. Sendeckyj, ed., Academic Press, pp. 23-45, 1974.
37. Sun, C. T. and S. Li., “Three-Dimensional Equivalent Elastic Constants for Thick Laminates,” *Journal of Composite Materials*, Vol.22, pp 629-639, 1988.
38. Sun, C. T. and W. C. Liao., “Analysis of Thick Section Composite Laminates Using Equivalent Moduli,” *Journal of Composite Materials*, Vol. 24, pp 977-993, 1990.
39. Chan, W. S. and C. J. Chou., “Effects of Delamination and Ply Fiber Waviness on Equivalent Axial and Bending Stiffnesses in Composite Laminates,” *Composite Structures*, Vol. 30, 1995, pp 299-306.
40. Chan, W. S. and D. J. Chen., “Use of composite effective moduli for lumping layers in finite element analysis”, Proceedings of 37th AIAA/ASME/ASCE /AHS/ASC Structures, Structural Dynamics, and Materials Conference American Institute of Aeronautics and Astronautics, pp. 2199-2209, 1996.
41. Chan, W. S., C. Y. Lin, Y. C. Liang and C. Hwu., “Equivalent thermal expansion coefficients of lumped layer in laminated composites”, Composite science and Technology, Vol. 66, Pp2402-2408, 2006.
42. Rios, G., Chan, W. S., “A Unified Analysis of Stiffener Reinforced Composite Beams,” Proceedings of the American Society for Composites 25th Technical Conference, 2010.

43. Tavakoldavani, K., “Composite Materials Equivalent Properties in Lamina, Laminate, and Structural Levels”, Masters Thesis, Department of Mechanical and Aerospace Engineering, University of Texas at Arlington, Dec. 2014.
44. ANSYS 15.0 User Manual.
45. Rider, K., Pinas, N., Mayta, H., “Composite I-Beam Fabrication and Testing in Response to 14th Annual SAMPE Bridge Competition”, Senior Project, California Polytechnic State University, San Luis Obispo, 2011.
46. HexPly 8552 Epoxy Matrix Product Data, Hexcel, Feb. 2014.
47. Camanho, P. P. and Lambert, M., “A Design Methodology for Mechanically Fastened Joints in Laminated Composite Materials,” Composites Science and Technology, 66(15), 3004-3020, 2006.
48. Daniel, I.M., Ori, I., Engineering Mechanics of Composite Materials, second edition, Oxford University Press, New York, 2006.

BIOGRAPHICAL INFORMATION

Peter LeBoulluec received his Bachelor's and Master's degree at the University of Texas at Arlington (UTA) from the Mechanical Engineering Department. His Master's degree thesis is titled, "Optimization of Stiffener Attachment of Composite Skin Panels". Dr. LeBoulluec also received a Master's degree from UTA in the Bioengineering Department while researching hyperspectral imaging and photoacoustics.

Dr. LeBoulluec will pursue a career in structural analysis and design with an interest in composite materials.